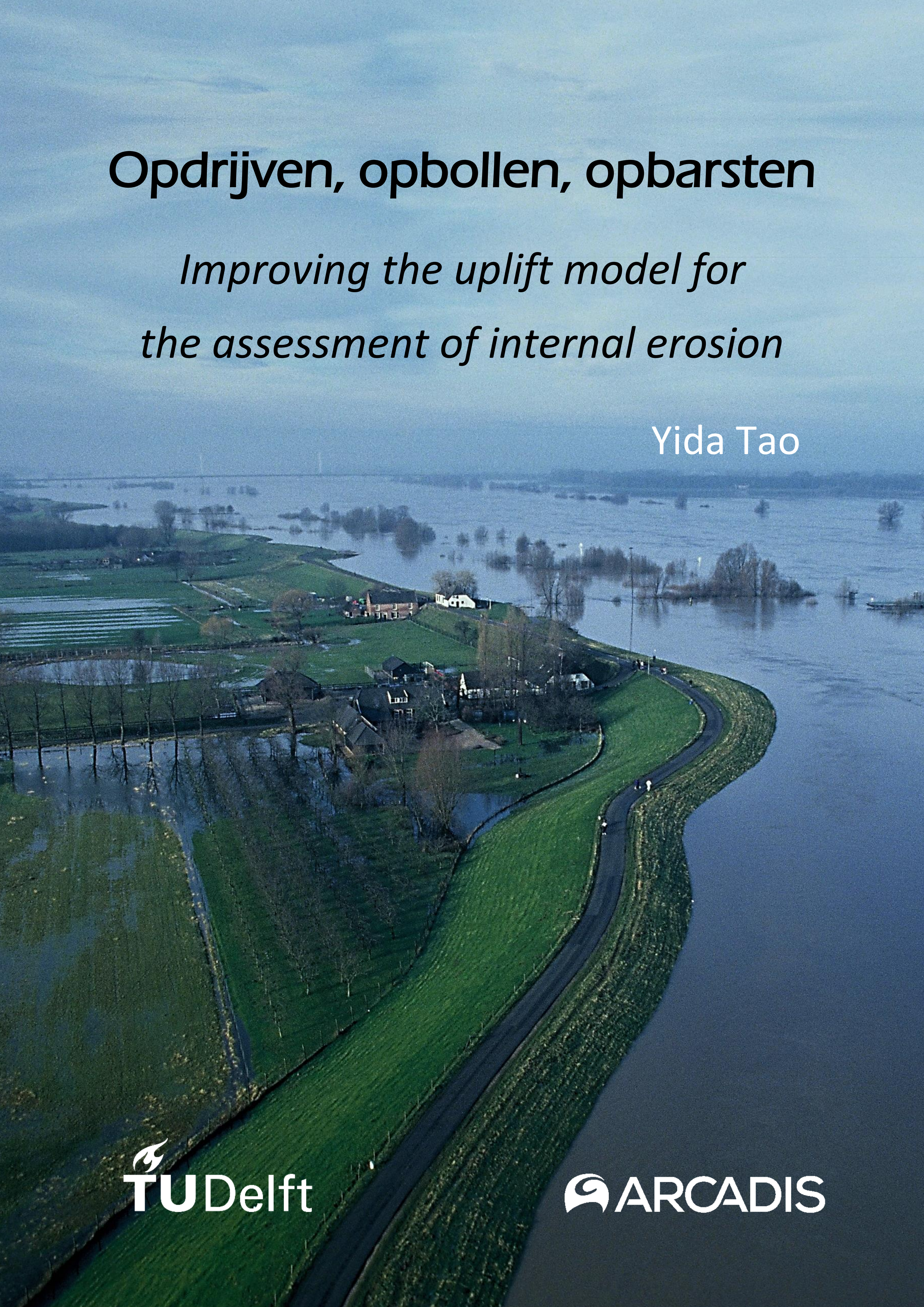

Opdrijven, opbollen, opbarsten

Improving the uplift model for the assessment of internal erosion

Yida Tao

Opdrijven, opbollen, opbarsten

Improving the uplift model for the assessment of internal erosion

by

Yida Tao

to obtain the degree of Master of Science
at the Delft University of Technology,
to be defended publicly on Friday July 3, 2020 at 13:00.

Student number:	4360125	
Project duration:	September 2nd, 2019 – July 3rd, 2020	
Thesis committee:	Phil Vardon,	TU Delft (chair)
	Myron van Damme,	TU Delft
	Robert Lanzafame,	TU Delft
	Rimmer Koopmans,	Arcadis
	Leo Kwakman,	Arcadis

Note on the title: Opdrijven, opbollen, and opbarsten are Dutch terms that all translate to uplift in English in the flood defenses context. These words invoke the behavior of the complex uplift phenomenon, and can be literally translated to floating, bulging, and bursting.

Cover image: High water in the Waal river near Beuningen (Rijkswaterstaat / Bart van Eyck, 1993)

TU Delft Delft University of Technology

ARCADIS Design & Consultancy for natural and built assets

PREFACE

This thesis was written for the completion of the Master Hydraulic Engineering at the Faculty of Civil Engineering and Geosciences, carried out during a graduation internship at Arcadis. The objective is to research the uplift phenomenon in the flood defences framework, and to improve the model and the assessment. I was engaged with the thesis work during the academic year of 2019-2020.

During this period, I learned many things. Not only did I develop my knowledge regarding the details of the WBI and many possibilities to capture the complex soil behavior, but also did I have to apply learning strategies, such as task orientation, self-monitoring, and reflection. The challenge was to keep focus during this long-term project, which turned out even more challenging when corona arrived in the Netherlands. Nevertheless, I am grateful for the experience of not only invited content-wise but also regarding the process. I enjoyed the freedom in the project, utilizing present knowledge, and steering the direction of new topics to research for my thesis.

Furthermore, I want to express my thanks to many people. First and foremost, to my supervisors Phil Vardon, Myron van Damme, and Robert Lanzafame at the TU Delft, for your gentle but elaborate feedback, thoughts and contributions, and encouragement to dive in the world of the strains and stresses in soils. Moreover, to Rimmer Koopmans and Leo Kwakman, for your enthusiasm on the subject, the critical remarks based on your extensive experience, and for giving an insight into the engineering practice at Arcadis. I liked the dynamics during the committee meetings and the variety in opinions about possible approaches. Additionally, the help provided by Ana Teixeira, Karolina Wojciechowska, Ruben Jongejan, Cor Zwanenburg, Timo Schweckendiek, Mark van der Krogt, Rahman Özdemir, and Wilfried Jansen Of Lorkeers was deeply appreciated. Lastly, thanks to David, family, and friends for the support and encouraging words. As one friend said it ‘since it’ll probably be your last thesis ever, don’t forget to enjoy’.

Before you lies the final product of this graduation project, I sincerely hope you will enjoy reading the thesis report.

Yida Tao
陶一达

Delft, June 2020

ABSTRACT

The Netherlands consist of low-lying areas, which are protected by dikes. Dike failure leads to inundation, and dike reinforcements are needed to ensure the safety level of the hinterland. Internal erosion is a frequent cause of failure, also known as piping or backward erosion. Uplift is considered a submechanism of internal erosion, together with heave and piping, where all three submechanisms must occur in order for the dike to reach a failure condition. The principle of the uplift phenomenon is straightforward: it occurs when high pore water pressures in the aquifer underneath a dike lift the cover layer, which is located at ground surface. If the pressure is great enough, the cover layer begins to float ('*opdrijven*'), and may also bulge ('*opbollen*') or crack ('*opbarsten*'). This thesis aims to investigate in what way the uplift assessment may be improved, both to describe the complex behavior better and to decrease the need for costly countermeasures.

Currently, the assessment for uplift is based on a vertical equilibrium, which relates to a floating condition of the cover layer. However, if the safety against uplift is insufficient, it is assumed that an exit point for the concentrated seepage pressures can form as a crack through the cover layer. In other words, crack formation is presumed to happen simultaneously with the increase in uplift pressure and is therefore not explicitly considered in the current assessment. In the thesis, the evaluation of uplift is conducted in two parts: by making explicit what the causes of uncertainty are in the current assessment, as well as by proposing a new model to better describe the complete uplift behavior. The causes of uncertainty are retrieved by conducting expert interviews and a review on the calibration equations for the semi-probabilistic safety factors. Furthermore, a conceptual model was developed to account for the crack formation. With the use of soil mechanics and simple numerical models the conceptual model was developed into a design criterion for the critical thickness of the cover layer.

Regarding the current assessment, based on the vertical equilibrium condition, many sources of conservatism were found. Since the uplift assessment for internal erosion is based on effective stresses, assuming that the phreatic surface lies at ground level is conservative, for thick cover layers (>3 m) with controlled water levels. Furthermore, some variables are highly uncertain and are therefore often applied (over)conservatively. Examples include the covariance of the model factor (10%) and the default value for the damping factor (μ = 0.8, cov = 10%). Lastly, the calibration of the required safety factor based on probabilistic outcomes for WBI2017 was reviewed. Three subjects for improvement are recommended. First, further evaluation on the model factor for uplift based on the vertical equilibrium is suggested for future research, since experts think a lower variation is more suitable. When 1% instead of 10% is substituted as the variation of the model factor, a decrease of about 5% in the prescribed safety factor is achieved for the calibration cases considered. Second, the calibration criterion, which is the fitting criterion through the gamma-beta point cloud (i.e., the relationship between reliability index and safety factor) is very conservative and not robust. A proposal to decrease this source of uncertainty is to either calibrate the required safety factors for a smaller, more homogeneous region or not to use the semi-probabilistic approach but the probabilistic approach instead. Thirdly, the calibration dataset contained many default values for the coefficient of variation, and subsequently, the outcome of the probabilistic results are conservative. For example, the thickness, effective volumetric weight, and damping factor had a coefficient of variation of 10% that was implemented for 36.4%, 27.6%, and 99.4% of the data set, respectively. More accurate data is recommended for a better representation of reality and may give better probabilistic outcomes.

The behavior of the uplift zone consists of a complex interplay between the length, load, and the vertical deformations. Based on literature and expert interviews, it was found most suitable to schematize the cover layer as a beam during the 'bulging-cracking'-stage. The beam length corresponds with the length of the uplifted zone and the upward pressure in this zone is constant, as confirmed by a 2D finite-difference groundwater flow model. The outcomes from Plaxis FEA show that the soil beam is able to withstand some upward load when non-linear deformation models are used. The formation of an exit point in the bottom of an intact cover layer occurs by a tensile opening or a shear crack located near the toe of the dike, at the end of the conceptualized beam model. This thesis proposes two equations for the critical thickness against tensile and shear cracks for this location; if the cover layer is thicker, cracking will not occur. Further research is needed to validate this conceptual framework and should also take time-dependency into account.

In this thesis, an updated framework of the uplift submechanism is presented to improve the overall assessment of internal erosion. It is recommended to evaluate the ‘floating’ and ‘bulging-cracking’ phases directly. In the ‘bulging-cracking’ phase, the forming of an exit point can either occur by a tension or shear failure.

CONTENTS

Nomenclature **vii**

1 Introduction **1**

1.1 Flood protection 1
1.2 Uplift as part of failure mechanisms 2
    1.2.1 Internal erosion 2
    1.2.2 Slope-instability 3
    1.2.3 Uplift assessment in other countries 4
1.3 Detailed phenomelogical description of uplift 4
    1.3.1 Water/load 5
    1.3.2 Soil/resistance 5
    1.3.3 Field observations 6
1.4 Research background 7
    1.4.1 Uncertainty qualification 7
    1.4.2 Causes for conservatism 7
1.5 Relevance 8
1.6 Scope 9
1.7 Problem statement 9
1.8 Research questions 10
1.9 Structure thesis and method 10

2 Current vertical stress model **11**

2.1 Uplift equations 11
    2.1.1 Advantages and disadvantages of each probabilistic method 12
2.2 Deterministic 13
    2.2.1 Vertical equilibrium 13
    2.2.2 Phreatic level at ground surface: upper limit 13
2.3 Fully probabilistic 14
    2.3.1 Model factor 14
    2.3.2 Damping factor 15
2.4 Semi-probabilistic 15
    2.4.1 Calibration procedure for the safety factor for uplift 16
    2.4.2 Calibration criterion 16
    2.4.3 Calibration dataset VNK2 17
    2.4.4 Sensitivity analysis 18
2.5 Discussion and recommendations 19

3 Uplift soil beam model **21**

3.1 Conceptual model: beam and relations 21
3.2 Model design - part A: water/load 22
    3.2.1 Literature 22
    3.2.2 Model selection and boundary conditions 23
    3.2.3 Geohydrological FD model outcome 25
3.3 Model design - part B: soil/resistance 26
    3.3.1 Literature 26
    3.3.2 Model selection and boundary conditions 28
    3.3.3 Plaxis FEM outcome 30
    3.3.4 Analytical approach for critical thickness against tensile cracks 36
    3.3.5 Analytical approach for critical thickness against shear cracks 38
3.4 Discussion 38

4 Improved uplift model: cartoon, fault tree, case 41
4.1 Visual representation of the phases in uplift 41
4.2 Uplift in the internal erosion framework 45
4.3 Case: Wijk bij Duurstede - Amerongen, the Netherlands 46
4.3.1 Introduction of the area 46
4.3.2 Uplift - floating (WBI2017) 47
4.3.3 Uplift soil beam model 50
4.3.4 Discussion on case outcome 51

5 Discussion 53

6 Conclusion 57
6.1 Main findings 57
6.2 Recommendations 59

Bibliography 61

Appendices

NOMENCLATURE

Greek Symbols

α	SHANSEP coefficient [-]
β	Reliability index
β_{cross}	Reliability index for the cross section
β_{norm}	Norm requirement or safety standard
γ_f	Shear strain at failure [-]
γ_{eff}	Effective volumetric weight of cover layer $[kN/m^3]$ $\gamma_{eff} = \gamma_{sat} - \gamma_{water}$
γ_{sat}	Saturated volumetric weight of the cover layer $[kN/m^3]$
γ_{up}	Safety factor for uplift [-]
γ_{water}	Volumetric weight of water $[kN/m^3]$
λ	Leakage factor $[m]$
λ_f	Leakage factor of the foreland $[m]$
λ_h	Leakage factor of the hinterland $[m]$
ν	Poissons ratio [-]
ϕ	Friction angle [°]
ϕ_g	Limit potential $[m]$ $(\phi_g = \gamma_{eff}/\gamma_w * D_{cover})$
ϕ_p	Potential of the polder $[m]$
ϕ_r	Potential of the river $[m]$
$\phi_{c,u}$	Equivalent downward pressure from the cover layer $[m]$
ϕ_{exit}	Hydraulic head at exit point in the aquifer $[m\,+$NAP$]$
ψ	Dilantancy angle [°]
$\sigma(z)$	Internal stress distribution of cover layer $[kPa]$

Latin Symbols

B	Toe-to-toe distance dike $[m]$
c	Cohesive forces $[kPa]$
c_{entry}	Entry resistance/river bed resistance $[s]$
d_w	Distance between the phreatic surface and the aquifer-aquitard interface [m]
D_{aq}	Thickness aquifer $[m]$
D_{cover}	Effective thickness of the cover layer $[m]$
D_f	Thickness foreland

E	Youngs Modulus/Stiffness/Elasticity [MPa]
e	Void ratio [-]
E_{50}	Triaxial stiffness [MPa]
E_{cover}	Elasticity of cover layer $[MPa]$
E_{oed}	Oedometer loading stiffness [MPa]
E_{ur}	Triaxial unloading/reloading stiffness [MPa]
h	Outside water level [m +NAP]
h_{exit}	Phreatic level at exit point [m +NAP]
h_{polder}	Phreatic level at hinterland [m +NAP]
k_{aq}	Horizontal hydraulic conductivity of aquifer $[m/s]$
k_{cover}	Vertical hydraulic conductivity of cover layer $[m/s]$
k_f	Hydraulic conductivity of the foreland
L	Uplift length $[m]$
L_f	Length of foreland $[m]$
L_h	Length of hinterland
m	SHANSEP power [-]
m	Stress dependency parameter for power relationship for Hardening soil model [-]
m_u	Model factor for uplift [-]
p^{ref}	Reference confining pressure for triaxial tests [kPa]
P_f	Failure probability [per year]
P_s	Phreatic storage in unsaturated core of the dike $[m^{-1}]$
r_{exit}	Damping factor at exit [-]
S_s	Elastic storage of water in soil skeleton $[m^{-1}]$
s_u	Undrained shear strength [kPa]
S_w	Swelling of dike material $[m^{-1}]$
x_{exit}	Distance mid-dike to exit point $[m]$
Z_{up}	Limit state function for uplift [-]

1

INTRODUCTION

This chapter presents the broader context of flood protection and provides the link to the uplift phenomenon in the flood protection assessment. Furthermore, this chapter sets out the research background and the relevance. It contains the problem statement and research question and finally, it provides an overview of the structure of this thesis.

1.1. FLOOD PROTECTION

The Netherlands consist of low-lying areas, which are protected by dikes from high water levels of seas, lakes, channels, and rivers. Failure of dikes leads to flooding of the hinterland. In the past, this lead to many casualties and severe economical damage. To prevent this in the future, the safety level is continuously assessed for each dike section. Where needed, countermeasures are subsequently applied. Internal erosion is a frequent cause of failure, also known as piping or backward erosion. Uplift is considered a submechanism of internal erosion, together with heave and piping. The principle of uplift is straightforward: Uplift occurs when high pore water pressures in the aquifer lift the cover layer. A typical situation is shown in Figure 1.1. There should be a cover layer, without holes, cracks or whatsoever, laying over a permeable layer.

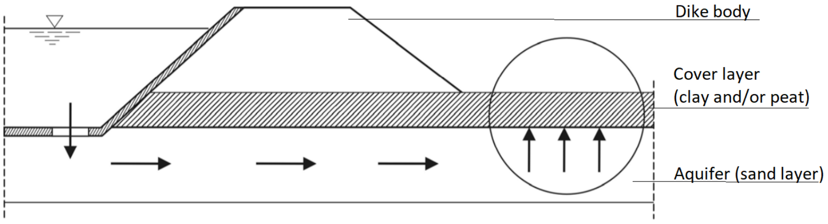

Figure 1.1: Typical situation in which uplift of a soil layer may occur (Bundesanstalt für Wasserbau, 2011) (adapted)

Over the years, problems regarding uplift are expected to grow. Van et al. (2005) put it as follows:

"Due to the natural land-subsidence and water level rise, the uplift phenomenon now occurs more frequently in the Dutch lowlands than in the past, seriously jeopardizing the safety of dikes. Consequently, costly countermeasures are required and existing houses have to be demolished in order to establish a proper safety against inundation."

This thesis focuses on the uplift submechanism in the failure mechanism of internal erosion. The aim of this thesis is to investigate in what way this uplift assessment could be improved to decrease uncertainties and the need for overconservative measures.

1.2. UPLIFT AS PART OF FAILURE MECHANISMS

In the flood defences framework, the uplift phenomenon is relevant in two failure mechanisms. These are explained in detail in this section. The main focus of this thesis is uplift as submechanism of internal erosion. However, uplift also plays a role in assessing the stability for the inner slope of a dike, of which there are interesting notes in literature found.

1.2.1. INTERNAL EROSION

Internal erosion is one of the ways a dike could fail. It stands for the forming of a through pipe, by which a dike looses its water-retaining function. The dike could also collapse into the pipe, which reduces the water-retaining height and the stability. The failure mechanism of internal erosion itself is complex, and shown in Figure 1.2.

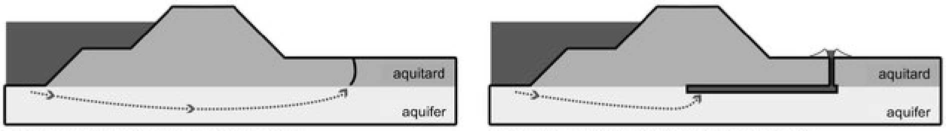

a) Excessive Pressure in Aquifer (Uplift)

d) Upstream Erosion ("Pipe Development")

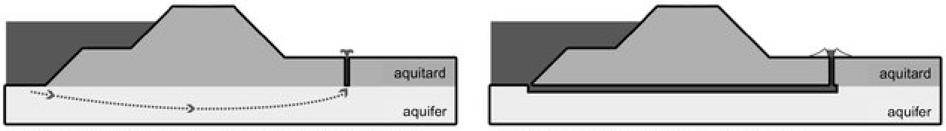

b) Groundwater Flow towards Leak in Aquitard (Seepage)

e) Continuous "Pipe", Accelerated Erosion

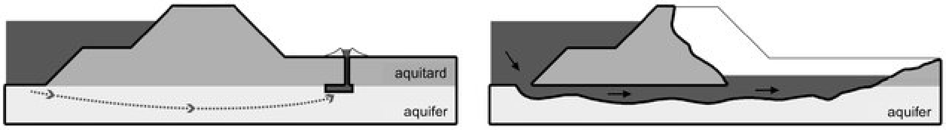

c) Start of Erosion of Granular Material (Heave)

f) Structural Collapse by Undermining

Figure 1.2: Phases of the internal erosion process (Schweckendiek et al., 2014a)

In the current Dutch guidelines WBI2017 (Ministerie van Infrastructuur en Milieu, 2017), internal erosion is split into three submechanisms, of which uplift is the first:

1. Uplift: due to high water pressures, the cover layer detaches from the aquifer and starts to float. It can cause cracks in the cover layer, thus bursting open. An exit point is formed.
2. Heave: concentrated seepage occurs through the exit point caused by the head gradient over the cover layer. When the threshold velocity of the seepage or the head gradient is exceeded, the water will carry sand grains to flow out of the exit point. In the field, a sand boil is observed. The database of piping contains over 300 field observations of sand boils in the Netherlands (RWS & USACE, sd).
3. Piping: with the water-sand mixture flowing out, the water pressure should be large enough to erode the whole length of the dike base to form a through pipe.

These three submechanisms as schematized in a parallel system, meaning that all three submechanisms must occur, will the dike fail on internal erosion. The corresponding fault tree is shown in Figure 1.3.

UPLIFT IN INTERNAL EROSION

In the Dutch safety assessment, vertical equilibrium (see Equation 2.1 (Ministerie van Infrastructuur en Milieu, 2017)) determines mathematically whether uplift occurs. The load for uplift is the excess water pressure in the aquifer pushing the cover layer, whereas the resistance against uplift contains the weight of the cover layer ('t Hart, 2018).

$$h_{polder} + (h - h_{polder}) * r_{exit} - h_{exit} = (\gamma_{sat} - \gamma_{water}) / \gamma_{water} * D_{cover} \tag{1.1}$$

't Hart (2018) states that the formation of cracks is dependent on the characteristics of the cover layer, such as thickness and elasticity. Also, it is noted that there is yet no difference in calculating the first submechanism, i.e. differentiation between uplift (vertical equilibrium) and the forming of cracks.

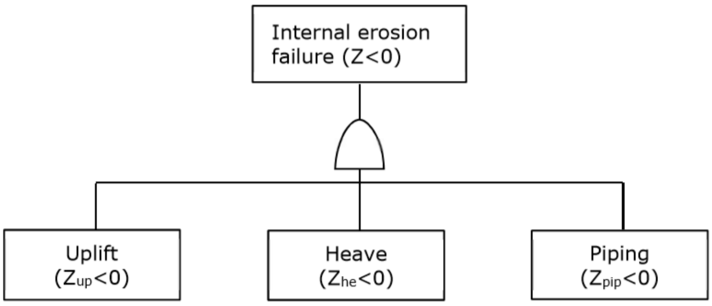

Figure 1.3: Fault tree for failure due to internal erosion (Jongejan, 2017)

Uplift here is a condition or requirement for the subsequent submechanisms to occur. If a dike stretch is found unsafe against uplift, one proceeds with calculating the safety against heave and piping. If a dike stretch is found safe against uplift, the dike stretch meets the safety standard of internal erosion as well.

COUNTERMEASURES AGAINST INTERNAL EROSION

When a dike trajectory is found to be insufficient safe for piping, a piping berm is applied in most cases. The toe-to-toe distance of a dike increases, which means the piping length increases. This is an economic measure, but requires room. Other, more expensive measures include a piping screen, relief wells, and gravel filters.

Intermezzo: definitions of internal erosion and piping

In the Netherlands, the internal erosion failure mechanism is also known as piping. The submechanism piping is also called backward erosion (Teixeira et al., 2016). 'Piping' can thus refer to two locations of the fault tree. In this report, the terms internal erosion and piping will be used in consistency with Figure 1.3. Note that in Germany, the term 'internal erosion' also contains the mechanisms suffosion and contact erosion, next to piping (Bundesanstalt für Wasserbau, 2011).

1.2.2. SLOPE-INSTABILITY

Apart from internal erosion, uplift also plays a role in the failure mechanism slope-instability, also referred to as macro-stability. Higher pore water pressures due to uplift decrease the strength of the cover layer and the aquifer-aquitard interface strength, by Terzaghi's principle of effective stresses and the Mohr-Coulomb relations.

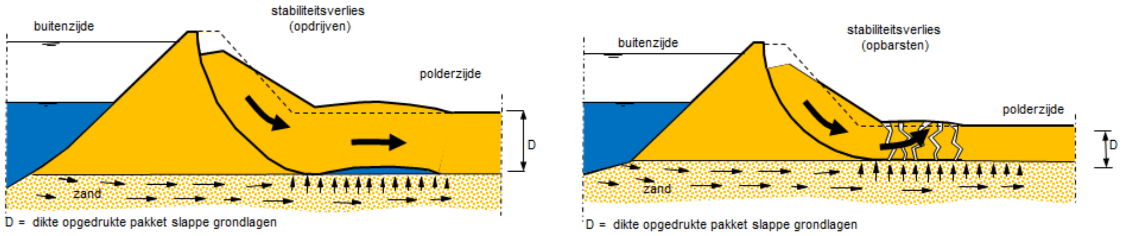

Figure 1.4: Uplift causing instability of the slope (Wiki Noodmaatregelen Waterkeringen, sd)

UPLIFT IN SLOPE-INSTABILITY

Unlike with internal erosion, uplift here is not a condition or requirement for instability to occur. However, a situation sensitive to uplift reduces the strength of the dike stretch and influences the model choice regarding the stability of the inner slope. Uplift situations with regard to macro-stability are assessed with the Uplift-Van model.

Similar to internal erosion, the determination on whether uplift occurs is checking the vertical equilibrium. However, subsequently, there is a difference made between a cracked and an intact cover layer. In Figure 1.4, this is shown schematically. In the case of an intact cover layer, the friction between the aquifer and the aquitard is fully reduced to zero in the calculations, but the cover layer contains strength. If the cover layer contains cracks, the overburden pressure from the aquifer is relieved. In this case, the shear strength of the cover layer is reduced to zero in calculations.

The criterion for cracking is a critical thickness of 4 meters. It is assumed that only thin cover layers, i.e. with a thickness of less than 4 meters, contain vertical cracks ('t Hart, 2018; Hoffmans, 2015; Zwanenburg et al., 2013). However, this value seems not to originate from any academic insights or statistical validation. It is based on expert judgment.

A statistical study on this value for the critical cover layer thickness has been performed by Ane Wiersma as part of a larger research (van Hoven et al., 2018). For this study, the cover layer thickness at the location of sand boils was determined. Generally, it is found that the cover layer is relatively thin at the case locations (n=289). In 10% of the cases, the cover layer was thicker than 4 meters. Unfortunately, this meant that the value of 4 meters could not be validated. However, the relatively large percentage of sand boils on thick cover layers could originate from the roughness and inaccuracy of geological data and subsurface maps.

COUNTERMEASURES AGAINST SLOPE INSTABILITY

Common countermeasures against slope instability are to construct a berm or to build shallower slopes, which reduces the sliding moment. Other measures are applying geotextile and/or structural elements to provide for extra resistance (Jonkman et al., 2018).

1.2.3. UPLIFT ASSESSMENT IN OTHER COUNTRIES

In other countries, uplift is assessed in a similar way. The German Code of Practice (Bundesanstalt für Wasserbau, 2011, 2013) refers to TAW (1999) for calculation guidelines. These are an older version of the guidelines in the Netherlands.

From the USA, the Bureau of Reclamation (US Bureau of Reclamation, 2018) describes: "The limit-state condition for uplift of the confining layer is reached when the uplift pressure at the base of the confining layer equals the weight of the confining layer (at the time the corresponding uplift pressure is applied)." Also, it is noted that blowout is a special condition: "Check for blowout in cases where there is limited depth of cover over the filter material, comparing the seepage head at the downstream face of the core to the weight of soil cover" (US Bureau of Reclamation, 2018). However, the criterion for limited depth is unspecified.

1.3. DETAILED PHENOMELOGICAL DESCRIPTION OF UPLIFT

This section deals with more detailed existing descriptions, experiences, and expert judgments on uplift to gain a better understanding of the real-world problem. The starting point is a description of uplift by 't Hart (2018) in *Phenomelogical description of the failure mechanisms in WBI.*

> The pore water pressure in the aquifer rises due to a higher river water level. When the pore water pressure in the aquifer on the inner side of the dike will exceed the weight of the cover layer, this will lift up. The cohesive cover layer has a vertical permeability, but orders of magnitude smaller than that of the aquifer. Due to the uplifting, cracks or holes will occur, through which the water will find a way to the ground surface. This open exit point is a condition for the subsequent submechanisms in internal erosion to occur ('t Hart, 2018).

The submechanism uplift in internal erosion requires the forming of an exit point. Without question, uplift starts with exceeding the vertical equilibrium, i.e. 'floating' of the cover layer. The behavior after this point, i.e. 'cracking' of the cover layer, does not have a convincing description or mathematical approach. The 'floating' and 'cracking' phases of the cover layer are therefore considered as two subsequent parts.

The interplay between the aquifer and the cover layer determines the uplift behavior. The description hereafter is split also into two parts: the pore water pressure in the aquifer, which is the load, and the subsequent reaction of the cover layer, which is the resistance. For uplift as part of macro-instability, a third part is considered being the stability and deformation behavior (Van and Molendijk, 1997). This third part is not considered in this thesis and the interests lie in the occurrence of an open exit point in uplift conditions.

1.3.1. WATER/LOAD

A head difference from the water side to the land side of a dike creates a gradient in the aquifer. The cover layer is schematized as a leaky layer and is subject to seepage. Through the aquifer, there is a flow rate, which magnitude depends on the thickness and permeability of the aquifer and the gradient of the head over the dike body ('t Hart, 2018).

BEFORE FLOATING

The point of interest here is to determine the head in the aquifer at the exit point. This pressure should not exceed the self weight of the cover layer. To find the head, different approaches exist. Analytical Dupuit flow equations are a good starting point when assuming that the groundwater flows predominantly horizontally (Jonkman et al., 2018). The parameters needed are listed in Table 1.1, as well as some secondary parameters neglected in the Dupuit equations. TAW (2004) provides a different formula based on mostly the same parameters. Equation 1.2 shows the Dupuit equation, and Equation 1.3 contains the leakage factor.

$$r_{exit} = \frac{\lambda}{L_f + B + \lambda} \exp((B/2 - x_{exit})/\lambda), \quad x_{exit} > B/2 \tag{1.2}$$

$$\lambda = \sqrt{k_{aq} * D_{aq} * D_{cover} / k_{cover}} \tag{1.3}$$

Furthermore, geohydrological models are available, e.g. MODFLOW, dgflow, iMODFLOW, and WATEX (Van Esch et al., 2016). Finally, conducting water-pressure-response-measurements for calibration purposes gain more precise results (Förster et al., 2012).

Table 1.1: Parameters regarding water/load (Förster et al., 2012; 't Hart, 2018; Jonkman et al., 2018; TAW, 2004)

Parameters for calculating ϕ_{exit} with Dupuit flow equations	Neglected parameters of minor importance
h: Outside water level h_{exit}: Phreatic level at hinterland k_{aq}: Horizontal hydraulic conductivity of aquifer k_{cover}: Vertical hydraulic conductivity of cover layer D_{aq}: Thickness aquifer D_{cover}: Thickness cover layer L_f: Length foreland B: Toe-to-toe distance dike x_{exit}: Distance mid-dike to exit point	c_{entry}: entry resistance/river bed resistance S_s: Elastic storage of water in soil skeleton P_s: Phreatic storage in unsaturated core of the dike S_w: Swelling of dike material Time dependent leakage factors for non-stationary situations

DURING FLOATING CONDITIONS

When the cover layer detaches from the aquifer, a gap exists between the aquifer and aquitard. The pressure from the water in this gap is the load acting on the cover layer, inducing bending moments and shear forces. Also, from coupled numerical analyses it is shown that the Dupuit equations to describe the head are insufficient (Hoffmans, 2015). The exact load under floating conditions is yet unknown.

1.3.2. SOIL/RESISTANCE

The weight of the cover layer defines the strength of the cover layer against uplift. Due to the excess water pressure, the cover layer can crack or burst. Currently, no difference made is in exceeding the vertical equilibrium and the forming of cracks.

BEFORE FLOATING

To determine whether the cover layer detaches from the aquifer and starts to float, the stresses in vertical direction are compared. In the left column of Table 1.2, the parameters currently applied on the vertical equilibrium analysis are listed. In the right column, other parameters are listed, which physically play a role, but have not been accounted for.

Table 1.2: Parameters regarding soil/resistance (Jongejan, 2017; 't Hart, 2018; Calle, 2002)

Parameters for calculating vertical resistance following WBI201	Parameters yet neglected
D_{cover}: Thickness cover layer γ_{eff}: Effective volumetric weight of cover layer	E_{cover}: Elasticity cover layer c: cohesive forces $\sigma(z)$: internal stress distribution

DURING FLOATING CONDITIONS

During floating conditions, the equilibrium conditions change from 1D to 2D. The cover layer is subjected to a load. This induces shear forces and bending moment in the cover layer in the uplift zone. In Figure 1.5, it is shown that the vertical downward forces consist of the shear forces at the end of the uplift zone, next to the self weight.

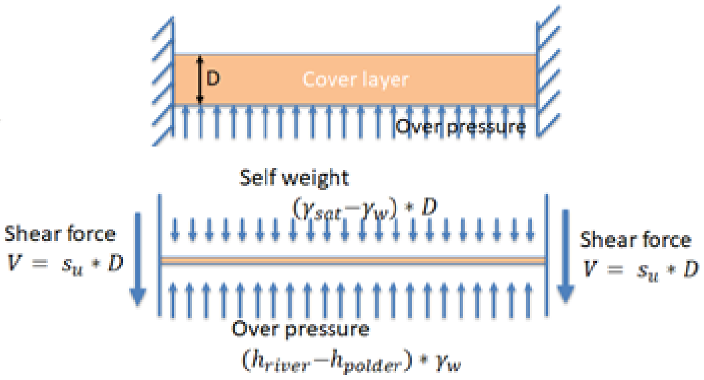

Figure 1.5: Beam schematization and vertical equilibrium

The crucial point here is to determine the crack forming. The maximum internal shear stresses are expected at the ends the ends of the beam, which is the beginning and the end of the uplift zone, which possibly leads to shear cracks. The bending moment causes horizontal stress changes. Cracks by horizontal tensile stresses are expected in the tensile zones, which in the middle at the top and at side at the bottom, see also Figure 1.6.

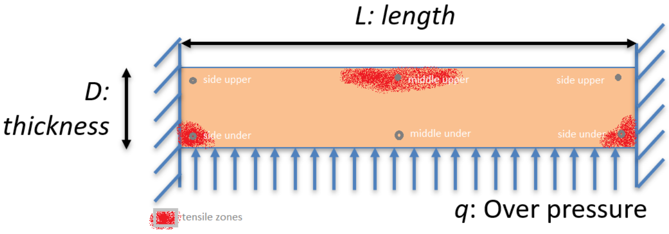

Figure 1.6: Points of interest in beam including zones with tensile stresses in horizontal direction

In the literature, cracking in the cover layer during uplift is linked to several parameters. For example, the thickness and elasticity of the cover layer are suggested ('t Hart, 2018). Also, cohesive forces and the internal stress distribution are mentioned for the uplift case (Calle, 2002). Furthermore, van Hoven et al. (2018); Hoffman (2019) mention the strength, stiffness, and thickness of the cover layer, as well as on the thickness and permeability of the aquifer as important parameters which determine whether uplift including cracks occurs, based on a numerical study using Diana FEA.

1.3.3. FIELD OBSERVATIONS

't Hart (2018) mentions that sometimes an uplifted cover layer exhibits wave-like movements upon entering. This means that there is a gap present between the aquifer and the cover layer, filled with water. TAW (2004) names 'blistering' as an observation phenomenon, which means that the cover layer is bulging. It proves that at uplift ('floating') conditions, floating only does not automatically lead to cracking of the cover layer.

Quite recently, similar observations are reported. In 2015, there was an infiltration test carried out at the Ommelanderzeedijk in Groningen, the Netherlands (Tissink, 2015). From reports, the following was observed during uplift conditions: the dike was 'dancing' upon entering, and the cover layer was 'bulging' (Dutch: 'opbollen') as well as tearing apart.

1.4. RESEARCH BACKGROUND

From Arcadis, the question has risen whether there is currently too much conservatism in the uplift assessment regarding internal erosion. Therefore, this section starts with the definition of conservatism, which is closely related to uncertainties. Then, a general division in uncertainties is given. This is followed by causes for conservatism regarding to uplift, linked to the uncertainty quantification.

Intermezzo: definition of conservatism

Conservative (adj.) means cautiously moderate or purposefully low. In engineering practice, a conservative value means being on the safe side of a parameter, taking into account the uncertainties. The acceptable amount of uncertainty depends on the consequence if something goes wrong. However, if accounting for uncertainties too heavily, it leads to an overconservative design and subsequently high costs.

1.4.1. UNCERTAINTY QUALIFICATION

In literature, there are many characterizations for uncertainty. One common quantification is the distinction between aleatoric and epistemic uncertainty (Diermanse, 2016):

1. Aleatoric uncertainties, also known as natural or statistical uncertainties. These match with natural deviations and the inability to measure parameters correctly (experimental uncertainty). Examples are the extreme values of the water height, measurement errors, and the thickness of the subsoil layers.

2. Epistemic uncertainties, also known as knowledge or systematic uncertainties. These are due to knowledge gaps, which could be known if enough effort is put in it. Examples are the unknown soil characteristics at each point of a dike trajectory due to limited data (interpolation uncertainty), and structural uncertainties. The latter is also known as model bias, which is the lack of knowledge of the underlying physics in a problem, thus a simplification of the problem.

Kennedy and O'Hagan (2001) discuss another way of uncertainty classification for computer models. They make a distinction between parameter uncertainty, model inadequacy, residual variability, parametric variability, observation error, and code uncertainty.

1.4.2. CAUSES FOR CONSERVATISM

From the viewpoint of an engineering consultant, there is a combination of causes for this conservatism. After a literature study, the following groups regarding conservatism in uplift are found:

SPATIAL VARIABILITY

The cover layer in Figure 1.1 is assumed to be one homogeneous slab but is in fact heterogeneous. This is a source of aleatoric uncertainty. The effect of heterogeneity is stated by Popescu et al. (2008): 'mechanical effects induced by material heterogeneity are more pronounced for phenomena governed by highly nonlinear laws; loose zones control the deformation mechanisms; and the effects of material heterogeneity are stronger for certain values of the load intensity.' Yet, there is no description for the degree of variability on the soil behaviour of the cover layer, so there is also a structural uncertainty here.

LIMITED DATA

Second, the precise soil stratification is unknown due to limited data from CPTs and borings on a section. Next to epistemic uncertainty of the layer thickness and measurement uncertainties, this causes various other aspects of conservatism. Firstly, for unknown values, a conservative value is often chosen based on expert judgement. Secondly, a normative cross-section must be determined, which also depends significantly on the human factor (Van et al., 2005). All together, often a conservative schematization is made.

POLICY AND PROBABILISTICS

Conservatism by policy cannot be shared under aleatoric nor epistemic uncertainties. Politicians have debated to an answer to the question: 'How safe is safe enough?' In the Netherlands, this has lead to high safety standards, in terms of a very low probability of inundation, thus to strict safety standards.

The basis of the probabilistic safety approach is simplified, thus there the uncertainty is of an epistemic nature. The different failure mechanisms are assumed to be uncorrelated. In fact, these are partly correlated, all depending on the same outer water level, soil conditions and geometry of the dike, thus a conservative assumption. The same holds for internal erosion (see Figure 1.3); the three submechanisms are treated as fully correlated (Teixeira et al., 2016).

The system itself of failure mechanisms and submechanisms holds another form of simplicity, i.e. leaving out the residual strength. For example, if a dike section has slid, the dike still could retain water to some extend. This residual strength is not taken into account in the actual failure probability. Van der Krogt et al. (2019) state that conservatism lies in the assumption that the probability of flooding is equal to the probability of instability. Similarly, this reasoning holds for all failure mechanisms, including the time-dependency of the load.

In the probabilistic and semi-probabilistic approach, there are also choices made on the safe side. The model uncertainty is accounted for explicitly for the probabilistic calculations, with the model factor. In the partial factor of the semi-probabilistic assessment, conservatism is also found. As Jongejan et al. (2020) put it: "Partial factors that are broadly applicable may sometimes be too conservative. This gives rise to a trade-off: differentiating between groups of cases may reduce conservatism, but it may also be impractical and error-prone."

SOIL MODEL

The current uplift assessment is based on a vertical equilibrium, only taking into account the thickness and the saturated volumetric weight of the cover layer. Other soil parameters, such as elasticity, tension strength and soil behaviour as during the cracking of the layer, are neglected. These contribute to the resistance of the layer, thus one could say that there is a conservative soil model applied in this case. This conservatism comes from uncertainty of an epistemic nature.

In conclusion, the literature points out that the thickness of the cover layer, the strength, and the stiffness or elasticity are important in crack-formation. However, due to the heterogeneity and uncertainties of the subsoil, it is questionable if including these parameters is worthwhile in a probabilistic assessment. Jongejan et al. (2020) points out that differentiation between groups of cases may reduce conservatism but it may be impractical and error-prone. Still, it is very useful to gain knowledge of the uplift phenomenon.

1.5. RELEVANCE

Why is a better uplift assessment needed? One could answer this question from the following four viewpoints:

SOCIETAL

For society, dike reinforcement programs can have a large impact on the built environment. As already pointed out, problems regarding uplift are expected to grow (Van et al., 2005). Firstly, research about uplift will lead to a better estimation of the strength of the cover layer, and hopefully a decrease in the quantity and the extensiveness of the countermeasures.

One example of a typical countermeasure against internal erosion is the application of a berm at the hinterland site. This would have a large impact on the local stakeholders, since (part of) their land will have to be acquired by water boards including the possibility of demolishing houses. Furthermore, residents also can encounter major hindrance by the construction of the countermeasures, depending on the construction method. This is merely the case if a piping screen will be constructed instead of a berm.

ECONOMICAL

Improved estimates of the resistance against uplift decreases the costs of the countermeasures. Since uplift is linked to two failure mechanisms, both were investigated. For uplift concerning macro-instability, an estimation of the potential savings for the Netherlands is quantified by Hoffmans (2015). These are estimated at 3 to 6 million euros.

For uplift in relation to internal erosion, such an estimate is not yet available in the literature. However, based on rough reasoning and engineering judgement, it is estimated that the potential savings for uplift regarding internal erosion are more than 6 million euros. Firstly, the length of the rejected dike sections on macro-stability (STBI) is about 300 km (Hoffmans, 2015), whereas, for internal erosion (STPH) this is 1100 km (Vrijling et al., 2010). Looking at the type of countermeasure, often a berm is applied; both for macro-instability of the inner side, and internal erosion. However, the berm needed to encounter internal stability problems is generally about five times longer (Rimmer Koopmans & Leo Kwakman, personal communication). This leads to more soil volume needed and potential costs to acquire land.

ENGINEERING

Since internal erosion is schematized as consisting of three submechanisms, a better assessment of uplift also decreases the calculating effort. In the case uplift is the submechanism with the lowest failure probability, lower than the target probabilities, calculations regarding heave and piping could be omitted.

SCIENTIFIC

As the current assessment is strict and many dikes stretches fail on the assessment, a better understanding of the calculations behind the uplift assessment gives insight into the causes of conservatism. Tweaking the input of causes, one could do a sensitivity analysis and a possible modulation on the safety assessment.

Moreover, diving in the theoretical framework behind the uplift assessment would lead to insight regarding the strength of the cover layer and the subsoil behaviour during uplift conditions. Taking into account the soil behaviour next to the weight of the cover layer will resemble the first submechanism of internal erosion more accurately. The understanding of uplift and cracking of the cover layer is fundamental for experimental research and for developing an updated theoretical framework.

1.6. SCOPE

As discussed before, it is beneficial to have a better uplift assessment to decrease the number of countermeasures which could be radical for the direct environment. The improvements on the uplift assessment are originating from a wide range of different scientific approaches and general viewpoints. The uplift phenomenon is treated in two phases: the floating part and the bulging-fracturing part.

For the floating part based on the vertical equilibrium, the current uplift assessment as described in WBI2017 is the starting point of this research. For the bulging-fracturing part, the problem is assessed in a two-dimensional plane. Furthermore, investigating the time-dependency is not attempted in this study. Here, the cover layer is assumed to behave fully undrained, which resembles the short-term behavior of the cover layer during a river flood wave.

Besides these model conditions, there are some other assumptions regarding an idealized cover layer. The focus of this thesis lies on thick layers without holes or pre-existing cracks. The cover layer is assumed to have a uniform thickness and strength parameters. Furthermore, there are causes for uncertainty on a larger level, regarding the inter-dependency of uplift with other (sub)mechanisms and the residual strength in the flood defenses assessment. These fall outside the scope of the thesis.

In conclusion, this thesis mainly focuses on the probabilistics and the soil model regarding uplift. Policy, measurement uncertainties and natural spatial variability are left out. Hence, epistemic uncertainties are the subject of research in the uplift assessment.

1.7. PROBLEM STATEMENT

The aim is to research in what way the structural uncertainties or model inadequacies causing conservatism could be decreased in order to improve the safety assessment for uplift regarding internal erosion for dikes with thick cover layers in the Netherlands.

1.8. RESEARCH QUESTIONS

Following from the problem statement and the detailed phenomelogical description of uplift, the following research questions are formulated:

1. For the uplift assessment based on a vertical equilibrium, as currently in use in WBI2017: What is the impact of assumptions included in deriving the (a) Deterministic equation, (b) Probabilistic equation, and (c) Prescribed safety factor for semi-probabilistic assessment? What improvements could be made?
2. What aspect of soil behaviour should be included in the model for uplift? In what way does the resistance change in the uplift assessment subsequently?
3. How are the improvements working in practice, for (a) specific location(s) in the Netherlands?

1.9. STRUCTURE THESIS AND METHOD

Figure 1.7 gives an overview of the structure of the thesis and the relations between the chapters. A detailed description of the content of each chapter is given below.

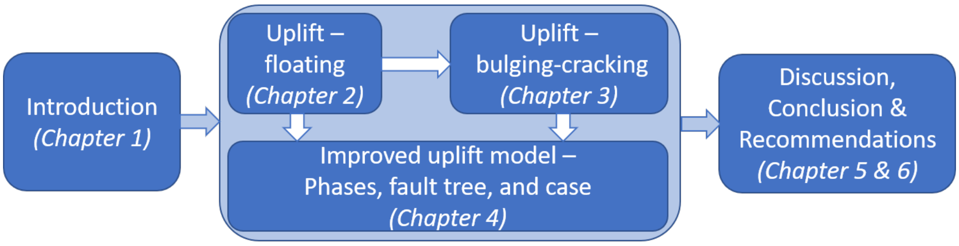

Figure 1.7: Visual thesis outline

Chapter 2 focuses on the uplift assessment based on a vertical equilibrium, as is now in use in the WBI2017. First of all, it starts with the current equations, split among three approaches. These are deterministic, fully probabilistic, and semi-probabilistic. Second, the current equations are evaluated in detail. This is done both for the basic deterministic equations, as well as for the distribution and variance of stochastic parameters in the fully probabilistic approach. Subsequently, the probabilistic calibration procedure for deriving semi-probabilistic safety factors is performed in Python. Using this as a basis, a sensitivity analysis is performed as well. This chapter's method is based on literature study, expert interviews, and carrying out probabilistic calculations in Python. The expert interviews were used to find causes for (over)conservatism in the current guidelines and explanations on certain parameter choices.

The new model including soil behavior is discussed in Chapter 3. As is stated in the introduction, the goal is to incorporate the soil strength into the problem. The ultimate failure state is a full crack through the cover layer. For that, analogies are looked for in other problems that contain similarities. The development of the model begins with a conceptual model to find the most important relations in an abstract framework. After, the problem is split into two parts: load/water and resistance/soil. Computer models are selected and used to find a solution. For the load part, the head is modeled in Python using a 2D Finite difference method. For the resistance, calculations are made in Plaxis FEA.

Chapter 4 consists of three parts. First it provides a summary of the uplift model as is investigated in Chapter 2 and 3 by means of a cartoon. Further, it shows the updated fault tree for uplift in the internal erosion failure mechanism. Then, it makes use of the findings by applying it to a case. The case location selected is between Wijk bij Duurstede and Amerongen in Utrecht, the Netherlands. Here, the safety against uplift is assessed using different approaches and compared.

While there are many critical notes at the end of each chapter or section, the main points for discussion are listed in Chapter 5. Subsequently, the conclusions are drawn in the final chapter.

2

CURRENT VERTICAL STRESS MODEL

In the Netherlands, the safety of and behind the dikes is continuously assessed. Guidelines are in place to determine the safety of the current situation and to design new or updated geometries. In 2017, the latest version of the safety assessment for dikes in the Netherlands was published, the WBI2017. In this guideline, uplift is assessed based on a vertical equilibrium. The chapter starts with discussing the three uplift formulae for uplift in WBI2017, which depend on the mathematical approach: deterministic, fully probabilistic and semi-probabilistic.

The core of this chapter discusses several ways of improving the current uplift assessment based on a vertical equilibrium. First of all, the basic formula is investigated critically. There, some conservative assumptions lie within and a new formula is proposed. Second, the model factor is explained, which is distinctive for the fully probabilistic approach. Furthermore, some remarks about the damping factor are given. Thirdly, the calibration of the safety factors is discussed, which is an important factor in a semi-probabilistic calculation. The calibration procedure is explained, as well as the calibration criterion. Subsequently, the results of a sensitivity analysis on the prescribed safety factor are discussed. This chapter ends with a conclusion and a recommendation on how to deal with the uncertainties found.

2.1. UPLIFT EQUATIONS

Below, the corresponding uplift formulae of WBI2017 are given.

DETERMINISTIC

As already mentioned in Section 1.3, uplift occurs when the high pore water pressures in the aquifer lift up the cover layer. This can be expressed mathematically in either total stresses or effective stresses. For internal erosion, the WBI2017 makes use of an effective stress approach for uplift (Ministerie van Infrastructuur en Milieu, 2017).

$$h_{polder} + (h - h_{polder}) * r_{exit} - h_{exit} = (\gamma_{sat} - \gamma_{water})/\gamma_{water} * D_{cover} \tag{2.1}$$

The description of the symbols is given in Table 2.1.

A deterministic formula describes the essence of the problem, and is used to verify the safety in which the resistance must be larger than the load, without taking into account the probabilities. The deterministic formula for uplift is described by a vertical equilibrium in WBI2017. The formula does not include any uncertainties in the input parameters. Since all variables are treated as deterministic, with negligible variation in time and space, the deterministic approach is unsuitable to assess safety and a fully probabilistic or a semi-probabilistic approach is used.

FULLY PROBABILISTIC

In the fully probabilistic approach, each input variable has its distribution and variance. All important uncertainties are taken in account explicitly. A probabilistic calculation can be performed using FORM or Monte Carlo calculations. Equation 2.2 contains the limit state function for uplift, which describes failure when

$Z_{up} < 0$. Using a FORM or Monte Carlo calculation, the failure probability P_f and reliability index β are calculated.

The probabilistic formula for uplift is (Jongejan, 2017):

$$Z_{up} = m_u \Delta\phi_{c,u} - (\phi_{exit} - h_{exit}) \tag{2.2}$$

with

$$\Delta\phi_{c,u} = D_{cover} * (\gamma_{eff}) / \gamma_{water} \tag{2.3}$$

$$\gamma_{eff} = \gamma_{sat} - \gamma_{water} \tag{2.4}$$

$$\phi_{exit} = h_{exit} + (h - h_{exit}) * r_{exit} \tag{2.5}$$

The description of the symbols used can be found in Table 2.1. This Table also contains the distribution types of the symbols and the characteristic values used for the semi-probabilistic assessment.

SEMI-PROBABILISTIC

The semi-probabilistic approach makes use of prescribed safety factors, which is a ratio between the strength and the load. Also, the input variables are taken as the design values, which are chosen unfavourable. The strength or resistance then is larger than the load by the ratio of the safety factor. For uplift, the semi-probabilistic formula is (Jongejan, 2017):

$$\gamma_{up} \geq \frac{R_{char}}{S_{char}} = \frac{D_{cover,char} * \gamma_{eff,cover,char}}{\gamma_{water,char} * (h(T) - h_{exit,char}) * r_{exit,char}} \tag{2.6}$$

The description of the symbols used can be found in Table 2.1. The subscript *char* stands for characteristic values as input values. In Figure 2.1, the distribution of the parameters and its characteristic value is shown in blue and red, respectively.

Table 2.1: Input parameters for uplift calculation

Symbol [unit]	Description	Distribution type	Default	$char$ value
m_u [-]	Model factor for uplift	log-normal	μ 1.0 σ 0.10	1.0
γ_{water} $[kN/m^3]$	Volumetric weight of water	-	10	10
γ_{sat} $[kN/m^3]$	Saturated volumetric weight of the cover layer	shifted log-normal (+10)	-	5%
r_{exit} [-]	Damping factor at exit	log-normal	-	95%
D_{cover} $[m]$	Effective thickness of the cover layer	log-normal	-	5%
h_{exit} $[m+\text{NAP}]$	Phreatic level at the exit point	normal	-	5%
h $[m+\text{NAP}]$	Outside water level	$Hydra-Ring$	-	Design water level

2.1.1. ADVANTAGES AND DISADVANTAGES OF EACH PROBABILISTIC METHOD

In the WBI2017, there are two types of calculations included: semi-probabilistic and fully probabilistic. Diermanse (2016) discusses the advantages and disadvantages of both:

In the probabilistic approach, the flooding probability of a section or structure will be quantified explicitly. Then, this flooding probability will be compared to the target probability. In the semi-probabilistic approach, the result will only give a pass or fail for a certain target probability. The advantage for the probabilistic approach is that the difference between the actual flooding probability and the target probability is known, thus helping policymakers to quantify the urgency for taking countermeasures.

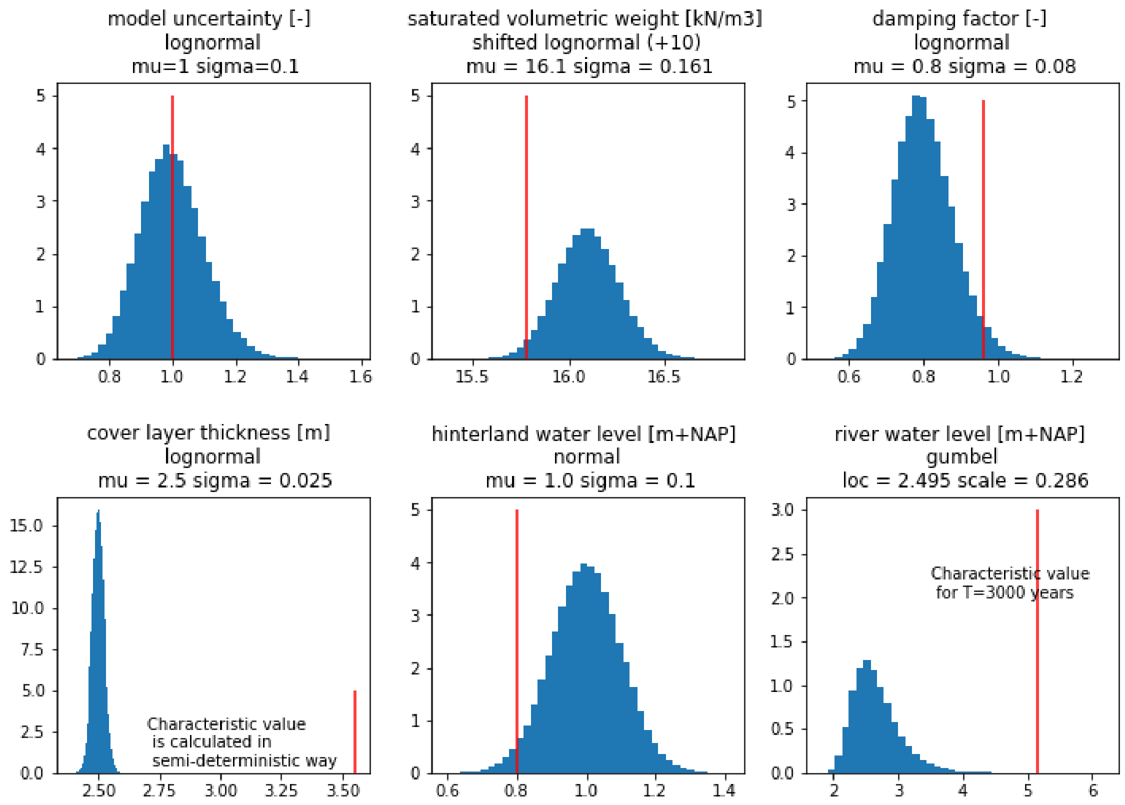

Figure 2.1: Parameter distributions and characteristic values for location with vakid 11001009

The semi-probabilistic approach makes use of safety factors. These could be very strict due to the broad applicability in different situations. Thus, the semi-probabilistic approach generally gives less certainty about the reliability of a section and the probabilistic approach is more precise.

On the other hand, the semi-probabilistic approach has some advantages, mostly related to calculation effort and practicability. The probabilistic approach is only used by a limited group of experts and it is more difficult to grasp. Also, some of the probabilistic analyses do have high computing requirements.

In conclusion, the semi-probabilistic approach takes less effort but gives more conservative outcomes than the probabilistic approach.

2.2. DETERMINISTIC

The deterministic formula is the basic formula regarding uplift, which gives the relation between the input arguments. Concerning the formulation of the basic equation, there are two ways to decrease conservatism.

2.2.1. VERTICAL EQUILIBRIUM

As discussed before, the vertical equilibrium approach only describes when the cover layer starts 'floating'. However, it does not describe the actual failure, i.e. the forming of an exit point. This is crucial for the following submechanisms, heave and piping, to occur. A proposal to improve this model uncertainty is discussed in the next chapter.

2.2.2. PHREATIC LEVEL AT GROUND SURFACE: UPPER LIMIT

In WBI2017, the effective stress is given by $(\gamma_{sat} - \gamma_{water}) * D_{cover}$. Here, it is assumed that the phreatic level lies at ground surface. This leads to the smallest value of the effective stress, which is an upper limit.

In cases where the phreatic level is known to lie below ground surface, the effective stress is larger than expressed by $(\gamma_{sat} - \gamma_{water}) * D_{cover}$, but is in fact $\gamma_{sat} * D_{cover} - \gamma_{water} * d_w$. Therefore, proposal for a more accurate formula is:

$$h_{polder} + (h - h_{polder}) * r_{exit} - h_{exit} = \gamma_{sat}/\gamma_{water} * D_{cover} - d_w \tag{2.7}$$

In which d_w is the distance between the phreatic surface and the aquifer-aquitard interface. The parameters of Equation 2.7 are shown graphically in Figure 2.2. *N.B. This approach is also given in Appendix 4.1 of Technisch Rapport Waterspanningen bij Dijken (TAW, 2004).*

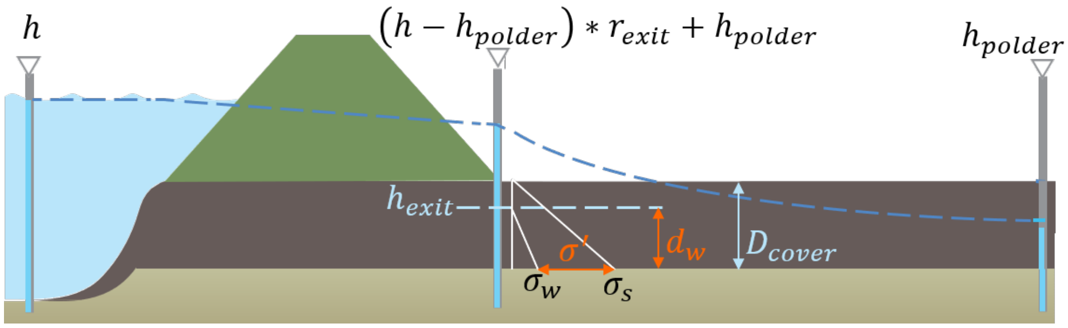

Figure 2.2: Sketch with parameters of Equation 2.7

To include d_w in the uplift assessment has a particular large benefit for cases with thick cover layers, where the difference between d_w and D_{cover} is relatively large, and for cases with low volumetric weight. Using this formula, a significant increase in calculated safety factor is obtained. This is worked out for 5 example cases in Appendix A.

LIMITATIONS OF THE PROPOSED FORMULA

In practice, the application of the proposed formula is with care, including uncertainties regarding the level of the phreatic surface during uplift conditions. This means that one must make sure the phreatic surface does not rise during uplift conditions. From the aquifer, the high pore water pressures intrude into the cover layer, affecting the pore water distribution in the clay layer. In theory, this causes the phreatic surface to rise after an indefinite amount of time.

However, in practice there are safe estimates determined for the intrusion lengths. These are set to 3 meters for lake and upper river areas and to one meter for tide dominated areas and lower river areas respectively (TAW, 2004). This means that for a cover layer thicker than the intrusion length, part of the layer are not affected by the rising pore water pressures. Thus, the application of the proposed formula is in particular useful for thick cover layers, with low uncertainties regarding the phreatic surface, for example at polders with regulated water levels.

2.3. FULLY PROBABILISTIC

In the set equations of the fully probabilistic approach, one extra parameter appears: the model factor. Seen from a theoretical angle, the addition of this parameter has a conservative nature, which is explained below. Furthermore, the default value of the damping factor is conservative in practice.

2.3.1. MODEL FACTOR

Generally speaking, the model factor is implemented to account for model errors: the difference in model predictions and reality, and the difference between experiments in controlled lab-conditions, versus behavior in non-controlled conditions. It describes the imperfection of the model.

Schweckendiek et al. (2014b) sets out that the causes of model uncertainty are partly of reducible and partly of irreducible nature. Reducible uncertainty lies in the accuracy of the model prediction. An example of irreducible factors is time-dependent influencing factors.

In the ideal case, the model factor is based on discrepancies between modeled outcomes and real results. However, there is no data available to base the calibration of the model factor on. On the other hand, there were other criteria to choose the model factor. To be consistent with ISO2394, implementing a model factor was desirable. The coefficient of variation for uplift was chosen as 10%, where the ISO-norm gives a default value of 20%. Lastly, the choice for a lognormal distribution is based on the principle that no negative values could be obtained, other than with the normal distribution (Timo Schweckendiek, personal communication). However, a coefficient of variation of 10% still seems on the high side for a model based on the vertical equilibrium (Ruben Jongejan, personal communication).

2.3.2. DAMPING FACTOR

The damping factor is a parameter what ratio of the hydraulic head is left from the river water level at the exit point. The upper limit for this value is 1, that means that the hydraulic head at the exit point equals the head at the river. A value larger than 1 is impossible in reality.

There are several ways to determine the damping factor. The options are a trade-off between precision and effort. The most accurate but also most costly approach is to install monitoring wells and interpret their long term data. For computing, the most extensive option is using numerical software, for example Watex. Second, analytical equations exists, for example the Dupuit-equations. Thirdly, expert judgement is sometimes used. The values based on expert judgement tend to be overconservative (Ruben Jongejan, personal communication).

The default value for the damping factor in the national database VNK2 is set to $LN \sim (\mu = 0.8\ ,\ \sigma = 0.08)$. Using this distribution, there is a small but not unimportant chance that values larger than 1 are used for the damping factor. The distribution of this case is shown graphically in Figure 2.1. As discussed before, a damping factor larger than one is unrealistic. This means that the hydraulic head at the exit point is larger than the head at the river. In the current probabilistic assessment, there is no notion to set the maximum value of the damping factor distribution to 1.

2.4. SEMI-PROBABILISTIC

The WBI2017 differs from previous versions because the safety factors for the semi-probabilistic approach are calibrated using probabilistic calculations. This means that the semi-probabilistic test is merely consistent with the fully probabilistic assessment. If inconsistent, the outcome of the semi-probabilistic calculations will be more conservative then the probabilistic calculations (Diermanse, 2016). The following relationship for the safety factor for uplift is now in use:

$$\gamma_{up} = 0.48 * exp(0.46 * \beta_{cross} - 0.27 * \beta_{norm}) \tag{2.8}$$

In which γ_{up} is the prescribed safety factor, β_{cross} the actual reliability index for the cross-section and β_{norm} the norm requirement or safety standard. The relation between the partial safety factors γ_{up} and the reliability index β are shown in Figure 2.3, where the shape and complexity of the function changes. Note that the safety factor in 2006 is generally low because uplift was assessed based on total stresses instead of effective stresses. Figure 2.4 shows the fit for the established safety factor in 2015 which is implemented in WBI2017 (Jongejan, 2017). This safety factor relationship depends both on the reliability index (β_{cross}) and the norm requirement (β_T, β_{norm} or as return period). The points shown are the 20%-quantile of the reliability indices per safety factor and per return period of the load, through which a fit is plotted.

To study whether there are causes for conservatism in the calibration of the safety factor, the calibration is performed according to the procedure in literature (Teixeira et al., 2016), with data generously provided by Ana Teixeira and Karolina Wojciechowska of Deltares. Hereafter, first the calibration procedure is summarized. Then, two parameters are highlighted: these deal with uncertainties independent on the location, but dependent on the mathematical model: the calibration criterion and the model factor.

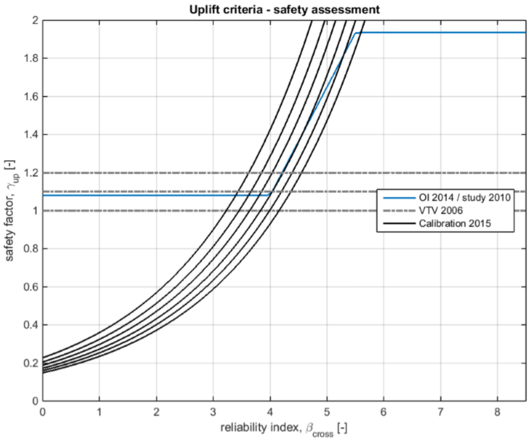

Figure 2.3: Safety factor relations for uplift submechanism (Teixeira et al., 2016)

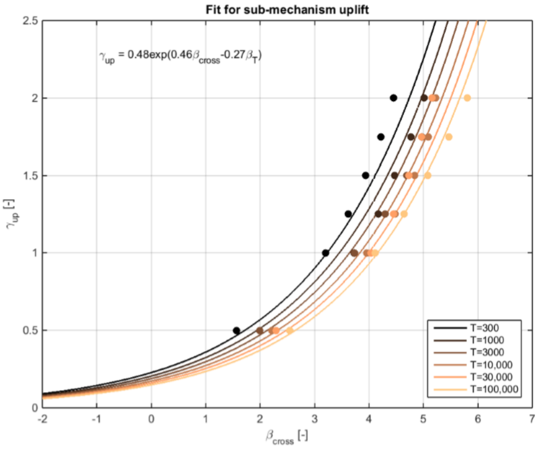

Figure 2.4: Derived functional $\gamma_{up} - \beta_{cross}$ relation for the uplift sub-mechanism (Teixeira et al., 2016)

2.4.1. CALIBRATION PROCEDURE FOR THE SAFETY FACTOR FOR UPLIFT

Section 7.3 of the report *'Derivation of the semiprobabilitistic safety assessment for piping - WTI 2017 Cluster C piping failure mechanism* by Teixeira et al. describes the calibration procedure for the submechanism uplift. This algorithm visualized in Figure 2.5.

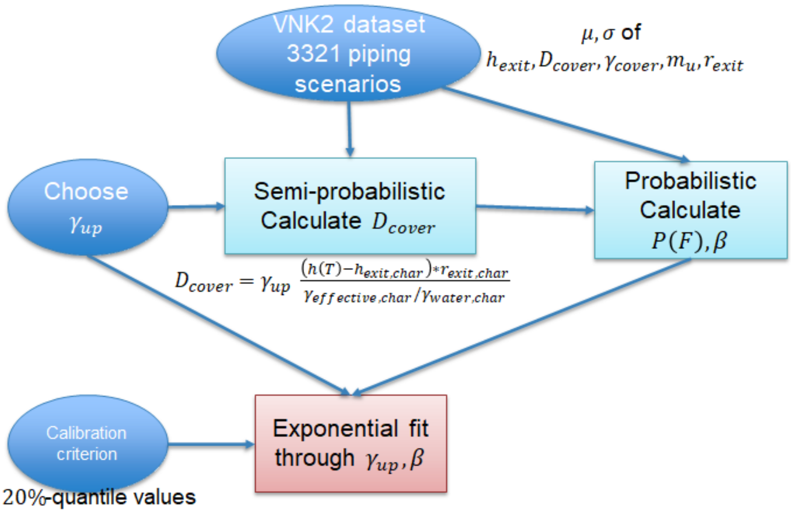

Figure 2.5: Flow chart for calibration algorithm

Many model sets are used to obtain a reliability index and corresponding partial safety factor. Using these outcomes in the form of a scatter plot, a relation is found using the calibration criterion. For an elaborate explanation of the flow chart, the algorithm itself, and the Python code, it is referred to *Appendix B - Calibration of the safety factor for uplift.* In the calibration procedure, the calibration criterion is an input parameter that requires explanation, which is given below.

2.4.2. CALIBRATION CRITERION

The calibration criterion is a mathematical choice to determine for which values the safety factor is sufficiently safe. In literature, common values are that the relation holds for 80% of the data sets (Förster et al., 2012; Teixeira et al., 2016) or 95% (Lopez de la Cruz et al., 2011). From the definition of the calibration criterion, one could argue that the semi-probabilistic approach is much more conservative than the probabilistic approach. For uplift, the calibration criterion is set as an 80% exceedance or 20% undershoot, also referred to the 20% quantile. This value was chosen based on existing research, which is explained next.

Regarding the calibration criterion, Jongejan and Calle (2013) set out two premises:

I. *The average probability of flooding over all consequence segments should be smaller than the safety standard*

   Vrouwenvelder sets out the economic reasoning for this premise, in Appendix B of the WBI Code calibration (Jongejan, 2017). The goal is to minimize the total costs in terms of net present value. The total costs consists of fixed costs and variable costs, of which the latter is assumed to be dependent on the safety factor. The optimization is done by differentiating the total costs with respect to the safety factor and solving for zero.

II. *The average probability of flooding equals to the 20% quantile of the reliability index, given* $\beta_{cross,m,section} \sim N(\mu, \sigma = 0.5)$ *from the VNK2-dataset.*

   Here, the reasoning is as follows: 'For a set of reliability indices that is approximately normally distributed with a standard deviation of 0.5, the average cross-sectional probability of failure corresponds roughly to the 20%-quantile of the cross-sectional reliability indices as can easily be verified numerically.' (Jongejan et al., 2020) This premise is more convenient to use than the first premise, and also less sensitive to outliers in a relatively small dataset.

The 20% quantile is used consistently as the calibration criterion in the WBI2017 guidelines. Therefore, it is important that the statistical assumptions were checked for the second premise. In Appendix B, a detailed explanation and results are included. Below, these findings are summarized. Both assumptions are not precise and therefore some difference between the two premises is expected.

Firstly, the standard deviation of the reliability indices per safety factor is computed. Values are reported between 0.5 ~ 0.75 (Appendix B, Figure B.7). By observation, a normal distribution of the reliability indices fits well. Assuming a distribution of $N(\mu, \sigma = 0.5)$ is therefore accurate but not very precise.

A similar conclusion holds regarding the 20% quantile. It was checked whether this value matches with the average failure probability for a reliability index of the distribution $N(\mu, \sigma = 0.5)$. It matches well for a mean value of $\beta = 4$, but has a 0.1 difference for $\beta = 4$ and 0.2 difference for $\beta = 6$ (Appendix B, Figure B.8).

2.4.3. CALIBRATION DATASET VNK2

As seen in Figure 2.5, the input dataset used for WBI2017 is Veiligheid Nederland in Kaart 2 (VNK2). Here, there were 3321 piping scenarios defined. Teixeira et al. (2016) made use of all 3321 scenarios.

Upon further investigation, there were 1129 unique sets of scenarios. Also, there are many fields which contained default values. The most common noteworthy field is that the coefficient of variation is often set as 10%. Furthermore, for the damping factor the mean value is a default value as well. In the VNK2 database, 24% of the cases had a value of 0.7 and 73.6% a value of 0.8. For 99.4% of the cases, the coefficient of variation for the damping factor was 10%. In the probabilistic analysis, a combination of μ=0.8 and cov=10% sometimes gives a value for r_{exit} of larger than 1. This is also discussed in Section 2.3.2.

The default values are conservative values. Improvements are possible to replace the default values by local values. Also, in the probabilistic equations, the phreatic surface at the hinterland (h_{polder}) is assumed equal to the phreatic surface at the exit point (h_{exit}). This could lead to a conservative choice for the value of both parameters.

2.4.4. SENSITIVITY ANALYSIS

In Table 2.2, the outcome of the analyses are summarized for $\beta = 4$ & $\beta = 6$. These values are obtained from Figures B.9 to B.13 of Appendix B. Both the relative (expressed in percentages) and the absolute difference are presented. A low value means a reduction in the prescribed safety factor and is thus favourable.

Table 2.2: Sensitivity analysis on calibration criterion for $\beta = 4$ & 6

		$\beta = 4$ %	$\beta = 4$ Δ	$\beta = 6$ %	$\beta = 6$ Δ
Calibration criterion	30%	94	-0.05	93	-0.14
	40%	89	-0.10	88	-0.24
	50%	86	-0.13	84	-0.31
	$P_f(average)$	103	+0.03	167	+1.34
CoV of model factor	5%	97	-0.03	94	-0.12
	1%	96	-0.04	92	-0.16
Default value of damping factor	LN(0.9, 0.009)	111	+0.10	110	+0.18
	LN(0.95, 0.00095)	112	+0.12	112	+0.23
Method	$Hydra-Ring$	89	-0.11	84	-0.38

Table 2.2 shows that in many cases the sensitivity analysis show a smaller value as prescribed safety factor. Per type of sensitivity analysis, an explanation is included below.

SENSITIVITY ANALYSIS ON 20% QUANTILE AS CALIBRATION CRITERION

The outcome is as expected: A less strict calibration criterion results in lower prescribed safety factors. The default value is a calibration criterion as 20% quantile of β. Quantifying the difference, this in the order of magnitude of ~ 10%.

SENSITIVITY ANALYSIS ON TYPE OF CALIBRATION CRITERION

Here, the outcome differs from the expectation. The default value was using a calibration criterion of 20% quantile of β, and the compared value was using the average failure probability and the corresponding β. In other words: premise I was compared with premise II.

The expectation was that both premises would yield a similar outcome, since two assumptions are checked and were found not precise but still accurate. However, the outcome differs largely, in the order of magnitude of ~ 50%.

After a discussion with Ruben Jongejan, the following causes were pointed out for the large difference in outcome:

1. Premise I is more sensitive to outliers than premise II.
2. The assumption of β $N(\mu, \sigma = 0.5)$ does not hold precisely. The distribution of β's is not perfectly normally distributed, but the distribution is slightly skewed to the left. The standard deviation is also not exactly 0.5 but slightly higher.
3. The 20% quantile is an estimation of the average failure probability, it works perfect for $\beta = 4$ but differs for other values.

SENSITIVITY ANALYSIS ON MODEL FACTOR

The outcome is as expected: A lower coefficient of variation of the model factor results in lower prescribed safety factors. The default value is a coefficient of variation as 10%. Quantifying the difference, this in the order of magnitude of ~ 5%.

SENSITIVITY ANALYSIS ON STANDARD VALUES OF r_{exit} IN VNK2 DATASET

Now, the standard value is $\mu(r_{exit})$ =0.8 and cov=10%. One is curious to research a variety of default values with higher mean values and lower variance. This is done for $\mu(r_{exit})$ =0.9, cov=1% and $\mu(r_{exit}) = 0.95$, cov=0.01%. The outcomes for the proposed values turn out to be disadvantageous for the prescribed safety factor.

COMPARISON WITH ORIGINAL CALIBRATION

All above analyses were performed in Python, and for the probabilistic calculations a Monte Carlo simulation with Importance Sampling was used. This is different from the original calibration, which was performed in $Hydra-Ring$ (Teixeira et al., 2016). The probabilistic calculations are based on a FORM approach.

Three possible causes for the difference are listed below:

1. Probabilistic method: FORM in Hydra-Ring vs. Monte Carlo with Importance Sampling
2. Design water level: Hydra-Ring vs. Gumbel fit
3. Unique value dataset

2.5. DISCUSSION AND RECOMMENDATIONS

To conclude, there are many causes of uncertainty in the uplift assessment regarding internal erosion found, thus several reasons for conservatism. It is important to keep in mind that aiming to reduce the uncertainty to zero is impossible, since some uncertainties are aleatoric thus irreducible. Also, it is undesirable, since one tends to aim to be at the safe side. Furthermore, seeing from the practical side, efforts to decrease the uncertainty might be disproportionate compared to the profits, since the costs of extensive field and lab tests are high. However, to optimize the assessment and to get rid of overconservative assumptions is advantageous in order to decrease the costs and impact of countermeasures against internal erosion. Hereafter, the main causes for (over)conservatism regarding the formulae, policy and probabilistics are summarized and reviewed.

DETERMINISTIC

In the basic uplift formula, it is assumed that the phreatic level lies at ground surface. This assumption is on the safe side if the phreatic level is unknown. However, it is more correct to account for the phreatic level when calculating the resistance to uplift. This of course, increases the resistance of the cover layer for cases at which the phreatic level is known to be constantly below ground surface, for example in polders. In practice, this is applicable only to thick cover layers, thicker than the intrusion length, and is in particular beneficial for cover layers with a low volumetric weight. Formula 2.7 is a proposal to account for this mathematically.

FULLY PROBABILISTIC

Looking into the probabilistic formula for uplift, its parameters and distributions, there are two parameters which definition and/or default value have reason to refined.

Firstly, the model factor is there to account for errors between the difference in outcome of the model versus in reality. Now, this is set to $\mu = 1$ and $\sigma = 0.1$. Based on a simple relation as the vertical equilibrium, this is overconservative, since all uncertainties by spatial variability and limited data are already taken explicitly into account as the variation per parameter. A reason to set a model factor is to be consistent with other limit state functions and norms and to build in a reasonable amount of conservatism. To quantify the decrease in variation of the model factor for uplift, further research is recommended. However, depending of the viewpoint, research efforts might be disproportionate to the profit in terms of costs and impact of countermeasures against uplift.

Secondly, there are some concerns regarding the distribution of the damping factor. Often, this distribution has a considerable tail at the unfavorable side which includes values larger than 1. This in fact, is not damping but amplification, which cannot occur for the hydraulic head under dikes. A proposal to avoid a unrealistic distribution of the damping factor is to set a maximum value for probabilistic calculations.

SEMI-PROBABILISTIC

Following from these analyses, the determination of the prescribed safety factor is a delicate process and is highly dependent on the method and calibration criterion type. The current calibration criterion choice is not robust.

The calibration criterion has a conservative nature, because it is applicable for the Netherlands as a whole. To decrease the uncertainty, there are two ways proposed:

1. Use probabilistic approach for uplift;
2. Calibrate using dataset specified for a dike traject.

The current calibration method provides reason for discussion. This method makes use of fake cover thicknesses, corresponding to a certain factor of safety. The other input arguments for uplift are coming from cases all over the Netherlands, some of which do not have a cover layer naturally. Since the uplift assessment is only interesting if uplift is normative, one is only interested in cases where β_{up} is normative for interal erosion assessment.

3

UPLIFT SOIL BEAM MODEL

With models, one tends to mimic the real world and simulate possible outcomes. As for now, with uplift, there is a simplistic mathematical model to determine whether uplift takes place: vertical equilibrium condition only of the overpressure against the self-weight of the cover layer. The purpose here is to find a new model to represent the problem in reality better. Finding more strength contributions than only the self-weight of the cover layer is a key element, as well as their relationships to the failure mechanism.

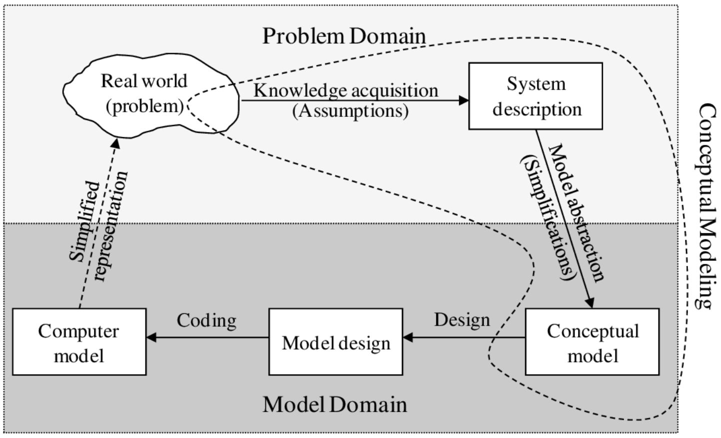

Figure 3.1: Domain of conceptual modelling (Robinson et al., 2015)

The proceeded method of this chapter follows the boxes in Figure 3.1. The system description has already been given in Section 1.3. Section 3.1 contains the conceptual model of uplift. For a more elaborate version, please refer to Appendix C. Moving on, the model design is split into two parts: Section 3.2 contains the schematization of the load, whereas Section 3.3 contains the resistance of the soil. Finally, 3.4 holds the discussion.

3.1. CONCEPTUAL MODEL: BEAM AND RELATIONS

Key features of a conceptual model are manipulating ideas as objects, exploring their relationships, and working with complex systems. The objective of this section is to qualify the relations between relevant parameters in the uplift submechanism. For internal erosion as a failure mechanism to develop, uplift is the first submechanism that has to occur. Failure by uplift results in the occurrence of an open exit point, which means that the cover layer contains a fracture.

In literature, several cases of soil fracturing are identified. The reason behind this is to gain knowledge about the causes of crack-forming and to select the most relating case to the uplift situation. Four situations were looked into detail, see also Appendix C:

1. At the crest of a landslide or vertical cutting;
2. By pumping or injecting air, fluids, grouts or chemicals in the soil, also known as hydraulic fracturing;
3. At the surface of clay by desiccation;
4. At the base of an excavation due to high artesian pressures.

After a comparing literature study and an expert interview with André van Hoven of Deltares, the beam model used in an excavation base is found most resembling with the uplift case behind a dike. This means that due to the pore water pressures, the cover layer deforms and internal stresses develop. The critical shear, tensile and compressive stresses have to withstand the stresses due to bending moments and shear forces.

A conceptual model is shown in Figure 3.2, indicating the main relationships in the uplift phenomenon regarding internal erosion. As seen in Figure 3.2, some boxes are red. These are soil-related and highly time-dependent and are discussed later.

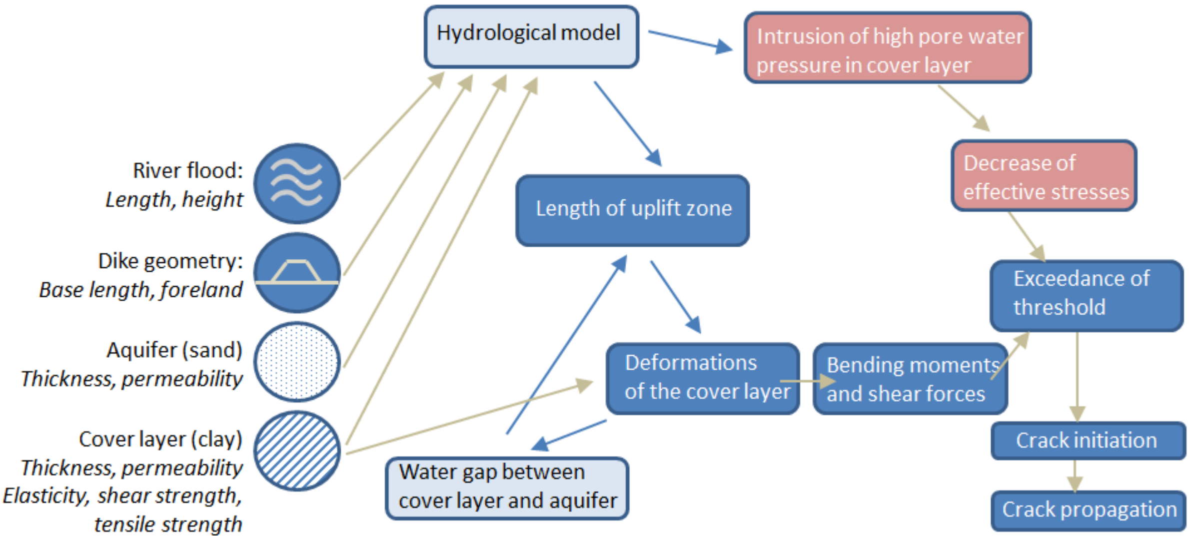

Figure 3.2: Conceptual model of cracking during uplift conditions (final version)

3.2. MODEL DESIGN - PART A: WATER/LOAD

The goal here is to find the appropriate load for the beam schematization, as well as the corresponding length of the uplift zone. To investigate this problem, first, a literature study is carried out regarding the length of the uplift zone. This is discussed in Section 3.2.1. Then, the problem is approached using finite-difference modeling. In the uplift zone, the head is constant. Also, for a certain fixed outer head, there is a unique relationship between the length and the head in the uplift zone, which depends on geohydrological conditions. This gives a range and combination of possible loading arrangements. Then, the uplift head is translated into a netload and using simple mechanical formulations the maximum possible bending moment and shear force. The corresponding length and load conclude the schematization of the normative beam.

3.2.1. LITERATURE

In literature, there are many suggestions regarding the head profile in the aquifer during high water. This overview contains two situations: before floating when the cover layer is still attached to the aquifer, and during floating when there is a gap between the cover layer and the aquifer acting as a hydraulic shortcut. Of course, the most interesting goes to the head and the uplift length in the latter situation.

HEAD IN AQUIFER BEFORE 'FLOATING'

The head in the aquifer is often computed using analytical equations, in which the cover layer is resembling a leaky layer. The blanket theory contains equations for confined flow and semi-confined blankets including the leakage concept. The leakage factor is an important parameter in geohydrology, of which the definition is given in Equation 3.1. The blanket theory is suitable if the leakage factor is larger than 30 meters or $k_{aq}/k_{cover} < 0.01$ or > 10 (Batool et al., 2015). However, the blanket layer is based on 1D flow conditions and is not including a hydraulic shortcut just beneath the uplifted cover layer.

$$\lambda = \sqrt{D_{aq} * D_{cover} * k_{aq}/k_{cover}} \tag{3.1}$$

UPLIFT LENGTH DURING 'FLOATING'

In literature, three types of evaluating the uplift length are found. They are discussed here under:

1. As a rule of thumb, the uplift length for macro-instability evaluations equals twice the cover layer thickness (Förster et al., 2012). This rule of thumb is irrespective of the outer river head.

2. Comprehensive analytical solutions for the uplift length are available for stationary situations (Barends, 1999). Equation 2 is an implicit formula for the uplift length L. D_{aq} and k_{aq} stand for the thickness and the permeability of the aquifer. B, λ_h and λ_f are the width of the dike, leakage factor of the hinterland and the foreland respectively. ϕ_r, ϕ_p, ϕ_g are the river, polder, and limit potentials.

$$\frac{2}{\pi}\arcsin\left(\frac{1}{\cosh(L\pi/2D_{aq}}\right) = \frac{k_{aq}D_{aq}(\phi_g - \phi_p)/\lambda_h}{\pi k_{aq}(\phi_r - \phi_g)/2}\left(\frac{\pi\lambda''}{2D_{aq}} + \operatorname{arcsinh}\left(\frac{\sinh((B+L)\pi/2D_{aq})}{\cosh(L\pi/2D_{aq})}\right)\right) \tag{3.2}$$

   In deriving this analytical solution, there are a few assumptions made. Firstly, Barends assumes that at the end of the uplift zone, there is a vertical potential line. In fact, this line is curved, and therefore the analytical solution is an overestimation. Secondly, ϕ_g is taken as a boundary condition with a fixed value. It stands for the limit potential, representing the head in the uplift zone. Here, this value is fixed and equals the self weight of the layer.

3. There are also numerical solutions reported using MSEEP software, based on FEM. Using this software evaluating a two-dimensional problem omits the rough assumption that the potential line at the end of the uplift zone is vertical. The use of MSEEP also use the limit potential as a boundary condition. Compared to the analytical outcomes, the numerical outcomes yield 25% to 100% smaller values (Barends, 1999).

The above methods to derive the uplift length depend on several rough assumptions. First of all, they are steady state solutions, for which Barends finds the limit potential a boundary condition to describe the equilibrium between the cover layer and the uplift pressure. However, during uplift, the head in the uplift zone exceeds the self weight of the layer. The cover layer is subjected to a net upward force inducing moments and shear forces. The net upward force is also observed by wave-moments of the cohesive layer upon entering, indicating that the cover layer has come loose from the soil underneath. Therefore, the references found in literature cannot directly be used.

3.2.2. MODEL SELECTION AND BOUNDARY CONDITIONS

To evaluate the length and load for the beam schematization, a finite differences (FD) approach is used. The approach used is treating both the length and the load as unknowns. This is because, if a flood wave arrives and disturbs the heads in the aquifer, both the head and the length of the uplift zone will increase simultaneously. With instationary situations, the potential in the uplift zone exceeds the limit potential from time to time. It is also possible using FD coding to compute the head in the uplift zone, given a certain length of the uplift zone.

GEOMETRY

In Figure 3.3 the geometry of the cross-section is shown. The geometry consists of three parts: the dike body, an uplift zone with a predefined length, and cover layer directly attached to the aquifer.

The horizontal length of the model domain represents a far-field boundary. The blanket theory gives a guideline for a length to model infinite conditions. Batool et al. recommends 2λ based on comparison to finite element analysis, in which λ is the leakage factor. For $x = 3\lambda$, the difference between outer and polder head has decreased by 95%. In this analysis the far-field boundary is specified by a model domain of equal to 5λ.

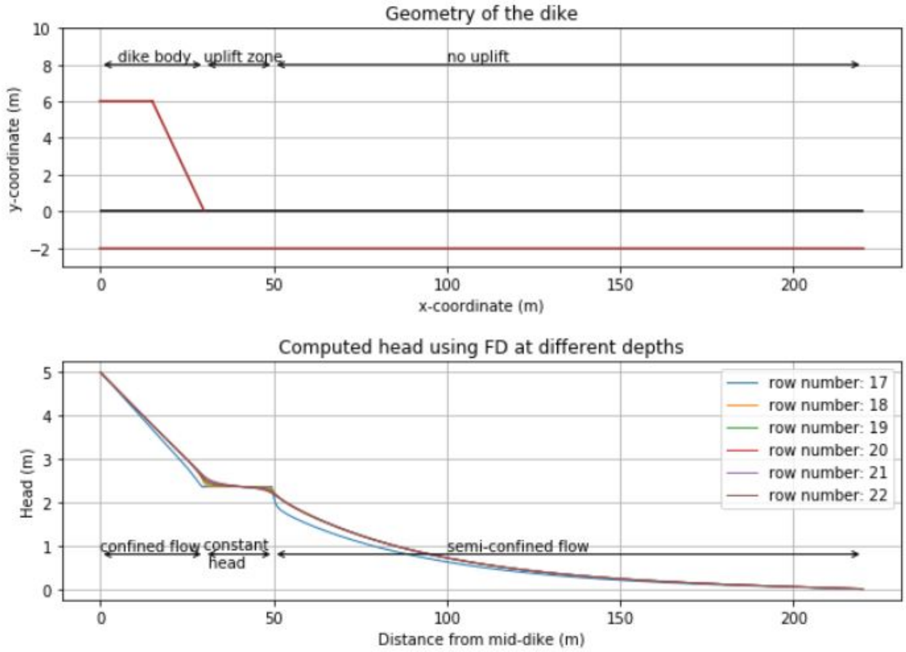

Figure 3.3: Geometry and flow regions of dike cross section

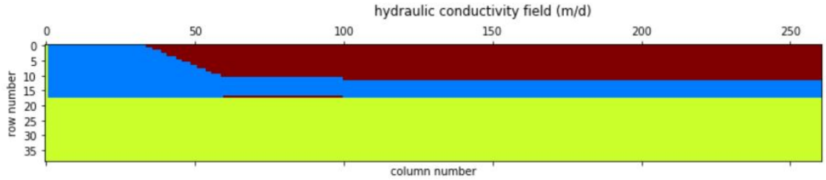

Figure 3.4: Hydraulic conductivity

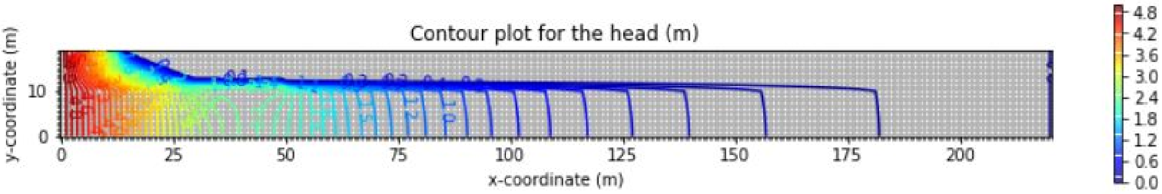

Figure 3.5: Head contour plot for full region

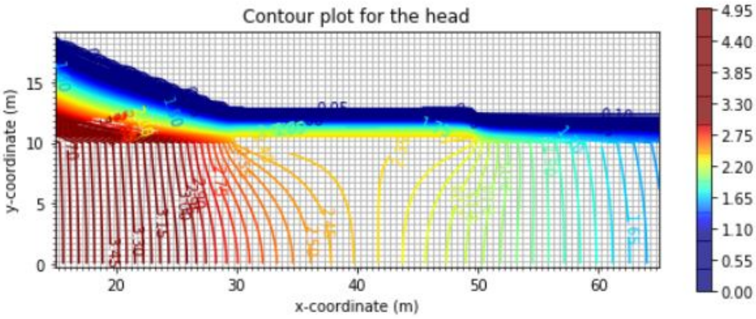

Figure 3.6: Head contour plot for uplift zone (detailed)

BOUNDARY CONDITIONS

At the edges of the model domain, the boundary conditions are specified. On the vertical boundaries the heads are given. In detail, this involves the following for the FD code: The heads are fixed at the first column, which corresponds to the water level at the center of the dike. Also, the last column has a fixed value, which corresponds to the hinterland water level. On the horizontal boundaries no-flow conditions are applied.

HYDRAULIC CONDUCTIVITY FIELD

The hydraulic conductivity pattern in shown in Figure 3.4. The colors red, yellow, and blue stand for very high, high to medium, and low conductivity respectively. There is a predefined gap length between the cover layer and the sand layer, beginning at the toe of the dike.

3.2.3. GEOHYDROLOGICAL FD MODEL OUTCOME

The results of the relations obtained using the FD geohydrological model are discussed here. For detailed information about the model and the Python code, refer to Appendix D.

OBSERVED FLOW TYPES AND HEAD CONTOUR PLOT

The lower graph in Figure 3.3 shows three different flow regions corresponding to the three zones in the graph above. Underneath the dike body, the head gradient is linear, indicating a confined flow. At the uplift zone, the head remains constant in consistency with the forming of a hydraulic shortcut between the cover layer and the aquifer. This hydraulic shortcut has a high conductivity. Lastly, the head profile turns into a typical semi-confined aquifer for the hinterland.

The head contour plots are shown in Figures 3.5 and 3.6. As seen in Figure 3.6 the potential lines are slightly curved at the begin and the end of the uplift zone, which is in line with the expectations of the outcomes of MSEEP by Barends (1999).

RELATION LENGTH AND LOAD

For a range of predefined uplift lengths, the corresponding head at the uplift zone is computed. Figure 3.7 shows the head at the top of the aquifer for various uplift lengths, as well as the relation between the uplift length and head directly. At the right, a horizontal line is plotted at 4.8 m. This equals the pressure from the self weight of the cover layer. Only points above this line resemble a situation of an uplifted cover layer.
Subsequently, the net load on the beam is easily obtained, by subtracting the self weight from the uplift pressure. Then, the shear force and bending moment is obtained easily, by applying basic mechanical formulas for a beam with two fixed ends. The formula for shear force is $V = 0.5 * q * L$ and for moment is $M = 1/12 * q * L^2$
All these outcomes are a range of possible lengths and heads. From this, the maximum value of this range is taken as the normative load.

In Figure 3.8, the result is shown for the situation in Figure 3.7. The maximum shear force occurs at an uplift length of about 20 meters, whereas the maximum bending moment is found at an uplift length of 30 meters.

This method is used to derive the maximum possible bending moment and shear force, given a fixed outer head, the geometry of the cross section and geohydrological parameters. However, it does not include deformation and/or cracking behavior of the cover layer. This method concludes the water/load part. Next, the soil/resistance part is discussed.

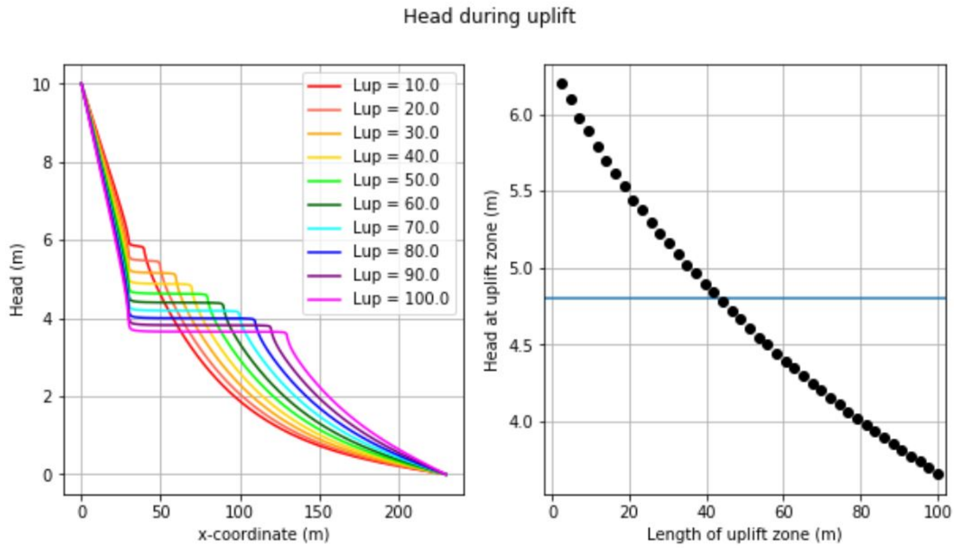

Figure 3.7: Length of uplift zone for different uplift lengths and fixed river head for $\lambda = 54.7m$

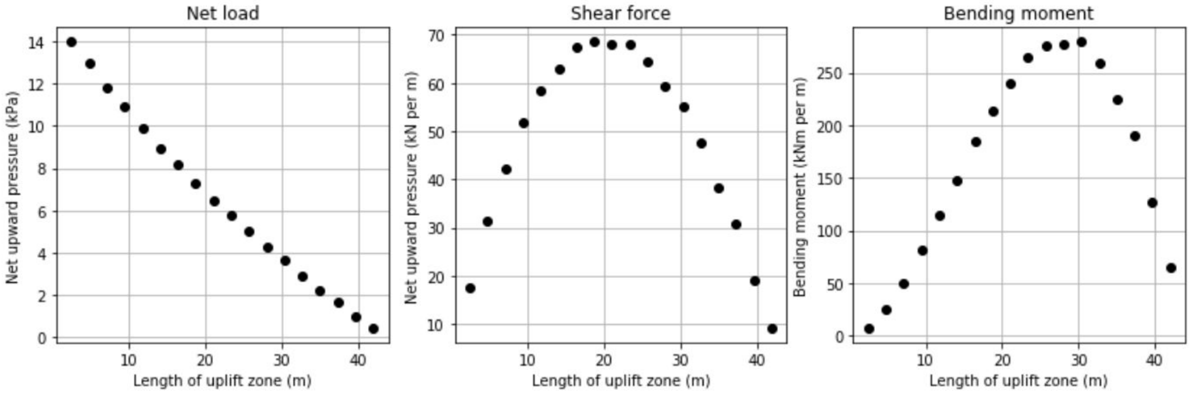

Figure 3.8: Load, shear force and bending moment

3.3. MODEL DESIGN - PART B: SOIL/RESISTANCE

The resistance to cracking in uplift conditions, is provided by the cover layer. The goal here is to find the normative failure mode and the location of failure. This section follows the same structure as the section before. First, relevant literature is summarized. These are regarding cracking modes, important dimensionless groups and the soil strength. Then, the process of model selection is explained, before discussing the model results. These outcomes provide insight in the key aspects of the soil behavior of the uplift zone. Utilizing this, two analytical equations to evaluate for tensile and shear cracks are proposed.

3.3.1. LITERATURE

This section summarized relevant literature on the soil behavior. Three subjects are discussed here. It starts by explaining several modes of cracking, as is prevailing in the fracture mechanics theory. Secondly, it discusses important dimensionless groups for an excavation base case. The key groups are related to the dimensions and the soil strength. Regarding the soil strength, two aspects are investigated as well: the tensile strength and the strain and stress profile under bending conditions.

FRACTURE MODES

In fracture mechanics, a subdivision is made between three modes of loading. The difference between the modes lies within the direction of the loading versus the direction of the crack (McGinty, 2014):

Mode I: Opening mode, caused by tensile stresses;

Mode II: Shearing mode, caused by in-plane shear stresses;

Mode III: Tearing mode, caused by out-of-plane shear stresses.

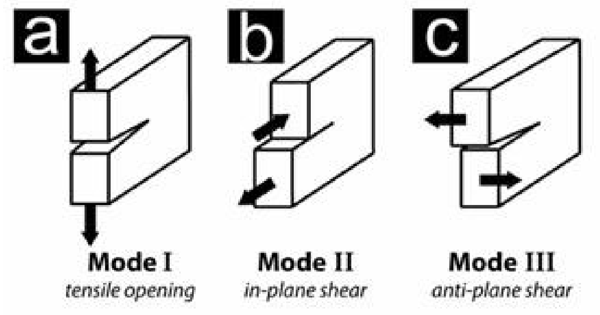

Figure 3.9: Three modes of loading in fracture mechanics (Zimmermann et al., 2009)

The modes are visualized in Figure 3.9. Since the crack in the cover layer is vertical, the tensile stresses for mode I are horizontally oriented. These horizontal tensile stresses are induced by the bending moment. For mode II, the in-plane shear stresses are induced by the shear force. The tearing mode, mode III, is not considered in the 2D analysis.

KEY DIMENSIONLESS GROUPS

There are two important parameter groups which determine the resistance. Firstly, these are strength parameters. Second, these are the dimensions: width and length. These two groups are also singled out by (Hong and Wang, 2016) as key dimensionless groups in an excavation base problem.

According to Hong and Wang (2016), the most important parameters in an excavation base are L, D, s_u, $\Delta\sigma_h$, and τ. This is reflected in the key dimensionless groups based on Buckingham's π method are: $\frac{L}{D}$ and $\frac{s_u}{\rho g D}$. The reasoning is as follows: The bending moment is counteracted by the horizontal stress profile, $M = f(\sigma(z))$. In case of the elastic bending theory: $\Delta\sigma_h \sim (\frac{L}{D})^2$. The shear stress is linearly dependent: $\tau \sim (\frac{L}{D})$. It is stated that $\frac{\tau}{s_u}$ is a constant, and that $\Delta\sigma_h$ is dependent on s_u as well.

As discussed in Appendix C, the bending moment has a high probability of being normative for the load. Hong and Wang also agree to this if $L/D > 1$. The bending moment comes from the horizontal stresses, which have a tensile and a compressive component, where the tensile capacity is much lower than the compressive capacity. Extra care is taken about how to handle the tensile behavior of cohesive soils, which is discussed below.

TENSILE TESTING FOR COHESIVE SOILS

The tensile testing is performed with non-standardized lab tests. Appendix E contains a detailed overview and discusses their suitability. The main objective there is to find an appropriate stress-strain relationship is researched for the tensile domain for cohesive soils, as well as suitable values for the peak tensile strength and strain. Here, the direct tension test and the bending test are discussed, as well as their use for the beam schematization.

DIRECT TENSION TEST: TENSILE CAPACITY, STRESS-STRAIN RELATIONSHIPS

The direct tension test is most interesting to find accurate stress-strain relationships for the soil in a stress-state because the stresses are measured directly.

The direct tension test gives the strength in terms of total stresses, varying from 10 to 150 kPa (see Appendix E, tables E.1 to E.3). The tensile strength depends on the type of soil, water content, and density. For clays, the stress-strain relationship is best approximated by a linear stress-strain relationship, until the tensile capacity. After, the failure is of brittle behavior (Li et al., 2019; Wang et al., 2007; Tang et al., 2014). For peat, the stress-strain relationship is of elastoplastic nature including strain-hardening (Helenelund, 1967).

There is little literature present on the effective tensile strength. For remolded clay, the effective tensile strength is generally assumed zero. For natural clays, the strength is suspected to be nonzero (Cor Zwanenburg, personal communication). Bagge (1985) proposes to approximate the effective tensile strength for clay as half of the value for cohesion. Helenelund also proposes that the tensile capacity of peat equals about half of the undrained shear strength, based on experimental results.

BENDING TEST: STRAIN DEVELOPMENT, STRESS PROFILE

On the other hand, the four-point bending test is useful to gain knowledge on the strain development and the bending moment capacity. This is needed for the strain and stress profile during bending, to calculate the bending moment resistance.

During the four-point bending test, the strain profile is found to be linear over depth (Ajaz and Parry, 1975; Šuklje, 1969; Thusyanthan et al., 2007). Over the subsequent stress profiles, the opinions in literature are divided. The simplest approach is to use the elastic bending theory. However, more sophisticated and non-linear elastic theories are applied as well. Lastly, the stress profile of a numerical discrete element modeling study is highlighted. It shows linear elastic turning into plastic behavior, just before failure (Ammeri et al., 2006).

3.3.2. MODEL SELECTION AND BOUNDARY CONDITIONS

MODEL APPROACH: PLAXIS FEM

Three options to approach the stress development were considered. Firstly, analytically, based on the linear elastic beam theory. Secondly, using a predefined stress-strain relationship, or thirdly using a finite element model. These approaches are briefly discussed hereafter. For a detailed explanation of the first two approaches, please refer to Appendix F.

Analytical beam equations

For a beam, there are analytical solutions present, based on the linear theory of elasticity. Given a tensile and shear capacity, the maximum resistance to the bending moment and the shear force is known. The outcome of the analytical beam equations, is that the failure of the beam is most likely started by exceedance of the flexural strength.

Using a predefined stress-strain relationship in Python

From literature, it is learned that the strain is linear over depth. With a stress-strain relationship, the strain can be translated to the stresses, to evaluate the resistance to the flexural moment. Firstly, the stress-strain relationship of the tensile behavior is approximated by a linear elastic relationship, until the tensile strength. When the this maximum strength is reached, the stress reduces to zero. For the compressive behavior, a linear elastic-perfectly plastic relationship is assumed. Also, the strain development during bending is linear over depth. With these starting points, the maximum resistance was found at the point of crack-initiation.

Plaxis FEM

There were a few significant shortcomings from the previous two approaches. They included only horizontal stresses to evaluate the bending moment, but not vertical stresses, the initial stress conditions or principal stress rotations.

Using numerical software, the problem is evaluated. Plaxis is selected here, which is based on the Finite Element Method (FEM) and developed for geotechnical analysis purposes. Its use includes numerous advantages. For example, Plaxis automatically computes the in-situ stresses during the initial phase of the program. Furthermore, the development of horizontal and vertical stresses in Plaxis is linked, and there are different (advanced) models available for the stress-strain behavior of soils. To model fracturing mode I (see Figure 3.9), in Plaxis a tensile cut-off criterion can be specified. The soil at that stress point can be considered failed in tension when the tensile cut-off is hit. For fracturing mode II, the soil is considered failed in shear if the shear capacity is mobilized over the entire depth of the clay layer. Plaxis indicates shear failure by reporting that the soil mass has become unstable. The Python script for the Plaxis model is included in Appendix G.

BOUNDARY CONDITIONS

Regarding the displacement, the following boundary conditions are imposed. The vertical boundaries are fully fixed, i.e. no displacement in x- and y-direction allowed. The horizontal boundaries are free. On the lower horizontal boundary, an upward constant line load is applied, equal to the effective self weight of the beam plus the net load.

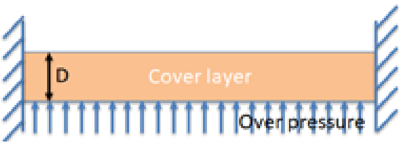

Figure 3.10: Points of interest in beam including zones with tensile stresses in horizontal direction

Fixities

When applying the boundary conditions as indicated, the soil beam is schematized as in Figure 3.10. There are a few concerns about the fixed ends, since the failure is clearly observed near the fixities in Plaxis outcomes, in terms of failure points and large deviatoric strains.

The main concern is that the fixed ends are in reality rotating outwards when the cover layer deforms. Instead of fixed ends, a pinned support with a torsional spring would be more accurate. This means that this schematization might lead to larger internal stresses than would be expected in reality. Secondly, the fixities influences the stress rotation. The maximum effective tensile strength is expected to be horizontal based on Figure 4.5 of Hoffman (2019) at points close at the beam ends. In the Plaxis results, the principal stress is rotated.

Other geometry set ups have been investigated. They show that the vertical ends of the uplift zone indeed rotate outwards. However, these geometries come with extra unknowns at the sides of the uplift zone. The largest values for the bending moment and shear force are still found at the ends of the uplift zone. Therefore, the geometry chosen is the same as in Figure 1.6, which is a conservative choice.

CONSTITUTIVE MODELS

Firstly, the first subject to discuss is the use of advanced constitutive models other than a linear elastic model as used in the analytical beam equations. Plaxis provides many options for a soil model, including user defined soil models (UDSM). However, here only three are discussed: the Mohr-Coulomb model, the Hardening Soil model, and the NGI-ADP-S model (Bakker et al., 2011; Brinkgreve et al., 2006; Brinkgreve, 2016; Panagoulias and Brinkgreve, 2017).

Linear elastic perfectly plastic: Mohr-Coulomb (MC)

The Mohr-Couloumb model is a linear-elastic perfectly-plastic model, and is recommended to use as a 'first approximation' of the soil behavior. The stiffness E is a constant value. Other input arguments are the Poissons ratio ν, cohesion c, friction angle ϕ and dilantancy angle ψ. Plaxis also allows specifying a tensile cut-off criterion.

Hardening Soil (HS)

The hardening soil model uses a non-linear stress-dependent stiffness and accounts for differentiating between primary loading and unloading/reloading behavior. This means that more input arguments are required for the stiffness, which are the traxial stiffness E_{50}, the triaxial unloading stiffness E_{ur} and the oedometer loading stiffness E_{oed} and their reference confining pressure p^{ref}. The stress-dependency of the stiffness is accounted for by the parameter m.

$$E_{50} = E_{50}^{ref}\left(\frac{c\cos(\phi) - \sigma_3'\sin(\phi)}{c\cos(\phi) + p^{ref}\sin(\phi)}\right)^m \tag{3.3}$$

This model incorporates both compression hardening and shear hardening. Plastic strains are mobilized by primary compression and friction. The stress history is accounted for by specifying a pre-overburden pressure (POP) or over-consolidation ratio (OCR), defining the cap. The mobilized friction angle cannot exceed the critical state friction angle. In this constitutive model, it is also possible to specify a tensile cut-off criterion.

SHANSEP NGI-ADP model (NGI-ADP-S)
The NGI-ADP-S model is the prescribed model for undrained behavior in cohesive soils during flood conditions (Visschedijk, 2018). The NGI-ADP model is based on a total stress approach and allows for anisotropy in the undrained shear strength parameters for different states. This model requires the shear failure strains γ_f^C, γ_f^D, and γ_f^E. These stand for the active, direct, and passive soil states and they are obtained using triaxial compression, direct simple shear and triaxial extension tests respectively. The undrained shear strengths (s_u^A, s_u^D, and s_u^P) are linked together. Furthermore, the active undrained shear strength s_u^A is calculated with the SHANSEP (Stress History and Normalized Soil Engineering Properties) equation, in which α is the SHANSEP-coefficient and m is the SHANSEP-power.

$$s_u^A = \alpha * \sigma_1' * OCR^m \tag{3.4}$$

The stiffness here is defined as a ratio of s_u^A and is thus stress-dependent. Since this model is total stress-based, it does not evaluate the pore stresses and effective stresses. Also, it is not possible to specify a tensile cut-off criterion. Because of the latter two arguments, the NGI-ADP-S is not used here.

Both the Mohr-Coulomb and the Hardening Soil model have advantages and disadvantages. On the one hand, the Hardening Soil model gives more realistic results but on the other hand requires more detailed input information. The use of the Mohr-Coulomb model is recommended, either for a first analysis (Brinkgreve et al., 2006) or if detailed input parameters are unknown , (Bakker et al., 2011). Here, both models are used and their outcomes are compared. The analysis starts with the Mohr-Coulomb model first. The input parameters for both constitutive models are given in Table 3.1 and 3.2

Table 3.1: Input parameters for Mohr-Coulomb model

parameter	value
γ_{sat} and γ_{dry}	16 kN/m^3
e_{init}	0.5
c'	5 kPa
ϕ'	25 °
ψ	0 °
Tensile strength	2.5 kPa
POP	15 kPa
OCR	1
E	1 MPa
ν	0.4 (E_{oed} = 2 MPa)

Table 3.2: Input parameters for Hardening soil model

parameter	value
γ_{sat} and γ_{dry}	16 kN/m^3
e_{init}	0.5
c'	5 kPa
ϕ'	25 °
ψ	0 °
Tensile strength	2.5 kPa
POP	15 kPa
OCR	1
$E_{oed,ref}$	2 MPa
$E_{50,ref}$	3.5 MPa
$E_{ur,ref}$	8 MPa
Power (m)	0.8

3.3.3. PLAXIS FEM OUTCOME

Firstly, the Plaxis outcomes are checked against the assumption of the fixed ends, by comparing the analytical beam equations to the Plaxis results for small loads when the soil still reacts elastically. Then, the outcomes of the Plaxis model are evaluated from a particle level to a 2D level. The evaluation starts with stress paths and stress-strain relationships. Subsequently, the strain profile and horizontal stress development are evaluated, and compared to the literature study from Appendix E. Moving on, relative shear stress in 2D is discussed for a beam at failure.

FIXED ENDS: COMPARISON WITH BEAM EQUATIONS FOR ELASTIC REGION

Using a geometry like in Figure 3.10 allows for a comparison with the beam equations $M = 1/12 * q * L^2$ and $V = 1/2 * q * L$. In the elastic domain, it is expected to resemble it well. Figure 3.11 confirms this, based on a

4 m thick cover layer with an upward load of $0.1 kPa$ (Mohr-Coulomb). Figure 3.12 shows the corresponding stress profiles over the depth of the beam at the beam's end.

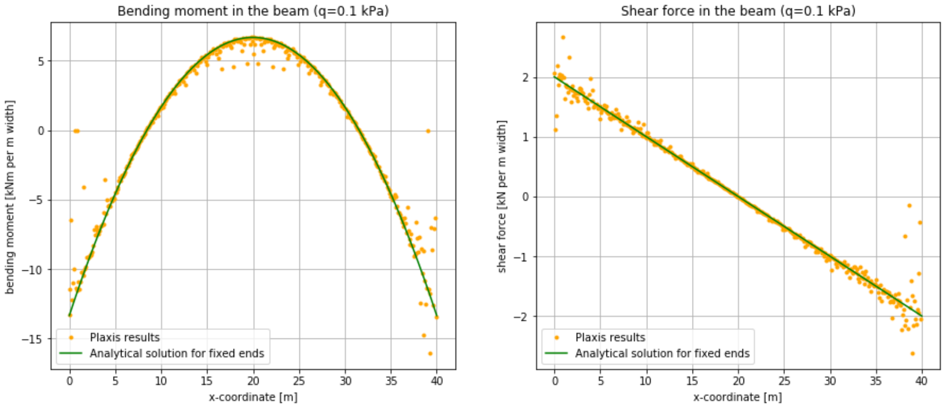

Figure 3.11: Comparison of the bending moment in the beam (MC, L=40 m, D=4 m, q = 0.1 kPa)

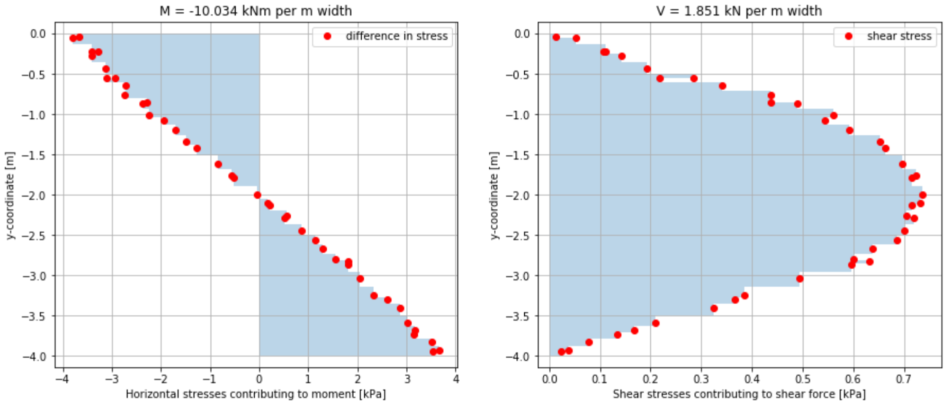

Figure 3.12: Horizontal and shear stress development at the ends of the beam (MC, x=1.3-1.8 m, L=40 m, D=4 m, q = 1.0 kPa)

Here, more explanation is given about the points from the Plaxis results. The stress plots are made based on the stress difference between the total horizontal stresses from the initial situation and the loading condition, for stress-points lying in a predefined cross-section. From this stress plot, the equivalent bending moment is computed. There is no result smoothing applied, which explains the few outliers from the Plaxis results.

STRESS PATHS OF POINTS IN THE BEAM

The effective stress development is interesting for detailed examination. Four stress-points in the beam are selected, which corresponds to the locations in Figure 1.6, and are plotted in Figure 3.13. In the Figures 3.14 and 3.15 the stress paths are visualized, including Mohr's circles, for the Mohr-Coulomb and Hardening Soil model respectively. Each circle corresponds to a Phase, and the phases have an increasing load. Phase 1 represents the equilibrium load (no net load), and the load increases with 0.1 kPa by every phase. Also, the black crosses indicate the poles of the Mohr's circles.

Tensile softening

Tensile softening stands for the behavior of the material in tension, after the peak tensile strength has been reached. This tensile strength is resembled by the tensile cut-off criterion in this analysis, which is set to 2.5 kPa. This value equals half of the value of the cohesion, as is proposed by Bagge (1985). In the Plaxis model, the tensile stress stays at the critical value when it is reached. In reality, however, the soil is expected to crack, and the strength subsequently reduces to zero. Since it is not yet possible to specify any tensile softening relationship in Plaxis, a workaround is applied. Whenever many tensile cut-off points in a soil polygon appear

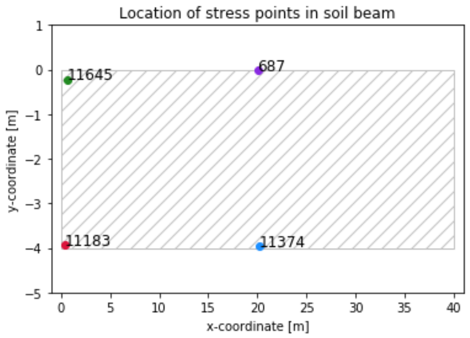

Figure 3.13: Location of interesting stresspoints

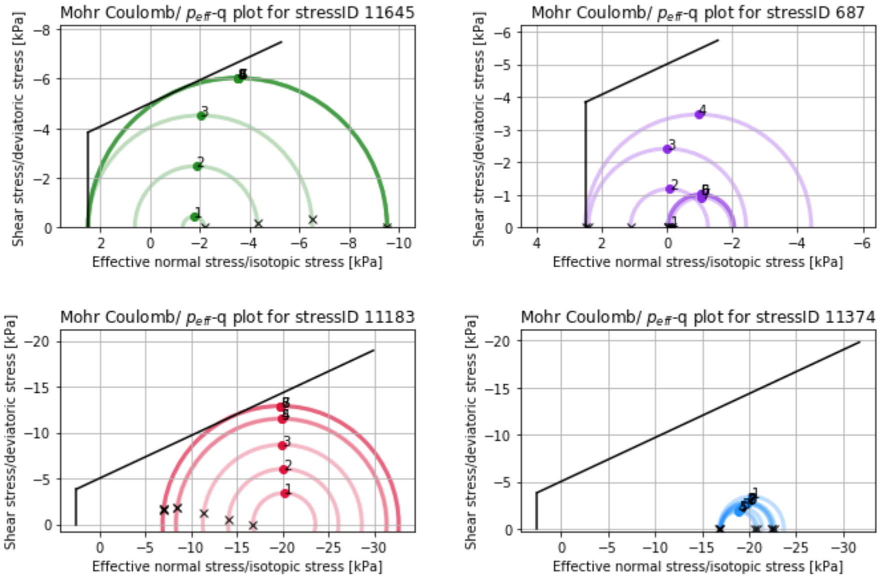

Figure 3.14: Stress development at interesting stresspoints in Mohr-Coulomb model (L=40m,D=4m,q=[0.0,0.1,0.2,...]kPa)

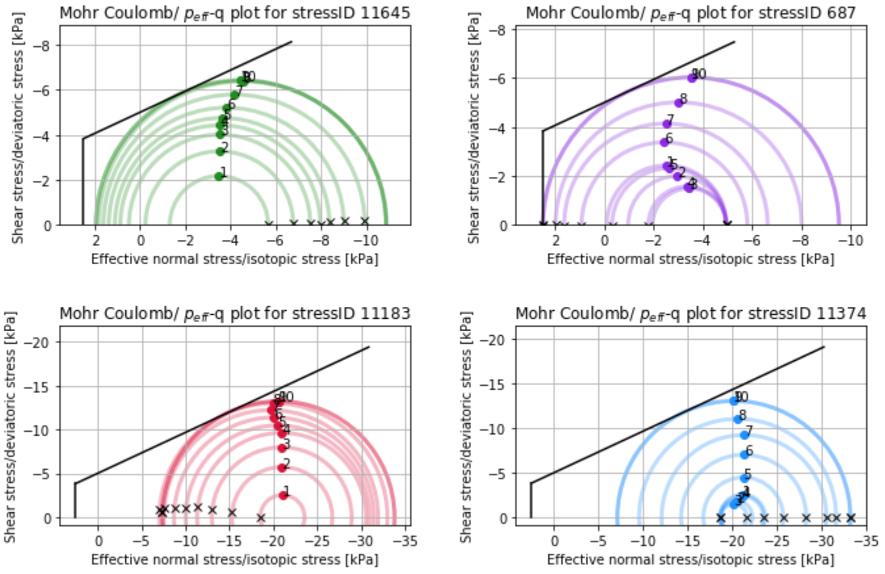

Figure 3.15: Stress development at interesting stresspoints in Hardening Soil model (L=40m,D=4m,q=[0.0,0.1,0.2,...]kPa)

in the Plaxis analysis, that soil gets lower strength parameters ($c' = 1\ kPa$, $\phi' = 1\ °$). This way, the decrease in soil strength after cracking is modeled and applied for tensile zones in the middle at the top.

The tensile limit is also reached at the ends of the beam at the top of the cover layer. There, the tensile stress direction is almost vertical, which is explained by an increase in major principal (almost horizontal) stress in undrained conditions, which leads to a decrease in the minor principal stress. Because of the zero-displacement edges, the tensile limit is reached faster than it would in reality, where the beam's ends are allowed to rotate. Since the stress development in real life is less, it is decided to leave the tensile cut-off points in the model unchanged at this location.

Comparison between MC and HS model

There are a few interesting observations of differences between the Mohr's circles of the two models. Firstly, the Mohr's circles in the Mohr-Coulomb model expand quicker, because there is no cap or shear hardening taken into account, and the elasticity is constant. Thus, for every load increase, the stress response is the same. In the Hardening Soil model, the stress-response becomes lower if the cap or shear hardening envelope is reached. Thus, for increasing load, the stress response becomes smaller. Secondly, the stress paths in the Mohr-Coulomb model are vertical until the envelope or cut-off criterion is hit, which is a feature of the Mohr-Coulomb model (Brinkgreve et al., 2006). Because of this, it could lead to optimistic shear strengths. The Hardening Soil model gives better results in this respect.

STRESS-STRAIN RELATION OF A POINT

As mentioned before, the Hardening Soil takes into account stress-dependent elasticity, and the stiffness is non-linear, which is a better formulation for the soil behavior. It also distinguishes between virgin loading and unloading/reloading behavior. This difference between MC and HS, and between different preconsolidation parameters is visualized in Figure 3.16.

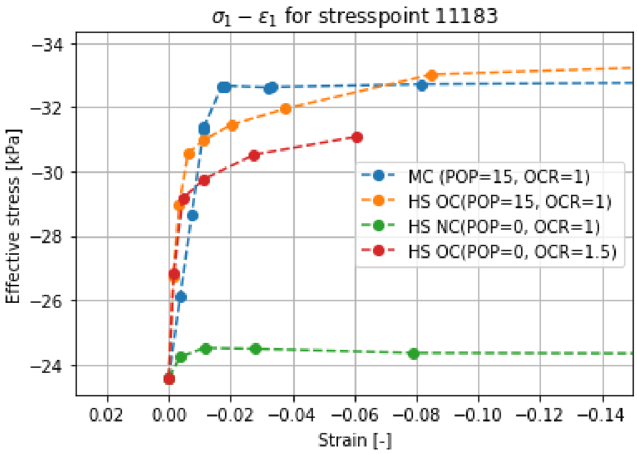

Figure 3.16: Stress-strain relationships for different models and different preconsolidation stresses for stresspoint 11183 'side under'

STRAIN AND STRESS PROFILE THROUGH CROSS-SECTION

The vertical cross-section located at the center of the beam is the most interesting to examine in the Plaxis model. Here, the shear force equals zero, and the bending moment is the only load governing. It allows for comparison to lab results since many bending tests are designed with a four-point loading system. There, only a moment applies as a load in the center part. In the past, many bending tests on cohesive soils are performed by Ajaz and Parry (1975); Suklje et al. (1961); Thusyanthan et al. (2007).

Firstly, the observed strain plots are compared. When comparing the strain plots from Plaxis with lab results, the strain plots generally match well, see Figure 3.17. The strain profile over depth is linear for small strains (<3%). Besides, the elevation in the beam at which $\epsilon = 0$ moves to the compressive side. Please note that in the Figures by Thusyanthan et al., the compressive side located at the upper part of the beam (between elevation from 40 to 80 mm), and in the Plaxis results, this is at the lower part of the beam (y-coordinate from -2 to -4 m). However, at phases near or at failure, the computed strains in Plaxis are unrealistically high (>3%).

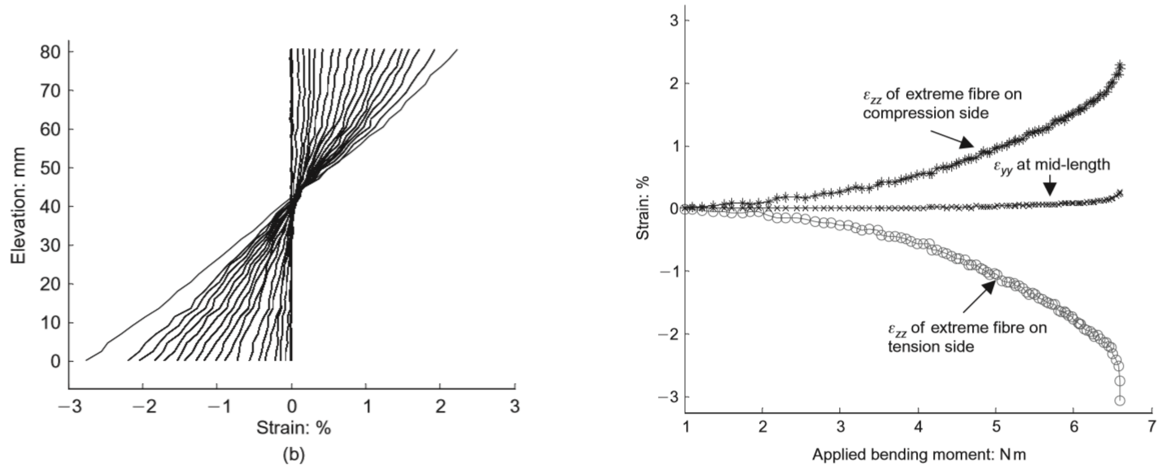

(a) Strain development in bending beam tests (Thusyanthan et al., 2007)

(b) Extreme strains in bending beam tests (Thusyanthan et al., 2007)

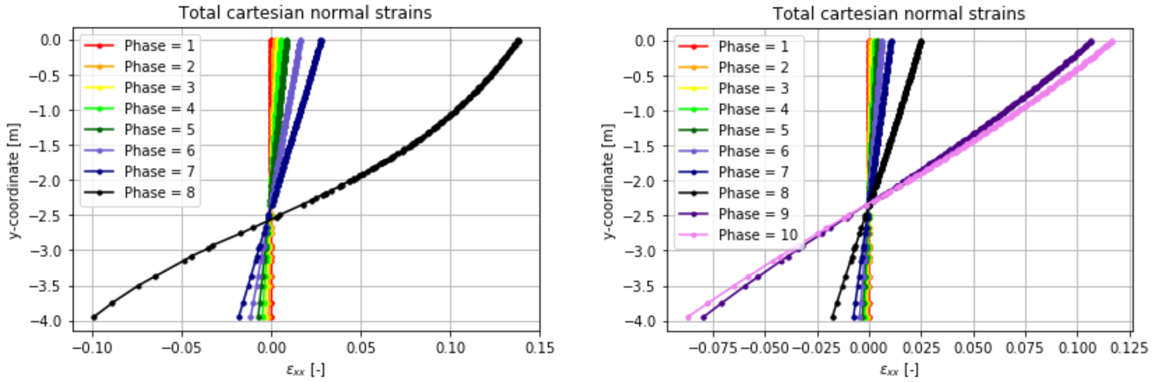

(c) Strain development in Mohr-Coulomb model (L=40m, D=4m, POP = 15 kPa, OCR = 1)

(d) Strain development in Hardening Soil model (L=40m, D=4m, POP = 15 kPa, OCR = 1)

Figure 3.17: Strain development in bending tests and Plaxis results

Secondly, the evaluation of the horizontal stresses is compared. The horizontal stress has not been measured directly in lab tests. Thusyanthan et al. (2007) translated the strains to stresses using a power-law function, which is seen in Figure 3.18. Furthermore, the stresses can also be obtained using Discrete Element Modeling (DEM). Ammeri et al. (2006) applied this on a bending test set-up with consolidated clay. The outcome with DEM also resembles the stress development by the Hardening Soil model well, because it also concludes that the compressive strength at failure is higher than the tensile strength.

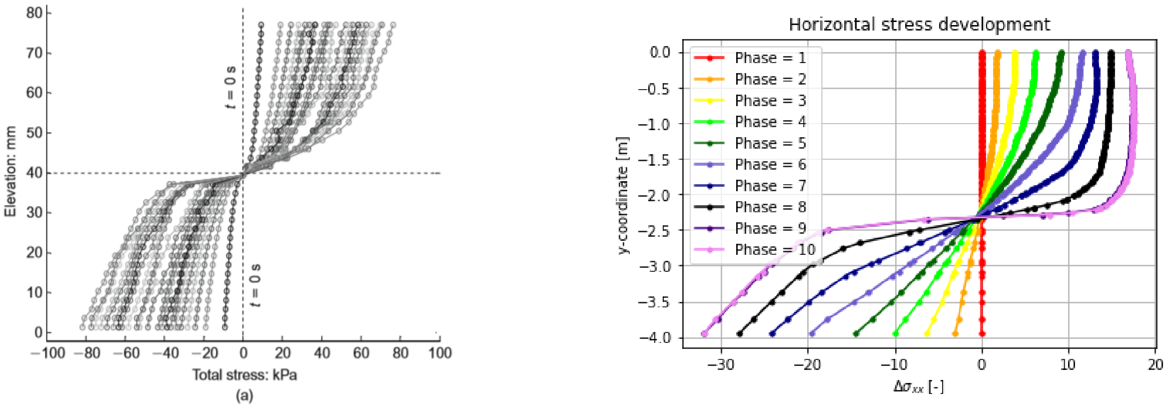

(a) Horizontal stress development obtained using DEM (Thusyanthan et al., 2007)

(b) Horizontal stress development in Hardening Soil model (L=40, D=4m, POP = 15 kPa, OCR = 1)

Figure 3.18: Horizontal stress development in DEM and Plaxis results

RELATIVE SHEAR STRESS AT FAILURE

At failure, the soil body becomes unstable in Plaxis. For the Mohr-Coulomb model, this happened at Phase 8, with a net load of 0.7 kPa, whereas this was at Phase 10, $q = 0.9\ kPa$ for the Hardening Soil model. It is interesting to see what the relative shear strength is for every stress-point in the beam. For the MC and HS constitutive model, the relative shear strength at failure is shown in Figure 3.19.

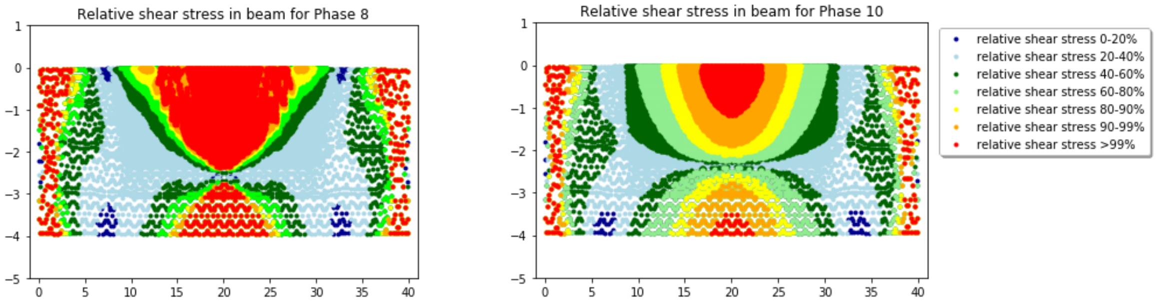

(a) Mohr Coulomb model

(b) Hardening Soil model

Figure 3.19: Relative shear stress at failure for MC and HS constitutive model (L=40, D=4, POP=15 kPa)

Comparison between MC and HS model

Here again, interesting observations of differences between the models are discussed. There is a striking difference in the development of the relative shear stress in the center of the beam. In the Mohr-Coulomb model, a relatively large area has reached the maximum shear strength (τ_{rel} between 99% – 100%). The domains corresponding to τ_{rel} between 80%–99% are barely visible. On the contrary, there is a clear and gradual transition in the relative shear stress pattern of the Hardening Soil model.

This observation is explained by the soil behavior models. In the Hardening Soil model, there is a transition in the soil behavior between fully elastic and fully plastic. If the soil starts to deform plastically, the stiffness decreases. Simultaneously, the load gets redistributed. In the Mohr-Coulomb model, the transition between fully elastic and fully plastic behavior is abrupt. Therefore, we see no transition zone (τ_{rel} between 80% – 99%).

This observation implies that by redistributing the load in the Hardening Soil model, this model is able to withstand higher upward pressures than the Mohr-Coulomb model under the same preconsolidation condition.

CONCLUSION

Ultimately, many insights are gained from the literature study and the Plaxis modeling results. These are discussed hereafter in detail, starting with failure by tension and then by shear.

Firstly, fracture mode 1 (tensile opening) is discussed in the context of uplift. Regarding the tensile behavior of cohesive soils, experimental results show a brittle failure when reaching the tensile capacity. In Plaxis, this means that reaching the specified tensile cut-off resembled fracture mode 1. The modeling results show that tensile cut-off points only occur in regions with low initial stresses, which can be explained using the Mohr-Coulomb criterion. For small isotropic initial stresses, the Mohr's circle is more likely to touch the tensile cut-off criterion first than reaching the shear capacity.

Looking at the beam in a 2D domain, tensile zones are expected at two locations. The first location is in the center of the beam at the top of the cover layer. Second, at the bottom of the cover layer, at the ends of the uplift zone, tensile stresses are expected. At the top of the cover layer, the initial stresses are small, and the tensile cracks will form. However, they will only propagate until a certain depth, since the initial stress increase. At the bottom of the cover layer, it depends on many parameters if a tensile crack occurs. However, if the tensile strength is reached, the crack will be going through the cover layer to the top. After the crack opening, the initial stresses decrease, and the crack propagates.

In the Plaxis models, the uplift zone is approximated as a beam, which is brought to failure by increasing the upward distributed load. Shear failure is observed for large overpressures, causing large deformations at the center of the beam, when the uplift length is kept constant. However, in reality, the uplift zone would lengthen due to the high deformations. The increase in length happens because the vertical reaction force of the hinterland boundary of the uplift zone is insufficient. If the length of the uplift zone increases, the head in the uplift zone drops simultaneously. This intercoupled process leads to the conclusion that high upward pressures cannot occur in reality for uniform cover layers, so shear failure is unlikely.

3.3.4. ANALYTICAL APPROACH FOR CRITICAL THICKNESS AGAINST TENSILE CRACKS

Using the same approach as deriving the Rankine states and the free-standing height (Verruijt and Van Baars, 2007), a formulation for the critical thickness against tensile cracks can be found. This approach is based on the Mohr-Coulomb criterion. First, the point of interest is explained before explaining the key features of the critical Mohr's circle in Figure 3.20. Subsequently, the derivation of the critical thickness against tensile cracks is explained, and the influence of the type of soil on the stress path is discussed.

POINT OF INTEREST

The location of the point of interest to evaluate the Mohr's circle is at the edge of the beam, at the bottom of the cover layer. Here, the bending moment is nonzero, as is proven by results from Plaxis. For small loads, the beam's ends act as fixities, and the beam responds elastically. The moment- and shear diagrams then correspond to the outcomes from the linear elastic beam theory. For larger loads, the soil starts to behave plastically and the beam's ends can be schematized as pinned supports with a torsional spring. Either way, a tensile zone is expected at the bottom of the cover layer, which is also observed in results by Hoffman (2019). If a tensile crack opens up at this location, it will propagate to the top and form an exit point in the cover layer. Also, the shear force is largest at the end of the beam and could lead to a shear fracture.

KEY FEATURES OF MOHR'S CIRCLES AND THE COULOMB ENVELOPE

To evaluate the stress-state, Mohr's circles can be used. The Mohr-Coulomb theory is explained first: A point on the Mohr's circle defines the normal stress and the shear stress in a certain plane. The Coulomb envelope defines the failure criterion for shear and contains the strength parameters cohesion and friction. When the Mohr's circle touches the Coulomb envelope, the maximum shear stress has reached (Verruijt and Van Baars, 2007). Furthermore, a vertical line is added to represent the tensile strength to account for the tensile failure criterion.

One specific Mohr's circle is defined for finding the critical thickness for tensile failure. This circle is positioned such that it represents the transition circle between tensile and shear failure. When the soil hits the tensile capacity, it fails in a brittle way (see Appendix E). With this Mohr's circle defined, the critical effective isotropic stress is found at failure. This critical value has the following meaning: if p' at failure is higher, the

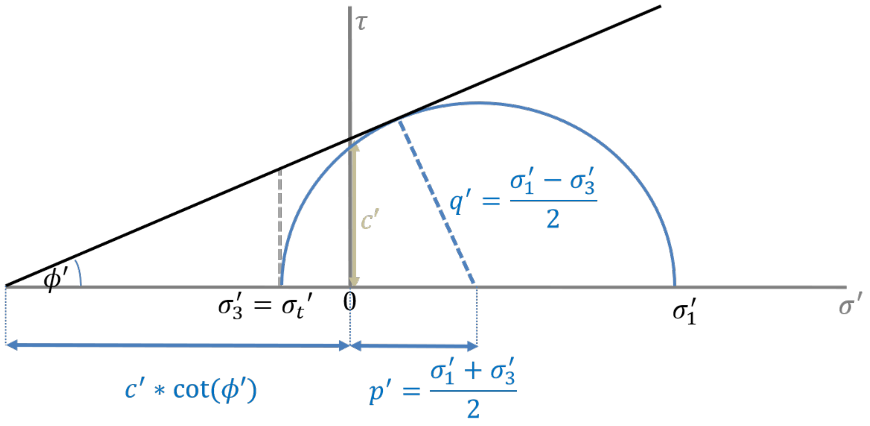

Figure 3.20: Critical Mohr's circle for tensile cracks, which touches both the tensile cut-off as the shear envelope

soil at the bottom-end location reaches the maximum shear stress. If p' at failure is lower, a tensile failure is expected. The critical value p' depends on the strength parameters cohesion (c'), friction (ϕ'), and tensile strength (σ'_t).

It is essential to note that if the shear envelope is hit first, the tensile limit cannot be hit anymore. The Plaxis outcomes for both the MC and HS model underline this statement, see also Figures 3.14 and 3.15. Furthermore, the plastic behavior of a soil particle at or near the shear envelope leads to stress redistribution in the 2D beam. Some areas in the beam will yield first, leading to redistributed stresses in the adjoining regions. It influences the stress development and reduces the likelihood of reaching the tensile capacity.

FROM MOHR'S CIRCLE TO CRITICAL THICKNESS

The critical thickness can be back-calculated from the effective isotropic stress (p') of the critical Mohr's circle. Here, the reasoning is explained based on assuming a vertical stress path.

The critical depth is found using the following steps: Assuming that the stress path is vertical implies that p' stays constant (Equation 3.5). Furthermore, the vertical and horizontal initial stresses are known (Equations 3.6 and 3.7. This yields to Equation 3.8. For a detailed elaboration, please refer to Appendix H.

$$p' = \frac{\sigma'_1 + \sigma'_3}{2} = \frac{\frac{1+\sin(\phi')}{1-\sin(\phi')}\sigma'_t + 2c'\sqrt{\frac{1+\sin(\phi')}{1-\sin(\phi')}} + \sigma'_t}{2} = \frac{\sigma'_{1,\,init} + \sigma'_{3,\,init}}{2} \tag{3.5}$$

$$\sigma'_{1,\,init} = \gamma_{eff} * D \tag{3.6}$$

$$\sigma'_{3,\,init} = K_o * \sigma'_{1,\,init} = \left(1 - \sin(\phi')\right) * \left(\gamma_{eff} * D\right) \tag{3.7}$$

$$D_{cover} = \frac{\left(\frac{1+\sin(\phi')}{1-\sin(\phi')}\sigma'_t + 2c' * \sqrt{\frac{1+\sin(\phi')}{1-\sin(\phi')}} + \sigma'_t\right)}{\gamma_{eff} * (2 - \sin(\phi'))} \tag{3.8}$$

Intermezzo: σ'_t in practice

To find a suitable value for tensile strength is quite difficult, since there are no standard lab test available. In literature, some suggestions are found. Bagge (1985) finds a relationship between the effective tensile strength and the cohesion and advises to use $\sigma'_t = 0.5 * c'$. Helenelund (1967) has performed experiments on peat, and gives the following guideline $\sigma'_t = 0.5 * s_u$.

Please note that for weak soil parameters, Equation 3.8 might give counter intuitive outcomes. From the formula, the required thickness against tensile cracks decreases for lower strength parameters (c and ϕ). This means in reality that weaker soil is more likely to fail in shear and therefore less likely to fail in tension.

3.3.5. ANALYTICAL APPROACH FOR CRITICAL THICKNESS AGAINST SHEAR CRACKS

Previously, in Section 3.3.3, it is reasoned based on Plaxis results, that shear failure is unlikely compared to tensile failure. At the observed shear failures in the Plaxis model, the deformation in the middle of the beam was unrealistically large. Furthermore, shear failure only occurs if a relatively large shear force could develop at the beginning and the end of the uplifted the cover layer. However, to allow the development of that large shear force, the beam's ends should be capable of providing sufficient reaction force. Nevertheless, on the hinterland side of the uplift zone, the vertical reaction force is insufficient, which means that the uplift zone could lengthen forever.

This reasoning implies that for infinitely high river water levels, the uplift length would be infinitely long. If the tensile limit is not hit, the cover layer will stay intact. In this case, the cover layer is in the bulging stage and would not crack. However, this implication might be too optimistic for extremely high river water levels and relatively low values for the soil strength in terms of cohesion and friction.

To be comprehensive for the bulging-cracking phase, the shear cracks are evaluated as well. The evaluation is based on a vertical equilibrium for a 2D beam:

$$2 * s_u * D_{cover} = \Delta h_{up} * \gamma_w * L_{up} - \gamma_{eff} * D_{cover} * L_{up} \tag{3.9}$$

For solving this equation, some crude approximations are applied. The maximum uplift length is estimated as $\frac{1}{4} * \lambda_h$, in consultation with Rimmer Koopmans. Also, the uplift head is assumed to be the average value of the head between the toe ($x = 0$) and $x = \frac{1}{4} * \lambda_h$ and the damping factor to account for the head at the toe itself is taken as the default value 0.8. The 'total damping factor' equals $0.8 * \int_{-\frac{1}{4}}^{0} e^x \, dx / \frac{1}{4} = 0.8 * 0.8875 = 0.71$

$$L_{up} = \frac{1}{4} * \lambda_h = \frac{1}{4} * \sqrt{k_{aq} * D_{aq} * D_{cover} / k_{cover}} \tag{3.10}$$

$$\Delta h_{up} = h_{polder} + 0.71 * (h_{river} - h_{polder}) - h_{exit} \tag{3.11}$$

Solving for D_{cover}, the critical thickness for the cover layer against shear cracks is:

$$\begin{aligned} D_{cover} = \frac{1}{D_{aq} * K_{aq} * \gamma_{eff}^2} * (D_{aq} * K_{aq} * \gamma_{eff} * \gamma_w * \Delta h_{up} + 32 * k_{cover} * s_u^2 - \\ 8 * \sqrt{D_{aq} * K_{aq} * k_{cover} * \gamma_{eff} * \gamma_w * \Delta h_{up} * s_u^2 + 16 * k_{cover}^2 * s_u^4}) \end{aligned} \tag{3.12}$$

Intermezzo: s_u in practice

To find a value for the undrained shear strength, many options are available. An undrained triaxial test may be executed. Also, it might be found using the Mohr-Coulomb envelope based on drained or undrained parameters, or the SHANSEP formula can be used.

3.4. DISCUSSION

To conclude, it is necessary to develop a more complex model for uplift, since a one-dimensional model is insufficient to describe the problem. The problem is treated here in two parts: firstly the water-part as the load and secondly the soil-part as the resistance. Both are tied together via the dike geometry and the subsoil composition. Not only the flow nets below, but the deformation of, and the stresses within the cover layer must be treated as two-dimensional problems.

The most suitable model for uplift is the beam model. In an uplift situation, there is a uniform distributed load acting on the beam, which comes from the hydraulic head beneath the cover layer. The thickness and strength parameters are originating from the cover layer characteristics. Regarding the constitutive model, the Hardening Soil model gives realistic results.

This chapter revolved around the question of how a full crack leading to an exit point for the forming of sand boils is formed under uplift conditions. In Section 3.3.4, an analytical approach using the Mohr-Coulomb criterion is found for the critical thickness against a tensile opening at the bottom of the cover layer. It is based on whether the tensile strength may be reached at the bottom of the cover layer before a plastic failure occurs there. For completeness, Section 3.3.5 discusses the evaluation of the critical thickness against shear cracks, which is based on a 2D vertical equilibrium.

During the model design, some assumptions are made. Hereafter, the most important are summarized and reviewed.

DISPLACEMENT AND ROTATION OF THE VERTICAL BOUNDARIES OF THE BEAM MODEL

In the application of the beam model, the vertical boundaries are schematized as fixed ends. These are fixed in x- and y-direction and cannot rotate outwards when the beam starts to deform, which might lead to larger moments and shear forces than in reality.

VERTICAL EFFECTIVE STRESS PATH

Here, the assumption of a vertical effective stress path under undrained conditions is discussed. The slope of the stress path is dependent on the constitutive model in Plaxis and on the type of soil in reality.

With a linear elastic perfectly plastic soil model, Mohr-Coulomb, the stress path is expected to develop vertically. The observed Mohr's circles' development matches the expectation. However, this constitutive model gives a crude approximation. Besides, for normally consolidated soils, the strength is overestimated. The Hardening Soil model gives better results for soft clays (Surarak et al., 2012). Also, the plastic compaction (cap hardening) that occurs in the HS model is ascribed to lead to a decrease in mean effective stress (Brinkgreve et al., 2006).

A vertical effective stress path is only applicable for lightly overconsolidated (OC) soils (Brinkgreve, 2019). For heavily overconsolidated soils, the vertical stress path assumption leads to a conservative answer. However, for normally consolidated clays, assuming a vertical stress path leads to optimistic results. Therefore, a very conservative value for Skemptons' A parameter for soft (NC) soils can be taken, leading to the assumption that the stress path develops under an angle of 45 degrees. For these soils, the critical thickness should be taken as twice the value for a vertical stress path. Note that in reality, no NC-behavior is expected. When high pore water pressures are intruding from the aquifer, the effective stresses decrease. The effective stress at that point is smaller than the initial stress, so the soil will behave in an overconsolidated manner.

TIME DEPENDENCY

Regarding time-dependent processes, there are a few assumptions. Firstly, the flood wave is assumed as a step increment. Secondly, the time-wise length of the flood wave is assumed short, such that undrained conditions apply. This means that the water takes all of the load by means of the excess pore water pressure. In time, the pore water pressures change and the soil skeleton takes on extra load as well. Three mechanisms in the uplift phenomenon including changing pore water pressure in time are identified:

1. Intrusion of high water pressures from the aquifer;
2. Stress transfer from excess pore water pressure to soil skeleton;
3. Internal drainage from high excess pore water pressures (compressive side) to low pressure (tensile side).

If time progresses, the most influencing mechanism will be the pore water intrusion. At the bottom of the cover layer, the pore water pressure will rise, leading to a decrease in effective stresses. For that area, the overconsolidation ratio (OCR) increases simultaneously. It is difficult to state how the strength against tensile cracks will change since the effective isotropic stress is lower but a larger OCR leads to an effective stress path bending to the right. For the shear strength, this is also challenging, since the effect of the effective stress and OCR counteract each other, as follows from the SHANSEP formula.

4

IMPROVED UPLIFT MODEL: CARTOON, FAULT TREE, CASE

This chapter brings the findings on uplift from the previous two chapters together and presents it in three ways: the phases of uplift in a visual way, the application of the uplift phases in terms of the limit state functions and the fault tree, and practically by applying it to a case. The case location selected is between Wijk bij Duurstede and Amerongen in Utrecht, the Netherlands.

4.1. VISUAL REPRESENTATION OF THE PHASES IN UPLIFT

This section provides a visual overview of the distinguished phases in uplift through a cartoon, also discussing the main highlights. The uplift phases are the initial situation, floating, bulging, and cracking. Subsequently, it proposes an updated fault tree to evaluate uplift in the context of internal erosion. The phases floating and bulging/cracking are reviewed separately in this thesis, in Chapter 2 and 3, respectively. Here the highlights are reported.

INITIAL SITUATION

Conditions susceptible for uplift are a dike hinterland consisting of a poorly permeable cover layer, the aquitard, on top of a permeable layer. The poorly permeable layer is of a cohesive type of soil, i.e. clay or peat. The permeable layer is composed of sand and is commonly referred to as the aquifer. The aquifer typically extends to the riverbed.

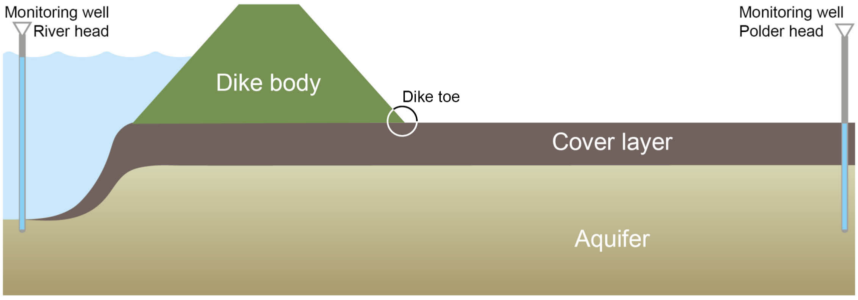

Figure 4.1: Phases of uplift - initial situation with subsoil layers

Any rise or drop of the river water level changes the groundwater head in the aquifer as well. The low permeability cover layer also ‘feels’ the change in the head by an increase in upward pressure. The head profile at the top of the aquifer for different river levels is shown in Figure 4.2.

In this situation, the head profile consists of different sections. Underneath the dike body, the head decreases linearly since the flow is assumed to be confined. In the hinterland, the cover layer is a so-called ‘leaky layer’, and there is a semi-confined flow. The head here is decreasing nonlinearly, which can be described by an exponential function (Blanket theory equations, Jonkman et al. (2018)) or by a hyperbolic sine (TAW, 2004). The rate of decline is dependent on the leakage length (Equation 1.3).

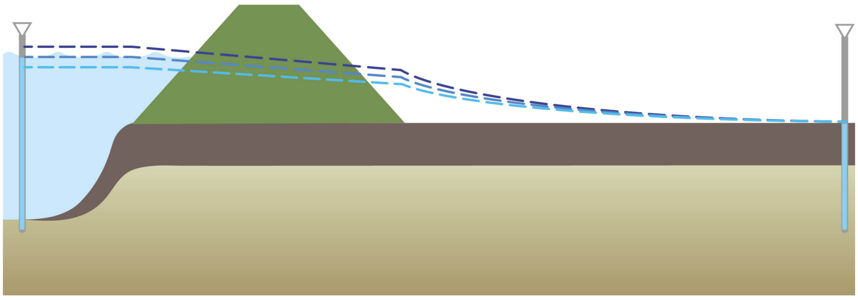

Figure 4.2: Phases of uplift - initial situation with groundwater head in aquifer

FLOATING

During a flood event, there is a chance that the cover layer is uplifted. In that case, the upward pressure equals or exceeds the downward pressure from the self-weight of the cover layer. The cover layer then may detach from the aquifer.

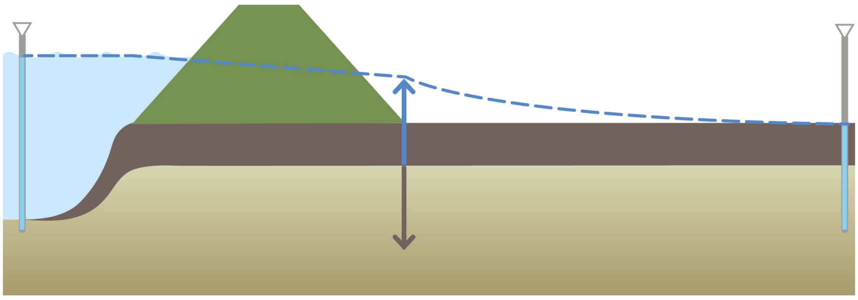

Figure 4.3: Phases of uplift - floating

In the current safety assessment for uplift (Jongejan, 2017), when the upward and downward pressures at the toe are equal, uplift is considered to occur, and the cover layer is considered as broken.

BULGING

The cover layer can detach from the aquifer, i.e. ‘floats’, and a gap forms at the aquitard-aquifer interface. Wave-like movements of the cover layer and bulges can be observed (Calle, 2002). The bulging is also called blistering and might only contain small vertical deformations (TAW, 2004).

The water pressure is constant in the gap. The bulging stage is equivalent to a situation in which a hydraulic shortcut is present. In the hydraulic shortcut, there is no resistance for a hydraulic gradient to develop. The head in the gap can be slightly larger than the weight of the cover layer because the cover layer will deform and lengthen during the uplift condition.

The value for the head in the uplift zone depends amongst others on the length of the gap. Using 2D groundwater models, the head profiles are evaluated. While the exact length of the uplift zone is unknown, it is found that the value of the head in the uplift zone can be approximated as the average value over the uplift length without a hydraulic shortcut present.

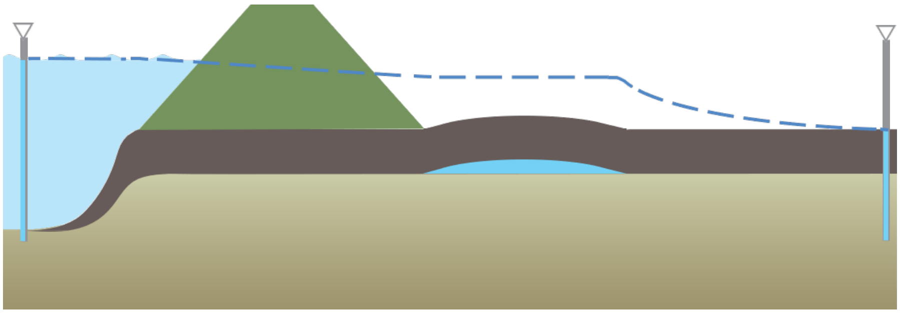

Figure 4.4: Phases of uplift - bulging

If the river level increases in uplift conditions, not only would the head in the gap increase, but the floating part of the aquitard would also lengthen. The extension is explained according to the following mechanism. The total load on the uplifted cover layer is given by the distributed net load and length of the uplifted zone. If the river head increases and only the uplift head would increase, large deformations would occur in the cover layer. Subsequently, at the edges, a large reactive shear force is required. At the hinterland side, the vertical resistance is insufficient, and the uplift zone increases in length. Simultaneously, the head in the uplift zone drops.

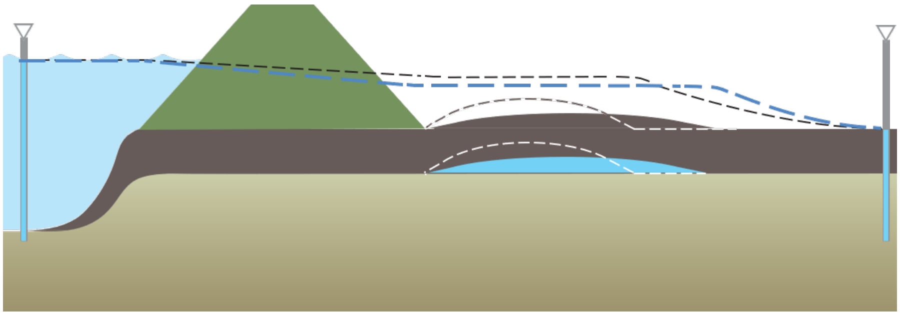

Figure 4.5: Phases of uplift - uplift length increases

CRACKING

Cracking could occur due to tensile forces or due to shear forces. Failure of the cover layer depends on:

a. the initial stresses (thickness, effective volumetric weight)

b. strength parameters (cohesion, friction)

c. elastic parameter and

d. the geometry of the deforming cover layer.

The two fracturing modes, tensile and shear, are discussed separately:

For tensile cracks, there are two areas in which tensile cracks are expected, if the initial stresses/self-weight is not taken into account:

1. At the top, in the middle of the uplift zone
2. At the bottom, at the toe of the dike/beginning of the uplift zone

These areas are indicated in yellow in Figure 4.6.

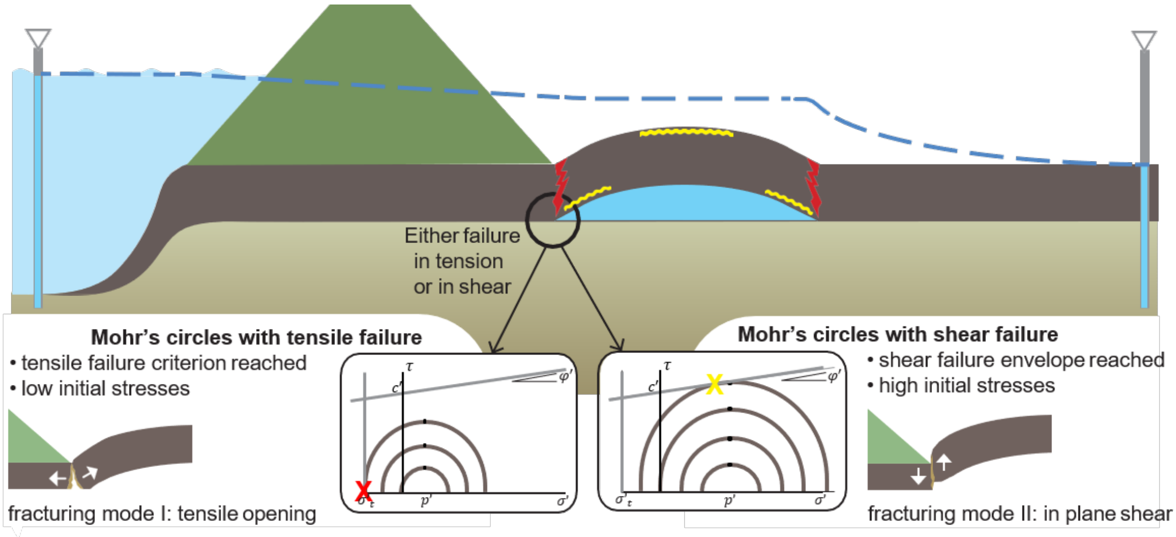

Figure 4.6: Phases of uplift - possible cracking areas

At the top of the cover layer, the initial stresses are low. Tensile cracks will occur at this location, propagating from the top, and increasing in depth as the cover layer further deforms. They are limited to a certain depth in the cover layer since deeper in this layer the initial stresses become larger.

At the bottom of the cover layer, where it joins with the aquifer, the tensile limit might be hit, possibly leading to a tensile crack. Whether the tensile limit might be hit can be deducted from the strength parameters, the type of soil, and initial stresses. Here, we are looking specifically at the soil state at the bottom of the cover layer. The evaluation is carried out by defining a Mohr-Coulomb envelope based on the basic strength parameters cohesion and friction, and a tensile maximum. If the initial stresses are relatively low, the Mohr's circle is likely to hit the tensile criterion. For higher stresses, the Mohr's circle is likely to hit the shear envelope and a tensile crack cannot occur. Using this argument, a formulation for the critical thickness for tensile cracks can be found.

In red, the shear zones are indicated. Shear cracks are expected at the beginning and end of the uplift zone. Whether the soil might fail in shear is evaluated using a vertical equilibrium for a 2D beam, including shear forces at the end. For relatively thin cover layers with weak strength parameters, the soil is likely to fail.

If both cracking by tension and by shear are out of the question, the cover layer stays in the bulging phase during uplift conditions. In this case, there is no exit point formed, and heave and piping cannot occur. So, adding the cracking phase improves the uplift assessment with regard to internal erosion.

4.2. UPLIFT IN THE INTERNAL EROSION FRAMEWORK

In this section, the proposal to improve the uplift assessment is set out. The current uplift assessment only evaluates the 'floating' phase, whereas the succeeding 'bulging'/'cracking' phase is neglected. The uplift assessment should be improved by adding the cracking phase so that tensile cracks and shear cracks are evaluated. The fault tree for internal erosion is shown in Figure 4.7.

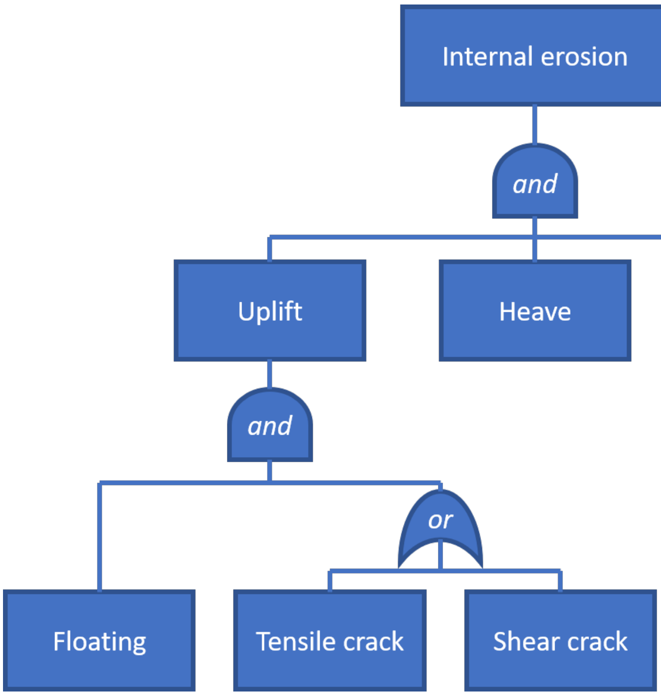

Figure 4.7: Fault tree for internal erosion - extended

The limit state for internal erosion is given by:

$$Z = \max\left(Z_{uplift}, Z_{heave}, Z_{piping}\right) \tag{4.1}$$

For uplift, it is proposed to apply:

$$Z_{uplift} = \max\left(Z_{floating}, \min(Z_{tensilecrack}, Z_{shearcrack})\right) \tag{4.2}$$

The uplift - floating

$$Z_{floating} = m_u * D_{cover} * \gamma_{eff}/\gamma_w - \left(h_{polder} + (h_{river} - h_{polder}) * r_{exit} - h_{exit}\right) \tag{4.3}$$

Uplift - tensile cracks

$$Z_{tensilecrack} = m_u * D_{cover} * \gamma_{eff} * (2 - \sin(\phi')) - \left(\frac{1+\sin(\phi')}{1-\sin(\phi')}\sigma'_t + 2c' * \sqrt{\frac{1+\sin(\phi')}{1-\sin(\phi')}} + \sigma'_t\right) \tag{4.4}$$

Uplift - shear cracks

$$Z_{shearcrack} = m_u * D_{cover} * D_{aq} * K_{aq} * \gamma_{eff}^2 + f(s_u) - D_{aq} * K_{aq} * \gamma_{eff} * \gamma_w * \Delta h_{up} \tag{4.5}$$

In which:

$$\Delta h_{up} = h_{polder} + 0.71 * (h_{river} - h_{polder}) - h_{exit} \tag{4.6}$$

$$f(s_u) = 8 * \sqrt{D_{aq} * K_{aq} * k_{cover} * \gamma_{eff} * \gamma_w * \Delta h_{up} * s_u^2 + 16 * k_{cover}^2 * s_u^4} - 32 * k_{cover} * s_u^2 \tag{4.7}$$

4.3. CASE: WIJK BIJ DUURSTEDE - AMERONGEN, THE NETHERLANDS

This section contains the results of determining the safety against uplift using different methods for a small dike stretch, DP42 to DP47 of dike ring 44. It starts with a description of the case location and an overview of input parameters. Then, the uplift assessment is performed, first based on the vertical equilibrium. Second, the soil beam model is used, as well as the analytical equations derived at the end of Chapter 3. This section shows how the insights from this report are applied in practice. For detailed elaboration on the calculations on DP47, please refer to Appendix I.

4.3.1. INTRODUCTION OF THE AREA

The location of interest is within the project 'Sterke Lekdijk' Wijk bij Duurstede - Amerongen (WAM), the Netherlands. It is the north dike stretch of river 'Nederrijn', part of dike ring 44, governed by the water board 'Hoogheemraadschap De Stichtse Rijnlanden' (HDSR). A general overview of this area is provided in Figure 4.8. In this dike ring, the cross-sections DP42 to DP47 are selected for the case. These are located in the dike sections (Dutch: 'dijkvakken') 44-03 and 44-04, see also Figure 4.9. This area consists of a cover layer of a few meters thick. In the dike stretch from DP42 to DP47, no piping observations have been reported in the piping database (RWS & USACE, sd). However, it scores insufficiently on the current uplift assessment.

Figure 4.8: Main waterways between Wijk bij Duurstede and Amerongen. The Amerongerwetering is shown in red (Kort, 2010)

SUBSOIL CHARACTERIZATION

In this area, the subsoil is characterized by a Holocene cover layer of a few meters thick, overlying a mainly Pleistocene aquifer. In Figure 4.10, the hinterland subsoil characterization is drawn by engineering company *Wiertsema Inpijn-Blokpoel*. Also, there is a characterization based on the outcomes of the CPT-tool, which distinguishes between 'light clay' ('KL') and 'heavy clay' ('KZO' & 'KZ').

INPUT DATA

The input data is summarized in Tables 4.1 to 4.3. There are three main sources of the data: the AHN (sd) provides the ground surface at the dike toe (h_{exit}), lowest point at the hinterland (h_{polder}) and the toe-to-toe distance of the dike (B). Soil investigation data give local parameters (Hertogh et al., 2018). From CPT and borings, the subsoil and its composition are obtained (D_{cover}, D_{aq}). Furthermore, lab experiments provide values for strength parameters (c, ϕ, s_u) and the volumetric weight (γ_{sat}). The volumetric weight per location is computed as the weighted average of light and heavy clay, of which the ratio differs per location (see Table 4.4). Furthermore, from the HydraRing output, the water levels (h) and corresponding return periods are obtained (provided by Ana Teixeira). Finally, default values based on an extensive geotechnical survey (Kwakman, 2019) are used as well for the hydraulic conductivity (k_f), thickness (D_f), and length of the foreland (L_f), the hydraulic conductivity for the aquitard (k_{aq}), the length of the hinterland (L_h) and the model uncertainty (m_u).

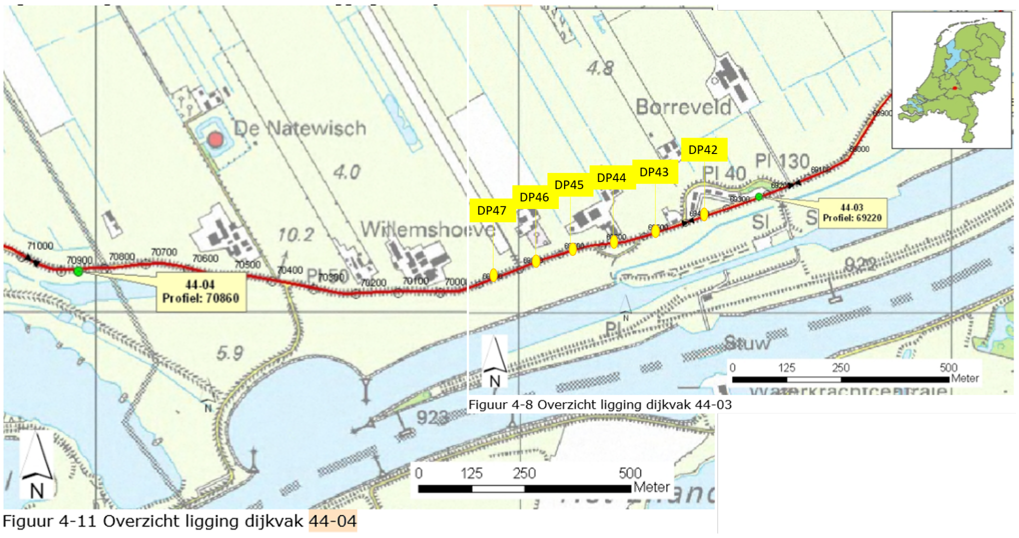

Figure 4.9: Dike sections 44-03 & 44-04 (Bisschop et al., 2011) (adapted)

Table 4.1: Input parameters for DP42-47

Symbol [unit]	Description	Distribution type	Mean	Variation	*char* value
B $[m]$	Toe-to-toe distance dike	-	*see Table 4.2*	-	-
D_{aq} $[m]$	Thickness of the aquifer	-	*see Table 4.2*	-	-
D_{cover} $[m]$	Effective thickness of the cover layer	log-normal	*see Table 4.2*	$\sigma = 0.25$ m	*see Table 4.3*
D_f $[m]$	Effective thickness of the foreland	-	1.5	-	-
h $[m+\text{NAP}]$	Outside water level	Gumbel	u = 6.41	$\alpha = 3.29$	MHW = 9.21
h_{exit} $[m+\text{NAP}]$	Phreatic level at the exit point	normal	*see Table 4.2*	$\sigma = 0.05$ m	*see Table 4.3*
h_{polder} $[m+\text{NAP}]$	Hinterland water level	normal	*see Table 4.2*	$\sigma = 0.15\ m$	*see Table 4.3*
k_{aq} $[m/d]$	Permeability of the aquifer	-	70	-	-
k_{cover} $[m/d]$	Permeability of the cover layer	-	0.02	-	-
k_f $[m/d]$	Permeability of the foreland	-	1	-	-
L_f $[m]$	Length of the foreland	-	15	-	-
L_h $[m]$	Length of the hinterland	-	5000	-	-
m_u [-]	Model factor for uplift	log-normal	$\mu = 1.0$	$cov = 10\%$	-
r_{exit} [-]	Damping factor at exit	log-normal	*see Table 4.2*	$cov = 1\%$	*see Table 4.3*
$\gamma_{eff,sat,cover}$ $[kN/m^3]$	Effective saturated volumetric weight of the cover layer	log-normal	*see Table 4.2*	$cov = 5\%$	*see Table 4.3*
γ_{water} $[kN/m^3]$	Volumetric weight of water	-	9.81	-	9.81

4.3.2. UPLIFT - FLOATING (WBI2017)

The calculation outcomes are presented here, based on the semi-probabilistic and fully probabilistic equations. Both equations are slightly different from Equations 2.2 to 2.6 (Jongejan, 2017), since the values for the polder water level and the phreatic surface at the exit point are not the same. The applied equations are presented on the next page.

$$Z_{up} = m_u \Delta D_{cover} * \gamma_{eff} / \gamma_{water} - (h_{polder} + (h - h_{polder}) * r_{exit} - h_{exit}) \tag{4.8}$$

$$\gamma_{up} = \frac{(\gamma_{sat} - * \gamma_{water}) * d_{cover}}{((MHW - h_{polder}) * r_{exit} + h_{polder} - h_{exit}) * \gamma_{water}} \tag{4.9}$$

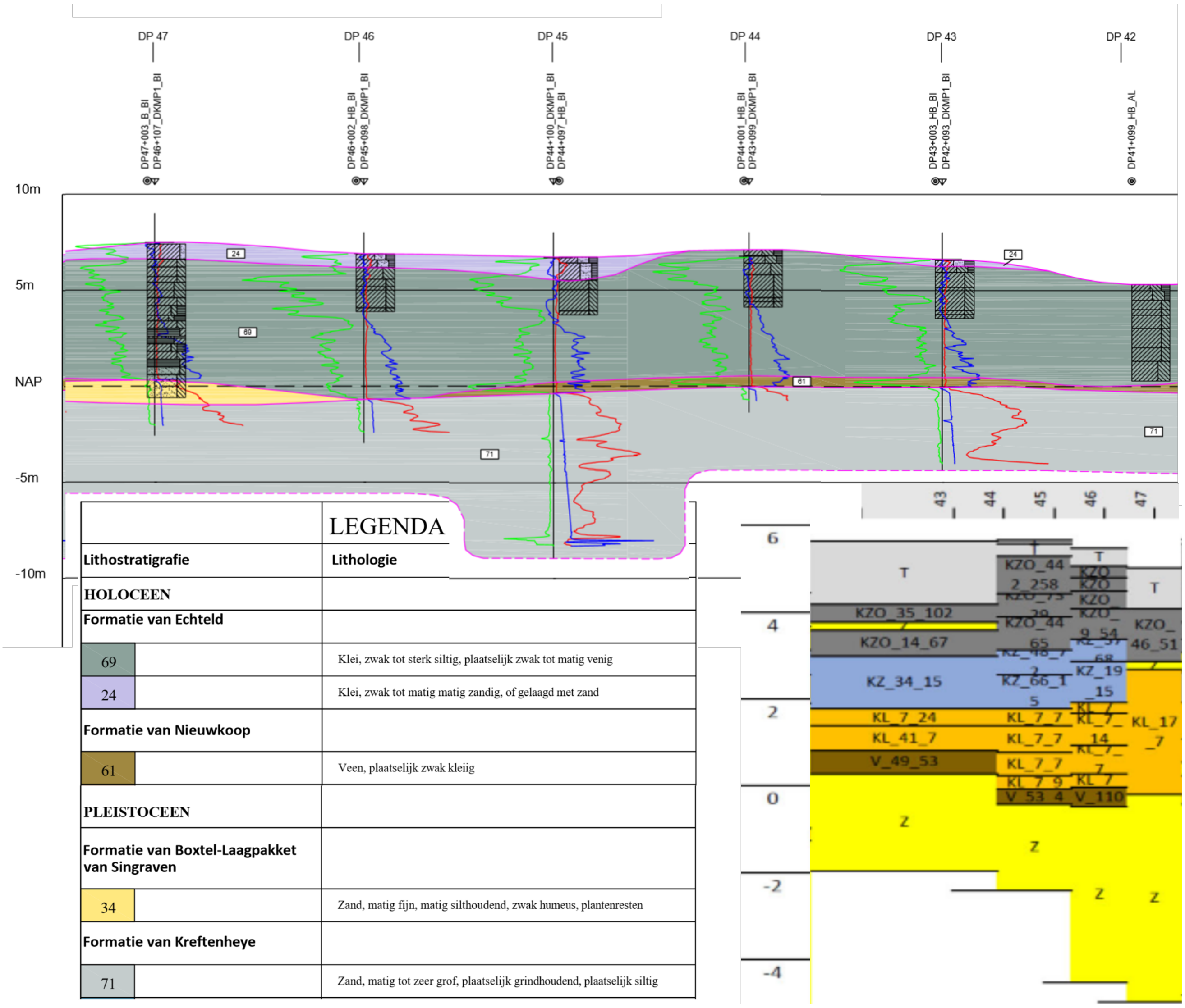

Lithostratigrafie	LEGENDA Lithologie
HOLOCEEN	
Formatie van Echteld	
69	Klei, zwak tot sterk siltig, plaatselijk zwak tot matig venig
24	Klei, zwak tot matig matig zandig, of gelaagd met zand
Formatie van Nieuwkoop	
61	Veen, plaatselijk zwak kleiig
PLEISTOCEEN	
Formatie van Boxtel-Laagpakket van Singraven	
34	Zand, matig fijn, matig silthoudend, zwak humeus, plantenresten
Formatie van Kreftenheye	
71	Zand, matig tot zeer grof, plaatselijk grindhoudend, plaatselijk siltig

Figure 4.10: Subsoil characterization of hinterland

Table 4.2: Mean values of location dependent parameters

DP	D_{cover} **(mean) [m]**	D_{aq} **[m]**	$\gamma_{sat,cover}$ **(mean)** $[kN/m^3]$	h_{exit} **(mean) [m + NAP]**	h_{polder} **(mean) [m + NAP]**	**B [m]**	r_{exit} **(mean) [-]**
42	4.94	10.15	17.861336	4.69	4.15	65.5	0.840451
43	4.89	10.51	18.130879	4.89	4.31	55.0	0.859975
44	5.37	11.00	18.092179	5.27	3.99	61.0	0.858252
45	5.86	11.31	18.108362	5.47	3.95	50.5	0.881704
46	5.99	11.56	18.044240	5.40	4.33	47.5	0.888728
47	4.98	11.29	17.504016	5.27	4.37	51.0	0.871997

CALCULATION OUTCOMES

The safety requirement for this area is a probability of failure in 1/10000 years. The matching reliability index is a β of 3.72 for the whole dike, and 5.03 for the submechanisms for internal erosion. The requirement in terms of the safety factor is 1.78. The outcomes of the uplift assessment are included in Figure 4.11 and show that the uplift submechanism fails the requirement. There, the 'characteristic value' points correspond to the uplift assessment, as is described by Jongejan and Calle (2013). However, in practice, the average values

Table 4.3: Characteristic values of location dependent parameters

DP	D_{cover} **(char)** **[m]**	$\gamma_{eff,sat,cover}$ **(char)** $[kN/m^3]$	h_{exit} **(char)** **[m + NAP]**	h_{polder} **(char)** **[m + NAP]**	r_{exit} **(char)** **[-]**
42	4.510170	6.576358	4.59	4.45	0.855456
43	4.460314	6.821614	4.79	4.61	0.875328
44	4.939048	6.786396	5.17	4.29	0.873575
45	5.427972	6.801122	5.37	4.25	0.897445
46	5.557716	6.742773	5.30	4.63	0.904595
47	4.550057	6.251354	5.17	4.67	0.887565

Table 4.4: Input parameters for uplift calculation

DP	**top cover (heavy) [m + NAP]**	**boundary light-heavy [m + NAP]**	**bottom cover (light) [m + NAP]**	D_{cover} **(mean) [m]**	**% heavy-light**	γ_{sat} **(mean)** $[kN/m^3]$
42	4.69	2.00	-0.25	4.94	54.5% - 45.5%	17.861336
43	4.89	1.70	0.00	4.89	65.2% - 34.8%	18.130879
44	5.27	1.85	-0.10	5.37	63.7% - 36.3%	18.092179
45	5.47	1.70	-0.39	5.86	64.3% - 35.7%	18.108362
46	5.40	1.70	-0.59	5.99	61.8% - 38.2%	18.044240
47	5.27	3.27	0.29	4.98	40.2% - 59.8%	17.504016

are taken as input arguments, except for MHW and h_p, since the OI2014 is unclear. Also, the results are included for the proposals made in Chapter 2. The 'clipped value' points mean that the maximum value for the damping factor is set to 1, and the minimum value for the volumetric weight for clay is set to 15 kN/m^3. Also, a sensibility analysis is made. For both the '$\sigma\gamma$' and 'σD' points, the variation is halved on the stochastic parameters.

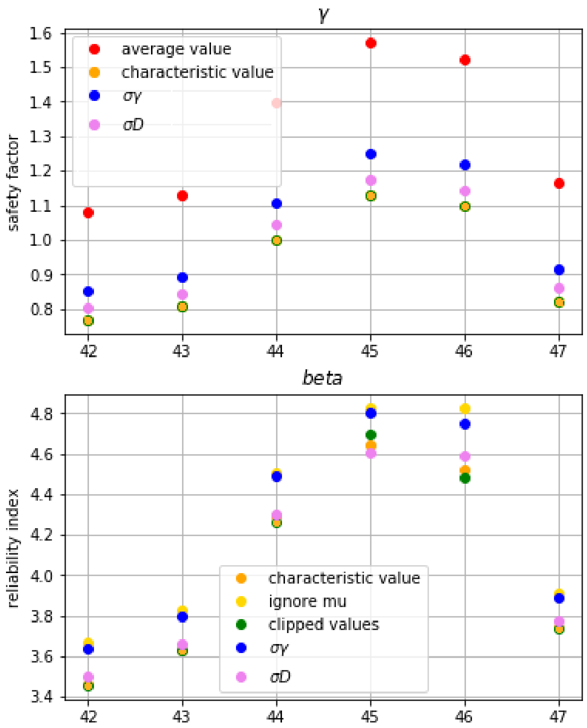

Figure 4.11: Outcomes on semi-probabilistic and fully probabilistic approach for uplift-floating

From the outcome, it can be concluded that reducing the variation on the volumetric weight and model factor contain the largest impact on the obtained reliability index.

Discussion

The hinterland is modeled as a very long cover layer, with a constant thickness, same as the thickness at the dike toe. The length of the hinterland was set at 5 km (see Table 4.1) and the thickness was in the range of 4.69-5.47 m (see Table 4.2). Here, it is discussed what the hinterland, in reality, looks like and what consequences it would have on the uplift assessment.

Description of the hinterland of DP42-47

The main feature of the hinterland is the presence of the Amerongerwetering, which is highlighted in Figure 4.8. This waterway was constructed for drainage purposes and is located at about 1.35 km from the river dike. For the relevant stretch, its base is located at 1.28-1.65 $m+NAP$ *(Hydrovak 8-10, Kort, 2010)*. Of the Amerongerwetering it is known that it drains the seepage from the river (Provincie Utrecht, 2019).

Furthermore, the cover layer is build up from *Echteld clay* (see Figure 4.10). Its hydraulic conductivity is yet set as a default value 0.02 m/d. However, other values are reported as well. Phernambucq (2015) reports a vertical conductivity of 0.04 and 0.0046 m/d for *Echteld sand and clay*. Besides, Gunnink et al. (2004) reports a vertical hydraulic conductivity of 0.0009 m/d for *Echteld 'komklei'* (clay from riverine deposits) and 0.0016 m/d for *Echteld sandy clay*.

Effect on uplift assignment

There are uncertainties regarding how to treat the leakage factor of the hinterland, which affects the damping factor. The presence of the Amerongerwetering leads to a local smaller leakage factor. Also, a smaller hydraulic conductivity leads to a smaller leakage factor. A lower value for λ_h means a lower value for the damping factor r_{exit}, thus a more favorable outcome of the uplift assessment. In general, the method from TAW (2004) to come to the hydraulic head below the cover layer is found to be conservative when comparing to measurements from monitoring wells (Willeboer et al., 2017).

4.3.3. Uplift soil beam model

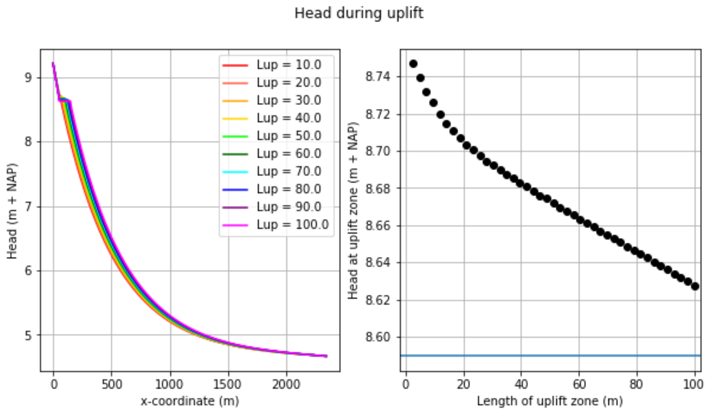

Figure 4.12: Head profile and head in uplift zone for DP47, MHW=9.21 m +NAP

Water/load

The evaluation of the new model is done for location DP47. The leakage factor of the hinterland equals 458 m. The model domain is taken as five times the leakage length, which is here 2342 m. Using the (average) geometry and hydraulic conductivity values from Table 4.1 and 4.2, the FD geohydrological model is set up. Figure 4.12 shows the result of the model outcome, in terms of the range of heads and corresponding uplift lengths for a mean high water river level of 9.21 m.

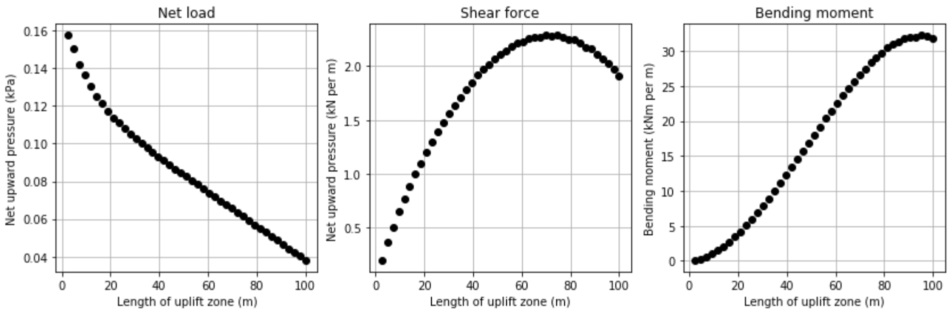

Figure 4.13: Expected shear en bending loads DP47, MHW=9.21 m +NAP

SOIL/RESISTANCE

Based on Figure 4.13, failure is expected either for L=70 m, q=0.07 kPa (normative for shear) or for L=90 m, q=0.05 kPa (normative for bending). Both lengths were evaluated in Plaxis. For L=90 m, the failure of the beam occurred at 0.3 kPa. For L=70 m, this was at 0.5 kPa.

Extra input parameters are needed to evaluate the soil beam behavior. For clay at DP47, the E_{oed} is found at 1.8 MPa from an oedometer test. From a CD triaxial test, E_{50} is found at 2.8 MPa. E_{ur} is assumed eight times larger than E_{50} (CUR2003-7) , thus equals 22.4 MPa. For the remaining soil parameters, a distinction is made between light clay and heavy clay. For light clay, $\gamma = 16.5 kN/m^3$, $\phi' = 30.8°$, and $c' = 3.28 kPa$. For heavy clay, $\gamma = 19 kN/m^3$, $\phi' = 30.4°$, and $c' = 4.93 kPa$ (Kwakman, 2019). For both clay types, the tensile capacity is assumed to be half the value of the effective cohesion (Bagge, 1985).

Using both 2D models for the geohydrology and the soil beam, it is found that for cross-section DP47 the forming of a full crack during uplift will not occur. However, using this approach, it is difficult to define a degree of safety by means of a safety factor or reliability index.

ANALYTICAL EQUATIONS TO EVALUATE FOR TENSILE AND SHEAR CRACKS

The limit state functions for tensile and shear cracks are given in Equation 4.4 and 4.5. For the sake of completeness, the semi-probabilistic equations are given below:

$$\gamma_{tensile} = \frac{D_{cover} * (\gamma_{eff} * (2 - \sin(\phi')))}{\left(\frac{1+\sin(\phi')}{1-\sin(\phi')}\sigma'_t + 2c' * \sqrt{\frac{1+\sin(\phi')}{1-\sin(\phi')}} + \sigma'_t\right)} \tag{4.10}$$

$$\begin{aligned}\gamma_{shear} = D_{cover} * D_{aq} * K_{aq} * \gamma_{eff}^2 / (D_{aq} * K_{aq} * \gamma_{eff} * \gamma_w * (h_{polder} \\ + 0.71 * (h_{river} - h_{polder}) - h_{exit}) + 32 * k_{cover} * s_u^2 \\ -8 * \sqrt{D_{aq} * K_{aq} * k_{cover} * \gamma_{eff} * \gamma_w * (h_{polder} + 0.71 * (h_{river} - h_{polder}) - h_{exit}) * s_u^2 + 16 * k_{cover}^2 * s_u^4})\end{aligned} \tag{4.11}$$

Additional stochasts are defined, which are the friction angle $\phi' \sim N(\sigma = 30°, \mu = 5°)$, cohesion $c' \sim N(\sigma = 4kPa, cov = 10\%)$ (Kwakman, 2019), tensile strength $\sigma'_t \sim N(\sigma = 2kPa, cov = 10\%)$ (Bagge, 1985), shear strength ratio ($S = 0.3$), SHANSEP-power ($m = 0.8$) (Kwakman, 2019), and Over-consolidation ratio $OCR \sim N(\sigma = 2, cov = 10\%)$ (Hertogh et al., 2018). The outcome for the cracking part of uplift is shown graphically in Figure 4.14.

4.3.4. DISCUSSION ON CASE OUTCOME

For dike stretch DP42 to DP47 between Amerongen and Wijk bij Duurstede, the safety against uplift is evaluated. It is done based on the floating part based on vertical equilibrium and the bulging-cracking part, which is the improvement on the model.

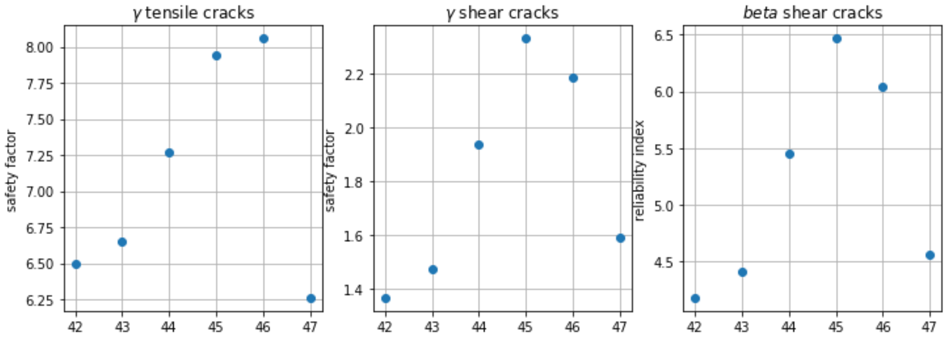

Figure 4.14: Outcomes on semi-probabilistic and fully probabilistic approach for uplift-cracking

For the floating phase in uplift, the assessment is done based on the WBI2017 guideline. The requirements for this dike stretch were $\gamma = 1.78$ and $\beta = 5.03$. These requirements are not met.

For the cracking phase in uplift, there is a possibility that the layer will not crack open. Two methods are used to evaluate the problem, using two 2D models, and using analytical equations. Both show that shear cracks are normative compared to tensile cracks. For DP44, DP45, and DP46, the calculated reliability index lies above 5.03, so these locations are safe against any cracks during uplift conditions.

THEORY VERSUS PRACTISE

Apparently, there is a difference between the calculation approach between academic people and practical engineers in the use of average or characteristic values to calculate the safety factor.

From a practical point of view, it is contradictory that the required safety factor is calibrated based on stochastic variables, and that the uncertainties are again accounted for by the use of characteristic values. It is understandable, since the safety factor based on characteristic parameters gives small values (γ = 0.78-1.13), and the required safety factor is quite high ($\gamma = 1.78$). Moreover, compared with the calculated reliability indices (β = 3.45-4.6) the calculated safety factors are low.

From theory, a semi-probabilistic calculation should make use of characteristic values. The translation from the required reliability index to the prescribed safety factor is merely a question of fitting a line. The prescribed safety factor of $\gamma = 1.78$ is so high because of three reasons: (1) the line should be fitted such that outcomes are generally on the safe side, (2) the point cloud through which the fit goes has a wide variance, and (3) the γ, β-relationship is fitted using an exponential function.

To conclude, applying the γ, β-relationship on this dike trajectory leads to conservative outcomes. It would be better to omit this relationship by either executing a fully probabilistic approach or to find a new γ, β-relationship for this specific (type of) region so that the variance of the point cloud reduces.

UPLIFT IN INTERNAL EROSION VERSUS MACRO-STABILITY

Furthermore, there is a difference between the calculation of uplift in internal erosion and macro-stability, while the phenomenon is the same. It is, amongst others, reflected by the required safety factor, which is 1.78 for internal erosion and 1.2 for macro-stability at this location.

When comparing these, there are two counterintuitive aspects. Firstly, the basis of the two assessments is different. Whereas uplift in internal erosion is based on effective stresses, in macro-stability uses total stresses. Because of this difference, higher safety factors for uplift based on the effective stress approach are foreseen. Secondly, safety factors are better defined if it is based on the required safety level. For uplift in internal erosion, this is already the case, leading to a high prescribed safety factor, but not for uplift in macro-stability. It is recommended for policymakers to harmonize the uplift assessment in the failure mechanisms.

5

DISCUSSION

This chapter contains the discussion on the research on the uplift phenomenon in the flood protection assessment. It starts with a link to the introduction regarding the causes of uncertainty leading to conservatism. The discussion points then follow, ranging from specific to general points. Finally, a summary of the discussion is provided based on the areas of relevance as appointed in the introduction.

This study's objective is to investigate uncertainties and decrease overconservatism in the uplift assessment of internal erosion. In the introduction, four domains regarding conservatism in uplift are found: spatial variability, limited data, policy and probabilistics, and the soil model. Their causes are a combination of aleatoric and epistemic uncertainties. This thesis mainly focused on the soil model as structural system uncertainty, as well as how the natural uncertainties are dealt with in the fully and semi-probabilistic approach. Hereunder, the implications and limitations for this research are discussed from specific model details to a comprehensive framework.

1. Soil/resistance model
2. Water/load model
3. Coupled behavior for uplift analysis
4. Non-uniformity for engineering practices
5. Uplift in flood defenses framework
6. Practical: input data

SOIL/RESISTANCE MODEL

The presented results incorporate more parameters than the self-weight only. The problem was mainly improved by extending the description for uplift with a bulging-fracturing part. The problem was evaluated using Plaxis FEA, but this approach included some limitations that are discussed below.

Undrained assumptions

The presented results are based on fully undrained behavior. In practice, the problem is partially drained, which influences the pore water pressure and strength. However, the hydrodynamic period for the problem is relatively short, so an undrained approach as the first approach is suitable. The loading time, which is the rise of the river head to the peak value, is in hours, which is much shorter than the consolidation time for thick cover layers.

Constitutive models

In this study, three constitutive models were investigated. These three models range from a first-order approximation (MC) to a reasonable model (HS) to the best standard model for undrained behavior (NGI-ADP-S) (Brinkgreve, 2019). The differences between the models are described in detail in section 3.3.2. With three different models, a choice is presented to select a matching model for the level of detail wanted. The downside to a detailed model is the need for many input parameters.

Considering that the NGI-ADP-S model is based on a total stress approach, the outcomes were not evaluated in this thesis. It meant that the effective stresses were unknown, and there was no possibility to specify a tensile cut-off criterion. For the Mohr-Coulomb and Hardening Soil models, specifying a tensile cut-off criterion was possible. Also, in the middle of the beam, the strain development over depth by increasing load matches well with lab results of beam tests (Ajaz and Parry, 1975; Šuklje, 1969; Thusyanthan et al., 2007). Also, the horizontal stress development in the HS model matches well with numerical outcomes of Ajaz and Parry (1975) and Thusyanthan et al. (2007). However, these constitutive models, as predefined in Plaxis, still have limitations on the tensile behavior and cracking. The main point is that the models do not incorporate tensile softening. As a work-around, the tensile softening relationship was tried to stimulate 'by hand', by assigning low-strength soil parameters for soil polygons that hit the tensile cut-off.

In Plaxis, the soil behavior at the tensile and compressive side are similar. Experimental tests show that the tensile behavior of clay tends to be linear elastic, followed by brittle behavior.

Finite element approach
It could be argued that the finite element approach is not suitable to investigate cracking on a detailed level. Cracking can only be observed indirectly, by hitting the tensile cut-off for fracture mode I or by large shear strains for fracture mode II. However, FEM-based modeling was applied in this study because it is most suitable for modeling the deformations of soft soils. Also, previous work by Hoffmans (2015) was done using finite element modeling (FEM), which showed a 'proof of concept' for modeling the deformations during uplift conditions.

WATER/LOAD MODEL

Comparing with previous research, the head profiles found using FD modeling are in agreement with Barends (1999) and Hoffmans (2015). The main features of the outcome are a constant head in the uplift zone and a curved headline starting at the toe of the dike. Even though Barends and Hoffmans also reported that the head in the uplift zone should be equal to the pressure of the self-weight of the cover layer, here it is argued that the head is larger. Field observations (Calle, 2002; Tissink, 2015) support that situations occur in which the cover layer has detached from the aquifer. In this situation, the pressure in the water gap must be larger than the downward pressure from the self-weight.

COUPLED BEHAVIOR FOR UPLIFT ANALYSIS

Because of the complexity of the problem, the investigation on the relations was performed using separate models. Treating the groundwater flow and soil behavior models apart captures the key relationships between the most important parameters. However, one disadvantage regarding the methodology is that the actual quantification of the relationship between the length of the uplift zone, the head in the uplift zone, and the deformation of the cover layer is unknown. Because of this concern, the normative case was defined as the worst-case scenario from the groundwater model.

Unfortunately, it was not possible to investigate the significant relationship of time-dependency in this problem using the current approach. It is a relevant aspect since experts from water boards agree that the uncertainty regarding time-dependency is left out in the WBI2017 (Bink, 2017). Also, the models are evaluated in a 2D plane. It remains unclear to which extend this assumption is suitable, and whether a 3D approach would be better. These subjects were beyond the scope of the study.

NON-UNIFORMITY IN ENGINEERING PRACTICES

As the focus of the study was on finding and evaluating the key relationships in uplift, the results are not immediately useful for engineering purposes. Assumptions of uniformity limit the generalizability of the results. For non-uniform thicknesses of the hinterland, for example, when ditches are present, the use of the proposed relationships should be restricted. Also, in reality, the strength-parameters are non-uniform. Furthermore, there are some concerns regarding pre-existing cracks, holes, and animal burrows penetrating through the cover layer. One suggestion to approach this problem is to model the soil above the phreatic surface with weaker strength parameters. Below the phreatic surface, desiccation cracks are generally not present.

Uplift in the flood defenses framework

The implication of the findings in modeling a separate bulging/cracking part of uplift is that the uplift assessment containing only the vertical equilibrium part is found insufficient to describe the full phenomenon. The uplift assessment should be split into two parts: the floating assessment and the bulging-fracturing assessment, as visualized in Figure 4.7. Alternatively, the failure mechanism internal erosion could consist of four submechanisms, for a better model representation of the reality. The four submechanisms would be: (1) uplift floating; (2) uplift bulging/cracking; (3) heave; (4) piping.

As the focus of the study was on the uplift phenomenon in internal erosion, there is a possibility that small shifts in accent would be different if the focus had been on slope-instability. For macro-stability, uplift also occurs, so questions regarding bulging/cracking are also relevant, as is visualized in Figure 5.1. However, it is more of an issue of how the shear strength is modeled best for each case.

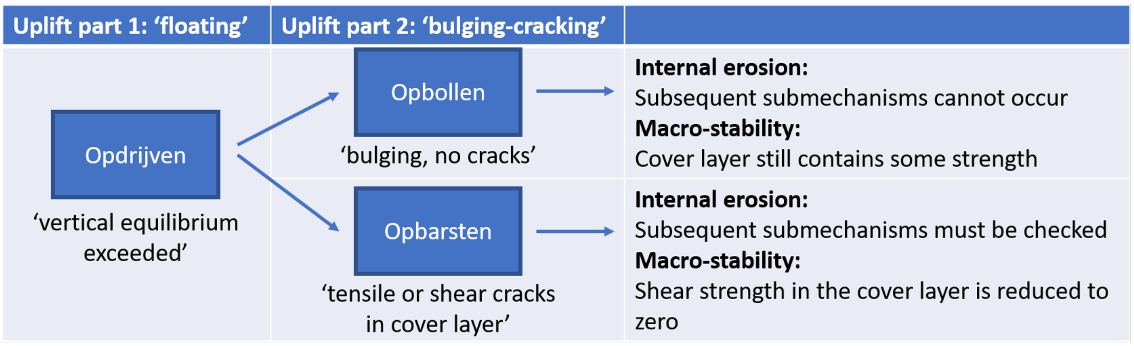

Figure 5.1: Diagram of detailed description of uplift using Dutch words 'opdrijven', 'opbollen', and 'opbarsten'

Furthermore, there are some remarks about the probabilistic approach in the flood defenses assessment. Both the failure mechanisms, as the submechanisms, as the input parameters are treated as uncorrelated. In reality, one could argue that the assumption of independence is conservative, and the actual failure probability is lower. However, this point was outside the scope of the study.

Also, the residual strength of a dike, after the dike is considered as failed, was outside the scope of the study. In reality, there is a probability that emergency repairing works are carried out before the dike has fully breached.

Practical: input data

The present findings suggest several courses of action to describe and evaluate the assessment for the uplift better. All propositions are related to or based on an updated assessment with more input data. New input variables were also proposed. In section 2.2.2, the phreatic surface at the exit point is mentioned, whereas in section 3.3.2 soil strength parameters were required.

However, there are practical limitations in obtaining detailed input data. These are in terms of costs in time, equipment, and money. Regarding the accuracy of the variation of stochastic parameters, this is a practical problem. Therefore, often slightly conservative assumptions are used in practice. Secondly, there are many new input parameters introduced. When the input data is lacking, default values are used, which could also contain high uncertainties.

In the current VNK2 dataset, many default values are encountered. The lack of precise data is a source of uncertainty, mainly for the variation coefficient of the cover layer thickness, and for the damping factor in general. The calibration of the safety factors is based on the VNK2 data, so this source of uncertainty works through.

6

CONCLUSION

6.1. MAIN FINDINGS

The present study confirmed the hypothesis that the uplift assessment based on vertical equilibrium does not fully describe the submechanism and is leaving out the soil behavior, including cracking. This study proposes to split up the current uplift assessment into a floating part based on vertical equilibrium, and a bulging/cracking part based on soil behavior. The latter part is a proposed extension of the internal erosion assessment. The detailed answer to the research questions is given below:

1. **For the uplift assessment based on a vertical equilibrium, as currently in use in WBI2017: What is the impact of assumptions included in deriving the (a) Deterministic equation, (b) Probabilistic equation, and (c) Prescribed safety factor for the semi-probabilistic assessment? What improvements could be made?**

DETERMINISTIC

In the current assessment, the equation is based on vertical equilibrium only. The net upward water pressure depends on the phreatic surface, and this might be lower than at ground level. However, for the soil, it is assumed it is fully saturated and that the phreatic surface is at ground level. This way, the resistance is calculated with the effective volumetric weight. This observation is disadvantageous for thick cover layers at which the phreatic surface lies constantly below the ground level, especially with low volumetric weights. For these situations, a new formula is proposed for cover layers thicker than the expected intrusion length.

PROBABILISTIC

In the probabilistic approach, there are two aspects which were found conservative and need improvement.

Firstly, the model factor in the uplift calculation has a conservative value, and its distribution is LN(1, 0.1). The coefficient of variation here is a rough choice. Theoretically speaking, the model factor is implemented to account for the difference in the performance of the model versus the phenomenon in reality. Many experts think a lower value is more suitable. For the vertical equilibrium condition here, it can be argued that the equation captures the physics well.

Secondly, a high value for the variation leads to unrealistic results in reality, which is mainly concerning the damping factor and the volumetric weight. For the damping factor, the default value is $LN \sim (\mu = 0.8, cov = 10\%)$. In a probabilistic Monte Carlo evaluation, this could lead to values larger than one, which is unrealistic because it implies that the hydraulic head at the exit point is larger than the river head. Similarly, the default value for variation of the volumetric weight equals 10%, which could lead to unrealistic low values compared to the soil type.

To improve the probabilistic assessment, one must avoid unrealistic values due to wide variations. For the damping factor, one could restrict the maximum value when performing Monte Carlo simulations. Regarding the volumetric weights, one could consider setting minimum and maximum values corresponding to soil classifications.

SEMI-DETERMINISTIC

The semi-deterministic approach prescribes the use of safety-factors. These are calibrated using probabilistic calculations, based on the VNK2-dataset. The required safety factors following the calibration are highly dependent on the type and nature of the calibration criterion. The calibration criterion has a very conservative nature because it accounts for a large variety of situations in the Netherlands.

The calibration criterion, including its conservatism, can be omitted by substituting a semi-probabilistic approach by a probabilistic approach. Another proposal to decrease the conservatism is to calibrate the safety factors against smaller areas with more homogeneous dike trajectories.

2. **What aspect of soil behavior should be included in the model for uplift? In what way does the resistance change in the uplift assessment subsequently?**

This question investigates the situation during uplift conditions when the cover layer has detached from the aquifer but still is intact.

SCHEMATIZATION OF THE PROBLEM

This study shows that this situation can be modeled adequately in a two-dimensional plane since two- dimensional patterns are observed both in the groundwater flow analysis and the behavior of the cover layer. For the model of the cover layer, it is proposed to schematize the uplift situation as a beam with a constant overburden pressure underneath. The overburden pressure equals the head at the aquifer-aquitard interface subtracted by the pressure from the self-weight from the cover layer.

Using a groundwater flow analysis based on finite differences, an indirect relationship is found between the length and the load on the uplift zone, which are interdependent. From this indirect relationship, normative situations are obtained for the maximum expected shear and bending forces. Subsequently, the beam behavior is evaluated to find a failure state in either shear or tension.

Important soil parameters are the models' respective elastic and strength parameters and the tensile capacity of the soil. For the uplift situation, other parameters were the volumetric weight, geometry, and preconsolidation stresses. The Hardening Soil constitutive model performed more realistically compared to the Mohr-Coulomb model, mainly concerning the non-linear elasticity in compression and handling of preconsolidation stresses. However, the linear elastic stress-strain relationship for clay in tension, including brittle failure after the tensile capacity is reached, is not incorporated.

TENSILE AND SHEAR CRACKS

Tensile failure occurs when the minor principal stress reaches the tensile capacity, which is more likely to happen in tensile zones with low initial stresses. Tensile cracks at the top will likely occur. However, they are limited to a certain depth in the cover layer, since the initial stresses increase with depth. In contrast to the situation when a tensile crack starts at the bottom, the crack will likely propagate to the top since the initial stresses decrease. A crude determination if a tensile crack can propagate through the blanket leading to an exit point under undrained assumptions is using the Mohr-Coulomb envelope with the Rankine states.

Shear failure happens when in the uplift beam the shear capacity is reached. In the model, a beam with a constant length was studied under increasing load conditions. Shear failure is observed at large vertical deformations. In reality, when the deformations become large, the beam would elongate, and the overburden pressure would decrease. To be comprehensive a formulation for the shear cracks for cover layers with a uniform thickness is obtained by assuming the maximum uplift length to be equal to one-quarter of the leakage length of the hinterland.

3. **How are the improvements working in practice, for (a) specific location(s) in the Netherlands?**

The case location is at dike stretches 44-3 and 44-04, between Wijk bij Duurstede and Amerongen (WAM). Firstly, uplift was evaluated using the vertical equilibrium equations, as is prescribed in WBI2017. Using semi-probabilistic calculations, the proposals for improvement of the current assessment did not have a significant influence. However, using a fully probabilistic approach, the calculated reliability index was reaching the demanded reliability index. It is noted that it may be beneficial to calibrate new regional safety factors for this river region.

The obtained approach to model the bulging-cracking phase of uplift was implemented here, using mean values for the geometry and soil parameters. The outcome is that at the current design river flood, the failure of the cover layer will not occur. However, it is difficult using these 2D models to quantify uncertainties and find a basis to calculate a safety factor.

The analytical equations for shear and tensile cracks were also applied. Shear failure was normative over tensile failure. The safety against cracking reached the required reliability index for half of the evaluated cross-sections.

6.2. RECOMMENDATIONS

In the introduction, four viewpoints were singled out, from which one could answer the following questions: Why is a better uplift assessment needed? These were: societal, economical, engineering, and scientific. The latter three give the structure for the recommendations for further research.

ECONOMICAL

It is a question of further research to investigate an optimum trade-off between obtaining input parameters and their variances, versus the costs of collecting the information. These hold for not only the type of model (analytical/numerical) used, as well as for the constitutive model, and the variation of the stochastic parameters. This issue is already encountered in the VNK2-data. It contained a large share of default values, on which subsequently the calibration of the safety factor is based.

ENGINEERING

Future research should examine strategically which method and constitutive model to apply at locations where uplift is critical.

Further research is also recommended for situations including varying thicknesses for the cover layer, for example containing ditches or overlying an old river branch, which makes the cover layer locally thinner or thicker. It is worthwhile for the robustness of the applicability to real-life situations.

To make sure the cover layer is undisturbed and uncracked, a minimum thickness of 1 meter is recommended. Any thinner cover layer is assumed to have pre-existing cracks, open drill holes, post holes, root holes, rodent holes, or animal burrows. This minimum thickness is worthwhile to research.

SCIENTIFIC

Cracking in soils

Future studies should address the fracturing behavior of cohesive soils under uplift conditions. To model cracking in detail, a DEM approach would be more suitable. Alternatively, one could consider using an Adaptive RPIM-FEM Coupled Method (Yuan et al., 2014) to model tensile cracks.

Besides, more research is needed on the cracking criteria. In this research, tensile opening and shear cracks are treated separately. However, Thusyanthan et al. (2007) observed failure in stress states on the Hvorslev line, which lies beyond the critical state line. Also, further research is needed to incorporate tensile softening in tensile regions, in which the tensile strength is nonzero. More generally, research is needed on crack-propagation in thick cover layers.

Time dependency

Adopting a time-dependent evaluation of the problem is a strong recommendation for further research because many processes are time-dependent but now assumed as steady-state or fully undrained. Examples are the increase in river head, the response of the aquifer, the deformation of the cover layer, and the intrusion of the pore water pressures and the subsequent change in effective stresses. For the first two aspects, incorporating transient groundwater flow equations is recommended for further research. For the latter two, the soil behavior should be evaluated time-dependently.

Coupled problem

It is highly recommended to evaluate the uplift problem in a model where both the groundwater flow and the soil deformation are coupled. This way, the relation between the lengthening of the uplift zone and the deformations within can be investigated. Also, using a more advanced model could investigate the time-dependent response of the model. Besides, the uplift zone would behave more naturally than a beam with fixed vertical boundaries.

2D - 3D

Another point which lies outside the scope is the determination of whether 3D effects are playing a significant role in the uplift phenomenon for both the groundwater flow and the cover layer behavior. In this study, a failure of the 2D-model resembles an infinite long crack in reality. However, in reality, exit points in the occurrence of a (sand) boil are observed. 3D effects could influence the resistance of the layer positively and therefore is important for further research.

Validation

Future investigations are necessary to validate the conclusions that can be drawn from this study. Also, validating against real-life cases would give a measure of how good simple constitutive models are working, and if the other assumptions are valid.

BIBLIOGRAPHY

AHN (s.d.). Actueel Hoogtebestand Nederland. https://www.ahn.nl/.

Ajaz, A. and Parry, R. H. G. (1975). Stress–strain behaviour of two compacted clays in tension and compression. *Geotechnique*, 25(3):495–512.

Ammeri, A., Jamei, M., Guiras, H., Bouassida, M., Villard, P., Plé, O., Camp, S., and Gourc, J.-P. (2006). A numerical study of compacted clay tensile strength by discrete element modelling: A bending test application. In *First Euro Mediterranean In Advance on Geomaterials and Structures*.

Bagge, G. (1985). Tension cracks in saturated clay cuttings. In *International conference on soil mechanics and foundation engineering. 11*, pages 393–395.

Bakker, H., Breedeveld, J., and Teunissen, H. (2011). Analyse Macrostabiliteit Dijken met de Eindige Elementen Methode. *Deltares rapport 1202121-012-GEO-0005 voor Rijkswaterstaat*.

Barends, F. B. J. (1999). Opdrijven van het achterland bij hoogwater. *Grondmechanica Delft voor Provincie Zuid-Holland*.

Batool, A., VandenBerge, D. R., and Brandon, T. L. (2015). Practical application of blanket theory and the finite-element method to levee underseepage analysis. *Journal of Geotechnical and Geoenvironmental Engineering*, 141(4):04015001.

Bink, J. J. C. (2017). Flood safety: What is an acceptable level of uncertainty in the safety assessment of piping. Master's thesis, University of Twente.

Bisschop, C., Huisman, C. E., Jansen, P., Westhof, W., and Zantige, A. M. (2011). Veiligheid Nederland in Kaart 2. Dijkring 44: Achtergrondrapport.

Brinkgreve, R. B. J. (2016). Ongedraineerd rekenen met de EEM: Ontwikkeling van een geavanceerd SHANSEP model op basis van NGI-ADP. Technical report, POV-Macrostabiliteit. https://www.povmacrostabiliteit.nl/wp-content/uploads/2015/03/POVM-voorstel-SHANSEP-model-obv-NGI-ADP.pdf.

Brinkgreve, R. B. J. (2019). Lecture slides of course CIE4361 Behaviour of Soils and Rocks (2019-2020). TU Delft Brightspace.

Brinkgreve, R. B. J., Kumarswamy, S., and Swolfs, W. M. (2006). Plaxis material models manual. *The Netherlands: Delft University of Technology & PLAXIS B.V.*, 2006.

Bundesanstalt für Wasserbau (2011). BAW Merkblatt: Standsicherheit von Dämmen an Bundeswasserstraßen (MSD). Technical report, Bundesanstalt für Wasserbau. https://izw.baw.de/publikationen/merkblaetter/0/BAWMerkblatt_Standsicherheit_Daemme_MSD_2011.pdf.

Bundesanstalt für Wasserbau (2013). BAW Code of Practice: Internal Erosion (MMB). Technical report, Bundesanstalt für Wasserbau. https://izw.baw.de/publikationen/merkblaetter/0/BAWCodeofPractice_Internal_Erosion_MMB_2013.pdf.

Calle, E. O. F. (2002). Dijkdoorbraakprocessen: Beschrijving, doorbraakprocessen en reststerkte.

CUR2003-7 (2003). Bepaling geotechnische parameters. Technical report.

Diermanse, F. (2016). WBI - Onzekerheden. Overzicht van belasting- en sterkteonzekerheden in het wettelijk beoordelingsinstrumentarium. *Deltares rapport 1220080-001-ZWS-0004 voor Rijkswaterstaat*.

Förster, U., Van den Ham, G., Calle, E. O. F., and Kruse, G. (2012). Zandmeevoerende wellen. *Deltares rapport 1202123-003-GEO-0002 voor Rijkswaterstaat*.

Gunnink, J. L., Veldkamp, J. G., Dam, D., Weerts, H. J. T., and van der Linden, W. (2004). Deklaagmodel en geohydrologische parametrisatie voor het beheersgebied van het Hoogheemraadschap "De Stichtse Rijnlanden". *Nederlands Instituut voor Toegepaste Geowetenschappen, TNO rapport NITG 04-090-B0609 voor Hoogheemraadschap "De Stichtse Rijnlanden".*

Helenelund, K. V. (1967). *Tension Tests on Fibrous Peat.* Internal Report; no. DBR-IR-346. National Research Council of Canada, Division of Building Research, Ottawa, Canada. doi: `https://doi.org/10.4224/20338044`.

Hertogh, K. K., Stellema, G. A. M., and Geurtjens, H. M. (2018). Grondonderzoek Sterke Lekdijk Wijk bij Duurstede / Amerongen (WAM): Resultaten terrein- en laboratoriumonderzoek. *Wiertsema-Inpijn-Blokpoel V.O.F voor Hoogheemraadschap "De Stichtse Rijnlanden".*

Hoffman, C. (2019). POVM Rekentechieken - FEM Analysis of Uplift. Technical report, POV-Macrostabiliteit. Projectnummer 11201267.

Hoffmans, G. (2015). PvA Deelstudie 'Opbarsten'. Technical report, POV-Macrostabiliteit.

Hong, Y. and Wang, L. (2016). *Deformation and failure mechanism of excavation in clay subjected to hydraulic uplift.* Springer.

Jongejan, R. and Calle, E. (2013). Calibrating semi-probabilistic safety assessments rules for flood defences. *Georisk: Assessment and Management of Risk for Engineered Systems and Geohazards*, 7(2):88–98.

Jongejan, R. B. (2017). WBI2017 Code Calibration: Reliability-based code calibration and semi-probabilistic assessment rules for the WBI2017. Technical report, Rijkswaterstaat, Ministerie van Infrastructuur en Milieu.

Jongejan, R. B., Diermanse, F., Kanning, W., and Bottema, M. (2020). Reliability-based partial factors for flood defenses. *Reliability Engineering & System Safety*, 193:106589.

Jonkman, S. N., Jorissen, R. E., Schweckendiek, T., and van den Bos, J. P. (2018). *Flood Defences: Lecture Notes CIE5314.* Delft University of Technology, 3rd edition.

Kennedy, M. C. and O'Hagan, A. (2001). Bayesian calibration of computer models. *Journal of the Royal Statistical Society: Series B (Statistical Methodology)*, 63(3):425–464.

Kort, J. W. (2010). De Amerongerwetering: Een detailstudie met SOBEK Channel Flow. HBO's thesis, Hogeschool VanHall-Larenstein. `https://edepot.wur.nl/149046`.

Kwakman, L. (2019). Beoordeling binnen- en buitenwaartse macrostabiliteit, Dijkversterking Wijk bij Duurstede - Amerongen. *Sweco en Arcadis rapport C03011.000750 voor Hoogheemraadschap "De Stichtse Rijnlanden".*

Li, H.-D., Tang, C.-S., Cheng, Q., Li, S.-J., Gong, X.-P., and Shi, B. (2019). Tensile strength of clayey soil and the strain analysis based on image processing techniques. *Engineering Geology*, 253:137–148.

Lopez de la Cruz, J., Calle, E. O. F., and Schweckendiek, T. (2011). Calibration of piping assessment models in the Netherlands. *Knowledge, Technology Policy.*

McGinty, B. (2014). Modes I, II, and III. *Fracture Mechanics.* `https://www.fracturemechanics.org/modes123.html`.

Ministerie van Infrastructuur en Milieu (2017). Schematiseringshandleiding piping wbi 2017. Technical report, Den Haag.

Panagoulias, S. and Brinkgreve, R. B. J. (2017). SHANSEP NGI-ADP: Model description and verification examples. Technical report, POV-Macrostabiliteit. `https://www.povmacrostabiliteit.nl/wp-content/uploads/2015/03/SHANSEP_NGIADP.pdf`.

Phernambucq, I. H. (2015). The vertical hydraulic resistance of the Lek River and consequences for travel times. Master's thesis, Universiteit Utrecht. `https://www.oasen.nl/files/importedthe-vertical-hydraulic-resistance-lek-river-and-consequences-travel-times`.

Popescu, R., Deodatis, G., and Prévost, J.-H. (2008). Randomly heterogeneous soils under static and dynamic loads. *Reliability-Based Design in Geotechnical Engineering: Computations and Applications*, 224.

Provincie Utrecht (2019). Beheerplan 2019-2025 N2000-gebied Kolland en Overlangbroek. `https://www.provincie-utrecht.nl/sites/default/files/2020-03/beheerplan_2019-2025_kolland_en_overlangbroek.pdf`.

Rijkswaterstaat / Bart van Eyck (1993). Waal linkeroever Beuningen hoogwater 1993 luchtfoto. `https://beeldbank.rws.nl/MediaObject/Details/329218`.

Robinson, S., Arbez, G., Birta, L. G., Tolk, A., and Wagner, G. (2015). Conceptual modeling: Definition, purpose and benefits. *2015 Winter Simulation Conference (WSC)*, pages 2812–2826.

RWS & USACE (s.d.). Backward erosion piping field observations database. `http://www.pipingdb-rws-coe.nl/fieldobs/#`.

Schweckendiek, T., Vrouwenvelder, A. C. W. M., and Calle, E. O. F. (2014a). Updating piping reliability with field performance observations. *Structural Safety*, 47:13–23.

Schweckendiek, T., Vrouwenvelder, A. C. W. M. (promotor)., and Vrijling, J. K. (promotor). (2014b). *On reducing piping uncertainties: A Bayesian decision approach.* PhD thesis, Delft Univeristy of Technology. ISBN: 9789053358801 `https://doi.org/10.4233/uuid:f9be2f7e-7009-4c73-afe5-8b4bb16e956f`.

Šuklje, L. (1969). *Rheological aspects of soil mechanics.* Wiley-Interscience London.

Suklje, L., Vercon, M., Oliver-Martin, D., and Trollope, D. H. (1961). Barrages en terre, talus et tranchees ouvertes - Earth dams, slopes and open excavations. Technical report. Retrieved from `https://www.issmge.org/uploads/publications/1/40/1961_03_0008.pdf`.

Surarak, C., Likitlersuang, S., Wanatowski, D., Balasubramaniam, A., Oh, E., and Guan, H. (2012). Stiffness and strength parameters for hardening soil model of soft and stiff bangkok clays. *Soils and foundations*, 52(4):682–697.

’t Hart, R. (2018). Fenomenologische beschrijving - Faalmechanismen WBI. *Deltares rapport 11200574-007-GEO-0005 voor Rijkswaterstaat.*

Tang, C.-S., Pei, X.-J., Wang, D.-Y., Shi, B., and Li, J. (2014). Tensile strength of compacted clayey soil. *Journal of Geotechnical and Geoenvironmental Engineering*, 141(4):04014122.

TAW (2004). Technisch rapport waterspanningen bij dijken. Technical report. TR26-DWW-2004-057, ISBN 90.269. 5565.3.

Teixeira, A., Wojciechowska, K., and ter Horst, W. (2016). Derivation of the semi-probabilistic safety assessment for piping. WTI 2017: Cluster C, piping failure mechanism. *Deltares rapport 120080-002-ZWS-0006 voor Rijkswaterstaat.*

Thusyanthan, N. I., Take, W. A., Madabhushi, S. P. G., and Bolton, M. D. (2007). Crack initiation in clay observed in beam bending. *Geotechnique*, 57(7):581–594.

Tissink, A. (2015). Blaren in de berm van de livedijk. *Cobouw.* `https://www.cobouw.nl/infra/nieuws/2015/04/blaren-in-de-berm-van-de-livedijk-1019876?_ga=2.111936836.1765564603.1588758012-613152936.1588758012`.

US Bureau of Reclamation (2018). Internal Erosion Risks for Embankments and Foundations. Technical report. `https://www.usbr.gov/ssle/damsafety/risk/methodology.html`.

Van, M. and Molendijk, W. (1997). Construction on peat and organic soils. *report for TC 15:" Peat and Organic Soils" technical committee of the ISSMFE rapport CO-369400/36.*

Van, M. A., Koelewijn, A. R., and Barends, F. B. (2005). Uplift phenomenon: Model, validation, and design. *International Journal of Geomechanics*, 5(2):98–106.

Van der Krogt, M., Schweckendiek, T., and Kok, M. (2019). Do all dike instabilities cause flooding? `https://doi.org/10.371/153546`.

Van Esch, J., Verkaik, J., and Nuttall, J. (2016). Numerical modelling of water pressures in dikes. In *RD Highlights 2016*. Deltares.

van Hoven, A., Noordam, A., and Wiersma, A. (2018). Cluster rekentechnieken. Technical report, POV-Macrostabiliteit. Projectnummer 11201267-002.

Verruijt, A. and Van Baars, S. (2007). *Soil mechanics*. VSSD Delft, the Netherlands.

Visschedijk, M. A. T. (2018). POVM Rekentechnieken: Basisrapport Eindige-elementenmethode (onderdeel 6.2.6A). Technical report, POV-Macrostabiliteit. `https://www.povmacrostabiliteit.nl/wp-content/uploads/2019/02/20180119_B-EEM_11201406-002-GEO-0003.pdf`.

Vrijling, J. K., with contributions from Kok, M., Calle, E. O. F., Epema, W. G., van der Meer, M. T., van den Berg, P., and Schweckendiek, T. (2010). *Piping: Realiteit of rekenfout?* Rijkswaterstaat, Waterdienst. `http://resolver.tudelft.nl/uuid:f5b79879-f4d2-4fce-9b11-38547db4509f`.

Wang, J.-J., Zhu, J.-G., Chiu, C., and Zhang, H. (2007). Experimental study on fracture toughness and tensile strength of a clay. *Engineering Geology*, 94(1-2):65–75.

Wiki Noodmaatregelen Waterkeringen (s.d.). Opdrijven en opbarsten. `https://v-web002.deltares.nl/sterktenoodmaatregelen/index.php/Opdrijven_en_opbarsten`.

Willeboer, M., Beurskens, P., and Kooman, J. (2017). Veiligheidsanalyse dijkversterking Nederbetuwe - Deelrapportage Macrostabiliteit & Piping. Technical report, Waterschap Rivierenland.

Yuan, H., Peng, C., Lin, Q., and Zhang, B. (2014). Simulation of tensile cracking in earth structures with an adaptive rpim-fem coupled method. *KSCE Journal of Civil Engineering*, 18(7):2007–2018.

Zimmermann, E. A., Launey, M. E., and Ritchie, R. O. (2009). Mixed-mode fracture of human cortical bone. `https://www2.lbl.gov/ritchie/Programs/BIO/MixedModeFracture.htm`.

Zwanenburg, C., Van Duinen, A., and Rozing, A. (2013). Technisch rapport macrostabiliteit. *Deltares rapport 1204203-007-GEO-0003-gbh voor Rijkswaterstaat*.

CONTENTS OF APPENDICES

A Effective stress approach on uplift as formulated in WBI2017 5

A.1 Equations . . . 6
A.2 Example of 5 cases . . . 6
A.3 Conclusion . . . 8

B Calibration of the safety factor for submechanism uplift 9

B.1 Theory . . . 9
  B.1.1 Overview of theoretical equations . . . 9
  B.1.2 Calibration criterion and model factor . . . 10
B.2 Method . . . 11
  B.2.1 Preprocessing data . . . 11
  B.2.2 Semi-probabilistic: Corresponding thickness . . . 15
  B.2.3 Probabilistic: Corresponding reliability index . . . 15
  B.2.4 Exponential fit . . . 16
B.3 Python notebook . . . 17
  B.3.1 Preprocessing data . . . 17
  B.3.2 Semi-probabilistic: Corresponding thickness . . . 19
  B.3.3 Probabilistic: Corresponding reliability index . . . 20
  B.3.4 Exponential fit . . . 22
B.4 Results . . . 23
  B.4.1 Checking assumptions for 20% quantile as calibration criterion . . . 23
  B.4.2 Sensitivity analysis on 20% quantile as calibration criterion . . . 24
  B.4.3 Sensitivity analysis on type of calibration criterion . . . 25
  B.4.4 Sensitivity analysis on model factor . . . 25
  B.4.5 Sensitivity analysis on damping factor . . . 26
  B.4.6 Comparison with original calibration . . . 26
B.5 Conclusion and discussion . . . 28
  B.5.1 Recommendations . . . 28

C Developing a conceptual model 29

C.1 Introduction . . . 29
C.2 Cracking in cohesive soils . . . 30
  C.2.1 Cracks on top of a slope . . . 30
  C.2.2 Hydraulic fracturing . . . 30
  C.2.3 Desiccation . . . 31
  C.2.4 Excavation base . . . 31
  C.2.5 Uplift leading to heaving and piping . . . 33
  C.2.6 Summary . . . 33
C.3 Detailed phenomenological description for uplift . . . 34
  C.3.1 Rising water pressure in the aquifer . . . 34
  C.3.2 Behavior of the cover layer . . . 35
C.4 Crack-initiation . . . 36
  C.4.1 Beam model . . . 36
  C.4.2 Hydraulic fracturing . . . 37
C.5 Crack-development . . . 37
C.6 Conceptual model . . . 38
  C.6.1 Influence of time . . . 39
C.7 Appendix C.I: schematization of the beam . . . 40

D Geo-hydrological analysis for the uplift zone **43**
D.1 Introduction . . . 43
D.1.1 Beam model (excavation base case) . . . 43
D.2 Theory: Analytical model by Barends . . . 44
D.3 Method: Numerical FD approach . . . 45
D.4 Python notebook . . . 46
D.4.1 Model set-up. . . . 46
D.4.2 Computing head and plotting figures . . . 48
D.5 Results and discussion . . . 52
D.5.1 Comparison with Barends . . . 52
D.5.2 Relation length and load . . . 53

E Internal soil stresses **55**
E.1 Tensile testing. . . . 57
E.1.1 Tensile test types . . . 57
E.1.2 Test results . . . 58
E.2 Stress strain relationships . . . 60
E.2.1 Types of stress-strain modelling . . . 60
E.2.2 Reported tensile stress-strain curves . . . 60
E.2.3 Conclusion. . . . 62
E.3 Stress and strain profile in bending test . . . 63
E.3.1 Strain profile . . . 63
E.3.2 Stress profiles . . . 64
E.3.3 Conclusion. . . . 66
E.4 Other . . . 66
E.4.1 Relationship with other parameters . . . 66

F Beam evaluations using simple models **67**
F.1 Linear elastic analytical equations . . . 67
F.2 Python: $\sigma - \epsilon$ and $\epsilon(z)$ relationships . . . 69
F.2.1 Discussion . . . 69

G Python scripting for Plaxis **71**
G.1 Remote scripting server . . . 71
G.2 Set up Python notebook. . . . 72
G.3 Plaxis 2D Input . . . 72
G.3.1 Soil menu . . . 72
G.3.2 Structures menu . . . 73
G.3.3 Mesh menu . . . 73
G.3.4 Staged construction menu . . . 73
G.4 Plaxis 2D Output . . . 74
G.5 Postprocessing . . . 76

H Analytical derivation of critical thicknesses for tensile cracks **85**
H.1 Introduction . . . 85
H.2 Critical thickness for tensile cracks . . . 85
H.2.1 Vertical effective stress path . . . 87
H.2.2 Stress paths and Skempton's A parameter . . . 88

I Case WAM DP47 **89**
I.1 Data collection for Dikering 44 DP47 . . . 90
I.1.1 Location . . . 90
I.1.2 Hydraulic conditions. . . . 90
I.1.3 Subsoil (CPTs and borings). . . . 91
I.1.4 Volumetric weight . . . 91
I.1.5 Other parameters . . . 93

I.2 Safety assessment . . . 93
  I.2.1 Reproduction of current approach . . . 93
  I.2.2 Updated semi-probabilistic approach . . . 94
  I.2.3 Fully probabilistic approach . . . 95
  I.2.4 Uplift soil beam model . . . 96
  I.2.5 Shear and tensile cracks . . . 97
Bibliography **99**

A

EFFECTIVE STRESS APPROACH ON UPLIFT AS FORMULATED IN WBI2017

In the WBI2017, the current assessment of uplift regarding internal erosion is based on vertical effective stresses. The effective soil stress is calculated with the effective volumetric weight, which implies that the water level is at the ground surface. The objective of this Appendix is to show what influence this assumption has on the calculated safety factor, by comparing two equations for situations where the phreatic level is below the ground surface. It starts with an overview of the equations in Section A.1 and subsequently, the outcomes of example cases are compared in Section A.2.

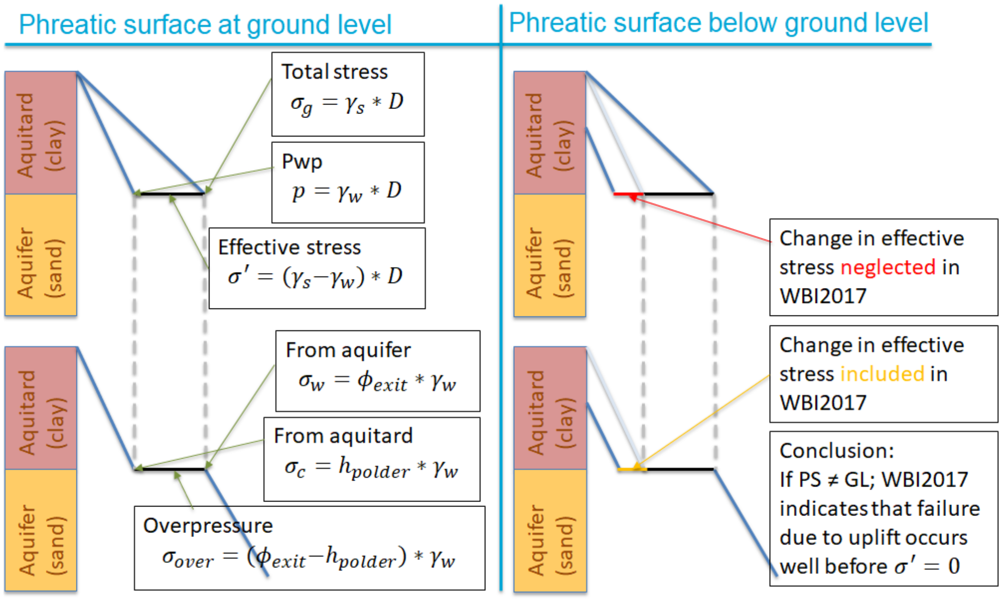

Figure A.1: Stresses at aquifer-aquitard interface for different levels of the phreatic surface

A.1. EQUATIONS

WBI2017:

$$\gamma_{up} = \frac{D_{cover} * (\gamma_{sat,cover} - \gamma_{water})}{\gamma_{water} * (h(T) - h_{exit}) * r_{exit}} \tag{A.1}$$

- Used since 2017 (WBI2017), assuming the phreatic surface in the cover layer at the exit point equals the hydraulic head in the aquifer at the hinterland ($h_{exit} = h_{polder}$);
- Also used in calibration of safety factors;
- Assumes phreatic surface is at ground level.

More accurate proposal:

$$\gamma_{up} = \frac{D_{cover} * \gamma_{sat,cover} - d_w * \gamma_{water}}{\gamma_{water} * (h(T) - h_{exit}) * r_{exit}} \tag{A.2}$$

- d_w = thickness of cover layer below phreatic surface
- Calculates effective stress accurately for all cases
- Assumes $\gamma_{sat,cover}$ is same above and below phreatic surface

A.2. EXAMPLE OF 5 CASES

CASE 1

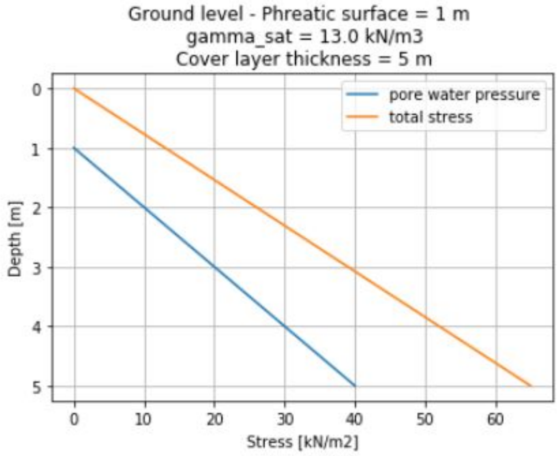

$h(T) = 2m, h_{exit} = 0m, r_{exit} = 0.8$

WBI2017:

$$\gamma_{up} = \frac{D_{cover} * (\gamma_{sat,cover} - \gamma_{water})}{\gamma_{water} * (h(T) - h_{exit}) * r_{exit}} = \frac{5 * (13 - 10)}{10 * (2 - 0) * 0.8} = \frac{15}{16} = 0.9$$

Proposed formula:

$$\gamma_{up} = \frac{D_{cover} * \gamma_{sat,cover} - d_w * \gamma_{water}}{\gamma_{water} * (h(T) - h_{exit}) * r_{exit}} = \frac{5 * 13 - 4 * 10}{10 * (2 - 0) * 0.8} = \frac{25}{16} = 1.6$$

Figure A.2: Case 1

CASE 2

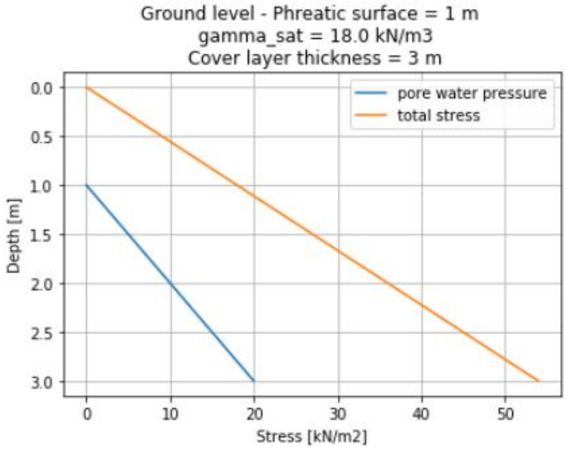

$h(T) = 2m, h_{exit} = 0m, r_{exit} = 0.8$

WBI2017:

$$\gamma_{up} = \frac{D_{cover} * (\gamma_{sat,cover} - \gamma_{water})}{\gamma_{water} * (h(T) - h_{exit}) * r_{exit}} = \frac{3 * (18 - 10)}{10 * (2 - 0) * 0.8} = \frac{24}{16} = 1.5$$

Proposed formula:

$$\gamma_{up} = \frac{D_{cover} * \gamma_{sat,cover} - d_w * \gamma_{water}}{\gamma_{water} * (h(T) - h_{exit}) * r_{exit}} = \frac{3 * 18 - 2 * 10}{10 * (2 - 0) * 0.8} = \frac{34}{16} = 2.1$$

Figure A.3: Case 2

CASE 3

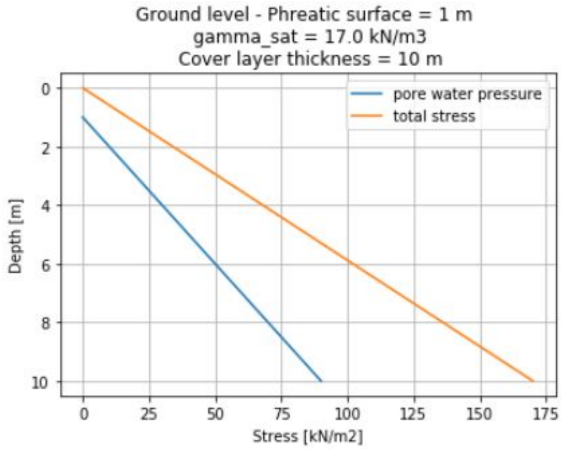

$$h(T) = 2m, h_{exit} = 0m, r_{exit} = 0.8$$

WBI2017:

$$\gamma_{up} = \frac{D_{cover} * (\gamma_{sat,cover} - \gamma_{water})}{\gamma_{water} * (h(T) - h_{exit}) * r_{exit}} = \frac{10*(17-10)}{10*(6-0)*0.8} = \frac{70}{48} = 1.5$$

Proposed formula:

$$\gamma_{up} = \frac{D_{cover} * \gamma_{sat,cover} - d_w * \gamma_{water}}{\gamma_{water} * (h(T) - h_{exit}) * r_{exit}} = \frac{10*17-9*10}{10*(6-0)*0.8} = \frac{80}{48} = 1.7$$

Figure A.4: Case 3

CASE 4

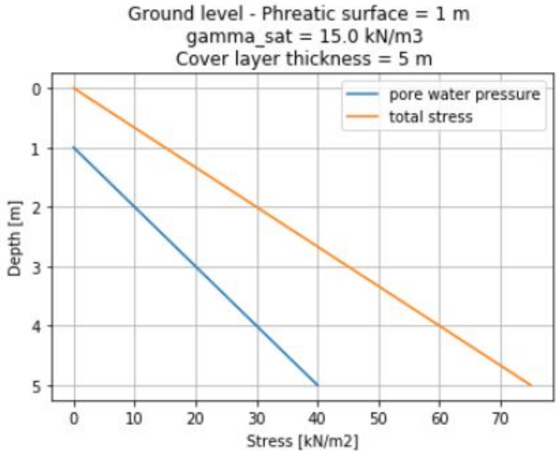

$$h(T) = 2m, h_{exit} = 0m, r_{exit} = 0.8$$

WBI2017:

$$\gamma_{up} = \frac{D_{cover} * (\gamma_{sat,cover} - \gamma_{water})}{\gamma_{water} * (h(T) - h_{exit}) * r_{exit}} = \frac{5*(15-10)}{10*(3-0)*0.8} = \frac{25}{24} = 1.0$$

Proposed formula:

$$\gamma_{up} = \frac{D_{cover} * \gamma_{sat,cover} - d_w * \gamma_{water}}{\gamma_{water} * (h(T) - h_{exit}) * r_{exit}} = \frac{5*15-4*10}{10*(3-0)*0.8} = \frac{35}{24} = 1.5$$

Figure A.5: Case 4

CASE 5

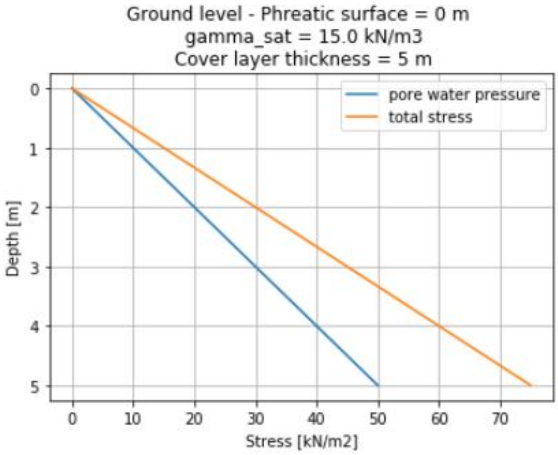

$$h(T) = 3m, h_{exit} = 0m, r_{exit} = 0.8$$

WBI2017:

$$\gamma_{up} = \frac{D_{cover} * (\gamma_{sat,cover} - \gamma_{water})}{\gamma_{water} * (h(T) - h_{exit}) * r_{exit}} = \frac{5*(15-10)}{10*(3-0)*0.8} = \frac{25}{24} = 1.0$$

Proposed formula:

$$\gamma_{up} = \frac{D_{cover} * \gamma_{sat,cover} - d_w * \gamma_{water}}{\gamma_{water} * (h(T) - h_{exit}) * r_{exit}} = \frac{5*15-5*10}{10*(3-0)*0.8} = \frac{25}{24} = 1.0$$

Figure A.6: Case 5

A.3. CONCLUSION

Adding d_w to the uplift equation leads to higher safety factors for situations in which the phreatic surface lies below the ground level. This has especially high consequences if:

1. d_w/D_{cover} is large
2. $\gamma_{sat} - \gamma_w$ is small

However, adding an extra parameter has some disadvantages:

1. Leads to a slightly higher computational effort. However, the results are significant.
2. Extra effort to obtain value in the field + uncertainty/standard deviation
3. Holds only for immediate response. Over a longer time, the PS in the cover layer rises.

On the other hand, the typical infiltration length during river flood waves in the Netherlands is 1 to 3 meters. For thicker cover layers, the pore water pressures of the upper part are not affected. The applicability of the proposed formula is for thick cover layers with controlled and known phreatic surfaces, for example, polders.

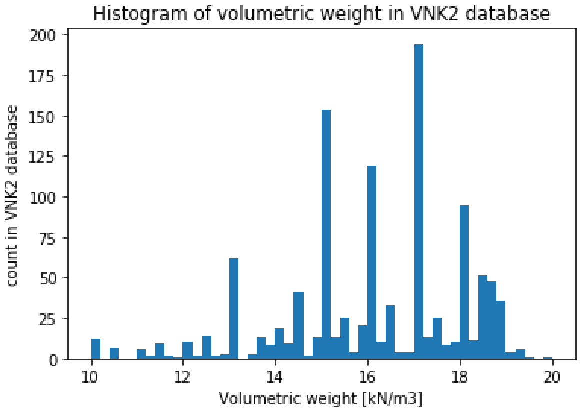

Figure A.7: Histogram of volumetric weights in VNK2 database

B

CALIBRATION OF THE SAFETY FACTOR FOR SUBMECHANISM UPLIFT

The aim of this document is to summarize the procedure of how the safety factors for the semi-probabilistic assessment are obtained and to analyze this process and the findings. Section B.1 contains the theoretical equations. Section B.2 describes the method and is a support to Section B.3, which contains the Python code. Subsequently, the results are reported. This Appendix ends with the conclusion and the discussion.

B.1. THEORY

B.1.1. OVERVIEW OF THEORETICAL EQUATIONS

Please see below for an overview of the equations for uplift, expressed as resistance and load, which are used in the WBI2017 Jongejan (2017). For the explanations of the parameters, it is referred to Table B.1.

Resistance: $R = D_{cover} * \gamma_{eff} / \gamma_{water}$
Load: $S = (h_T - h_e) * r_e$
Semi probabilistic: $\gamma_{up} = R/S$
Probabilistic: $Z = m_u * R - S$

Table B.1: Input parameters for uplift calculation

Symbol [unit]	Description	Distribution type	Default	$char$ value	Deviation type in $Hydra-ring$
m_u [-]	Model factor for uplift	log-normal	μ 1.0 σ 0.10	1.0	cov
γ_{water} $[kN/m^3]$	Volumetric weight of water	-	10	10	cov
$\gamma_{sat,cover}$ $[kN/m^3]$	Saturated volumetric weight of the cover layer	log-normal shifted (+10)	-	5%	cov
r_{exit} [-]	Damping factor at exit	log-normal	-	95%	cov
D_{cover} $[m]$	Effective thickness of the cover layer	log-normal	-	5%	cov
h_{exit} $[m +$ NAP]	Phreatic level at the exit point	normal	-	5%	σ
h $[m +$ NAP]	Outside water level	$Hydra-Ring$	-	Design water level	$-$

B.1.2. CALIBRATION CRITERION AND MODEL FACTOR

In the calibration procedure, there are two input parameters with uncertainties that do not depend on the location but on the mathematical model. These are explained here. The first one is the calibration criterion, which is currently set to 20% quantile of the computed β's per safety factor. The second one is the model factor for uplift. Figure B.6 shows their role in the calibration procedure.

CALIBRATION CRITERION

The use and the derivation of the calibration criterion is explained in this section. The two calibration types are discussed mathematically, and some premises are checked.

The calibration criterion is a mathematical choice to determine for which values the safety factor is sufficiently safe. Jongejan and Calle (2013) explained two types of calibration criteria, which could be applied.

1. Type I. 'The average probability of flooding over all consequence segments should be smaller than the safety standard"
   (a) $P_{cross,m,avg} \leq P_{cross,m,T}$
   Average failure probability for a cross section due to failure mechanism m should be smaller to the target value for the failure probability for a cross section *cross* for a failure mechanism m
   (b) It assumes that the probabilities of failure on average should be equal or smaller than the target probability. Vrouwenvelder set out the economic reasoning for this premise. The present value of the total costs is differentiated with respect to the safety factor and set to zero.

   The disadvantage of this premise, is that the average value is sensitive to outliers in case of limited test set members.

2. Type II. The average probability of flooding equals to the 20% quantile of the reliability index, given $\beta_{cross,m,section} \sim N(\mu, \sigma = 0.5)$ from the VNK2-dataset.
   (a) $\beta_{cross,m,T} = -\Phi^{-1}(P_{cross,m,T})$
   (b) $\beta_{cross,m,20\%} \geq \beta_{cross,m,T}$

There are some assumptions in this reasoning, which are highlighted hereafter:

1. The premise that the average of the failure probability per section should equal the total cross-sectional failure probability, based on economic considerations (point 1a).
   (a) The costs are assumed to be a linear function of fixed costs and variable costs
   (b) That the average variable costs are a fixed value.
2. The premise that $\beta_{cross,m,20\%} \approx P_{cross,m,avg}$ (point 2b)
   (a) The reliability indices are assumed to have a distribution of $N(\mu, \sigma = 0.5)$
   (b) Assuming the average of any parameter with $N(\mu, \sigma = 0.5)$ equals to the 20% quantile.

   These assumptions are checked in Section B.4.1.

MODEL FACTOR

Generally speaking, the model factor is implemented to account for the model errors: the difference in the performance of the model versus in reality and experiments in controlled lab-conditions versus behavior in non-controlled conditions. It describes the imperfection of the model.

Following from Schweckendiek et al. (2014), the causes of model uncertainty are partly of reducible and partly of irreducible nature. Reducible uncertainty lies in the accuracy of the model prediction. An example of irreducible factors is time-dependent influencing factors.

In the ideal case, the model factor is based on discrepancies between modeled outcomes and real results. However, there is no data available to base the calibration of the model factor on. On the other hand, there were other criteria to choose the model factor. To be consistent with ISO2394, implementing a model factor was desirable. The coefficient of variation for uplift was chosen as 10%, where the ISO-norm gives a default value of 20%. Lastly, the choice for a lognormal distribution is based on the principle that no negative values could be obtained, other than with the normal distribution (Timo Schweckendiek, personal communication).

B.2. METHOD

The procedure to calibrate the beta-dependent safety factors is described in section 7.3 of *'Derivation of the semiprobabilitistic safety assessment for piping - WTI 2017 Cluster C piping failure mechanism. Deltares report 1220080-002-ZWS'* Teixeira et al. (2016).

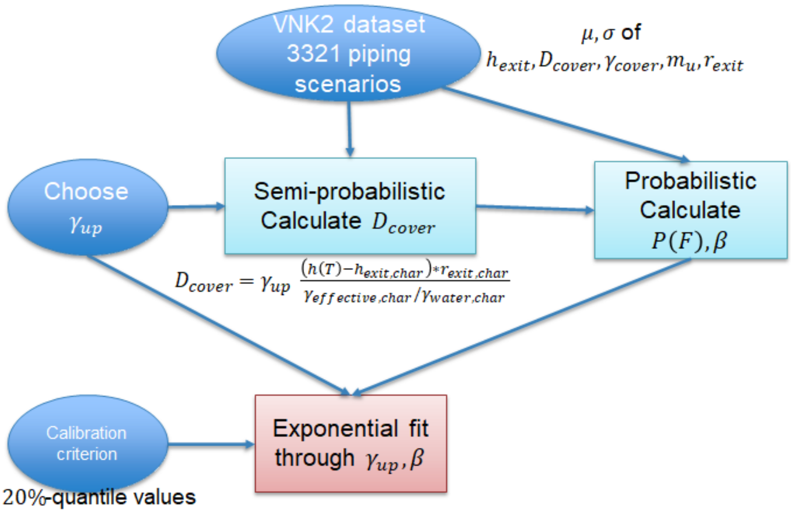

Figure B.1: Flow chart for calibration algorithm

The following algorithm is applied and visualized in Figure B.6:

1. Given:
   (a) a chosen safety factor, proposed range: $\gamma_\beta = [0.5; 1; 1.25; 1.5; 1.75; 2]$
   (b) the water levels (for one test set) corresponding to the exceedance probability of $1/T$ per year, where T is the return period defined per dike segment
   (c) the characteristic values (for one test set) of all variables present, except the cover layer thickness (D_{cover}).

   apply the semi-probabilistic rule of D_{cover} such that $S_{char} * \gamma_\beta = R_{char}$ to obtain D_{cover} (for one test set for a certain safety factor).

2. The obtained characteristic values of D_{cover} are used to back-calculate the mean value, which is subsequently used to perform probabilistic computations at cross-section level. This results in a reliability index (β) for a corresponding test set and safety factor.

3. Repeat points 1. and 2. for different values of $\gamma_\beta = [0.5; 1; 1.25; 1.5; 1.75; 2]$ for each test set member.

4. Find a relation between γ and β in a functional form. Using a calibration criterion and best fit techniques, an exponential fit is proposed to describe this relation.

Figure B.2 shows the outline of the report next to the python code.

B.2.1. PREPROCESSING DATA

First, the data was preprocessed before actually performing the calculations. Starting off, an overview of the provided data is given first. The first part consisted most of the data, except the water levels. These were provided in the second set.

The data were analyzed, and the piping scenarios reduced from 3321 to 1129 sets. The data on the water levels contained the water levels on 691 locations for different return periods. A Gumbel distribution is applied for each location. These Gumbel parameters are then added to the first adapted dataset.

The details of the raw data is found hereafter, as well as the intermediate steps of the combining and analyzing the data.

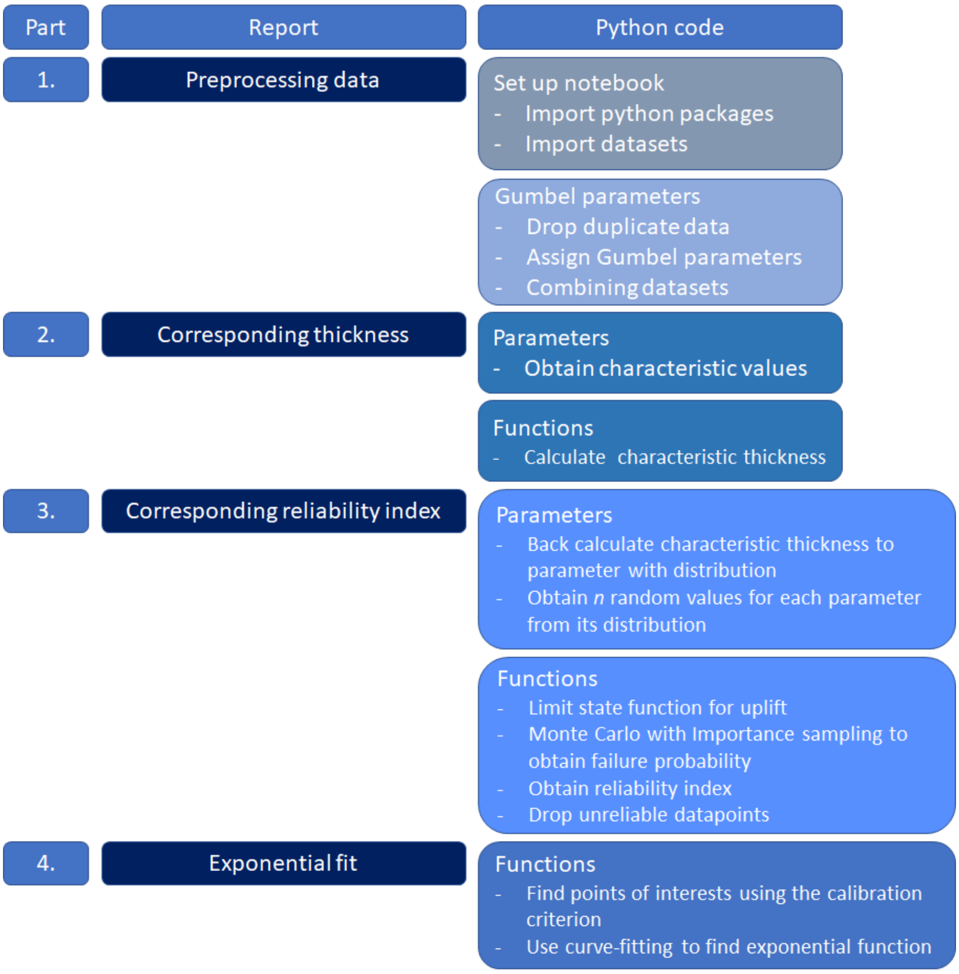

Figure B.2: Outline method and python code

OVERVIEW OF PROVIDED DATA

Courtesy of Ana Teixeira, Karolina Wojciechowska, Wouter ter Horst of Deltares. These datasets were used for the report *'Derivation of the semiprobabilitistic safety assessment for piping - WTI 2017 Cluster C piping failure mechanism. Deltares report 1220080-002-ZWS'.*

1. **Excel:** pipingWTI_Matrix_2016_2019-uplift

2a. **Excel:** WaterLevels_locations_300

2b. **Excel:** WaterLevels_locations_1000

2c. **Excel:** WaterLevels_locations_3000

2d. **Excel:** WaterLevels_locations_10000

2e. **Excel:** WaterLevels_locations_30000

2f. **Excel:** WaterLevels_locations_100000

The first Excel file contains most of the data:

- 3321 piping scenarios, including their location (x- and y-coordinate), ID (vak id), dikering (Dkr) and segment (segm);
- the return period for the design water level and the corresponding design water level;

- the mean and the standard deviation of the hinterland phreatic level (h_polder), thickness of the cover layer (d), saturated volumetric weight of the cover layer (gamma_sat), model uncertainty (mu), dampening factor (r_exit);
- the calculated thicknesses for several different safety factors;
- the calculated reliability indices for several different safety factors and the convergance.

The Excel files 2a-2f contains the water level per '*vak id*' per return period
$T = [300, 1000, 3000, 10000, 30000, 100000]$ years.

NON UNIQUE DATA SETS

It drew attention that some piping scenarios contained almost the same data. The outcome of an analysis of non unique data sets is shown in Table B.2. Data sets which were exactly the same, were dropped using the *drop.duplicate* function of the pandas package in Python. It checks for the input column(s) and drops duplicate data for that/those column(s). After doing so, the dataset was reduced from 3321 to 1129 sets of piping scenarios.

Table B.2: Analysis on unique sets of piping scenarios

Dataset evaluation	Count of sets	% of dataset (100%=3321)
Total dataset	3321	100
Original vak id	692	20.8
Original vak id, d(μ)	1055	31.8
Original vak id, d(μ), d(σ)	1062	32.0
Original vak id, d(μ), d(σ), h_polder(μ)	1112	33.4
Original vak id, d(μ), d(σ), h_polder(μ), h_polder(σ)	1119	33.7
Original vak id, d(μ), d(σ), h_polder(μ), h_polder(σ), gamma_sat(μ)	1127	33.9
Original vak id, d(μ), d(σ), h_polder(μ), h_polder(σ), gamma_sat(μ), gamma_sat(σ)	1129	34.0

NON-UNIQUE/DEFAULT VALUES

It was also noted, that there were frequently occurring values. These are summarized in Table B.3. Here the occurrence of the mean (μ) and standard deviation (σ) of the parameters and their coefficient of variation (cov) is evaluated. In many cases, one could say that a default value is used.

Table B.3: Analysis on non-original values in the dataset

Dataset evaluation	Count of sets	% of dataset (100%=1129)
d(cov) = 0.1	411	36.4
d(cov) = 0.3	71	6.3
h_polder(σ) = 0.01 m	72	6.4
h_polder(σ) = 0.1 m	772	68.4
gamma_sat(cov) = 0.01	18	1.6
gamma_sat(cov) = 0.1	312	27.6
r_exit(μ) = 0.7	271	24.0
r_exit(μ) = 0.8	831	73.6
r_exit(cov) = 0.1	1122	99.4

WATER LEVELS h_T AS GUMBEL DISTRIBUTION

An exceedance probability function should be found for the water levels h_T per location. The Gumbel function is a probable option to model extreme water levels. Using the Gumbel function and the curve fitting (*curve_fit imported from scipy.optimize*) , for each location a corresponding Gumbel scale and location parameter was found. The *curve_fit* function also returned a covariance, which is used to mark unreliable results.

COMBINING DATASETS

The Gumbel parameters (loc, scale, and convergence) are assigned to the first Excel dataset. They are added in the row with the corresponding locations.

An example of the Gumbel fit for location 11001009 can be found in Figure B.3. On the left, it presents graphically the datapoints for water level per return period in years. In the middle graph, the Gumbel fit is plotted through these points. The right figure plots the same values on a smaller scale. It can be concluded from theses graphs that the Gumbel distribution fits well.

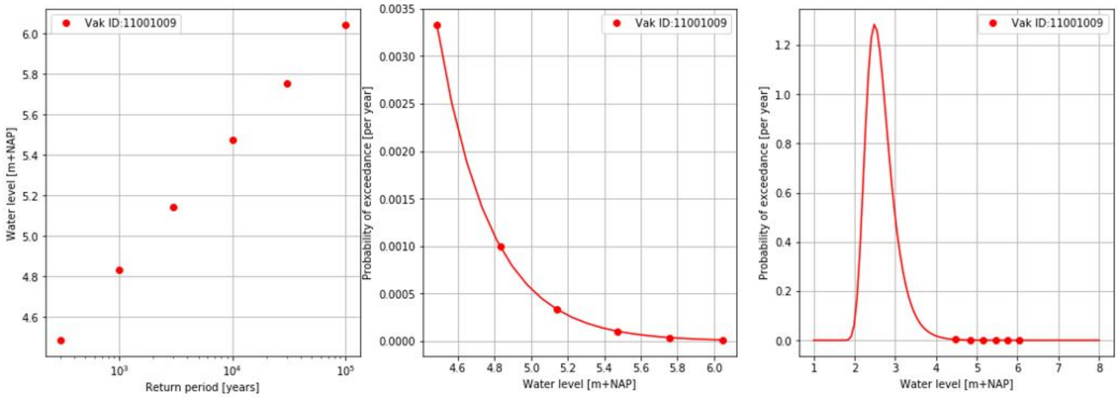

Figure B.3: Gumbel fit for water level on location 11001009

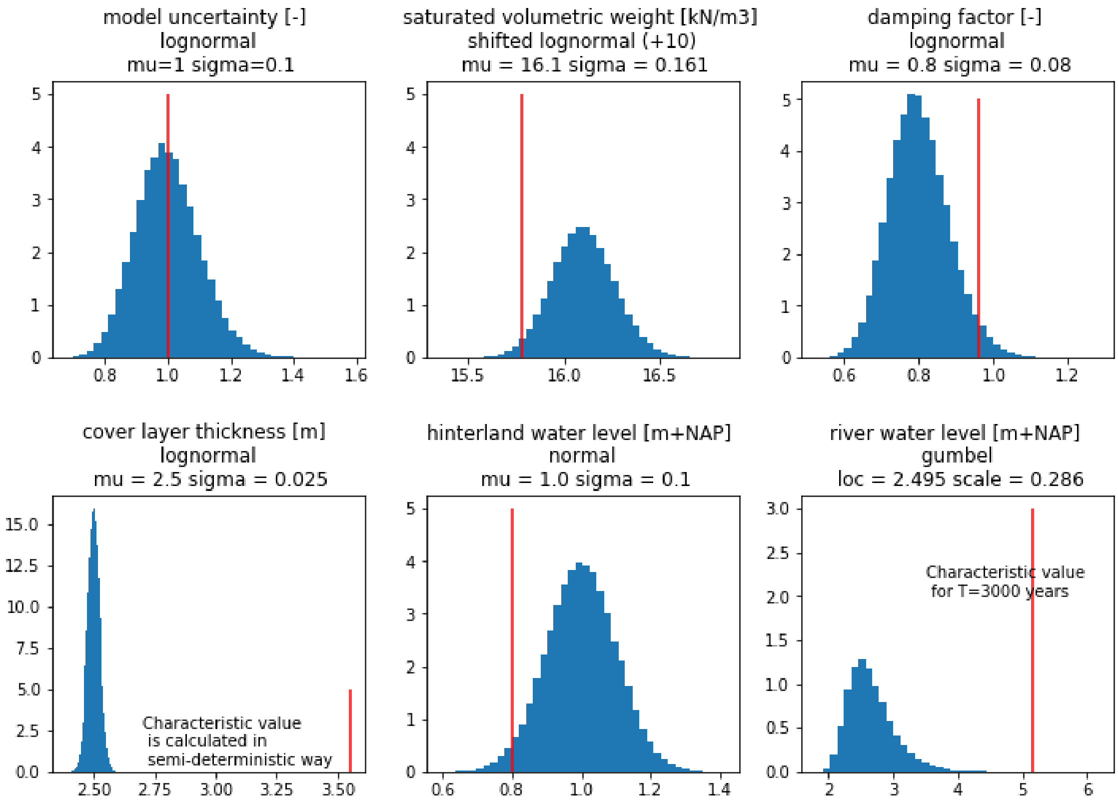

Figure B.4: Parameter distributions and characteristic values for location 11001009

B.2.2. SEMI-PROBABILISTIC: CORRESPONDING THICKNESS

The governing semi-probabilistic equation is described below. The cover layer thickness is calculated per safety factor ($j = 6$) per set of piping scenarios ($i = 1129$).

$$\gamma_{up} \geq \frac{R_{char}}{S_{char}} = \frac{D_{cover,char} * \gamma_{eff,cover,char}}{\gamma_{water,char} * (h(T) - h_{exit,char}) * r_{exit,char}}$$

In which the characteristic values were calculated using an inverse CDF function for lognormal parameters ($\gamma_{eff,cover,char}$ and $r_{exit,char}$). The characteristic value for the Gaussian distributed hinterland water level is computed as $h_{exit,char} = h_\mu - 2 * h_\sigma$. Lastly, the design river level was prescribed in the original dataset.

B.2.3. PROBABILISTIC: CORRESPONDING RELIABILITY INDEX

The probabilistic equation which will be evaluated is the limit state function for uplift. This is:

$$Z_{up} = m_u * D_{cover} * (\gamma_{sat,cover} - \gamma_{water})/\gamma_{water} - (H - h_{exit}) * r_{exit}$$

Now, the goal is to find the reliability index per safety factor ($j = 6$) per set of piping scenarios ($i = 1129$) using the semi-probabilistically computed $D_{cover,char}$. First, the $D_{cover,char}$ should be transformed to $D_{\mu,\sigma}$. Then, the failure probability is determined using a Monte Carlo simulation with importance sampling. Lastly, the corresponding reliability index to the failure probability is determined.

MONTE CARLO SIMULATION FOR PROBABILISTIC CALCULATIONS

The choice for a Monte Carlo simulation is explained here since it differs from the method used in Teixeira et al. (2016). In this report, the software *Hydra-Ring* is used, which is based on a First Order Reliability Method (FORM). Due to unfamiliarity with this program, it was discouraged to use. Another program that can perform a FORM analysis, is Prob2b. However, it is more suitable to use Python to process large data files. Therefore, it is chosen to program a Monte Carlo analysis in Python.

BACK CALCULATE D_{cover} TO PROBABILISTIC DISTRIBUTION

One assumption should be made here regarding the standard deviation to back-calculate the mean cover layer thickness. It is chosen here not to keep the standard deviation as a fixed value, but the coefficient of variation. The coefficient of variation is also the default deviation type in $Hydra-ring$ for the cover layer thickness (see Table B.1). The inverse cumulative density function or percent point function for a lognormal distribution was used to back-calculate the mean value.

CRUDE MONTE CARLO VS. MONTE CARLO WITH IMPORTANCE SAMPLING

Using Crude Monte Carlo to determine the failure probability, the function is given below, with Z = limit state function for uplift.

$$p_{A,MC} = \frac{1}{n}\sum_{i=1}^{n}\eta_A(\mathbf{x}^{(i)}) = 1 \qquad \begin{cases} \eta_A = 1 & if Z < 0 \\ \eta_A = 0 & if Z > 0 \end{cases}$$

However, using this technique in this assessment was not optimal. The computational efforts to compute small failure probabilities were too high in terms of memory errors or computing time. To increase the 'success rate' of failure of low failure probabilities, the importance sampling technique can be used. Graphically, this technique can be explained by moving the cloud points of the realizations Z(R,S) towards the failure line (Z=0). Mathematically approached, the probability density function of one variable is set as less favorable, in order to create more counts of failure. Then, each count of failure is multiplied by a function that describes the probability of that failure with the original distribution of the changed variable.

$$p_{A,IS} = \frac{1}{n}\sum_{i=1}^{n}\frac{f_x(\mathbf{y}^{(i)})}{f_y(\mathbf{y}^{(i)})}\eta_A(\mathbf{y}^{(i)}) = 1$$

In this approach, $f_y(\mathbf{y}^{(i)})$ is chosen such, that the mean is shifted with two times the standard deviation towards the disadvantageous zone. It is chosen to transform the saturated volumetric weight of the cover layer. For the values of location 11001009, the results are visualized in Figure B.5.

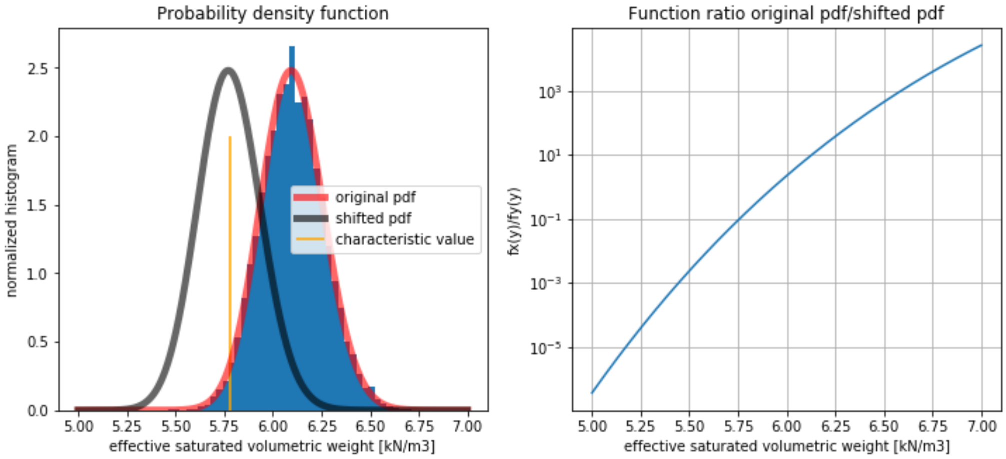

Figure B.5: Shift effective volumetric weight on location 11001009

$\Phi(-\beta)$

From the Monte Carlo analysis, a failure probability is obtained. The final step of this section is to convert the failure probability to a reliability index. This relationship is given by the following equation.

$$\Phi(-\beta) = \frac{1}{\sqrt{2 * \pi}} \int_{-\infty}^{-\beta} \exp\left\{-\frac{(-\beta)^2}{2}\right\} d\beta = P_f$$

$$\beta = -\Phi^{-1}(P_f)$$

The second relation is solved numerically by finding the nearest value of an array of $[\beta, P_f]$.

B.2.4. EXPONENTIAL FIT

As explained before, the calibration criterion now comes into use to fit a proper line through the obtained results. The fitted line should be sufficiently safe. This condition determines how the calibration criterion is defined. Currently, the calibration criterion is defined as the 20% quantile for the reliability indices. Per safety factor, the 20%-value is determined. Then, these values are used to fit an exponential function through it.

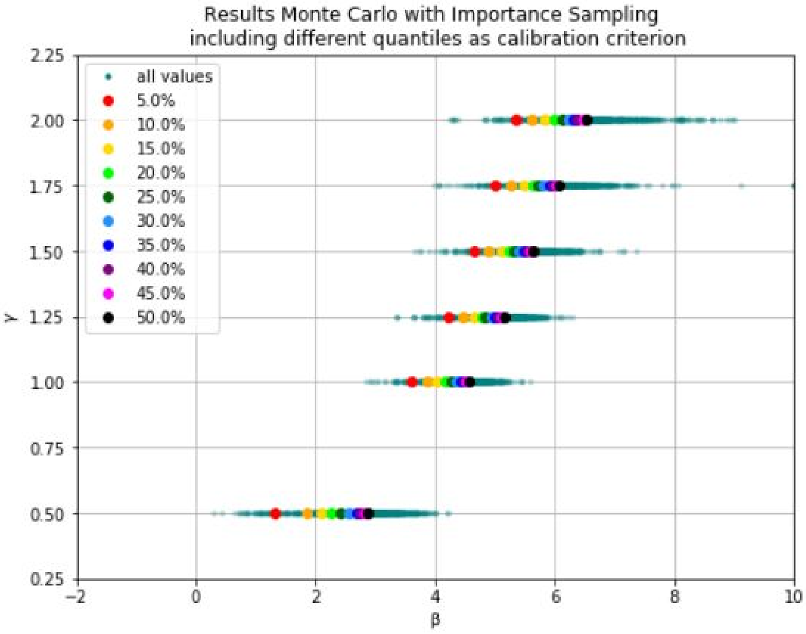

Figure B.6: Results of probabilistic analysis including different quantiles as calibration criterion

B.3. PYTHON NOTEBOOK

B.3.1. PREPROCESSING DATA

SETTING UP NOTEBOOK

```
import numpy as np
import matplotlib.pyplot as plt
%matplotlib inline
import pandas as pd
import math
import random
import scipy.integrate as integrate
import scipy.special as special
from scipy.stats import lognorm
from scipy.stats import norm
from scipy.optimize import curve_fit
from scipy.stats import gumbel_r
from pandas import DataFrame
```

```
y = [50, 100, 125, 150, 175, 200]
index = 139
index1 = 139
index2 = 256
n = 10**6 #number of draws
beta_range = np.linspace(-3,10,13000+1) #reliability index range
#parameters independent on location
gamma_w = 10
mu = 1
```

IMPORT DATA SETS

```
df_d = pd.read_excel (r'data\pipingWTI_Matrix_2016_2019-uplift2.xlsx')
print('shape␣dataset␣provided:', np.shape(df_d))
df_h = pd.read_csv(r'...\export_waterlevels_gumbel.csv')
print('shape␣dataset␣of␣waterlevels:', np.shape(df_h))
```

DROP DUPLICATE DATA

```
indices = np.arange(0, np.shape(df)[0],1)
df_d.drop_duplicates(subset=['vak␣id', 'd_mu', 'd_sigma', 'h_polder', \\
            'h_polder.1', 'gamma_sat', 'gamma_sat.1'], inplace=True)
print('shape␣dataset␣without␣duplicates:', np.shape(df_d))
indices = np.arange(0, np.shape(df_d)[0],1)
```

ASSIGN GUMBEL PARAMETERS

```
rp = np.array([300, 1000, 3000, 10000, 30000, 100000])
dfs = []
for i in range(len(rp)):
    df = pd.read_csv (r'data\WaterLevels_locations_' + str(rp[i])+'.csv', sep=';')
    dfs.append(df)
#import data, provided/courtesy from Karolina Wojciechowska and Ana Teixeira
df = pd.read_excel (r'data\pipingWTI_Matrix_2016_2019-uplift.xlsx')
```

```
def gumbel_pdf(x, loc, scale):
    z = (x - loc)/scale
    return (1./scale) * (np.exp(-(z + (np.exp(-z)))))
def gumbel_cdf(x, loc, scale):
    return np.exp(-np.exp(-(x-loc)/scale))
```

```
popt_gumbel, pcov_gumbel = [], []
for j in range(np.shape(dfs[0])[0]):
    n20, n21 = curve_fit(gumbel_pdf, wl_sets[j], 1/rp)
    popt_gumbel.append(n20)
    pcov_gumbel.append(n21)

infs = np.where(np.isinf(pcov_gumbel))
a = np.where((infs[1]==0) & (infs[2]==0))

print('The␣covariance␣could␣not␣be␣estimated␣for␣the␣following␣indices␣(row):')
print(infs[0][a])
print('These␣should␣be␣strickened␣out␣later')
```

Combining datasets

```
gumbel_loc = []
gumbel_scale = []
for i in range(np.shape(popt_gumbel)[0]):
    gumbel_loc.append(popt_gumbel[i][0])
    gumbel_scale.append(popt_gumbel[i][1])

inf_con = np.zeros(np.shape(popt_gumbel)[0])
inf_con[infs[0][a]] = 1

wl_gumbel = {
    'Dkr': np.array(dfs[0].loc[:,'Dkr']),
    'segment': np.array(dfs[0].loc[:,'segment']),
    'vak_id': np.array(dfs[0].loc[:,'vak_id']),
    'gumbel_loc': gumbel_loc,
    'gumbel_scale': gumbel_scale,
    'conv': inf_con
}
df = DataFrame(wl_gumbel, columns = ['Dkr', 'segment', 'vak_id', \\
               'gumbel_loc', 'gumbel_scale', 'conv'])
print(df[31:41])
```

B.3.2. SEMI-PROBABILISTIC: CORRESPONDING THICKNESS

OBTAIN CHARACTERISTIC VALUES

```
def lognormal(mean = df_t['r_exit'][index], std = df_t['r_exit.1'][index], n=n):
    Variance = std / mean
    scale = np.log(1+Variance**2)**0.5
    loc = np.log(mean) - 0.5*scale**2
    random_lognorm = np.random.lognormal(loc, scale ,n)
    return random_lognorm
def logn_pdf(x, m, s):
    macht = -(np.log(x)-m)**2/(2*s**2)
    frac = 1/(s*x*np.sqrt(2*np.pi))
    return frac*np.exp(macht)
def logn_ppf(p, m, s):
    h = np.sqrt(2)/special.erf(2*p-1)
    return np.exp(m+s*h)
def D_back_logn(p, value, cov, n=n):
    h = np.sqrt(2)/special.erf(2*p-1)
    scale = np.log(1+cov**2)**0.5
    #value = np.exp(loc+scale*h)
    #ln(value) = (loc+scale*h)
    #loc = ln(value)-scale*h
    loc = np.log(value) - scale*h
    random_lognorm = np.random.lognormal(loc, scale ,n)
    return random_lognorm
```

```
def gamma_sat_c(index): #resistance #lognormal
    mean = df_t['gamma_sat'][index] - 10
    std = df_t['gamma_sat.1'][index]
    variance = std / mean
    scale = np.log(1+variance**2)**0.5
    loc = np.log(mean) - 0.5*scale**2
    gamma_sat_c =  logn_ppf(0.05, loc, scale)
    return gamma_sat_c
def r_c(index): #load #lognormal
    mean = df_t['r_exit'][index]
    std = df_t['r_exit.1'][index]
    variance = std / mean
    scale = np.log(1+variance**2)**0.5
    loc = np.log(mean) - 0.5*scale**2
    r_c =  logn_ppf(0.95, loc, scale)
    return r_c
def he_c(index): #resistance #normal
    he_c = df_t['h_polder'][index] - 2* df_t['h_polder.1'][index]
    return he_c
def ht_c(index): #gumbel
    ht_c = df_t['wl'][index] ##navragen
    return ht_c
```

CALCULATE CHARACTERISTIC THICKNESS

```
def corresponding_thickness(gamma, index):
    d_c = gamma *((ht_c(index)-he_c(index))*r_c(index))/((gamma_sat_c(index))/gamma_w)
    return d_c
```

```
d_c = []
for i in range(len(indices)):
    d_c.append([])
    for j in range(len(y)):
        d_c[i].append(corresponding_thickness(gamma=y[j]/100, index=i))
```

B.3.3. Probabilistic: Corresponding reliability index

Back calculate characteristic thickness to parameter with distribution

```
def D_n(index, gamma): #lognormal
    value =  d_c[index][gamma]
    cov = df_t['d_sigma'][index]/df_t['d_mu'][index]
    p =0.05
    D_n = D_back_logn(p, value, cov, n=n)
    return D_n
```

Obtain *n* random values for each parameter from its distribution

```
#parameters, independent on location
mu_n = lognormal(mean = 1, std = 0.1, n=n) #model uncertainty (lognormal)

#parameters, dependent on location
def gamma_sat_n(index): #lognormal (shifted log normal +10)
    gamma_sat_n = lognormal(mean = df_t['gamma_sat'][index] - 10, std \\
        = df_t['gamma_sat.1'][index])
    return gamma_sat_n
def r_n(index): #lognormal
    r_n = lognormal(mean = df_t['r_exit'][index], std = df_t['r_exit.1'][index], n=n)
    return r_n
def he_n(index): #normal
    he_n = np.random.normal(df_t['h_polder'][index], df_t['h_polder.1'][index], n)
    return he_n
def ht_n(index): #gumbel
    ht_n = np.random.gumbel(df_t['gumbel_loc'][index], \\
            np.abs(df_t['gumbel_scale'][index]), n)
    #absolute value to resolve error in solving.
    #The unreliable result will be strickened out later on
    return ht_n
```

Limit state function for uplift

```
def LSF(mu, gamma_w, gamma_sat, r, D, he, ht):
    Delta_phi_cu = D*(gamma_sat)/gamma_w
    phi_exit = he + (ht - he)*r
    Z = mu*Delta_phi_cu - (phi_exit - he)
    return Z
```

Monte Carlo with Importance sampling to obtain failure probability

```
def gamma_sat_n1(index, shift): #lognormal (shifted log normal +10) #new sample
    gamma_sat_n = lognormal(mean = df_t['gamma_sat'][index] - 10 \\
            - shift*df_t['gamma_sat.1'][index], std = df_t['gamma_sat.1'][index])
    return gamma_sat_n
```

```
#find 'scaling function' fx(x)/fy(x) for importance sampling
def ratio_is(x, shift, index):
    mean = df_t['gamma_sat'][index] - 10
    std = df_t['gamma_sat.1'][index]
    variance0 = std / mean
    scale0 = np.log(1+variance0**2)**0.5
    loc0 = np.log(mean) - 0.5*scale0**2
    f0 = logn_pdf(x, loc0, scale0)
    mean_shift = mean - shift*std
    variance1 = std / mean_shift
    scale1 = np.log(1+variance1**2)**0.5
    loc1 = np.log(mean_shift) - 0.5*scale1**2
    f1 = logn_pdf(x, loc1, scale1)
    return f0/f1
```

OBTAIN RELIABILITY INDEX

```
#find beta for known failure probability (pf)
def integral(z):
    return np.exp(-z**2/2)
def integrand(z):
    return integrate.quad(integral, -np.inf, z)
def phi(z):
    return 1./np.sqrt(2*math.pi)*integrand(z)[0]

phi1 = []
for i in range(len(beta_range)):
    phi1.append(phi(-beta_range[i]))

def find_beta(pf):
    array = phi1
    value = np.ones(len(array))*pf
    idx = (np.abs(array-value)).min() #smallest difference
    ix = np.argmin(np.abs(array-value)) #location of smallest difference
    return beta_range[ix]
```

```
pf_matrix = []
beta_matrix = []
for i in range(len(df_index)):
    print(i)
    pf_matrix.append( [])
    beta_matrix.append( [])
    gamma1 = gamma_sat_n1(index=df_index[i], shift=2)
    for j in range(len(y)):
        Z = LSF( mu_n, gamma_w, gamma1,  r_n(df_index[i]),\
              D_n(df_index[i], gamma=j), he_n(df_index[i]), ht_n(df_index[i]))
        functie = ratio_is(gamma1, shift=2, index=df_index[i])
        pf1 = np.sum(functie[Z<0])/n
        pf_matrix[i].append(pf1)
        beta = find_beta(pf1)
        beta_matrix[i].append(beta)
```

OPTION TO SAVE RAW RESULTS

```
np.savetxt("betas_run7nov.csv", beta_matrix, delimiter=";")
np.savetxt("pf_run7nov.csv", pf_matrix, delimiter=";")
```

B.3.4. EXPONENTIAL FIT

FIND POINTS OF INTERESTS USING THE CALIBRATION CRITERION

```
def extractquantile(index=1, q=0.5):
    return df3['b'+str(y[index])].quantile(q)
```

```
gamma = [] #safety factor
for i in range(len(y)):
    gamma.append(y[i]/100.)
```

```
q_test = np.linspace(0.05, 0.5, 10)
q_results = []
for j in range (len(q_test)):
    q_results.append( [])
    for i in range (len (y)):
        q_results[j].append(extractquantile(index=i, q=q_test[j]))
```

USE CURVE-FITTING TO FIND EXPONENTIAL FUNCTION

```
def exponential(x,a,k,b):
    return a*np.exp(x*k)+b
```

```
popt_exponential, pcov_exponential = [], []
for j in range(len(q_test)):
    n10, n11 = curve_fit(exponential, q_results[j], gamma, p0=[0.2,0.1, 0.5])
    #p0 = initial guess shape exponential curve
    popt_exponential.append(n10)
    pcov_exponential.append(n11)
```

```
x = np.linspace(0,8,60)
p20 = popt_exponential[3]
yfit12 = p20[0]*np.exp(x*p20[1])+p20[2]
plt.plot(x,yfit12, '-', color='lime', label = '20%␣MC␣IS')
```

B.4. RESULTS

B.4.1. CHECKING ASSUMPTIONS FOR 20% QUANTILE AS CALIBRATION CRITERION

This check will be carried out in two steps:

1. Check if the Gaussian distribution $N(\mu, \sigma = 0.5)$ from the VNK2 dataset is a good approximation for the obtained reliability indices in the calibration.
2. Check if the premise holds for $\beta_{cross,m,20\%} \approx P_{cross,m,avg}$.

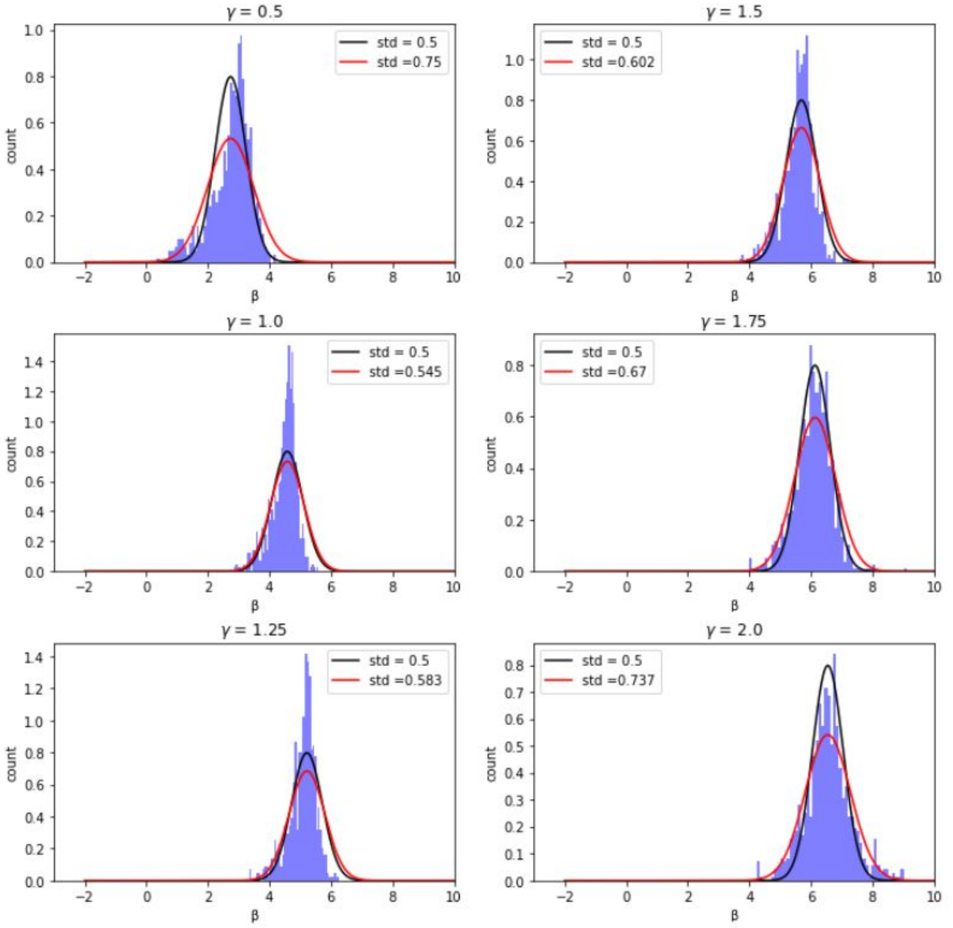

Figure B.7: First check: compute σ *for Gaussian distribution and compare to* $\sigma = 0.5$

The first check is carried out in the following manner. Per safety factor, the mean and standard deviation of the reliability indices are computed. The check is subsequently carried out visually, by comparing the normalized histogram, the corresponding probability density function (pdf) and the pdf with a standard deviation of 0.5. Figure B.7 contains the results. In general, $N(\mu, \sigma = 0.5)$ is a good approximation. However, the actual computed standard deviation is larger, which is reported in the Figure as the red line. Also, at for example $\gamma = 0.5$, the data is asymmetrically distributed.

The second check is carried out by assuming a certain mean value for the reliability index, a Gaussian distribution and $\sigma = 0.5$. For this distribution, the average failure probability is computed numerically and the corresponding reliability index. This is compared with the 20% quantile, see Figure B.8. For $\beta = 4$, the values correspond. However, for larger mean values, the premise is too strict.

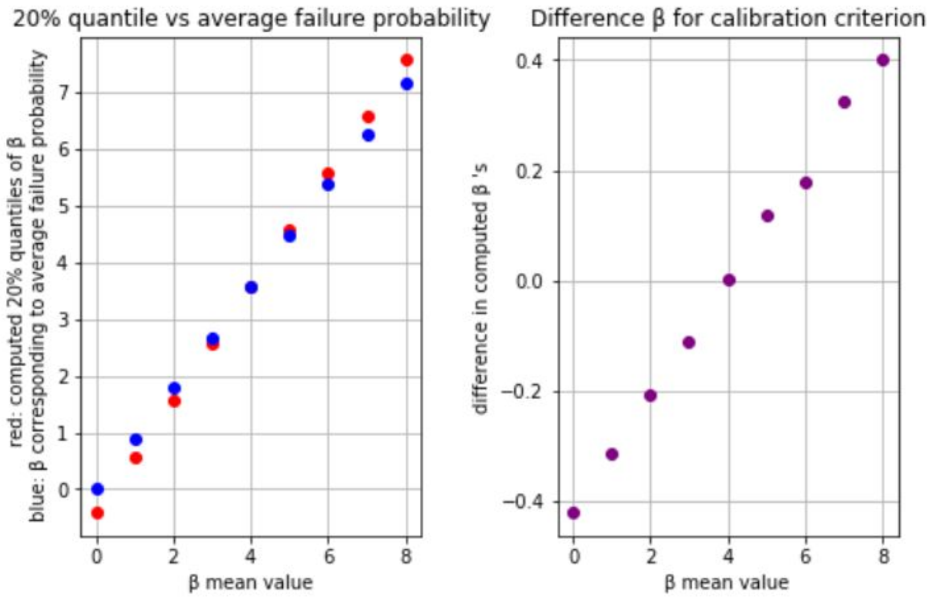

Figure B.8: Second check: compute average failure probability and compare to 20% quantile

B.4.2. SENSITIVITY ANALYSIS ON 20% QUANTILE AS CALIBRATION CRITERION

In Figure B.9, a sensitivity analysis for the calibration criterion is presented, where the left plot illustrates the γ, β-plot for the fit with different calibration criteria. The middle and the right plots show the effect of different calibration criteria relative to the 20%-case as normalized values and arithmetic differences, respectively.

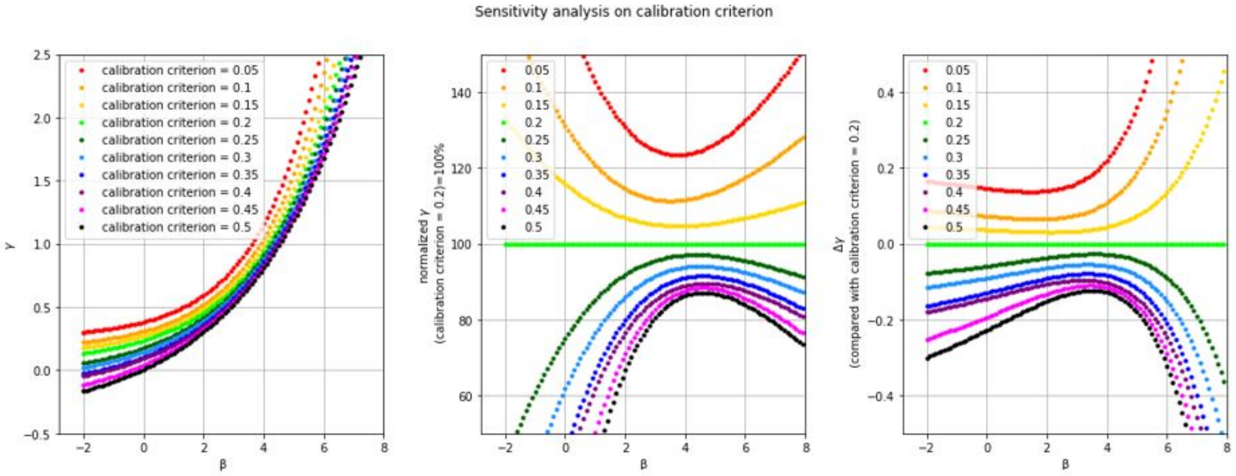

Figure B.9: Sensitivity analysis on different calibration criteria

B.4.3. SENSITIVITY ANALYSIS ON TYPE OF CALIBRATION CRITERION

Also, a different analysis is done regarding the calibration criterion. As explained before, the currently used calibration criterion (20% quantile of β) is based on the premise that the failure probability cannot be larger than the average probability. However, in Figure B.7 it can be seen that the assumption that the standard deviation equals 0.5 is not precise. Also, Figure B.8 shows that the 20% quantile of β resembles the average failure probability only at $\beta = 4$ and is off for other values. Therefore, the average failure probabilities are calculated, transformed into the corresponding reliability index. Finally, an exponential fit is made. It can be seen in Figure B.10 that the differences are significant for $\beta > 4$ and $\gamma > 1$.

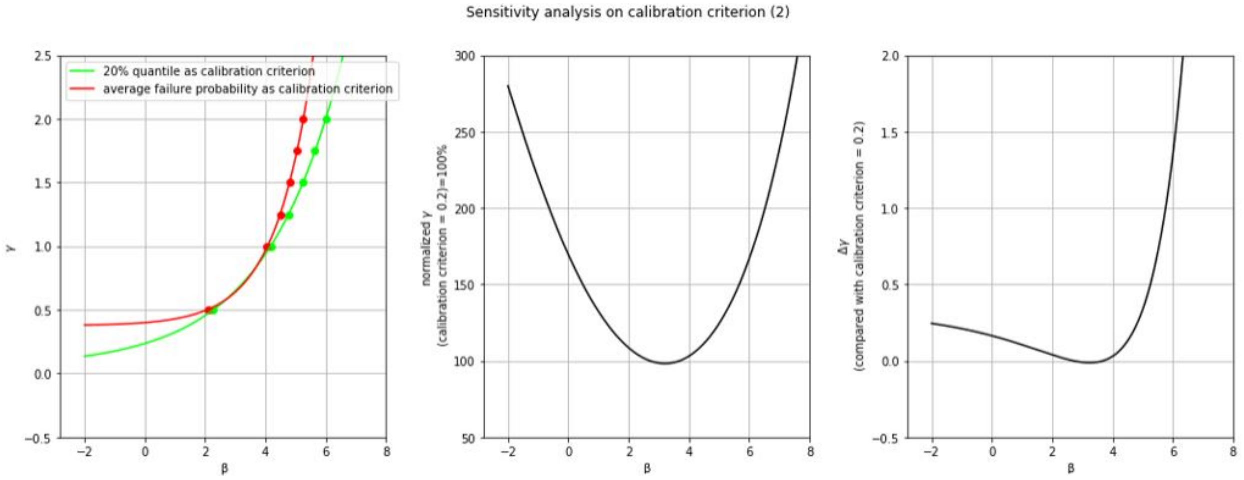

Figure B.10: Comparing calibration criteria based on β-quantile and average failure probability

B.4.4. SENSITIVITY ANALYSIS ON MODEL FACTOR

Similarly to the calibration criterion, a sensitivity analysis of the variation in the model factor is carried out as well. The default value of the coefficient of variation (CoV) is 10%. This is evaluated compared to CoV of 5% and 1%, see Figure B.11. On the left, there is the γ, β-plot for the fit with different coefficients of variation for a calibration criterium as the 20% quantile. In the middle and the right graphs contain the normalized values and arithmetic differences between the default value and changed values for the CoV of the model factor.

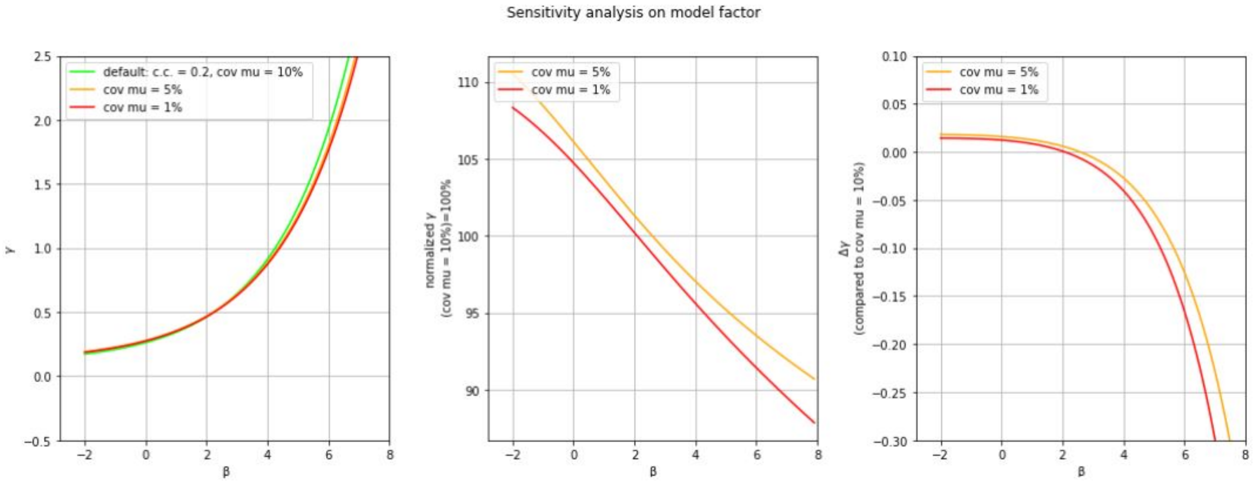

Figure B.11: Sensitivity analysis on different coefficients of variation for model factor

B.4.5. SENSITIVITY ANALYSIS ON DAMPING FACTOR

In Figure B.12, the outcomes are included about using different default values for the damping factor. In this analysis, all scenarios had the same value for the damping factor, i.e. LN(0.8, 0.08), LN(0.9, 0.009) or LN(0.95, 0.00095).

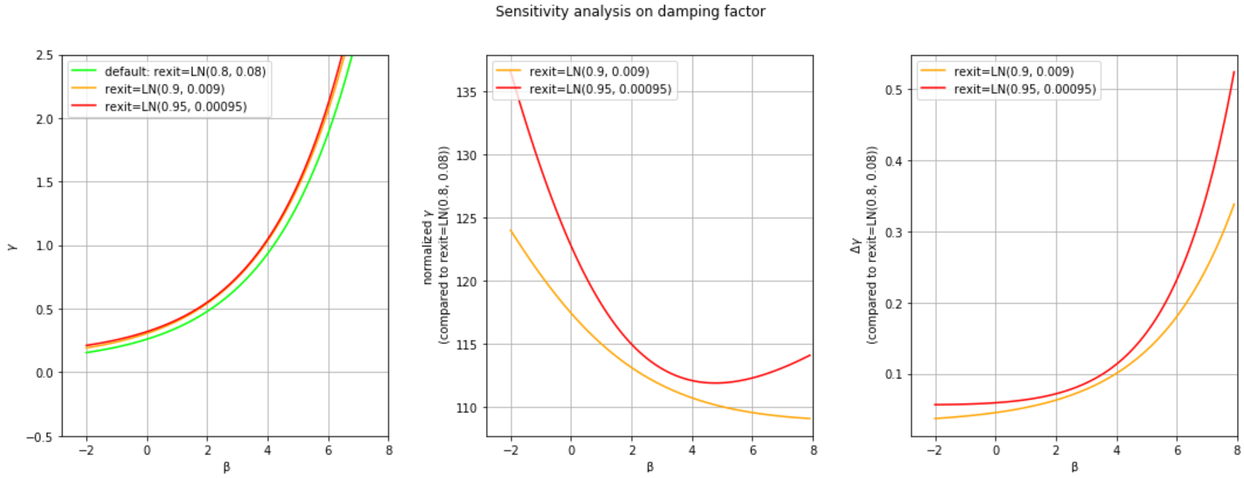

Figure B.12: Sensitivity analysis on different default values for the damping factor

B.4.6. COMPARISON WITH ORIGINAL CALIBRATION

Since the reliability indices from the $Hydra-Ring$ are provided, the results from both methods could be compared. The $\gamma-\beta$ fit of both results for calibration criteria of 5%, 20% and 50% are plotted in Figure B.13. In conclusion, the Monte Carlo analysis gives 80%-90% of the outcome of Hydra-Ring. Below, three causes for this difference are discussed:

PROBABILISTIC METHOD: FORM IN HYDRA-RING VS. MONTE CARLO WITH IMPORTANCE SAMPLING

As the method differs in which the probabilistic calculation was performed, the difference in outcome is discussed first. The $Hydra-Ring$ program is based on FORM and is used in Teixeira et al. (2016). It also provides the influence factor α per parameter.

At Deltares, a study was performed on the robustness of FORM. Also a comparison between FORM and Monte Carlo done. The actual differences were found small, with a maximum pf 0.1, of which FORM gave the larger value as result.

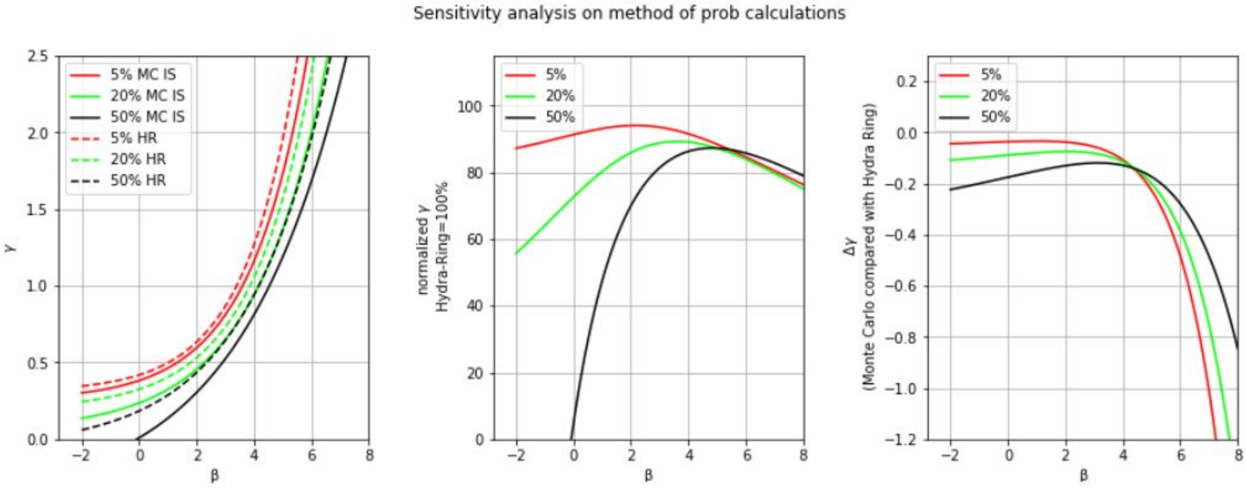

Figure B.13: Comparison results Monte Carlo Importance Sampling (MC IS) and Hydra-Ring (HR)

DESIGN WATER LEVEL: HYDRA-RING VS. GUMBEL FIT

Another difference is that the river water level distribution is computed automatically in $Hydra-Ring$, whereas for the Monte Carlo analysis outcomes of the $Hydra-Ring$ were used for a Gumbel distribution. $Hydra-Ring$ is more advanced and makes use of river discharges, wind speeds and sea water levels as input parameters (van Balen, 2016). It is more advanced than using a Gumbel fit. Also, Gumbel does not fit well for a few locations, for example locations which are influenced by opening/closing of a weir.

UNIQUE VALUE DATASET

Lastly, there were 1129 unique sets of data on a total of 3321 sets. The original calibration used all the sets, whereas here only the unique sets were used. However, after computing the point of interest with the calibration criterion, there was no significant difference.

B.5. CONCLUSION AND DISCUSSION

ASSUMPTIONS FOR 20% QUANTILE AS CALIBRATION CRITERION

There were two assumptions checked: *(i)* $\beta \sim N(\mu, \sigma = 0.5)$ and *(ii)* $\beta(20\%$ quantile$) \simeq P_f(average)$. After checking, both assumptions are found to be accurate but not very precise.

SENSITIVITY ANALYSIS ON 20% QUANTILE AS CALIBRATION CRITERION

The outcome is as expected: A less strict calibration criterion results in lower prescribed safety factors. The default value is a calibration criterion as 20% quantile of β. Quantifying the difference, this is in the order of magnitude of $\sim 10\%$ for using 35% instead of a 20% quantile.

SENSITIVITY ANALYSIS ON TYPE OF CALIBRATION CRITERION

Here, the outcome differs from the expectation. The default value was using a calibration criterion of 20% quantile of β, and the compared value was using the average failure probability and the corresponding β. In other words: premise I was compared with premise II.

The expectation was that both premises would yield a similar outcome, since two assumptions are checked and were found not precise but still accurate. However, the outcome differs largely, in the order of magnitude of $\sim 50\%$ as an addition.

SENSITIVITY ANALYSIS ON MODEL FACTOR

The outcome is as expected: A lower coefficient of variation of the model factor results in lower prescribed safety factors. The default value is a coefficient of variation (CoV) as 10%. Quantifying the difference, this reduction from changing the CoV from 10% to 1% is in the order of magnitude of $\sim 5\%$.

COMPARISON WITH ORIGINAL CALIBRATION

All above analyses were performed in Python, and for the probabilistic calculations a Monte Carlo simulation with Importance Sampling was used. This is different from the original calibration, which was performed in $Hydra-Ring$ (Teixeira et al., 2016). The probabilistic calculations are based on a FORM approach.

Three possible causes for the difference are listed below:

1. Probabilistic method: FORM in Hydra-Ring vs. Monte Carlo with Importance Sampling
2. Design water level: Hydra-Ring vs. Gumbel fit
3. Unique value dataset

B.5.1. RECOMMENDATIONS

Following from these analyses, the determination of the prescribed safety factor has a delicate process and is highly dependent on the method and calibration criterion type. The current calibration criterion choice is not robust.

It is recommended to look beyond the current calibration process (Teixeira et al., 2016). In the calibration process for slope stability (Kanning et al., 2017), the reliability index and safety factor were calculated simultaneously, for $\beta = [3.5 \sim 5.5]$. Then, a linear fit is used to determine the relation of the safety factor with the reliability index. To account for the 20% β-fit criterion, the linear fit is shifted with 0.84 times the error of the fit. Using this process for uplift regarding internal erosion, another safety factor calibration fit can be obtained.

Furthermore, a note on the model uncertainty: If it can be proven that the current mathematical model is too conservative by ignoring strength factors, it is recommended to reduce or neglect the coefficient of variation of the model factor.

A last thing to note, some the input values for the probabilistic calculations had a high frequency, see Table B.3. These are highly likely default values of the VNK2 dataset. A recommendation is thus to improve the quality of this dataset. However, this takes much effort. Therefore, the last recommendation is to omit the use of the safety factors for uplift in practice and directly compute the reliability index in a probabilistic way.

C

DEVELOPING A CONCEPTUAL MODEL

In current reports, uplift is described as 'The water pressure in the sand layer can cause the overlying cohesive soils to crack'. The mathematical model consists of a vertical equilibrium condition only of the overpressure against the self-weight of the cover layer. This is a simplistic and therefore a conservative approach. Here, it is investigated in what way the real-world problem can be modeled more realistically.

C.1. INTRODUCTION

With models, one tends to mimic the real world and simulate possible outcomes. As for now, with uplift, there is a simplistic mathematical model to determine whether uplift takes place. Also, scientific models, physical models and abstract models help to gain understanding about phenomena, identify assumptions, and grasp essentials about big or complex challenges. Another type of model is a conceptual model. Key features are manipulating ideas as objects, exploring their relationships and working with complex systems.

The objective of this document is to qualify the relationships in the uplift submechanism. Since exploring relationships is a key feature in conceptual models, a conceptual model is developed here. The purpose of this model is to find more strength contributions than only the self-weight of the cover layer, and their relationships to the failure mechanism. Also, it is used to gain insight into what level assumptions can be occurring. The following steps after developing the conceptual model is to design the model and the computer model, see Figure C.6. To define the scope: the last 'step' of the model is chosen as a full crack through the cover layer.

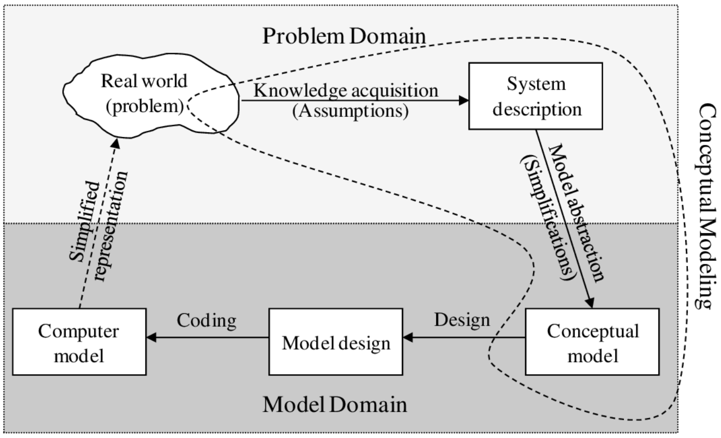

Figure C.1: Domain of conceptual modelling (Robinson et al., 2015)

The structure of this report is as follows: First, an overview is given of typical situations of crack-forming in soils. It is important to gain knowledge about how the mechanisms behind the different cases are explained. Then, the uplift phenomenon including the development of a crack is investigated in more detail. Using literature, a complete description of the problem behavior in the real world is obtained. The real-world problem and the system description are coupled together. The conceptual model for having a continuous fissure through the cover layer is split into two parts: crack-initiation (Section C.4) and the crack-development (Section C.5). Also using ideas proposed in the literature, several options of the soil behavior are discussed. Finally, the conceptual model is presented graphically in Section C.6.

C.2. CRACKING IN COHESIVE SOILS

There are several situations in which soil fracturing is observed in geotechnical practice (Mitchell and Soga, 2005). These are listed below and are discussed more elaborately hereafter.

1. At the crest of a landslide or vertical cutting;
2. By pumping or injecting air, fluids, grouts or chemicals in the soil, also known as hydraulic fracturing;
3. At the surface of clay by desiccation;
4. At the base of an excavation due to high artesian pressures;
5. Behind a dam, causing internal erosion.

C.2.1. CRACKS ON TOP OF A SLOPE

On top of a slope, tensile cracks can be observed. Subsequently, the failure mechanism is a rotational landslide. The problem even worsens itself if water fills up the crack, decreasing the effective stress and thus the shear strength of the earth body.

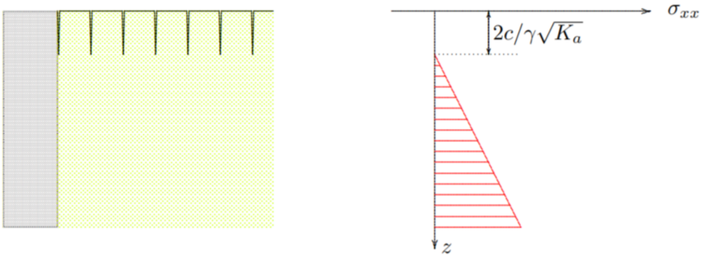

Figure C.2: Horizontal stresses with cracks in the soil . (Verruijt and Van Baars, 2007)

Figure C.3: Tensile crack at the slope crest (Ismail et al., 2008)

C.2.2. HYDRAULIC FRACTURING

Hydraulic fracturing is often done on purpose to create cracks in the subsoil. Below are two examples. In Figure C.4, a mixture of water, sand, and chemicals is injected under high pressure, to extract gas and oil. Figure C.5 shows compensation grouting, whose goal is to control settlements by reinforcing the soil with a grout mixture.

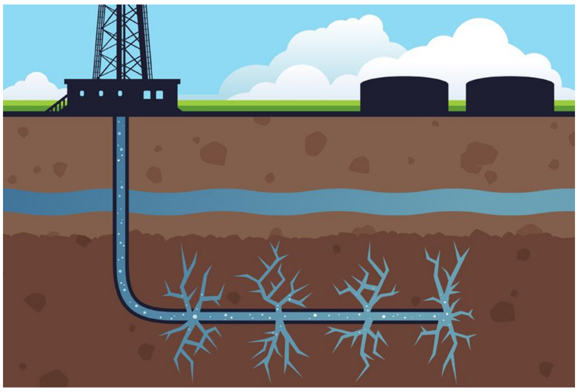

Figure C.4: Fracking for gas extraction [a]

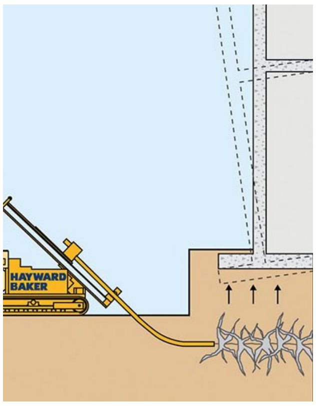

Figure C.5: Compensation grouting [a]

---

[a] Source: https://www.texastribune.org/2011/07/28/epa-issues-new-......standards-hydraulic-fracturing/

[a] Source: https://www.haywardbaker.com/... solutions/techniques/fracture-grouting

In both situations, the mixture is inserted under high pressure. This pressure exceeds a certain threshold value and causes the soil to crack. With hydraulic fracturing, there are two initiation mechanisms, based on a tensile or a shear failure criterion (Marchi et al., 2013).

C.2.3. DESICCATION

By desiccation, the water content in the clay decreases, leading to shrinkage. This shrinkage comes with tensile stresses. If the tension strength is exceeded, cracks will occur. This type of cracks often occurs in very plastic clays, poorly compacted and relatively wet during construction. Other factors playing a role in the desiccation rate are trees on a dike and an orientation to the west in windy regions (Ponsteen et al., 2019). Another way of evaluating desiccation cracks is to introduce a critical pore water pressure value (Konrad and Ayad, 1997).

Figure C.6: Dike in water board Delfland with cracks (Ponsteen et al., 2019)

C.2.4. EXCAVATION BASE

Due to high artesian water levels, uplift and cracks occur in excavations with a clayey base. In literature, it is assumed that the clay layer behaves undrained as a beam. Subsequently, bending moments and shear forces induce internal stresses (Hong and Wang, 2016; Šuklje et al., 1961). In Figure C.7, the schematization is shown for a simple excavation. The clay beam here has fixed supports at the end of the excavation. Figure C.8 contains the schematization of an excavation of the Tisza - Danube Canal in Yugoslavia. There, Suklje assumes that shear forces equal to zero at the boundaries of the schematization. Below the figure, more explanations are included.

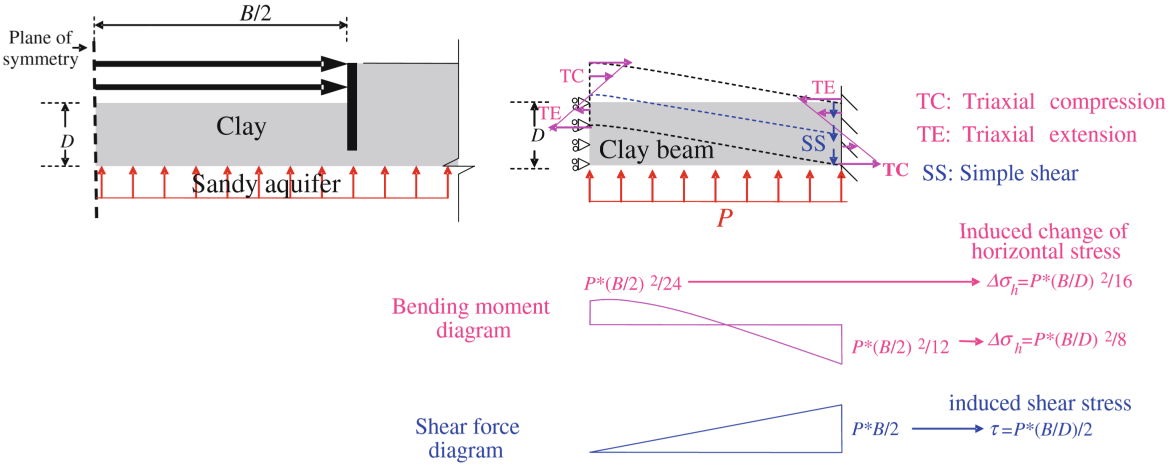

Figure C.7: Simplified model for uplift in an excavation (Hong and Wang, 2016)

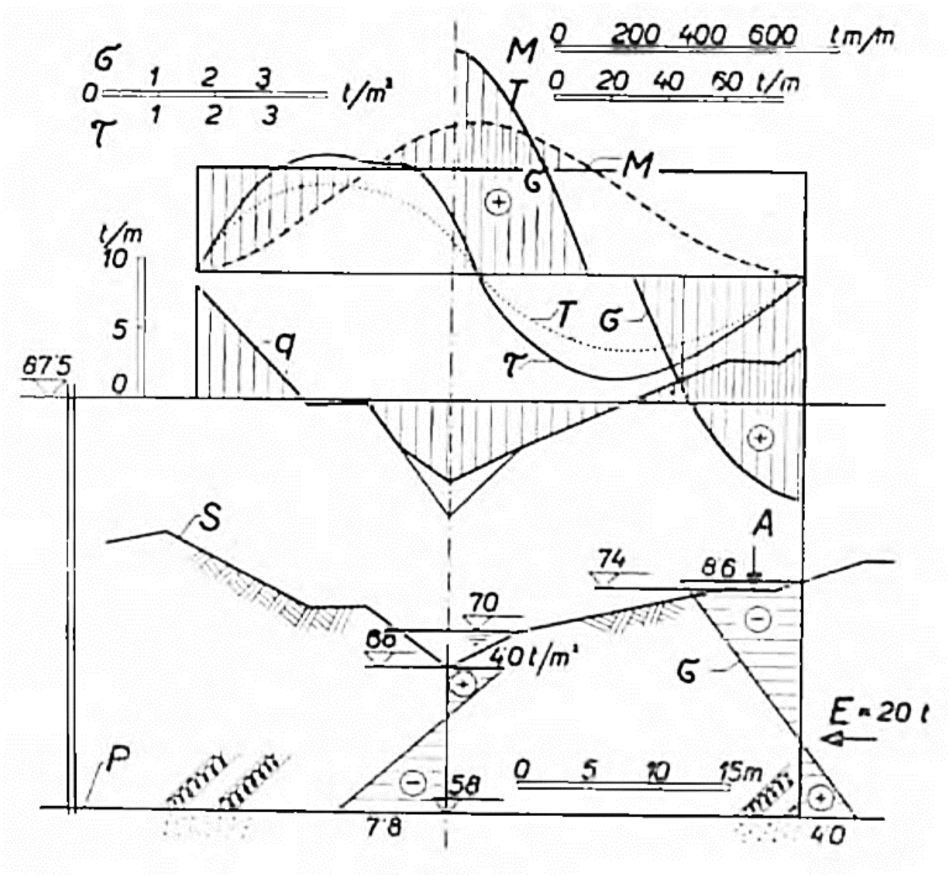

Figure C.8: Schematization of excavation of Tisza - Danube Canal in Yugoslavia (Šuklje et al., 1961)

There was a rupture of excavation of the Tisza - Danube Canal in Yugoslavia, covering a length of about 800 meters, the depth of the excavation being about 20 meters. The base of the excavation consisted of clay, overlaying a sandy aquifer containing high water pressures. This rupture was expected, but the wells, discharging the pressure of the artesian water proposed to prevent rupture, were not yet realized.

The system presented in Figure C.8 is analyzed as a static system, where the gravity forces were balanced by artesian pressure. This static system was assumed to be loaded at the boundary surfaces by embedding moments as well as by the surrounding ground pressure, the two loads were assumed to be in independent equilibrium and corresponding to the assumption that the tensile stresses at the upper limits and lower of the coherent basis were equal.

Figure C.8 shows the section of the excavation at the moment of rupture, where the first of the artesian sources preceding the rupture appeared. The position of the source (A) falls within the range of maximum tensile stresses. The analysis of the section where the first big hole/crack appeared, gave a similar result; but with the appearance of the hole/crack in the field of constraints maximum shear. (Šuklje et al., 1961)

C.2.5. UPLIFT LEADING TO HEAVING AND PIPING

Due to high water pressures during a flood wave, the water pressure in the aquifer rises. The layer lifts up and subsequently cracks. What exactly is the cause for the crack is unknown and is investigated later. Figure C.9 provides a possible schematization and stress distribution.

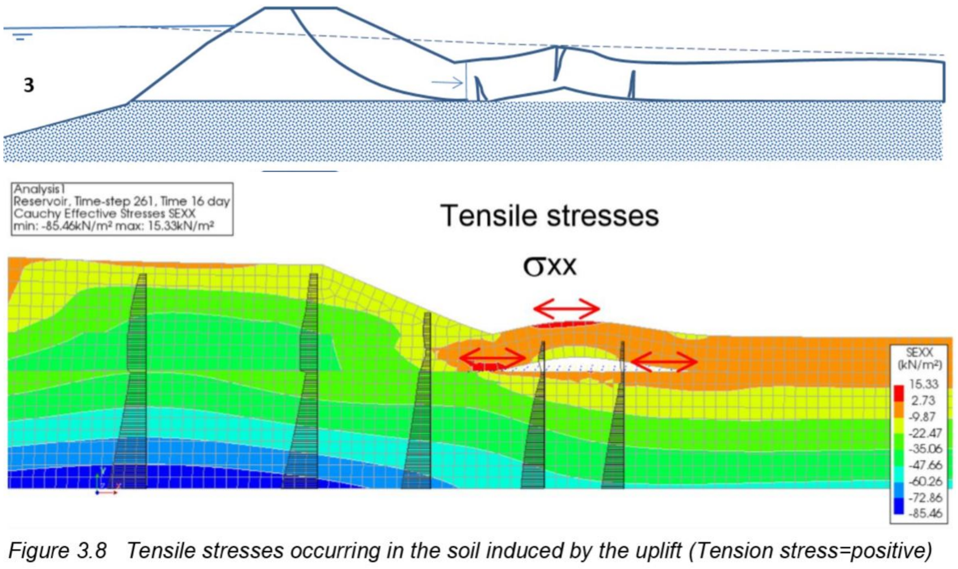

Figure C.9: Stress distribution in a FEM analysis (Hoffman, 2019)

C.2.6. SUMMARY

To summarize, several cases of cracks occurring in the soil are discussed in this Chapter. The causes are different, and Table C.2.6 provides an overview.

	Situation	Formula
1.	**Cracks on top of a slope** Due to horizontal deformations, negative horizontal stresses occur. Assuming there is no tensile strength, cracks develop.	$\sigma_{horizontal} < 0$
2.	**Hydraulic fracturing** Increasing the pressure decreases the effective stress, thus the soil strength. Fracture initiation pressure is the failure criterion.	$p > P_f$
3.	**Desiccation** Decreasing water content leads to volume decrease and tensile stresses. Due to evaporation, a critical suction value is reached.	$w < w_{critical}$
4.	**Excavation base** Artesian pressures lead to bending moments, internal stresses and cracks. Assuming a beam model, the maximum compression, tension, and shear stresses can be found.	$\sigma_{compression} > \sigma_{c,max}$ $\sigma_{tension} > \sigma_{t,max}$ $\tau > \tau_{max}$
5.	**Uplift** *T.b.d.*	*T.b.d.*
-	Other Earthquakes (seismic effects) and differential settlement (Vaníček, 2013)	-

Table C.1: Summary of situations in cohesive soils in which cracking occurs

When comparing the causes of the other four situations with the uplift case, two are useful. In uplift, high water pressures due to a river flood occur. This has a resemblance to hydraulic fracturing. Also, when the layer lifts, vertical deformations occur, having similarities with the excavation base. These two cases will be used later on when developing the conceptual model.

C.3. DETAILED PHENOMENOLOGICAL DESCRIPTION FOR UPLIFT

This chapter deals with more detailed existing descriptions, experiences, and expert judgments on uplift to gain a better understanding of the real-world problem. The starting point is a description of uplift by 't Hart (2018) in the report *Phenomelogical description of failure mechanisms WBI.*

> The pore water pressure in the aquifer rises due to a higher river water level. When the pore water pressure in the aquifer on the inner side of the dike will exceed the weight of the cover layer, this will lift up. The cohesive cover layer has a vertical permeability, but orders of magnitude smaller than that of the aquifer. Due to the uplifting, cracks or holes will occur, through which the water will find a way to the ground surface. This open exit point is a condition for the subsequent submechanisms in internal erosion to occur ('t Hart, 2018).

The interplay between the aquifer and the cover layer determines the uplift behavior. The description hereafter is split into two parts: the rise of the pore water pressure in the aquifer and the subsequent reaction of the cover layer.

C.3.1. RISING WATER PRESSURE IN THE AQUIFER

A head difference from the water side to the land side of a dike creates a gradient in the aquifer. The cover layer is schematized as a leaky layer and is subject to seepage. Through the aquifer, there is a flow rate, which magnitude is depending on the thickness and permeability of the aquifer and the gradient of the head over the dike body ('t Hart, 2018).

The point of interest here is determining the head in the aquifer at the exit point, for which different approaches exist. Analytical Dupuit flow equations are a good starting point when assuming that the groundwater flows predominantly horizontally (Jonkman et al., 2018). Furthermore, geohydrological models are available, e.g. MODFLOW, dgflow, iMODFLOW, and WATEX (Van Esch et al., 2016). Finally, conducting water-pressure-response-measurements for calibration purposes gain more precise results (Förster et al., 2012).

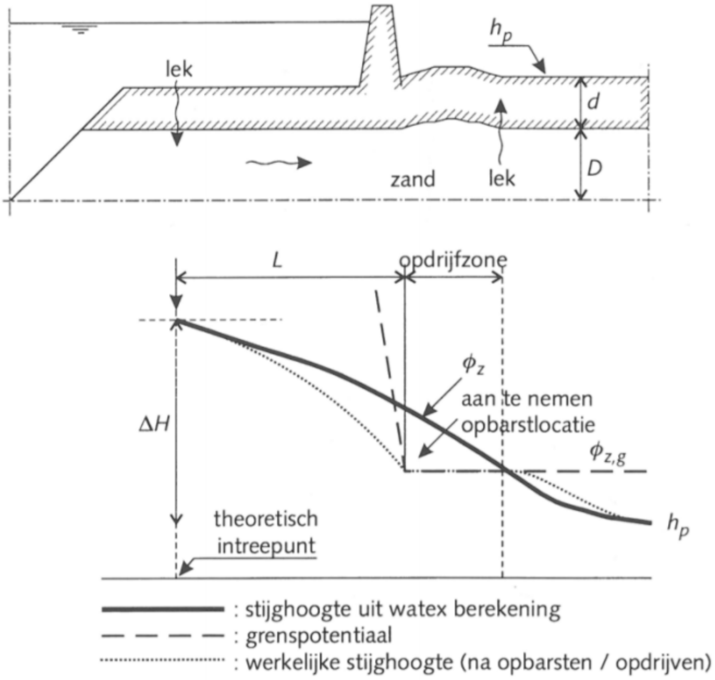

Figuur 5.1 Configuratie van een dijk met voorland en ondergrond met daarbij horende stijghoogte in zandlaag, grenspotentiaal, opbarstlocatie en opdrijfzone (voor Watex berekening, zie paragraaf 5.2.3)

Figure C.10: Potential in the sand layer in a typical uplift situation (Förster et al., 2012)

In Figure C.10 the situation is sketched for an uplift situation. In the lower graph, there are three interesting lines drawn. Firstly, the computed head in the aquifer (thick line) is gradually decreasing from the river water level to the polder water level. Secondly, the limit potential (dashed line) is drawn, which is the head at which the cover layer starts floating, i.e. equals the submerged weight of the cover layer. Thirdly, the dotted line represents the actual head after uplifting. The actual head does not exceed the limit potential.

Another factor to take into account is time-dependency, which magnitude is estimated by the hydrodynamic period. This period is related to the consolidation coefficient c_v linearly and to the thickness of the cover layer quadratically (Förster et al., 2012). In non-stationary situations, the clay layers at the foreland and hinterland have smaller leakage factors. Subsequently, the hydraulic head will be smaller at the exit point. This effect is thus larger for thicker cover layers.

The expected uplift length is used in the schematization, which depends on the length and height of the flood wave. As a rule of thumb, a first estimation is twice the cover layer thickness (Förster et al., 2012). Furthermore, comprehensive analytical solutions for the uplift length are available for stationary situations (Barends, 1999).

Other subsidiary processes which could lower the pore water pressure underneath the cover layer are:

1. Presence of a foreland, lengthening the distance thus lowering the gradient of the head over the dike body;
2. Thickness and permeability of the cover layer or sediment deposit layer at the water side of the dike, also known as 'entry resistance'. This lowers the head in the sand layer at the water side;
3. Elastic storage of water in the soil skeleton;
4. Phreatic storage in the unsaturated core of the dike;
5. Swelling of the dike material.

However, it is noted that these processes only lower the head temporarily ('t Hart, 2018).

C.3.2. BEHAVIOR OF THE COVER LAYER

The weight of the cover layer defines the strength of the cover layer against uplift. As a consequence of the excess water pressure, the cover layer can crack or burst open. Currently, there is no difference made in exceeding the vertical equilibrium and the forming of cracks. An uplifted layer is observable by weak wave-movements upon entering the uplifted zone ('t Hart, 2018). In the case when uplift occurs without cracking, the Dutch guideline now prescribes the following:

> In some cases, it is plausible that the cover layer will not crack during uplift conditions, for example with a thick cohesive cover layer. Although there is no channel through the cover layer, it does not mean that piping is ruled out. In this situation, a thin water bubble exists between the aquifer and the cover layer. Grains of sand can still be transported to this water bubble, depending on the seepage length. In this case, the head difference for the piping assessment should be taken as the difference between the river water level and the limit potential below the cover layer (Förster et al., 2012, section 6.2.8.3).

Whether a piping failure occurs under a thick, uplifted but uncracked cover layer is open for discussion. According to Förster et al. (2012), the seepage length is crucial. However, other decisive parameters in the development of a full-grown pipe are for example the size and the storage capacity of the water bubble.

The crucial point here is determining the crack forming. In the literature, this is linked to several parameters. For example, the thickness and elasticity of the cover layer are suggested ('t Hart, 2018). Also, cohesive forces and the internal stress distribution are mentioned for the uplift case (Calle, 2002).

Time-dependency is also important on the soil side of the problem. The soil behaves differently in drained and undrained conditions. From tensile test, it is observed that the behavior during undrained tests is close to the brittle character. In drained conditions, the material is more flexible and the elongation at failure larger (Vaníček, 2013).

PORE WATER PRESSURE IN COVER LAYER

The pore water pressure in the cover layer is varying from the instantaneous profile to the steady state profile, see Figure C.11. This is a time-dependent process, depending on the duration and height of the flood wave. For a typical river flood, the intrusion length is 1 to 3 meters in the Netherlands. The pore water pressure in the cover layer affects the effective stress. This is an important parameter in many strength models.

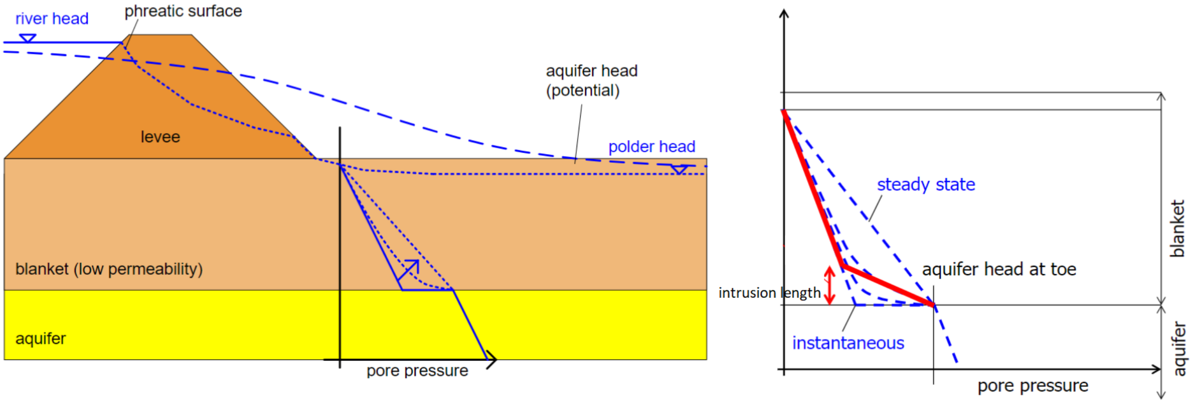

Figure C.11: Pore water distribution (Lanzafame, 2019)

C.4. CRACK-INITIATION

The modeling of crack initiation is by introducing a threshold value. In Table C.2.6, threshold values for different cases can be found. In this section, the excavation base and hydraulic fracturing case are discussed in detail, while looking for resemblance with the uplift phenomenon.

C.4.1. BEAM MODEL

The excavation base case uses the beam model, in which the cohesive cover layer is assumed to behave undrained (Hong and Wang, 2016). Due to the load induced by the water pressure in the aquifer, the layer deforms and subsequently bending moments and shear forces occur. This leads to compressive, tensile, and shear stresses. When any of these exceeds the corresponding strength component, failure occurs.

APPROXIMATION OF THE LOAD

The beam model as presented by both Hong and Wang (2016) and Šuklje et al. (1961) approximate the aquifer-aquitard interface as a straight horizontal line. Furthermore, the load is constant over time and constant along the cross-section. In the case of uplift, this equals the potential calculated by a geohydrological model. A linear relationship between the river water level and the polder water level is proposed as a first approximation.

SCHEMATIZATION OF THE BEAM

A basic analysis was carried out to determine at which location the maximum moments and shear forces occur on a cross-section described in the report *FEM Analysis on uplift* (Hoffman, 2019). Figures of the analysis are included in Section C.7. Here, the main findings are stated: The determination of the location of the end-points of the beam and thus the length is very important. It impacts the magnitude of the bending moments and shear forces greatly. Whether the beam has fixed-ends or pinned-ends does not influence the shear forces but does influence the bending moments.

CONCLUSION AND DISCUSSION

From literature, the analytical equations provide an estimation of the uplifted length (Barends, 1999), thus the length of the beam. When having a cover layer of a uniform thickness, it is proposed that the uplifted zone starts at the toe of the dike. Regarding the boundary conditions at the end of the beam, two options are possible: Firstly, both ends can be schematized as pinned-ends, if assumed the soil yields plastically. Secondly, the dike-toe can be schematized as a fixed-end, and the other end as a pin with spring. This option has more resemblance with the outcome of the FEM analysis (Hoffman, 2019).

The presented beam model has some limitations too. In the uplift case, there is a gap at the location of the aquifer-aquitard interface with water storage capabilities, which is not included in the model. This plays a role for instationary analysis. Just below the cover layer, the potential in the water gap is constant. Whether the value does or does not exceed the limit potential (Förster et al., 2012) is open for discussion. If it were never to exceed the limit potential, the layer cannot lift up in the vertical direction. The potential in the water gap influences the length of the uplift zone.

C.4.2. HYDRAULIC FRACTURING

Rising pore water pressures cause the failure of hydraulic fracturing, differently to the deformations in the beam model. The strength of the soil disappears. For saturated cohesionless soils, this occurs when the pore water pressures exceed the horizontal total stress. In cohesive layers, the undrained shear strength or the apparent tensile strength also contribute to resistance.

C.5. CRACK-DEVELOPMENT

To model the propagation of a crack, different approaches exist. Firstly, the beam model is discussed, which is frequently used for concrete modelling. For reinforced concrete, a moment-curvature plot is frequently used. Moallemi and Pietruszczak (2017) modelled the fracture development for pure concrete, see Figure C.12. When a small fracture exists, the effective thickness of the beam decreases, over which the internal stresses redistribute. A new crack will occur when an internal stress component exceeds the corresponding strength component again.

Secondly, the fracture mechanics theory is useful to model fracture propagation. Here, fracture mode 1 is applicable for tensile failure. The threshold value is the fracture toughness K_{IC}, which depends on the Poisson's ratio, elasticity modulus, and the crack energy G_c (Schick, 2003).

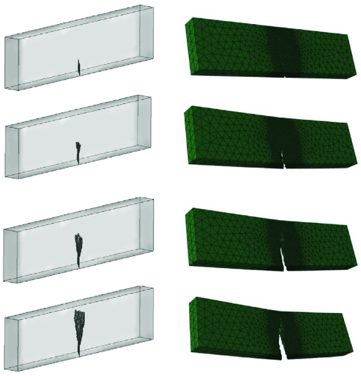

Figure C.12: Fracture development in a concrete beam (Moallemi and Pietruszczak, 2017)

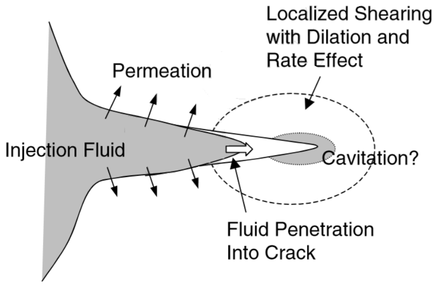

Figure C.13: Fracture propagation mechanisms in hydraulic fracturing (Mitchell and Soga, 2005)

Regarding the fracture development based on hydraulic fracturing, many processes play a role: 'It may involve plastic deformation at the crack tip, soil rate effects, penetration of injection fluid into the cracks, and permeation of injection fluid from cracks into the soil medium. If the clay is overconsolidated and saturated, the negative pore pressure generated by shearing in front of the crack could possibly lead to cavitation and dry cracks may develop in front of penetrating injection fluid' (Mitchell and Soga, 2005).

DISCUSSION

After crack initiation, the progress of crack propagation holds limited to no residual strength in growing a full crack through the cover layer. This is observed during beam test of E-grade kaolin clay:

'Shortly after the initiation of a crack on the tensile face, complete collapse occurred in the load-controlled tests, whereas in the strain-controlled tests the load was observed to decrease while the crack propagated vertically upwards into the beams. Complete collapse of the beams in the strain-controlled tests was observed once the crack had propagated through about two-thirds of the beam thickness (Thusyanthan et al., 2007)'.

Therefore, the focus lies on crack initiation and the mechanics behind crack development are neglected further on.

C.6. CONCEPTUAL MODEL

The relationships between different mechanisms leading to a crack investigated so far are shown in Figure C.14. The water pressure and the deformations are interdependent.

FIRST MODEL

The choice for the actual failure mechanism is left open, it can either be due to the water pressure below the cover layer or bending moments and shear forces.

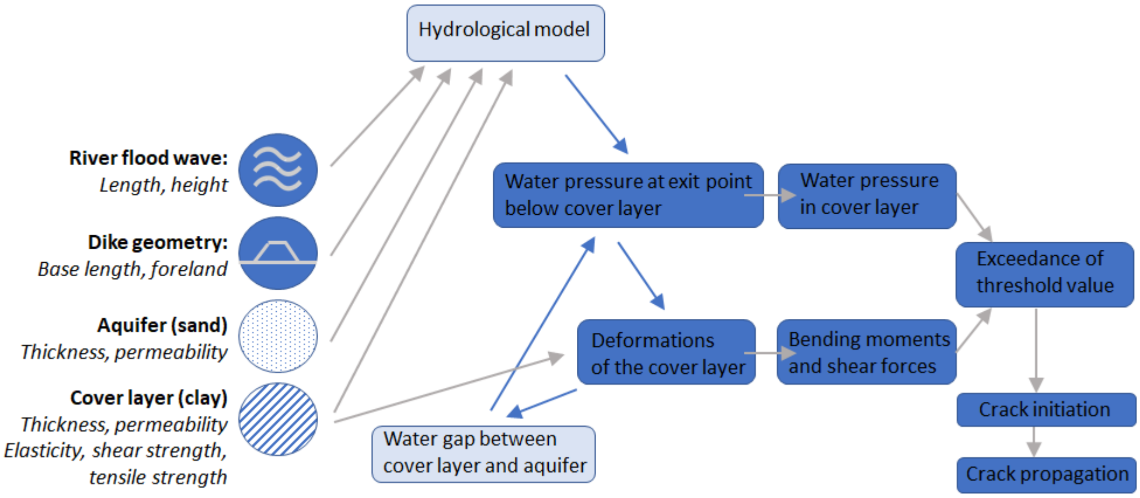

Figure C.14: Conceptual model of cracking during uplift conditions version 1

SECOND MODEL

After an expert interview with André van Hoven of Deltares, it is learned that the water pressure below the cover layer is unlikely to cause failure due to hydraulic fracturing. Hydraulic fracturing is namely based on a high pressure at a certain injection point. This pressure causes a crack, for which soil mass has to be displaced to the sides. For uplift, the load is distributed over a larger area. Hence, hydraulic fracturing is not likely the cause for failure. A better conceptual model is showed in Figure C.15.

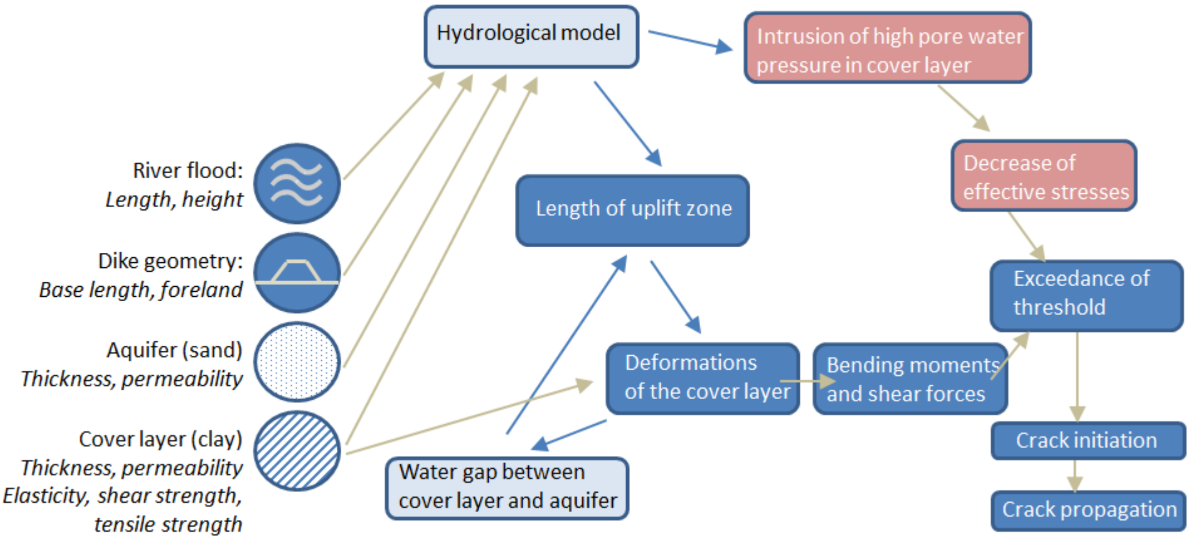

Figure C.15: Conceptual model of cracking during uplift conditions version 2

For the next step, there are a few challenges. Firstly, the threshold values need quantification: tensile strength, compressive strength, shear strength, minor principal stress, failure pressure in drained and undrained conditions. Secondly, the schematization of the beam and the load needs checking. Thirdly, the stress-strain relationship and the stress distribution of the cover layer must be determined.

Time dependency is not mentioned in the model explicitly. However, this also contributes to higher safety in regions with thick cover layers. When the flood wave is relatively short to the hydrodynamic period, the water pressure at the exit point does not reach the expected stationary value. Therefore, the cover layer is possibly not subject to uplift.

C.6.1. INFLUENCE OF TIME

The real-world uplift problem is time-dependent. It starts with the hydrological model, translating a river flood to piezometric heads underneath the blanket layer. The head at the exit point contains a time lag relative to the river flood wave. Also, the shape of the flood wave is flattened out and the peak value is decreased. This transient flow is captured by transient geohydrological modelling packages. The analytical Dupuit equations are based on steady-state flow.

At the soil side of the problem, time-dependent behavior also plays a role. The main aspects are discussed below:

PORE WATER DISTRIBUTION

The pore water pressure in the cover layer varies from the instantaneous profile to the steady state profile, see Figure C.11. The change by pore pressure is described by the 1D analytical consolidation, see Equation C.1.

$$\frac{\delta p}{\delta t} = c_v \frac{\delta^2 p}{\delta z^2} \tag{C.1}$$

For a typical river flood in the Netherlands, there are conservative limits set for the intrusion lengths. For lakes and rivers, this value is set as 3 meters. For sea dikes and rivers influenced by the tide, this value is 1 meter (TAW, 2004). The pore water pressure in the cover layer affects the effective stress. This is an important parameter in many strength models. Also, it affects the hydraulic conductivity.

An analytical solution of C.1 is derived, for a step-increase of the pore water pressure. The intrusion length is approximated by equation C.2. Subsequently, the cover layer can be treated as a two-layer system: the upper layer being just the original layer with original parameters, and the lower layer having a fictive permeability as given in Equation C.3. $s[-]$ here is the stationary part of the pore water pressure distribution over the cover layer (TAW, 2004).

$$L_i \approx 4\sqrt{c_v(t-t_0)} \tag{C.2}$$

$$k_i = \frac{k_{cover} L_i s}{D_{cover}(1-s)} \tag{C.3}$$

HYDRODYNAMIC PERIOD

The hydrodynamic period is linked to the degree of consolidation. The hydrodynamic period is a dimensionless parameter given by $T = c_v * t/h^2$, in which c_v is the coefficient of consolidation (m^2/s), t is loading time/time at measurement (s) and h is the drainage length (m). In Figure C.16 some limits are indicated for which a problem is considered fully drained or fully undrained (Brinkgreve, 2019).

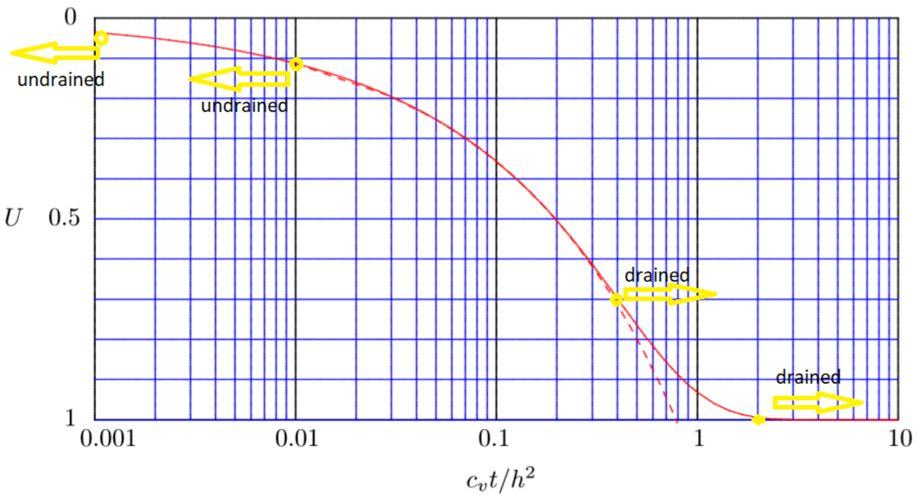

Figure C.16: Degree of consolidation (Verruijt and Van Baars, 2007) (adapted)

C.7. APPENDIX C.I: SCHEMATIZATION OF THE BEAM

The cross-section of the dike is shown in Figure C.17. The cover layer is 3 meters thick. The head difference between the river water level and the polder water level is 6 meters, over a horizontal length of 160 m.

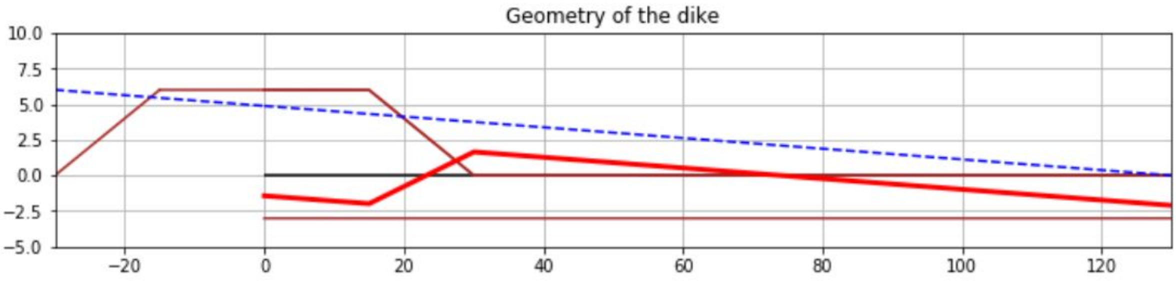

Figure C.17: Geometry of the dike

The goals was to obtain knowledge about the bending moments, shear forces, and the most likely failure mechanism of these two. Therefore, three options regarding boundary conditions were considered, see Figure C.18.

The moments and shear forces were subsequently solved using analytical equations. Next, the moment was translated into a tensile stress, assuming $\sigma = M/W = M/(1/6 * D^2)$ and similarly for the shear stress $\tau = V/D$. Other assumptions here are that the material behaves elastically and the stress distribution is symmetric.

Lastly, there are two unknowns which are treated as variables. These are the length of the schematization and the beginning point. Different lines are used with different begins. Below are the outcomes for a length of 6, 20 and 51 meters with pinned ends at both sides.

The threshold value is displayed as a dotted line. As a first approximation, the shear strength is assumed to equal the effective cohesion of clay; 16 kPa. The tensile strength of clay is taken as half of the shear strength; 8 kPa. From Figures C.19 to C.21, it is most likely that the tensile strength is exceeded first.

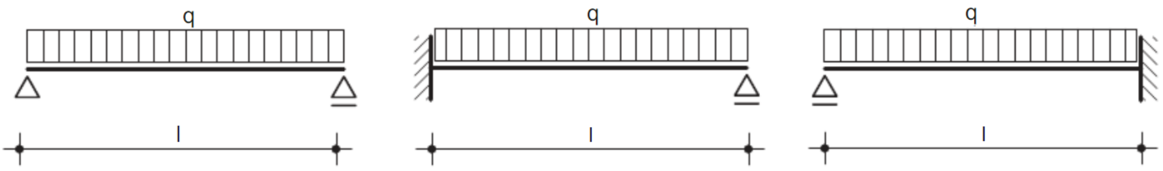

Figure C.18: Schematization

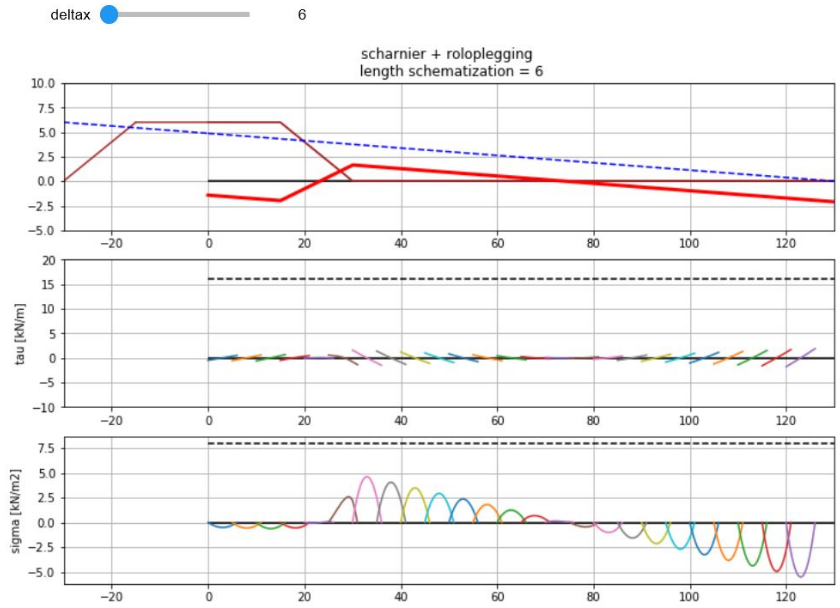

Figure C.19: Schematization with length 6 m

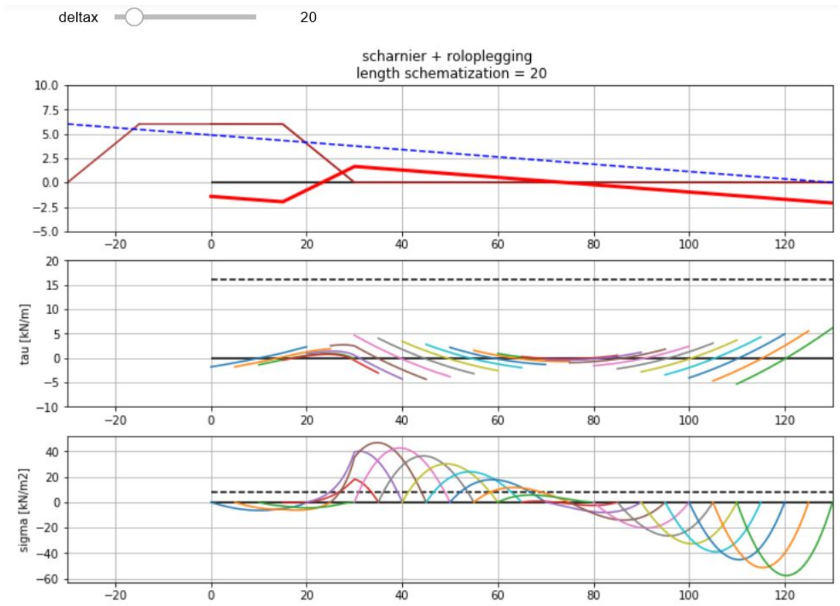

Figure C.20: Schematization with length 20 m

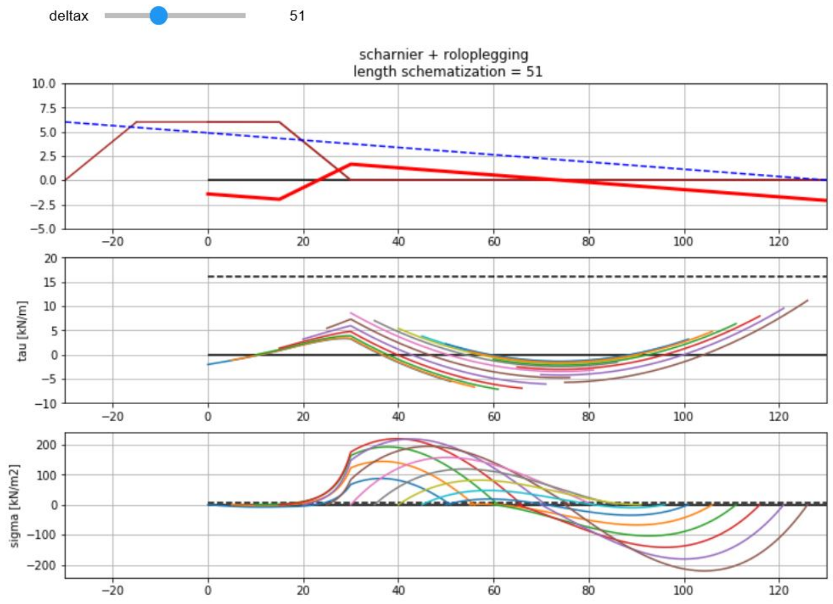

Figure C.21: Schematization with length 51 m

D

GEO-HYDROLOGICAL ANALYSIS FOR THE UPLIFT ZONE

D.1. INTRODUCTION

This Appendix discusses the geo-hydrological side of the problem. It tries to find the load on the uplift zone during floating conditions, as well as the exact length of the uplifted area. Section D.1.1 summarizes the main points of the beam model. Then, the theoretical model by Barends is discussed. The second part of this Appendix contains the finite difference (FD) model and its outcomes.

D.1.1. BEAM MODEL (EXCAVATION BASE CASE)

If uplift were treated as an excavation base, the upward load is the pressure in the aquifer minus the downward pressure by the weight of the cover layer. After this analysis, the most important outcomes are:

- The length of the beam plays a great role in the maximum moment, shear forces and corresponding stresses;
- The schematization of the end-points of the beam influence the maximum value of the moments. Applying both fixed or spring-pin ends are most suitable;
- Failure due to stresses induced by moments is more likely than by shear forces (for constant cover layer thickness).

However, this beam model cannot be applied directly on the uplift case. There is a difference in the load profile: for the excavation, the pressure in the aquifer is constant. For the uplift case, it decreases with increasing distance from the river. When uplift occurs, a water gap forms between the aquifer and the cover layer and a hydraulic shortcut is present. .

D.2. THEORY: ANALYTICAL MODEL BY BARENDS

Barends (1999) provides a set of analytical equations for the length of the uplift zone, to be found in Figure D.1.

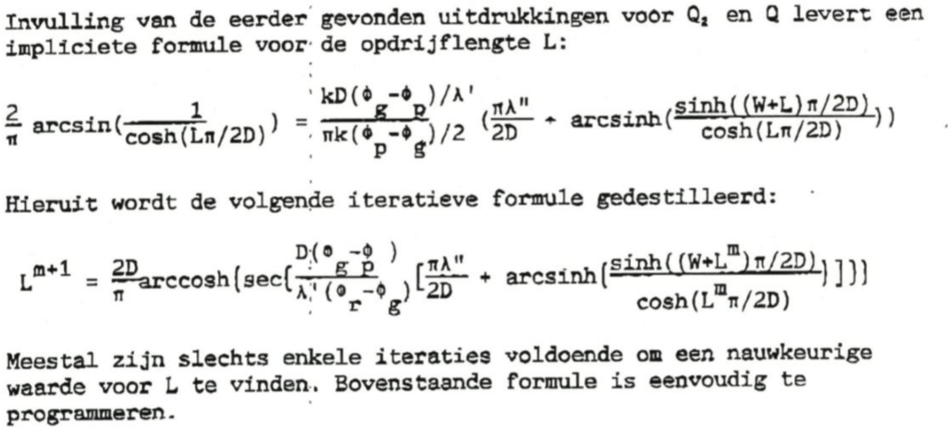

Invulling van de eerder gevonden uitdrukkingen voor Q_2 en Q levert een impliciete formule voor de opdrijflengte L:

$$\frac{2}{\pi}\arcsin\left(\frac{1}{\cosh(L\pi/2D)}\right) = \frac{kD(\phi_g-\phi_p)/\lambda'}{\pi k(\phi_p-\phi_g)/2}\left(\frac{\pi\lambda''}{2D} + \operatorname{arcsinh}\left(\frac{\sinh((W+L)\pi/2D)}{\cosh(L\pi/2D)}\right)\right)$$

Hieruit wordt de volgende iteratieve formule gedestilleerd:

$$L^{m+1} = \frac{2D}{\pi}\operatorname{arccosh}\left\{\sec\left\{\frac{D(\phi_g-\phi_p)}{\lambda'(\phi_r-\phi_g)}\left[\frac{\pi\lambda''}{2D} + \operatorname{arcsinh}\left(\frac{\sinh((W+L^m)\pi/2D)}{\cosh(L^m\pi/2D)}\right)\right]\right\}\right\}$$

Meestal zijn slechts enkele iteraties voldoende om een nauwkeurige waarde voor L te vinden. Bovenstaande formule is eenvoudig te programmeren.

Figure D.1: Analytical formula for uplift length (Barends, 1999)

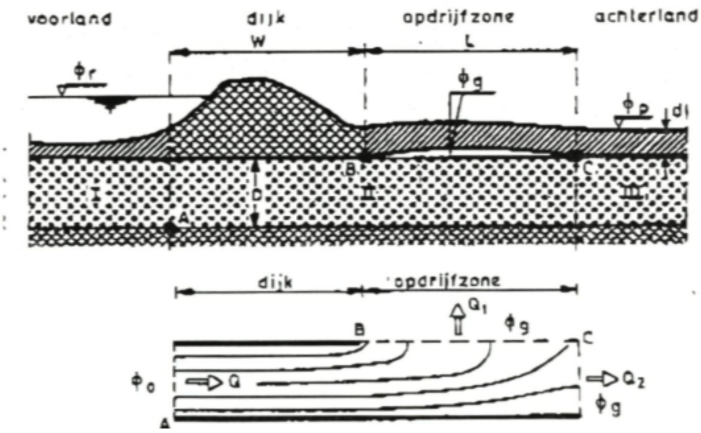

Figure D.2: Sketch of situation with uplift zone and hydraulic boundary conditions (Barends, 1999)

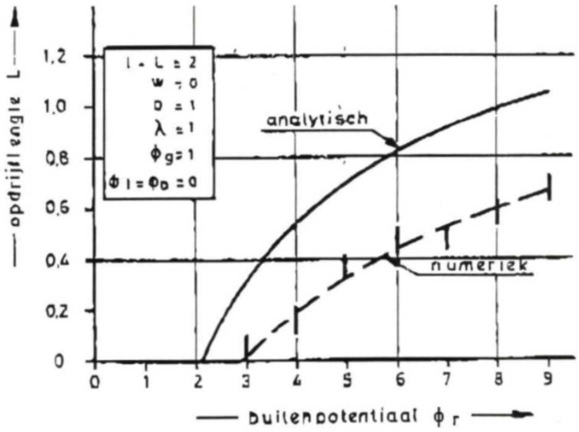

Figure D.3: Outcome of analytical and numerical method (Barends, 1999)

The key assumptions for the hydrological boundary conditions are:

- At the aquifer-aquitard interface in the uplift zone, and at x(*end of uplift zone*), the head equals the critical head ϕ_g (see Figure D.2);
- The critical head ϕ_g equals the weight of the cover layer, that is $D * \gamma_{sat}$ (based on total stress equilibrium).

Both statements above about the assumptions are refutable:

- Barends (1999) states: '*However, a rigorous assumption has been made regarding the transition from the uplift zone ('opdrijfzone') to the hinterland ('achterland'). Here, a constant potential is assumed vertically at the end of the uplift zone. In reality, the potential there is not constant over the height. The effect of this assumption can be viewed with a different solution method: variational inequalities.*'

  A better method is thus solving the problem numerically, for example with a FEM program. When comparing the numerical solution to the analytical solution, it is concluded that the analytical approach overestimates the length of the uplift zone by 25% to 100% (see Figure D.3).

- Assuming $\phi_g = D * \gamma_{sat}$ means that the cover layer is buoyant. However, $\phi_g > D * \gamma_{sat}$ must be in place, for the cover layer to deform and lift up.

The main conclusion here is that this problem has a non-linear character: '*An increase in the river level does lead to an increase in L, but not in the same proportion.*' (Barends, 1999).

D.3. METHOD: NUMERICAL FD APPROACH

The basic description of the groundwater flow is done using a partial differential equation. 1D analytical solutions exist, but a numerical approach is needed for a 2D analysis. In the finite difference (FD) model, the discretization is based on a rectangular grid. Also, the used approach is treating both the length and the load as unknowns. These two parameters are linked: If a flood wave arrives and disturbs the heads in the aquifer, both the head and the length of the uplift zone will increase simultaneously. With instationary situations, the potential in the uplift zone exceeds the limit potential from time to time. It is also possible using FD coding to compute the head in the uplift zone, given a certain length of the uplift zone. The length of the uplift zone is resembled by defining a hydraulic shortcut in the hydraulic conductivity field of exactly that length. Furthermore, this analysis is carried out based on material properties and geometries based on Hoffman (2019).

D.4. PYTHON NOTEBOOK

D.4.1. MODEL SET-UP

Import Python packages

```
%matplotlib inline
import numpy as np
import matplotlib.pyplot as plt
from matplotlib.colors import LogNorm
from scipy.sparse import diags
from scipy.sparse.linalg import spsolve
import statistics
```

Define functions for finite difference flow function (Bakker, 2019).

```
#functions to help with plotting
def xycenter(L, W):     # Center of lower left-hand cell is (0,0)
    dx = 0.5 * (L[:-1] + L[1:])
    x = np.hstack((0, np.cumsum(dx)))
    dy = 0.5 * (W[:-1] + W[1:])
    y = np.hstack((0, np.cumsum(dy)))
    y = y[::-1]
    return x, y
def xygrid(L, W):     # Center of lower-left hand cell is (0,0)
    xg = np.hstack((0, np.cumsum(L))) - 0.5 * L[0]
    yg = np.hstack((0, np.cumsum(W)))
    yg = yg - 0.5 * W[0]
    return xg, yg

def fdflow(nc, nr, L, W, k, H, Q, Fh):
    T = k * H
    W = W[:, np.newaxis]
    C = np.zeros((nr, nc))
    C[:, :-1] = W * 2 * T[:, :-1] * T[:, 1:] / (
                T[:, 1:] * L[:-1] + T[:, :-1] * L[1:])
    D = L * 2 * T[:-1, :] * T[1:, :] / (
        T[1:, :] * W[:-1] + T[:-1, :] * W[1:])
    C = C.ravel()[:-1]
    D = D.ravel()
    if len(D) == 0: #1D system
        A = diags([C, C], [1, -1], format='csr')  # model with 1 row
    else:
        A = diags([C, C, D, D], [1, -1, nc, -nc], format='csr')
    A -= diags(A.sum(1).A1, 0)
    rhs = -Q.ravel()
    fixed = np.flatnonzero(~np.isnan(Fh))
    i, j = A[fixed].nonzero()
    A[fixed[i], j] = 0
    A[fixed, fixed] = 1
    rhs[fixed] = Fh.ravel()[fixed]
    h = spsolve(A, rhs)
    h.shape = (nr, nc)
    return h
```

Input parameters

```
#constants geometry
L0 = 220 #m is total length of inspection
x4, y4 = 19, L0 #15 meter diep, 130 meter breed
```

```
#location of top of the cover layer
xL1 = 15 #first section goes from x=0 to x=15
xL2 = 30 #second section goes from x=15 to x=30
slope = 2.5 #for a slope 1:2.5

#cell sizes definition
H4 = 1 #m
L4, W4 = 0.5, 0.5 #length, width of a cell

#heads
hfixedwest = 5 #m #polder potential
hfixedeast = 0 #m #river potential
#gap
gap_left = 30
gap_right = 50

#thickness
L_c = 2 #m thickness of cover layer
L_s = 10 # m thickness of sand layer
#hydraulic conductivity
k_water = 1e10 #m/d
k_c = 0.087 # 1e-10*24*3600
k_s = 8.64 #1e-3*24*3600
#volumetric weight
y_water = 10
y_soil = 17

print ('The␣leakage␣factor␣equals', np.sqrt(k_s*L_s*L_c/k_c) )
print(np.sqrt(k_s*L_s*L_c/k_c)*5)
```

Calculations, input

```
nr4 = np.int(x4/L4)+1 #number of rows
nc4 = np.int(y4/W4)+1 #number of columns
W = W4*np.ones(nr4)
L = L4*np.ones(nc4)
Q4 = np.zeros((nr4, nc4))
Fh4 = np.full((nr4, nc4), np.nan)
Fh4[:, 0] = hfixedwest
Fh4[:, -1] = hfixedeast #river at the east
nnr = int(L_c/L4) #number of cells within the clay layer
nnc = int(L_s/L4) #number of cells within one sand layer
```

Make plot for hydraulic conductivity field

```
#make plot for hydraulic conductivity field
xk1 = np.ones((nr4,nc4))*k_water
xk1[int(x4/W4)-nnc:,:] = k_s
xk1[int(x4/W4)-nnc-nnr:int(x4/W4)-nnc,:] = k_c
xk1[int(x4/W4)-nnc-nnr:int(x4/W4)-nnc,:1] = k_s
xk1[int(x4/W4)-nnc-1:int(x4/W4)-nnc,
        np.int(gap_left/W4):np.int(gap_right/W4)] = k_water
xk1[int(x4/W4)-nnc-nnr-1:int(x4/W4)-nnc-nnr,
        np.int(gap_left/W4):np.int(gap_right/W4)] = k_c
for i in range(int(x4/W4)-nnc-nnr):
    xk1[inCoCom(x4/W4)-nnc-nnr-i-1,:np.int(gap_left/W4)-np.int(i*slope)+1] = k_c
xk1[:int(x4/W4)-nnc,:1] = k_s
plt.matshow(xk1, norm=LogNorm(), vmin = 1e1, vmax= 1e2)
```

```
plt.suptitle('hydraulic␣conductivity␣field␣(m/d)', y=1)
plt.xlabel('column␣number')
plt.ylabel('row␣number')
plt.colorbar()#ticks=[k_lucht, k_c, k_s, k_water], shrink=0.8) #log scale
plt.clim(1e−10, 1e10)
```

D.4.2. COMPUTING HEAD AND PLOTTING FIGURES

Compute head

```
h4a = fdflow(nc4, nr4, L, W, xk1, H4, Q4, Fh4)
x, y = xycenter(L, W)
```

Plot potential lines (large)

```
plt.figure(figsize=((30, 10)))
plt.subplot(121)
cs = plt.contour(x, y, h4a, 50, cmap='jet')
plt.clabel(cs, fmt='%1.1f')
plt.axis('scaled')
plt.title('Contour␣plot␣for␣the␣head␣(m)')
plt.xlabel('x−coordinate␣(m)')
plt.ylabel('y−coordinate␣(m)')
plt.colorbar(shrink=0.2)
# add the grid
xg, yg = xygrid(L, W)
ax = plt.gca()
ax.xaxis.set_ticks(xg, minor=True);
ax.yaxis.set_ticks(yg, minor=True);
plt.grid(which='minor')
plt.xlim(xg[0], xg[−1])
plt.ylim(yg[0], yg[−1]);
```

Plot potential lines (detailed)

```
plt.figure(figsize=((20, 10)))
plt.subplot(121)
cs = plt.contour(x, y, h4a, 100, cmap='jet')
plt.clabel(cs, fmt='%1.2f')
plt.axis('scaled')
plt.title('Contour␣plot␣for␣the␣head')
plt.xlabel('x−coordinate␣(m)')
plt.ylabel('y−coordinate␣(m)')
plt.clim(1,3)
plt.colorbar(shrink=0.35)
# add the grid
xg, yg = xygrid(L, W)
ax = plt.gca()
ax.xaxis.set_ticks(xg, minor=True);
ax.yaxis.set_ticks(yg, minor=True);
plt.grid(which='minor')
plt.xlim(15,65)
```

Plot head at different depths in the aquifer

```
fig = plt.figure(figsize=(10, 7))
plt.subplot(211)
plt.ylim(−3,10)
plt.grid()
```

```
plt.title('Geometry␣of␣the␣dike')
plt.xlabel('x-coordinate␣(m)')
plt.ylabel('y-coordinate␣(m)')
plt.plot(x, np.ones(len(x))*L_c*-1, 'brown')
plt.hlines(0,0,L0)
plt.plot(x[0:(xL1*2+1)], 6*np.ones(len(np.zeros(len(x))[0:(xL1*2+1)])), 'brown')
plt.plot(x[(xL1*2):(xL2*2+1)], xL1*2/slope-x[(xL1*2):(xL2*2+1)]/slope, 'brown')
plt.annotate(s='', xy=(xL2,8), xytext=(0,8),
        arrowprops=dict(arrowstyle='<->'))
plt.text(5,8.2, 'dike␣body')
plt.annotate(s='', xy=(gap_left,8), xytext=(gap_right,8),
        arrowprops=dict(arrowstyle='<->'))
plt.text(gap_left,8.2, 'uplift␣zone')
plt.annotate(s='', xy=(L0,8), xytext=(gap_right,8),
arrowprops=dict(arrowstyle='<->'))
plt.text(gap_right+50,8.2, 'no␣uplift')
plt.subplot(212)
Nrs =  np.arange(9+8,15+8)
for i in range(len(Nrs)):
    plt.plot(x,h4a[Nrs[i]], linewidth = 1, label='row␣number:␣'+str(Nrs[i]))
plt.xlabel('Distance␣from␣mid-dike␣(m)')
plt.ylabel('Head␣(m)')
plt.title('Computed␣head␣using␣FD␣at␣different␣depths')
plt.annotate(s='', xy=(xL2,0.8), xytext=(0,0.8),
        arrowprops=dict(arrowstyle='<->'))
plt.text(0,0.88, 'confined␣flow')
plt.annotate(s='', xy=(gap_left,0.8), xytext=(gap_right,0.8),
        arrowprops=dict(arrowstyle='<->'))
plt.text(gap_left,0.5, 'constant␣\n␣head')
plt.annotate(s='', xy=(L0,0.8), xytext=(gap_right,0.8),
        arrowprops=dict(arrowstyle='<->'))
plt.text(gap_right+50,0.88, 'semi-confined␣flow')
plt.grid()
plt.legend()
plt.subplots_adjust(left=None, bottom=None, right=None, top=None,
        wspace=None, hspace=0.4)
```

Function to determine head in uplift zone

```
def uplifthead(Lgap, hriver = 5, gap_left = 30):
    gap_right = gap_left+Lgap
    k_new = hydr_c(Lgap=Lgap, gap_left=gap_left, L0=220,
            k_s=k_s, k_c=k_c, k_water=k_water)
    hfixedwest = hriver #m
    Fh4[:, 0] = hfixedwest
    h4a = fdflow(nc4, nr4, L, W, k_new, H4, Q4, Fh4)
    return h4a[20]
```

Plot head, for equal uplift head and different river water levels

```
plt.figure(figsize=(10,5))
hr_range = np.linspace(5,10,11)
L_g_range = [0,0,0,6,13,23,31,40,48,57,65]

colours = ['r', 'tomato', 'orange', 'gold', 'lime', 'darkgreen',  'cyan',
        'blue',  'purple', 'fuchsia', 'k']
plt.subplot(121)
for i in range(len(hr_range)):
    plt.plot(x, uplifthead(L_g_range[i], hriver = hr_range[i]), color = colours[i],\\
            label = 'hr:␣'+str(hr_range[i]) +'␣m' )
plt.grid()
plt.axhline(L_c*17/9.81, label='limit␣potential')
plt.xlabel('x-coordinate␣(m)')
plt.ylabel('Head␣(m)')
#plt.xlim(0,220)
#plt.ylim(0,8)
plt.legend()
plt.subplot(122)
plt.plot(hr_range, L_g_range, 'ko')
plt.grid()
plt.xlabel('Head␣at␣x=0␣(m)')
plt.ylabel('Length␣of␣uplift␣zone␣(m)')
#plt.plot((6,10), (0, 65))
plt.xlim(4.8,10.5)
plt.ylim(0,200)
plt.suptitle('Length␣of␣uplift␣zone␣for␣Dupuit␣flow')
```

Function to determine head at top of aquifer

```
def headupliftzone1(h_river, Lgap=20, gap_left=30, L0=220,
        k_s=k_s, k_c=k_c, k_water=k_water):
    hfixedwest = h_river #m
    y4 = L0
    x4, L4, W4, H4 = 19, 0.5, 0.5, 1 #total depth, length cell, widt cell
    nr4 = np.int(x4/L4)+1 #number of rows
    nc4 = np.int(y4/W4)+1 #number of columns
    W = W4*np.ones(nr4)
    L = L4*np.ones(nc4)
    Q4 = np.zeros((nr4, nc4))
    Fh4 = np.full((nr4, nc4), np.nan)
    Fh4[:, 0] = hfixedwest #river at the east
    Fh4[:, -1] = hfixedeast
    nnr = int(L_c/L4) #number of cells within the clay layer
    nnc = int(L_s/L4) #number of cells within one sand layer
    xk0 = hydr_c(Lgap=Lgap, gap_left=gap_left, L0=L0,
```

```
            k_s=k_s, k_c=k_c, k_water=k_water)
    h4a = fdflow(nc4, nr4, L, W, xk0, H4, Q4, Fh4)
    x_roi = x[np.int(gap_left/W4):np.int((gap_left+Lgap)/W4)]
    h_layer = h4a[18]
    return h_layer
```

Function to determine head in uplift zone

```
plt.figure(figsize=(10,5))
plt.subplot(121)
plt.suptitle('Length␣of␣uplift␣zone␣for␣fixed␣outer␣head')
plt.grid()
L_g_range = np.linspace(5,90,34)
plt.xlabel('x-coordinate␣(m)')
plt.ylabel('Head␣(m)')
for i in range(len(L_g_range)):
    plt.plot(x, headupliftzone1(h_river=8, Lgap=L_g_range[i], gap_left=30, L0=220,\\
    k_s=k_s, k_c=k_c, k_water=k_water))
plt.axhline(L_c*17/9.81)
plt.subplot(122)
plt.grid()
h_range = []
for i in range(len(L_g_range)):
    h_range.append(headupliftzone(h_river=8, Lgap=L_g_range[i], gap_left=30,
            L0=220, k_s=k_s, k_c=k_c, k_water=k_water))
plt.plot( L_g_range, h_range,  'ko' )
plt.axhline(L_c*17/9.81)
plt.ylabel('Head␣at␣x=0␣(m)')
plt.xlabel('Length␣of␣uplift␣zone␣(m)')
```

Plot head, for different uplift heads, and same river water levels

```
plt.figure(figsize=(10,5))
plt.subplot(121)
plt.suptitle('Length␣of␣uplift␣zone␣for␣fixed␣outer␣head')
plt.grid()
L_g_range = np.linspace(5,90,34)
plt.xlabel('x-coordinate␣(m)')
plt.ylabel('Head␣(m)')
for i in range(len(L_g_range)):
    plt.plot(x, headupliftzone1(h_river=8, Lgap=L_g_range[i], gap_left=30, L0=220,
        k_s=k_s, k_c=k_c, k_water=k_water))
plt.axhline(L_c*17/9.81)
plt.subplot(122)
plt.grid()

h_range = []
for i in range(len(L_g_range)):
    h_range.append(headupliftzone(h_river=8, Lgap=L_g_range[i], gap_left=30,
    L0=220, k_s=k_s, k_c=k_c, k_water=k_water))
plt.plot( L_g_range, h_range,  'ko' )
plt.axhline(L_c*17/9.81)
plt.ylabel('Head␣at␣x=0␣(m)')
plt.xlabel('Length␣of␣uplift␣zone␣(m)')
```

D.5. RESULTS AND DISCUSSION

D.5.1. COMPARISON WITH BARENDS

In his previous research, Barends has obtained some results for the uplift length, see Figure D.6. The analytical solutions assume Dupuit flow underneath the dike and in the hinterland. This means the flow is predominantly horizontal. In the numerical approach based on FEM, this boundary condition is less stringent. In both approaches, the limit potential is used as a boundary condition in the uplift zone.

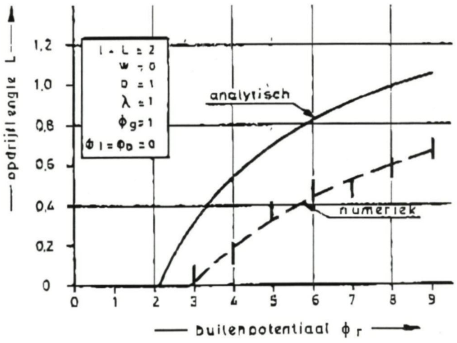

Figure D.4: Analytical and numerical outcomes to determine length of uplift zone for $\lambda = 1m$ (Barends, 1999)

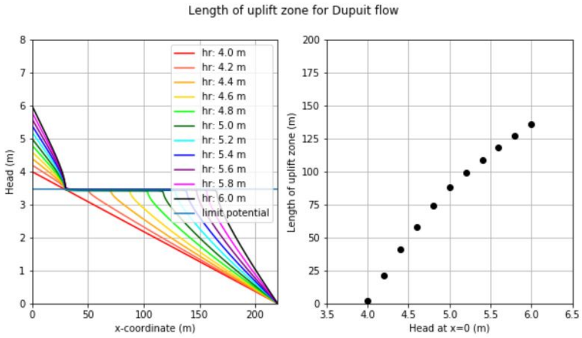

Figure D.5: Length of uplift zone for fixed head and different heads at river for $\lambda = 10000m$

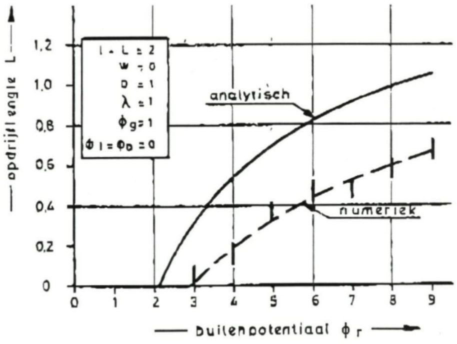

Figure D.6: Analytical and numerical outcomes to determine length of uplift zone for $\lambda = 1m$ (Barends, 1999)

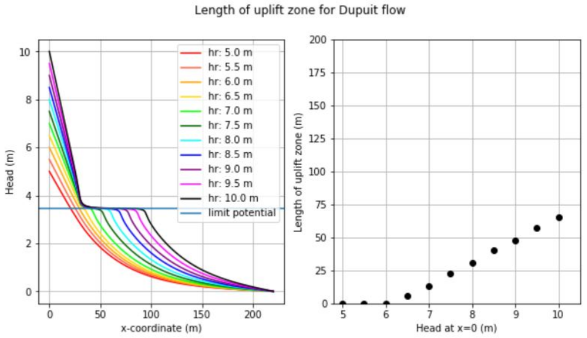

Figure D.7: Length of uplift zone for fixed head and different heads at river for $\lambda = 44.6m$

With the finite difference method the head is obtained easily for a given uplift length. With a large leakage length (see Figure D.5), the obtained solution shows similarities with the analytical solution by Barends, whereas a small leakage length (see Figure D.7) gives smaller uplift lengths, like the numerical solution in Figure D.6. Evaluating how the uplift length changes with a fixed head in the uplift zone is only done for comparison to Barends.

D.5.2. RELATION LENGTH AND LOAD

The following step is to find the uplift length based on a fixed head at x=0 instead of a fixed uplift head. For a range of predefined uplift lengths, the corresponding head at the uplift zone is computed. Figure D.8 shows the head at the top of the aquifer for various uplift lengths, as well as the relation between the uplift length and head directly. At the right, a horizontal line is plotted at 4.8 m. This equals the pressure from the self weight of the cover layer. Only points above this line resemble a situation of an uplifted cover layer.

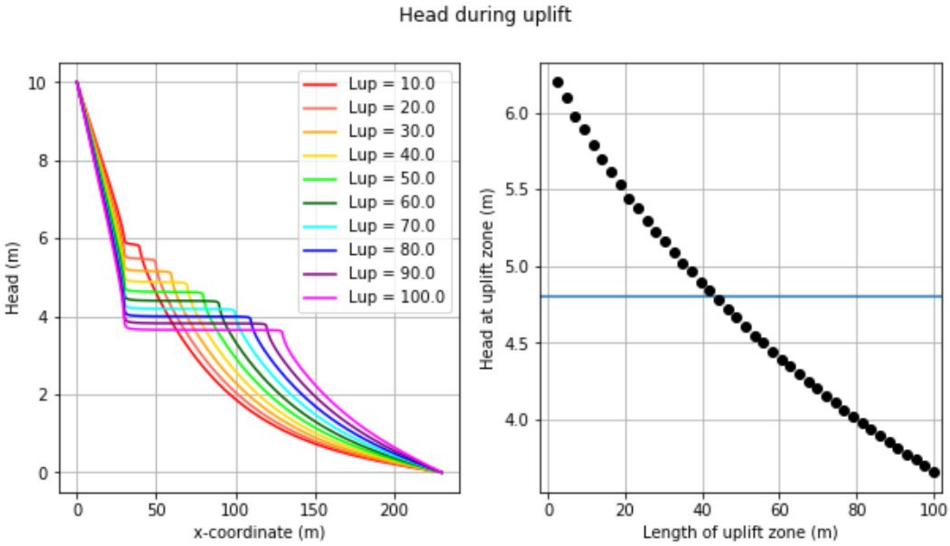

Figure D.8: Length of uplift zone for different uplift lengths and fixed river head for $\lambda = 54.7m$

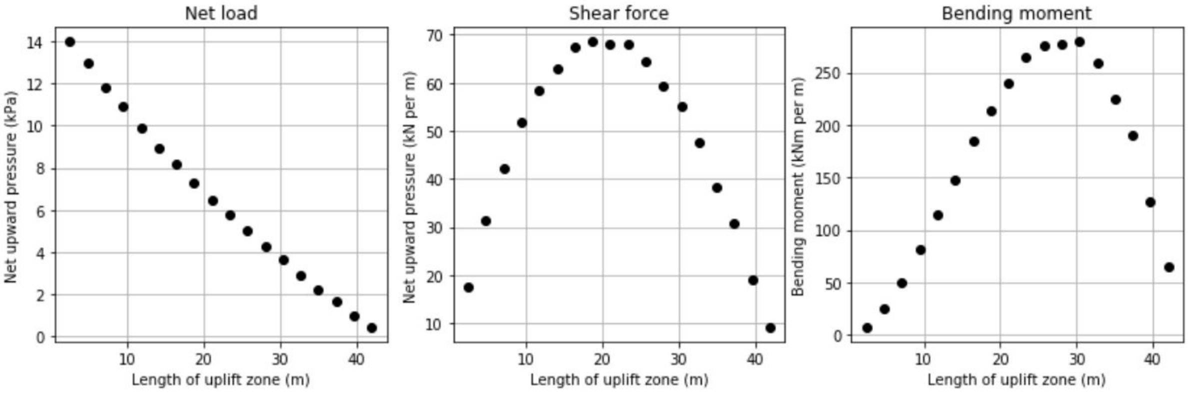

Figure D.9: Load, shear force and bending moment

Subsequently, the net load on the beam is easily obtained, by subtracting the self weight from the uplift pressure. Then, the shear force and bending moment is obtained easily, by applying basic mechanical formulas for a beam with two fixed ends. The formula for shear force is $V = 0.5 * q * L$ and for moment is $M = 1/12 * q * L^2$ All these outcomes are a range of possible lengths and heads. From this, the maximum value of this range is taken as the normative load.

In Figure D.9, the result is shown for the situation in Figure D.8. The maximum shear force occurs at an uplift length of about 20 meters, whereas the maximum bending moment is found at an uplift length of 30 meters.

VERTICAL EQUILIBRIUM

Currently, the uplift assessment only takes the self weight of the cover layer into account. However, there are shear forces which also play a role. These also counteract the water pressure forces from the aquifer. Figure D.10 shows a sketch of the forces acting in vertical direction.

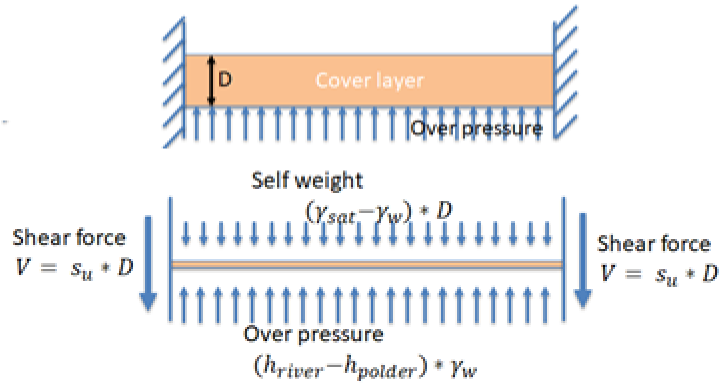

Figure D.10: Vertical equilibrium diagram

MOMENT EQUILIBRIUM

In the current assessment, moment equilibrium is not considered at all. However, horizontal stresses can develop. Figure D.11 indicates the tensile regions in the beam due to flexural loading.

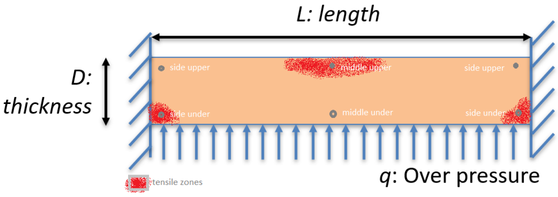

Figure D.11: Points of interest in beam including zones with tensile stresses in horizontal direction

E

INTERNAL SOIL STRESSES

The previous appendix dealt with the load and length of the beam. On the other side of the load is the resistance, which counteracts the shear force and bending moments. Therefore, the behavior of cohesive soils that make up the cover layer is discussed here. Šuklje (1969) states that only preconsolidated and cohesive soils withstand tensile loading.

This appendix focuses on the tensile side of the bending moment. This is important because it is highly probable that the bending moment is the normative load, as discussed in the previous appendix. With the beam subjected to a bending moment, horizontal tensile stresses occur. Also, the critical tensile strength is much lower than for compression.

Conducting tests help to understand material behavior. The formulation of the mechanical behavior of the soil is often in terms of a stress-strain relationship. Standard lab tests have controlled conditions for stresses and strains, which allow testing the soil behavior in a single point. Generally, the lab tests are standardized for shear and compression and not for tension (Vaníček, 2013). Tensile tests deal with the ultimate tensile stress or strain and its profiles due to a bending moment.

In concrete modeling, the modeling of the tensile side of the stress-strain relations is more advanced than in soils. It is worthwhile to discuss the concrete modelling and to compare this to the soil modelling. In Diana FEA (2017), there are several options to indicate the critical parameter which leads to cracking upon exceedance :

1. Tensile strength f_t
2. Ultimate tensile strain ϵ_u
3. Tensile fracture energy G_f in combination with crack bandwidth h

Figure E.1 shows predefined stress-strain relationships in concrete for the tensile behavior. Figure E.2 contains tensile softening relationships, which describe the behavior after the tensile peak stress. The concrete behavior in Figure E.3 is described using a Mohr-Coloumb failure criterion including a tensile cut-off. These established behavior models help with determining a suitable model for a cohesive cover layer.

The goal is to find an appropriate stress-strain relationship for the tensile domain for cohesive soils, as well as suitable values for the peak tensile strength and strain. Furthermore, the strain and stress profiles due to a bending moment are needed to calculate the bending moment resistance.

This Appendix deals with the following subjects: First, tensile test types, as well as their outcomes, are discussed and listed. Secondly, general stress-strain relationships in soils are discussed, as well as reported relations for the tensile behavior. Thirdly, the strain and stress distribution options over the depth of a beam are investigated. Lastly, some notes are added to other relevant parameters concerning the tensile capacity.

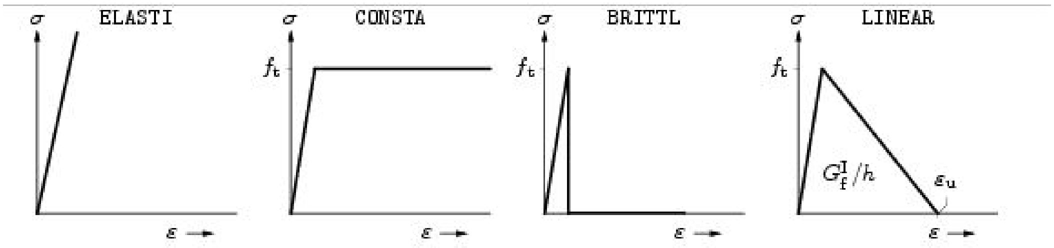

(a) elastic (b) ideal (c) brittle (d) linear

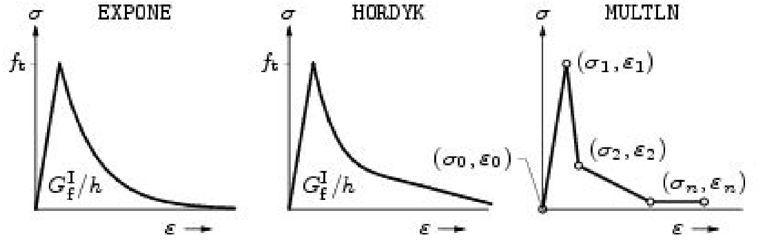

(e) exponential (f) Hordijk (g) multi-linear

Figure E.1: Tensile stress strain relationships, as predefined in Diana FEA (2017)

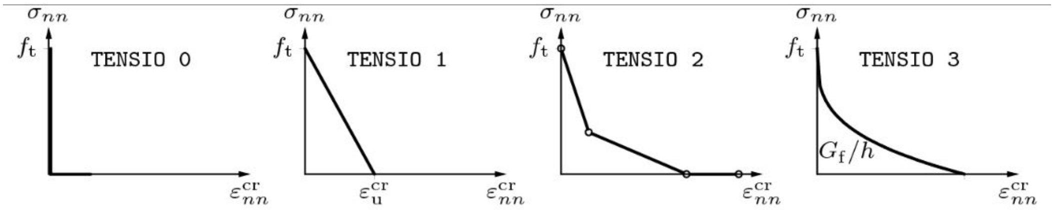

(a) brittle (b) linear, ultimate strain based (c) multi-linear (d) nonlinear, Moelands et al.

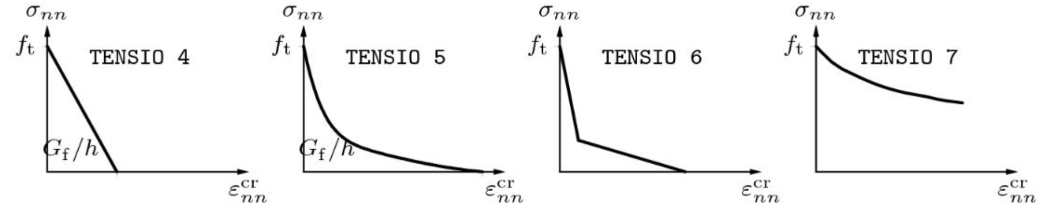

(e) linear, fracture energy based (f) nonlinear, Hordijk et al. (g) JSCE softening (h) JSCE stiffening

Figure E.2: Tension softening relationships, as predefined in Diana FEA (2017)

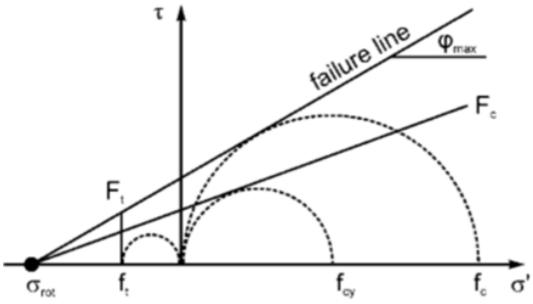

Figure E.3: Yield surfaces and failure envelope for Concrete material in Plaxis

E.1. TENSILE TESTING

This part discusses the tensile testing, starting with different types of tensile tests applicable to soils. These tests can be divided into two groups: direct and indirect testing methods. The direct tension test and the triaxial extension test measure the stresses directly, whereas the bending test, hollow cylinder test, and the Brazilian test only measure the strains. Second, the quantitative results of the tensile tests in literature are reported.

E.1.1. TENSILE TEST TYPES

In this section, the most common test types are discussed. This overview of test types is therefore incomplete. Other tensile tests, which are not discussed here, are the three-point bending test, the modified double punch test, the split tensile test, the unconfined penetration test, tensile tests in the centrifuge, and hanging cylinders (Tollenaar, 2017).

DIRECT TENSION TEST

Testing soils with only an uni-axial tensile normal stress isolates the problem. However, such as stress state is unlikely to appear in real life (Šuklje, 1969). In the test, the ends of the sample are pulled apart. The shape of the sample is cylindrical, rectangular or dog-bone shaped with expanded heads. Some challenges are encountered and overcome in various ways. To ensure an uniform tensile normal stress distribution, detailed attention is needed for the stress transmission from the test set-up to the sample. Some options are by connection clamps, nail plates, freezing, gluing, chemical stabilization, by using a trapezoidal test set up, etc. Furthermore, the effect of the self-weight is eliminated by either putting the sample on rollers or testing on a mercury surface (Helenelund, 1967; Vaníček, 2013; Tollenaar, 2017).

The deformation thus the strain is measured, using photographic recordings, together with the load or tensile stress. The direct tension test is generally considered as an undrained test. The soil behavior depends on the strain rate, thus the pull velocity (Tollenaar, 2017).

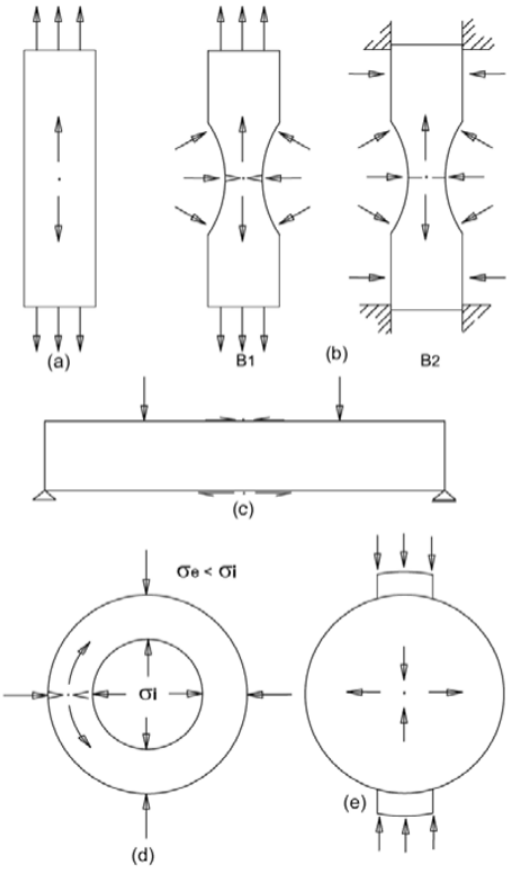

Figure 6. Division of tensile tests according to the principle of loading. a) Axial tensile tests (direct tension test). b) Triaxial tensile test. c) Bending test. d) Test on hollow cylinder. e) Indirect (Brazilian) tensile test.

Figure E.4: Schematics of tensile tests (Vaníček, 2013)

TRIAXIAL EXTENSION TEST

In the triaxial extension test, the lateral stress on the test sample is higher than the axial stress. In the triaxial cell, this is done by either increasing the lateral stress and keeping the vertical stress constant (Brinkgreve, 2019); or by keeping the lateral stress constant and relaxing the vertical stress (Vaníček, 2013).

The undrained triaxial extension test is carried out with a stiff sleeve applied to the central part of the sample (Vaníček, 2013).

BENDING TEST

A bending test is an indirect way to test the tensile strength. A four-point bending test allows the middle section of a beam to be subjected to a constant bending moment, while the shearing force is zero. The test is carried out either in a load-controlled or strain-controlled manner. The self-weight is often eliminated by using forces in equal but opposite direction, submergence in brine or testing the beam horizontally on a roller plate (Vaníček, 2013; Ajaz and Parry, 1975).

Here, also photographic recordings are used to obtain the displacement. Critical strain determines cracking (Šuklje, 1969). Some variations of the bending test also have tensiometers, pore water pressure measuring devices, in the beam (Thusyanthan et al., 2007).

This test is carried out as either a drained or undrained test. Undrained test conditions apply if the test duration is short or by applying a sample coating such as petrowax and petrolatum oil (Vaníček, 2013).

HOLLOW CYLINDER TEST

Using a soil sample in the shape of a hollow cylinder allows applying various internal and external hydrostatic pressures. Generally, the internal hydrostatic pressure is larger than the external pressure. This set-up causes the soil cylinder to dilate, with one tensile principal stress in the domain of Mohr-Coulomb stress circles.

Here, the axial strain is measured directly. With known external and internal pressures, the volume changes of the liquid give away the strains in the radial direction. Using these, the elasticity and the Poisson's ratio is determined (Šuklje, 1969). It is noted however that it is difficult to prepare undisturbed soil samples (Helenelund, 1967).

BRAZILIAN TEST

The Brazilian test is commonly known as the indirect test and often applied in rock mechanics. Sometimes, this test is used for soil samples (Vaníček, 2013; Mohammed and Vipulanandan, 2014). The sample is loaded vertically, during which horizontal tensile stresses develop.

CONCLUSION

The direct tension test and the triaxial extension test are most interesting to find accurate stress-strain relationships for the soil in a stress-state because the stresses are measured directly. On the other hand, the four-point bending test is useful to gain knowledge on the strain development and the bending moment capacity.

E.1.2. TEST RESULTS

Ajaz and Parry (1975) categorizes the results regarding tensile soil behavior into three categories:

1. Obtaining the total tensile strength, often with direct tension test under undrained conditions;
2. Obtaining the effective stress tensile strength, under drained triaxial conditions or undrained triaxial conditions with pore water pressure measurements;
3. Total stress/tensile stress-strain curves

In this section, the maximum stresses, both total and effective, and strains are reported for the tensile domain. The next section deals with the stress-strain relationships, see Tables E.1, E.2, and E.3.

CONCLUSION

There is a large difference between test results from drained and undrained tensile tests, both in terms of stresses and strains. An explanation is offered by Vaníček (2013). He states that 'the undrained tensile strength is mostly caused by capillary forces'.

Table E.1: *Tensile capacity in literature, in total stresses*

Author	Soil type	Total tensile strength	Test
Šuklje et al. (1961)	Clay (CH-CL)	40 kPa	unknown
Helenelund (1967)	Peat	3.6-11.3 kPa	Direct tensile test
Ajaz and Parry (1975)	Gault clay (CH)	30-60 kPa	Direct tensile test (strain rate controlled)
Ajaz and Parry (1975)	Gault clay (CH)	60-80 kPa	Direct tensile test (load controlled)
Ajaz and Parry (1975)	Balderhead clay (CL)	20-70 kPa	Direct tensile test (load controlled)
Tang et al. (2014)	Clay (CL)	10-90 kPa	Direct tensile test
Li et al. (2019)	Clay (CL)	20-60 kPa	Direct tensile test
Ajaz and Parry (1975)	Gault clay (CH)	50-100 kPa	Bending test
Ajaz and Parry (1975)	Balderhead clay (CL)	90-150 kPa	Bending test
Thusyanthan et al. (2007)	Remoulded clay (CL)	66 kPa	Bending test
Vaníček (2013)	Clay (CL)	15-120 kPa	Bending test
Vaníček (2013)	Clay (CL) PI>30	30-80 kPa	Bending test
Mohammed et al. (2014)	Sulfate soil (CL)	7.56 psi = 52 kPa	Indirect test

Table E.2: *Tensile capacity in literature, in effective stresses*

Author	Soil type	Effective tensile strength	Test
Bishop and Garga (Vaníček, 2013)	Clay (CL) (undisturbed)	26.3–33.3 kPa	Drained triaxial extension test
Bishop and Garga (Vaníček, 2013)	Clay (CL) (remoulded)	0 kPa	Drained triaxial extension test
Vaníček (2013)	Clay (CL) (remoulded)	3-8 kPa	Drained triaxial extension test

Table E.3: *Tensile capacity in literature, in critical strain*

Author	Soil type	Critical tensile strain	Test
Ajaz and Parry (1975)	Gault clay (CH)	0.15-0.5 %	Direct tensile test
Ajaz and Parry (1975)	Gault clay (CH)	0.05-0.3 %	Direct tensile test (load controlled)
Ajaz and Parry (1975)	Balderhead clay (CL)	0.1-0.5 %	Direct tensile test (load controlled)
Wang et al. (2007)	Clay (CL)	0.539 %	Direct tensile test
Li et al. (2019)	Clay (CL)	0.4 - 1.1 %	Direct tensile test
Bishop and Garga (Vaníček, 2013)	Clay (CL) (undisturbed)	2.19–16.7 %	Drained triaxial extension test
Vaníček (2013)	Clay (CL) (remoulded)	2–6 %	Drained triaxial extension test
Vaníček (2013)	Clay (CL) (remoulded)	0.2–0.6 %	Undrained bending test
Ajaz and Parry (1975)	Gault clay (CH)	0.6–1.6 %	Bending test
Ajaz and Parry (1975)	Balderhead clay (CL)	0.16–1.6 %	Bending test
Thusyanthan et al. (2007)	Remoulded clay (CL)	1.5-4 %	Bending test

E.2. STRESS STRAIN RELATIONSHIPS

This section contains two parts. In the first part, the theory regarding stress-strain relationships is discussed, which starts with the simplest relations. In the second part, the stress-strain results from tests are gathered. This section concludes by comparing the stress-strain results with the stress-strain relationships from theory and tensile softening methods from concrete modeling.

E.2.1. TYPES OF STRESS-STRAIN MODELLING

LINEAR ELASTIC

In an elastic model, the deformations are reversible. The material responds to stresses by deforming and returns to the original form if the stress is taken away. In a linear elastic model, the strain increment divided by the stress increment is constant. The stress-strain relationship is thus a straight line.

LINEAR ELASTIC - PERFECTLY PLASTIC

The linear elastic model can be extended by introducing a yield point. If the stress and strain pass this point, the deformations become plastic and are irreversible. In a linear elastic - perfectly plastic model, the plastic domain of the stress-strain relationship is represented by a straight horizontal line.

The Mohr-Coulomb failure criterion is a formulation of a plasticity formulation.

OTHER STRESS STRAIN RELATIONSHIPS

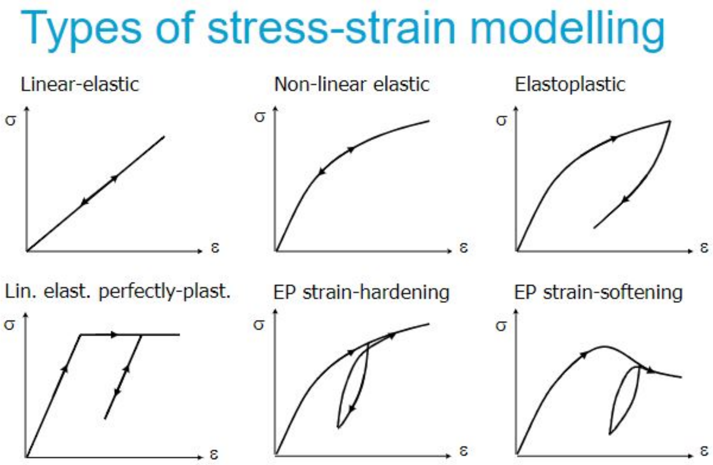

Figure E.5: Stress strain relationships (Brinkgreve, 2019)

Figure E.5 shows the common stress-strain relations. In some options, the linear elasticity is non-linear. If the unloading curve is the same as the (re)loading curve, the behavior is elastic. If not; it is elastoplastic. Furthermore, there is a difference between elastoplastic strain-hardening and strain-softening, which depends on stress history, preconsolidation, and state.

E.2.2. REPORTED TENSILE STRESS-STRAIN CURVES

Here, stress-strain curves from testing are summarized. The focus lies on direct tensile tests and triaxial extension tests, as these were found most useful in Section E.1.1 Tensile test types.

DIRECT TENSILE TEST (UNDRAINED)

Figure E.6 contains stress-displacement curves for different water contents at the direct tensile test. It is noted that the curve until the peak tensile stress is linear for four out of six tests.

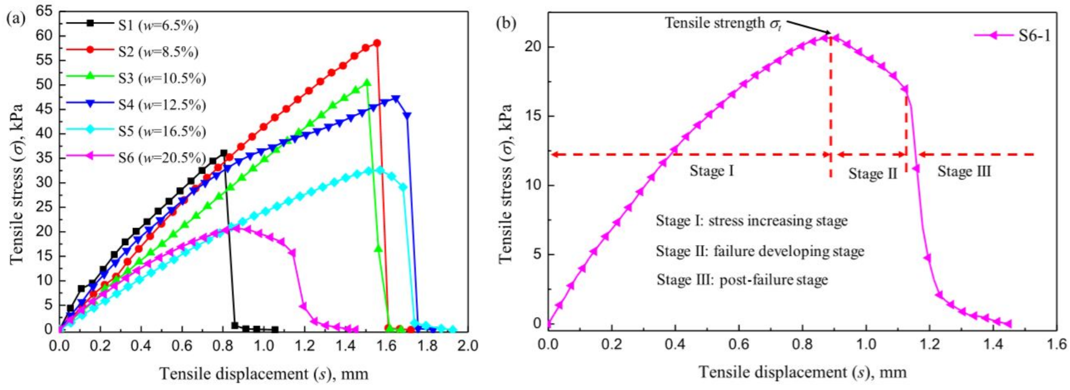

Fig. 6. (a) Typical tensile curves of samples with different water contents, and (b) typical three stages of the tensile curve ($w = 20.5\%$).

Figure E.6: Stress-displacement curves for direct tensile tests (Li et al., 2019)

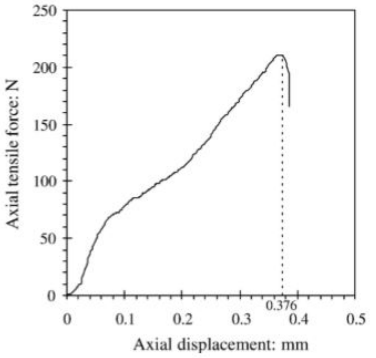

Figure E.7: Direct tensile tests (Wang et al., 2007)

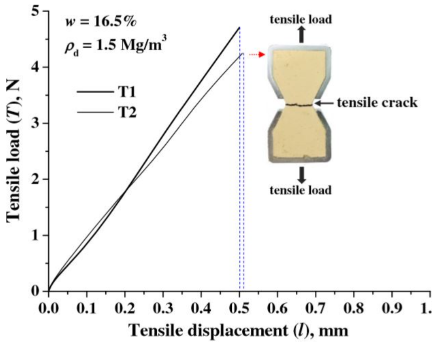

Figure E.8: Direct tensile tests (Tang et al., 2014)

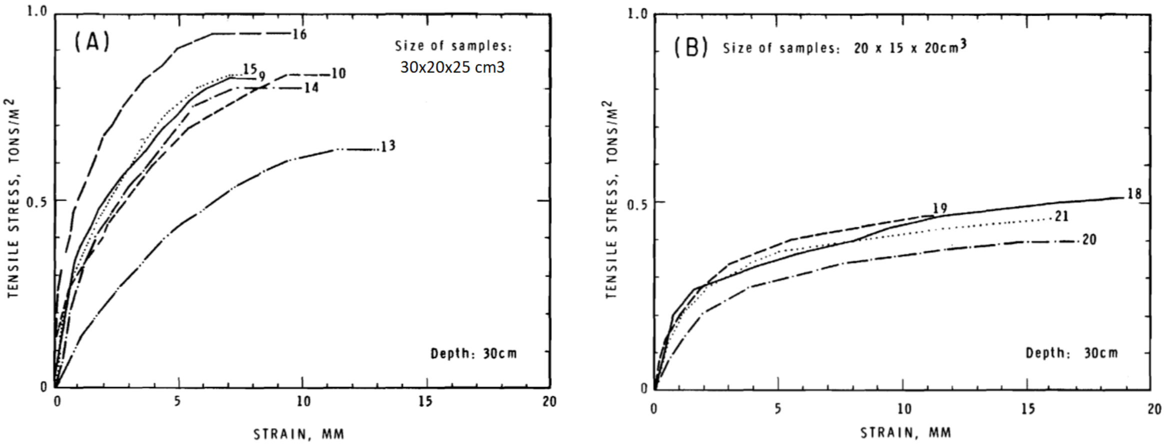

Figure E.9: Stress-strain curves for Sphagnum peat, Mer Blueu for different sample sizes (Helenelund, 1967)

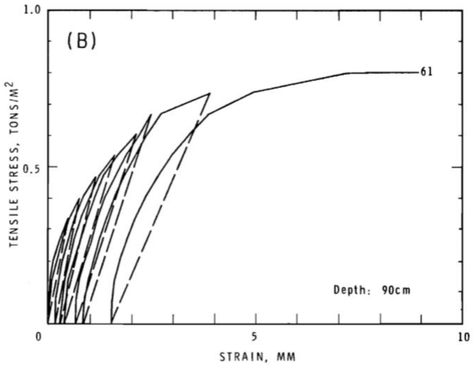

Figure E.10: Stress-strain curves for repeated unloading and reloading on Mer Bleue peat (Helenelund, 1967)

TRIAXIAL EXTENSION TEST (DRAINED)

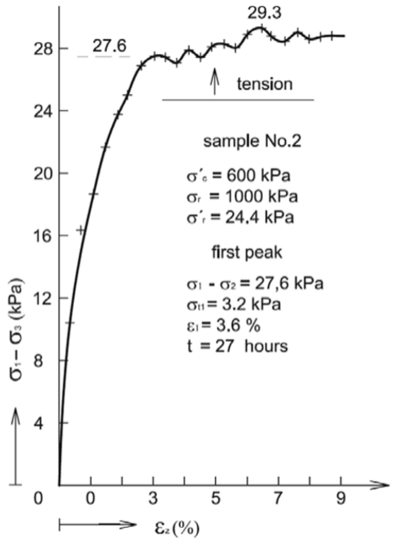

Figure 14. The typical result of drained triaxial tension test.

Figure E.11: Stress-displacement curves for direct tensile tests (Vaníček, 2013)

OTHER

Hoffman (2019): 'Both computations produce the same displacement curve, but failure is only predicted in the case with softening cut-off. Using the conventional cut-off results in an unrealistic soil behavior.' (see Figure E.12)

E.2.3. CONCLUSION

UNDRAINED

Figure E.6 shows great resemblance with a brittle stress-strain relationship as shown in Figure E.1. This is obtained for the (undrained) direct tensile test. Therefore, the brittle stress-strain relationship for undrained tensile behavior is most suitable.

For peat, Figure E.10 shows an elastoplastic strain hardening relationship, until tensile failure.

DRAINED

The triaxial extension test shows results (see Figure E.11) which resembles a linear elastic perfectly plastic relationship. However, using such a relationship in Diana FEA yields unrealistic behavior (Hoffman, 2019).

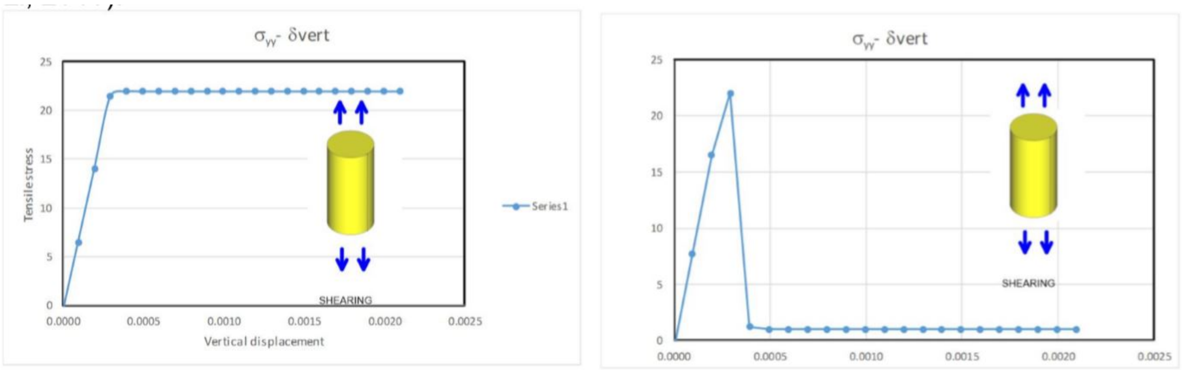

Figure E.12: Stress-displacement curves for direct tensile tests, without tension softening (left) and with tension softening (right) (Hoffman, 2019)

E.3. STRESS AND STRAIN PROFILE IN BENDING TEST

In literature, there are many suggestions on how the strain and stress profile evolve during a bending test. The strain is measured directly and regarding that, there is a consensus reached. In contrast, the stresses are obtained indirectly through the strains by various methods. Firstly, theory gives the stress-strain relationships. In literature, the linear elastic model and the non-linear elastic model are encountered. Secondly, there are methods not based on any predefined stress-strain relationship: the differential method and discrete element modeling (DEM).

E.3.1. STRAIN PROFILE

In literature, there is consensus regarding the development of the strain profile: it is linear over depth. The following sources state:

- Ajaz and Parry (1975): 'The strains along the mid-length of the beam for both clays were found to vary linearly with the depth of the beam.'
- Šuklje (1969) in Vaníček (2013): 'The results of the tests made by Šuklje proved that the strain plots are still approximately linear during the appearance of the first tensile cracks.'
- Thusyanthan et al. (2007): 'It is clear from these results that the strain profile is almost perfectly linear with depth for both the load-controlled and strain-controlled tests up until the point of crack initiation.' (see also Figure E.13)

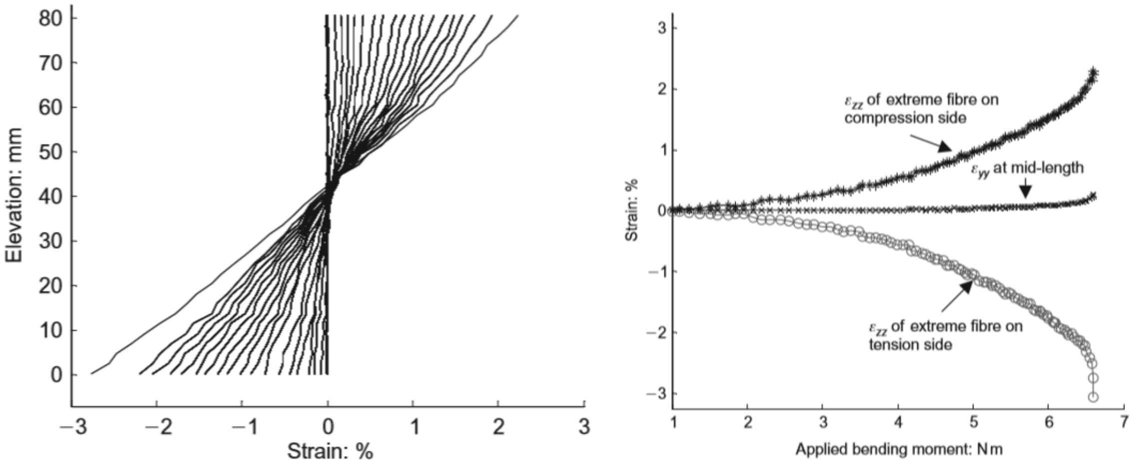

Figure E.13: Strain development in a strain rate controlled test (Thusyanthan et al., 2007)

E.3.2. STRESS PROFILES

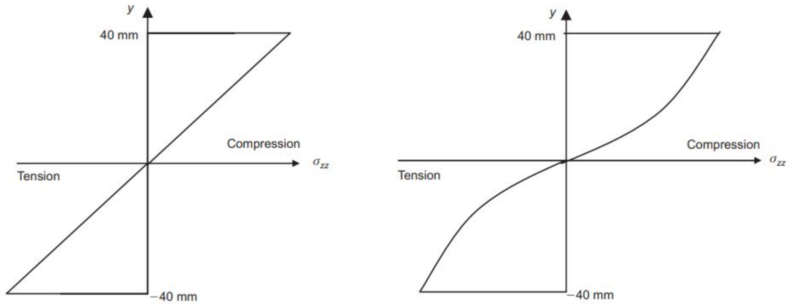

Figure E.14: Linear (left figure) and nonlinear (right figure) stress strain relationship (Thusyanthan et al., 2007)

LINEAR ELASTIC

The following stress profiles are based on purely elastic behavior of the soil, with constant values for the elasticity in compression and tension. Failure occurs if the tensile stress exceeds the critical tensile strength. There are three options on where the neutral axis of the stress distribution lies at the point of crack initiation, see also Figure E.15:

1. Neutral axis lies in the middle

   The **theory of elasticity** assumes that the neutral axis lies in the middle and that the stiffness modulus in tension and compression is equal. The maximum tensile stress equals the maximum compressive stress (Vaníček, 2013; Ammeri et al., 2006).

2. Neutral axis at tensile side

   Šuklje et al. (1961) assumes the maximum tensile strength is reached, which is 4.0 t/m^2 ($\approx$ 40 kPa). The compressive strength is larger, and the stress distribution is assumed linear. This way, the neutral axis ends up at the tensile side.

3. Neutral axis at compression side

   Navier's hypothesis assumes that the neutral axis is above the center of gravity. The deformations are planar and the compression and tension moduli are constant but not the same. The stresses are linear to the deformation (Vaníček, 2013; Ammeri et al., 2006).

NON LINEAR ELASTIC

A general formulation of the a non linear stress-strain relation is by the power law function $\sigma_{zz} = C * \epsilon_{zz}^{\beta}$. Assuming the tensile and compressive stress-strain relations to be identical, the constant C and β are obtained by curve fitting. In Thusyanthan et al. (2007), the stress-strain relationship is given by $\sigma_{zz} = 300 * \epsilon_{zz}^{0.4}$. This relation is plotted, together with the stress profile, in Figure E.16.

DIFFERENTIAL METHOD

The differential method also assumes planar deformations. Using the outer measured compressive and tensile strains, the stresses are computed. This method is however not based on any stress-strain law (Vaníček, 2013; Ammeri et al., 2006) and therefore considered superior to the elastic bending method (Ajaz and Parry, 1975). The stress distribution is shown in Figure E.17.

DISCRETE ELEMENT MODELLING (DEM)

With computational advancement, the numerical method based on DEM is taking the place of many experimental tests. Ammeri et al. (2006) came to the following stress profile using the software PFC, see Figure E.18.

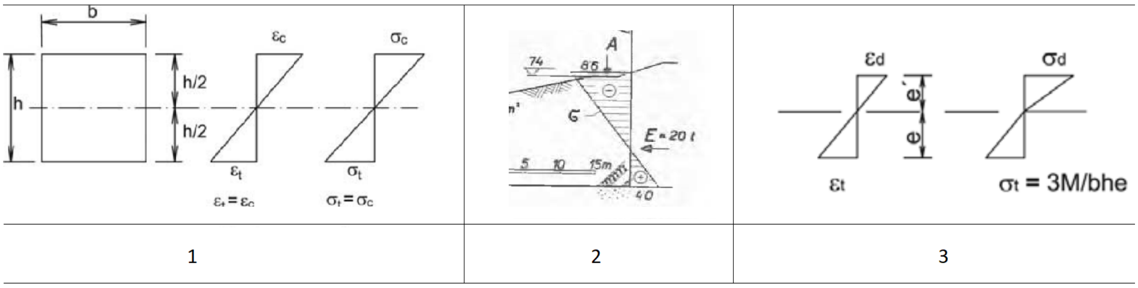

Figure E.15: *Different possibilities of neutral axis in stress strain diagram (Šuklje et al., 1961; Vaníček, 2013) (adapted)*

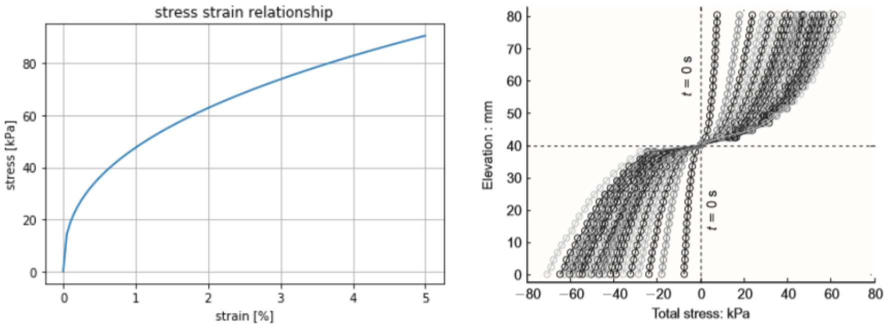

Figure E.16: *Stress profile based non linear elastic curve fitting (Thusyanthan et al., 2007)*

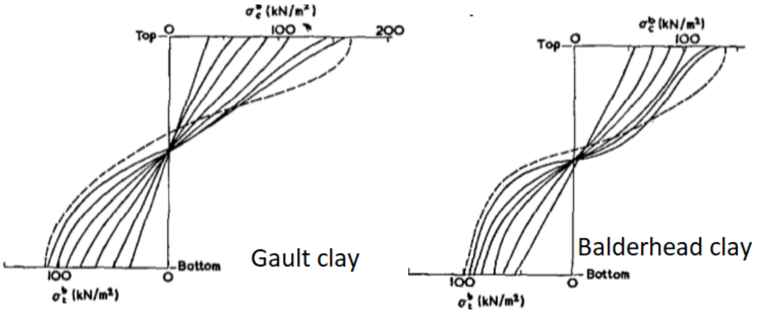

Figure E.17: *Stress profile based on differential method for two clay types (Ajaz and Parry, 1975)*

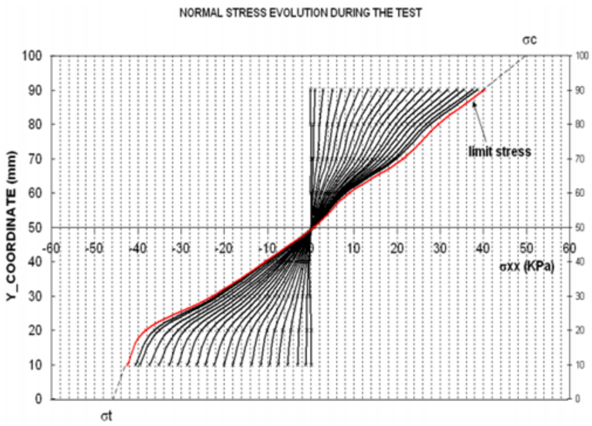

Figure E.18: *Stress profile based on numerical DEM (Ammeri et al., 2006)*

E.3.3. Conclusion

Ajaz and Parry (1975) state that the elastic bending theory is unsatisfactory for analyzing bending in soils. Using a non-linear stress-strain relationship is more realistic, but the proposed form of Thusyanthan et al. (2007) is too curved, comparing to the test results direct tensile tests on clay. Figures E.17 and E.18 point to a linear elastic relationship for small strains, transitioning in a plastic regime for larger strains. In both plots, the plastic regime is reached earlier on the tensile side than on the plastic side.

E.4. Other

E.4.1. Relationship with other parameters

Author	Soil type	Reported relation	Method (Test if experimental)
Bagge (1985)	Clay (CH-CL)	$\sigma'_t = \alpha_t * c'$	Coulomb failure criterion
		$\sigma'_t = 0.7 * c'$	For London clay
		$\sigma'_t = 0.5 * c'$	Reasonable conservative value
Vaníček (2013)	Clay (CL)	w (13-23%) $\uparrow \longrightarrow \sigma_t \downarrow$	Bending test
Li et al. (2019)	Clay (CL)	max(σ_t) around w=9%	Direct tensile test
Tang et al. (2014)	Clay (CL)	ρ_d (1.5-1.7 Mg/m^3) $\uparrow \longrightarrow \sigma_t \uparrow$	Direct tensile test
Helenelund (1967)	Peat	$\sigma_t \approx 0.5 * s_u$	Direct tensile test and vane test
Thusyanthan et al. (2007)	Remoulded clay	$\sigma'_t = 0$ & $\sigma_t = p$	Assumption

F

BEAM EVALUATIONS USING SIMPLE MODELS

The questions on the table, regarding the beam behavior, are:

a. How does it fail? Is the flexural or the shear strength exceeded?

b. Where exactly does the beam fail? In the middle or at the ends? The tensile cracks are expected to occur at the bottom of the cover layer at the toe, and at the top of the cover layer at the center of the uplift zone. Hoffman (2019) has also observed crack strains at these points.

This Appendix tries to answer the questions, based on simple beam equations.
N.B. these approaches do not take the initial stresses into account, which in fact are important.

F.1. LINEAR ELASTIC ANALYTICAL EQUATIONS

In case the beam is assumed to have fully fixed sides and behaves fully elastically, it is found that the flexural strength is probably normative. Hereafter, an explanation is given:

Firstly, the load is defined as $q[kN/m]$ (per meter width), which is the same as $q[kPa]$. The maximum load the soil is able to resist, is defined by the minimum resistance by bending moment or shear, i.e. q_M and q_V.

$$q = h_{up} * \gamma_w - \gamma_{sat} * D_{cover} \tag{F.1}$$

$$q_{resistance} = min\{q_M, q_V\} \tag{F.2}$$

The maximum moment for a beam with fixed sides is given in Equation F.3. For a beam with pinned sides 1/8 replaces 1/12, and the location of the failure is in the middle instead of at the ends. The linear theory of elasticity gives Equation F.4. Together, they give an expression for q_M.

$$M = 1/12 * q * L^2 \tag{F.3}$$

$$M = \Delta\sigma_h * W = \Delta\sigma_h * 1/6 * D_{cover}^2 \text{ (per m width)} \tag{F.4}$$

$$q_M = \frac{M}{1/12 * L^2} = \frac{\Delta\sigma_h * 1/6 * D_{cover}^2}{1/12 * L^2} = c_M \left(\frac{D_{cover}}{L}\right)^2 \tag{F.5}$$

For the shear, a similar approach is used. The maximum shear for a beam with fixed sides is given in Equation F.6. This is the same for a beam with pinned sides. The linear theory of elasticity gives Equation F.7. Together, they give an expression for q_V.

$$V = 1/2 * q * L \tag{F.6}$$

$$V = s_u * D_{cover} \text{ (per m width)} \tag{F.7}$$

$$q_V = \frac{V}{1/2 * L} = \frac{s_u * D_{cover}}{1/2 * L} = c_V \left(\frac{D_{cover}}{L}\right) \tag{F.8}$$

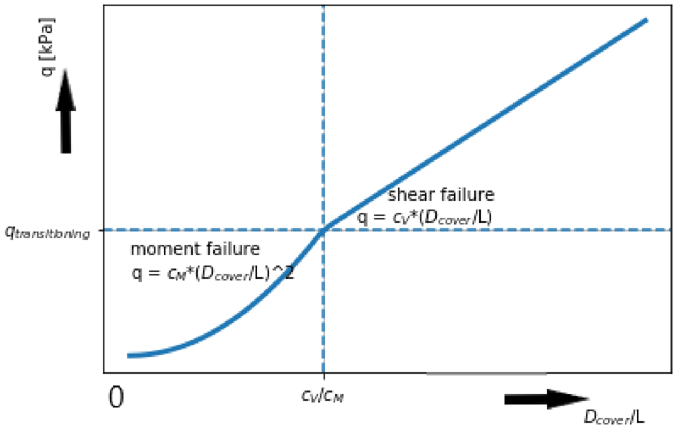

Figure F.1: Determining the normative failure mode: general

Whether q_M or q_V is normative, is shown in Figure F.1. The constants c_M and c_V introduced in Equations F.5 and F.8 are a key to determine the normative failure mode. In case of applying the linear elastic beam theory and assuming fixed ends, Equation F.9 holds.

$$\frac{c_V}{c_M} = \frac{2 * s_u}{2 * \Delta\sigma_h} = \frac{s_u}{\Delta\sigma_h} \tag{F.9}$$

What this means in reality, is explained with an example, see also Figure F.2. Assuming fixed ends, $s_u = 15kPa$, $\Delta\sigma_h = 10kPa$, linear elastic beam theory, this leads to $c_V/c_M = 1.5$. This means that for $D_{cover}/L < 1.5$ the bending moment is normative and $D_{cover}/L > 1.5$ it is the shear force. The load at which the transition takes place is in this case $q_{transitioning} = 22.5kPa$. However, this load will not occur in reality, because the load is linked with the uplift length. With greater loads, the length will increase, leading to a decrease of the load. This mechanism is not made explicit in the equations but leads to a decrease of both q and D_{cover}/L. In conclusion, the failure of the beam starts with exceeding the flexural strength.

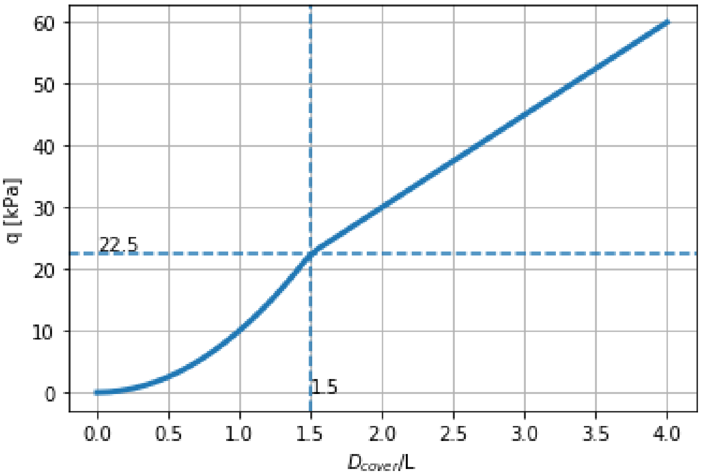

Figure F.2: Determining the normative failure mode: example

To conclude, the elastic beam equations determine the resistance due to the bending moment is normative. It is assumed now that the beam has fixed end-conditions. Also assuming no initial stresses, the elastic beam equations predict a failure at the location of 'side under'.

F.2. PYTHON: $\sigma - \epsilon$ AND $\epsilon(z)$ RELATIONSHIPS

Using the knowledge gained from experimental work in literature, and that the bending moment is probably normative from Appendix C.I, a first estimation of the resistance is made. It is assumed that the cohesion of the clay is 15 kPa. The tensile strength and the compressive strength are assumed to be half and twice the cohesion respectively. Also, the strain plots are linear over depth.

In Figure F.4, the results of an evaluation in Python of a simple beam are shown. The five strain plots (in the middle) show an increase in strain at the bottom of the beam. The strain at the bottom is a variable. For various strains at the bottom, the strain plots are translated into stress plots using the stress-strain relationship (at the left). The stress plot for which $\Sigma\sigma_h = 0$ holds, is plotted (at the right). The corresponding moment is reported as well.

To conclude, the maximum moment occurs when the strain at the bottom equals the critical tensile strain of 1%, which corresponds to the tensile strength of $0.5 * c = 7.5kPa$. This is also the moment of crack initiation, which is assumed to resemble the total failure of the beam.

F.2.1. DISCUSSION

There are a few points of concern using this approach. Firstly, the simple beam does not include any self-weight nor an initial horizontal stress distribution. That means that here $\Delta\sigma_h = \sigma_h$ at each moment. Secondly, the strength parameters are held constant and are specified independently of the vertical stresses. The Mohr-Coulomb circle, in this case, is resembled in Figure F.3.

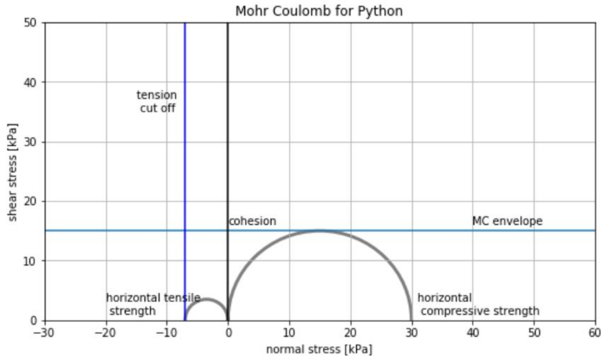

Figure F.3: Failure envelope for simple beam in Python

However, in-situ stresses ($\sigma_{h,0}$) play a large role in determining the mobilizable horizontal stresses ($\Delta\sigma_h$). The in-situ stresses are small at the top of the beam, and larger towards the bottom. The actual stress (σ_h) is important to determine whether the plastic capacity is reached. Equation F.10 gives the relation between the stresses.

$$\Delta\sigma_h = \sigma_{h,0} - \sigma_h \tag{F.10}$$

Lastly, this simple model does not take into account the deformations of the whole beam, possibly inducing extra horizontal stresses and thus extra resistance against bending.

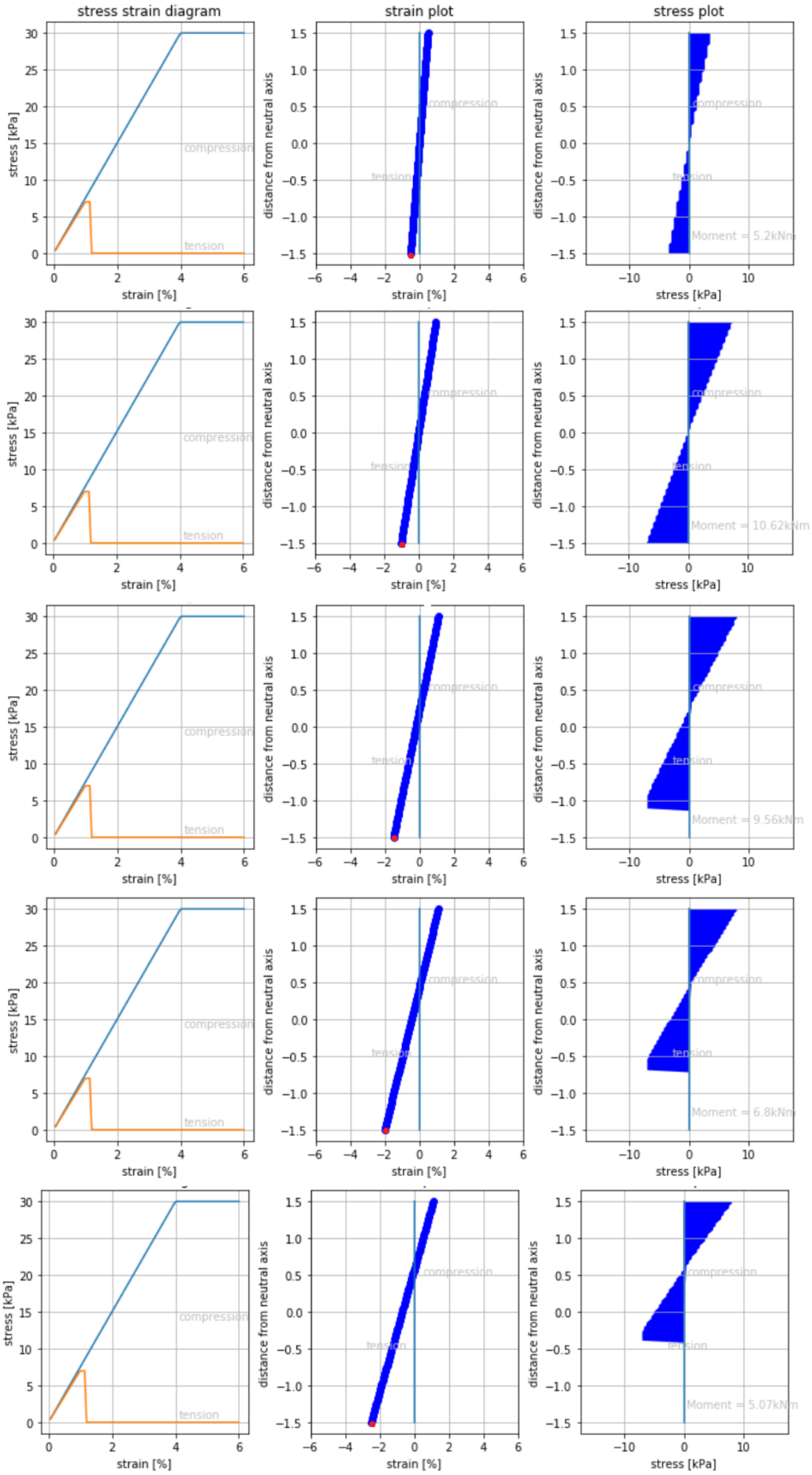

Figure F.4: Python plots for increasing strains

G

PYTHON SCRIPTING FOR PLAXIS

This Appendix reports how the remote scripting tool for Plaxis in Python is used, and it also includes the scripts for postprocessing the obtained results. The dimensions of the beam are 4 meters thick and 40 meters wide. The input parameters for Mohr-Coulomb and Hardening Soil constitutive models are given in Table G.1 and G.2. Regarding the displacement, the following boundary conditions are imposed. The vertical boundaries are fully fixed, which means that no displacement in x- and y-direction is allowed. The horizontal boundaries are free. On the lower horizontal boundary, an upward constant line load is applied, equal to the effective self-weight of the beam plus the netload.

Table G.1: Input parameters for Mohr-Coulomb model

parameter	**value**
γ_{sat} and γ_{dry}	16 kN/m^3
e_{init}	0.5
c'	5 kPa
ϕ'	25 °
ψ	0 °
Tensile strength	2.5 kPa
POP	15 kPa
OCR	1
E	1 MPa
ν	0.4 (E_{oed} = 2 MPa)

Table G.2: Input parameters for Hardening soil model

parameter	**value**
γ_{sat} and γ_{dry}	16 kN/m^3
e_{init}	0.5
c'	5 kPa
ϕ'	25 °
ψ	0 °
Tensile strength	2.5 kPa
POP	15 kPa
OCR	1
$E_{oed,ref}$	2 MPa
$E_{50,ref}$	3.5 MPa
$E_{ur,ref}$	8 MPa
Power (m)	0.8

G.1. REMOTE SCRIPTING SERVER

To set up the remote scripting server, please follow the following steps:

- Enable the additional license *Geotechnical SELECT Entitlements* the Plaxis 2D Input program. This can be found under *Help* ⟶ *License configuration*.
- Configure remote scripting server, both in Input and Output program of Plaxis. This is hidden under *Expert* ⟶ *Configure remote scripting server* ⟶ *Start server*. Use port 10000 (default) in the Input program and 10001 in the Output program.
- Open the Jupyter notebook by: *Expert* ⟶ *Python* ⟶ *Jupyter notebook*

G.2. Set up Python notebook

Import Python packages

```
import numpy as np
import matplotlib.pyplot as plt
from matplotlib.collections import PatchCollection
from matplotlib.patches import Rectangle, Circle, PathPatch
from math import radians
```

Establish the connection with the Python application

```
from plxscripting.easy import *

localhostport_input = 10000
localhostport_output = 10001

s_i, g_i = new_server('localhost', localhostport_input, password='yourpassword')
s_o, g_o = new_server('localhost', localhostport_output, password='yourpassword')
```

G.3. Plaxis 2D Input

Start a new project

```
s_i.new()
#ymax domain = height of soil beam
ymax = 4
#xmax domain = length of soil beam
xmax = 20
g_i.SoilContour.initializerectangular(0, 0, xmax, ymax)
g_i.setproperties("ModelType", 0) #Plane strain
#Check File -> Project Properties -> Model
g_i.setproperties("Title", 'test␣till␣failure')
g_i.setproperties("Company", 'Arcadis')
```

G.3.1. Soil menu

Set up borehole

```
g_i.borehole(0) #0 = x-coordinate of borehole
g_i.soillayer(ymax) #ymax = height of soil layer
```

Define material

```

gamma_A = 16
nu_A = 0.35
E_A = 1000
c_a = 5
phi_a = 25
psi_a = 0
k_a = 10**(-9)*24*3600

G_A = E_A/(2*(1+nu_A))
ts_a = 0.5*c_a

materialA = g_i.soilmat()
materialA.setproperties("MaterialName", 'ClayMCA')
materialA.setproperties("SoilModel", 2, #Mohr-Coulomb
```

```
                                "DrainageType", 1,  #Undrained A
                                "UndrainedBehaviour", 0, #standard, nu_undrained=0.495
                                "gammaUnsat", gamma_A, "gammaSat", gamma_A,
                                "Gref", G_A,
                                "cref", c_a,
                                "phi", phi_a,
                                "psi", psi_a,
                                "TensionCutOff", True,
                                "TensileStrength", ts_a,
                                "nu", nu_A,
                                "perm_primary_horizontal_axis", k_a,
                                "perm_vertical_axis", k_a)
materialA.setproperties("SoilTypeFlow",4) #very fine material
g_i.Soils[0].Material = materialA
#check: material.echo()
```

G.3.2. STRUCTURES MENU

Define upward load

```
g_i.gotostructures()
g_i.lineload((0,-ymax), (xmax,-ymax))
upwardload = g_i.LineLoad_1
startload = ymax*(gamma_A-10)
upwardload.setproperties('qy_start',startload)
upwardload.info()
```

G.3.3. MESH MENU

Define mesh

```
g_i.gotomesh()
g_i.mesh(0.03) #very fine
```

G.3.4. STAGED CONSTRUCTION MENU

```
load_string = np.arange(0.1, 2, 0.1)
print(load_string)
```

Define loading stages

```
g_i.gotoflow()
g_i.gotostages()
# Phase_1 (Equilibrium, change B.C.)
g_i.phase(g_i.InitialPhase) # Add Phase_1
g_i.setcurrentphase(g_i.Phase_1) # Make Phase_1 current
g_i.Phase_1.Identification = "Equilibrium" # Name the phase
g_i.LineLoad_1_1.activate(g_i.Phase_1)
g_i.deformations.setproperties('BoundaryYMin', g_i.Phase_1,"Free")
g_i.deformations.setproperties('BoundaryYMax', g_i.Phase_1,"Free")
g_i.deformations.setproperties('BoundaryXMin', g_i.Phase_1,"Fully␣Fixed")
g_i.deformations.setproperties('BoundaryXMax', g_i.Phase_1,"Fully␣Fixed")
# Phase_2 (Upward load of 1 kPa)
g_i.phase(g_i.Phase_1) # Add Phase_2
g_i.setcurrentphase(g_i.Phase_2) # Make Phase_2 current
g_i.Phase_2.Identification = 'Load␣=␣'+str(load_string[0])+'␣kPa' # Name the phase
g_i.Phase_2.Deform.ResetDisplacementsToZero = True
```

```
g_i.LineLoad_1_1.setproperties('qy_start', g_i.Phase_2, startload + load_string[0])
g_i.phase(g_i.Phase_2) # Add Phase_3
g_i.setcurrentphase(g_i.Phase_3) # Make Phase_2 current
g_i.Phase_3.Identification = 'Load␣=␣'+str(load_string[1])+'␣kPa' # Name the phase
g_i.LineLoad_1_1.setproperties('qy_start', g_i.Phase_3, startload + load_string[1])
g_i.phase(g_i.Phase_3) # Add Phase_4
g_i.setcurrentphase(g_i.Phase_4) # Make Phase current
g_i.Phase_4.Identification = 'Load␣=␣'+str(load_string[2])+'␣kPa' # Name the phase
g_i.LineLoad_1_1.setproperties('qy_start', g_i.Phase_4, startload + load_string[2])
g_i.phase(g_i.Phase_4) # Add Phase_5
g_i.setcurrentphase(g_i.Phase_5) # Make Phase current
g_i.Phase_5.Identification = 'Load␣=␣'+str(load_string[3])+'␣kPa' # Name the phase
g_i.LineLoad_1_1.setproperties('qy_start', g_i.Phase_5, startload + load_string[3])
g_i.phase(g_i.Phase_5) # Add Phase_6
g_i.setcurrentphase(g_i.Phase_6) # Make Phase current
g_i.Phase_6.Identification = 'Load␣=␣'+str(load_string[4])+'␣kPa' # Name the phase
g_i.LineLoad_1_1.setproperties('qy_start', g_i.Phase_6, startload + load_string[4])
g_i.phase(g_i.Phase_6) # Add Phase_7
g_i.setcurrentphase(g_i.Phase_7) # Make Phase current
g_i.Phase_7.Identification = 'Load␣=␣'+str(load_string[5])+'␣kPa' # Name the phase
g_i.LineLoad_1_1.setproperties('qy_start', g_i.Phase_7, startload + load_string[5])
g_i.phase(g_i.Phase_7) # Add Phase_8
g_i.setcurrentphase(g_i.Phase_8) # Make Phase current
g_i.Phase_8.Identification = 'Load␣=␣'+str(load_string[6])+'␣kPa' # Name the phase
g_i.LineLoad_1_1.setproperties('qy_start', g_i.Phase_8, startload + load_string[6])

g_i.phase(g_i.Phase_8) # Add Phase_9
g_i.setcurrentphase(g_i.Phase_9) # Make Phase current
g_i.Phase_9.Identification = 'Load␣=␣'+str(load_string[7])+'␣kPa' # Name the phase
g_i.LineLoad_1_1.setproperties('qy_start', g_i.Phase_9, startload + load_string[7])

g_i.phase(g_i.Phase_9) # Add Phase_10
g_i.setcurrentphase(g_i.Phase_10) # Make Phase current
g_i.Phase_10.Identification = 'Load␣=␣'+str(load_string[8])+'␣kPa' # Name the phase
g_i.LineLoad_1_1.setproperties('qy_start', g_i.Phase_10, startload + load_string[8])

g_i.phase(g_i.Phase_10) # Add Phase_11
g_i.setcurrentphase(g_i.Phase_11) # Make Phase current
g_i.Phase_11.Identification = 'Load␣=␣'+str(load_string[9])+'␣kPa' # Name the phase
g_i.LineLoad_1_1.setproperties('qy_start', g_i.Phase_11, startload + load_string[9])
```

```
g_i.calculate()
```

```
g_i.save(r'C:\yourpath')
```

G.4. PLAXIS 2D OUTPUT

See how all the parameters are called:

```
g_o.ResultTypes.Soil.echo()
```

Retrieve data

```
StressPointID = g_o.getresults(g_o.Phase_2, g_o.ResultTypes.Soil.StressPointID,
                        'stresspoint')
x = g_o.getresults(g_o.Phase_2, g_o.ResultTypes.Soil.X, 'stresspoint')
```

```
y = g_o.getresults(g_o.Phase_2, g_o.ResultTypes.Soil.Y, 'stresspoint')
print(StressPointID[-1])

#phase independent parameters (stresspoint)
xcoor_array = np.zeros(StressPointID[-1])
ycoor_array = np.zeros(StressPointID[-1])
stresspoint_array = np.zeros(StressPointID[-1])
for i in range(StressPointID[-1]):
    xcoor_array[i] = x[i]
    ycoor_array[i] = y[i]
    stresspoint_array[i] = StressPointID[i]
```

```
#get results in matrices, use memory
### stresses: se1, se2, se3, sxxT, syyT, szzT, pexcess, pactive

sigmaeffective1_all = np.zeros(( len(g_o.Phases)-1, len(stresspoint_array)))
sigmaeffective2_all = np.zeros(( len(g_o.Phases)-1, len(stresspoint_array)))
sigmaeffective3_all = np.zeros(( len(g_o.Phases)-1, len(stresspoint_array)))
sigmaangle_all = np.zeros(( len(g_o.Phases)-1, len(stresspoint_array)))
sigxxT_all = np.zeros(( len(g_o.Phases)-1, len(stresspoint_array)))
sigyyT_all = np.zeros(( len(g_o.Phases)-1, len(stresspoint_array)))
sigzzT_all = np.zeros(( len(g_o.Phases)-1, len(stresspoint_array)))
sigxy_all = np.zeros(( len(g_o.Phases)-1, len(stresspoint_array)))
pexcess_all = np.zeros(( len(g_o.Phases)-1, len(stresspoint_array)))
pactive_all = np.zeros(( len(g_o.Phases)-1, len(stresspoint_array)))

for i in range (len(g_o.Phases)-1):
    sigmaeffective1_all[i] = g_o.getresults(g_o.Phases[i+1],
            g_o.ResultTypes.Soil.SigmaEffective1, 'stresspoint')
    sigmaeffective2_all[i] = g_o.getresults(g_o.Phases[i+1],
             g_o.ResultTypes.Soil.SigmaEffective2, 'stresspoint')
    sigmaeffective3_all[i] = g_o.getresults(g_o.Phases[i+1],
             g_o.ResultTypes.Soil.SigmaEffective3, 'stresspoint')
    sigmaangle_all[i] = g_o.getresults(g_o.Phases[i+1],
             g_o.ResultTypes.Soil.SigmaTAngle, 'stresspoint')
    sigxxT_all[i] = g_o.getresults(g_o.Phases[i+1],
             g_o.ResultTypes.Soil.SigxxT, 'stresspoint')
    sigyyT_all[i] = g_o.getresults(g_o.Phases[i+1],
            g_o.ResultTypes.Soil.SigyyT, 'stresspoint')
    sigzzT_all[i] = g_o.getresults(g_o.Phases[i+1],
            g_o.ResultTypes.Soil.SigzzT, 'stresspoint')
    sigxy_all[i] = g_o.getresults(g_o.Phases[i+1],
            g_o.ResultTypes.Soil.Sigxy, 'stresspoint')
    pexcess_all[i] = g_o.getresults(g_o.Phases[i+1],
            g_o.ResultTypes.Soil.PExcess, 'stresspoint')
    pactive_all[i] = g_o.getresults(g_o.Phases[i+1],
            g_o.ResultTypes.Soil.PActive, 'stresspoint')


#this takes a long time to run: see Plaxis 2D command line for progress

### strains
# ehor, ever, eshear, evol, edev

ehor_all = np.zeros(( len(g_o.Phases)-1, len(stresspoint_array)))
ever_all = np.zeros(( len(g_o.Phases)-1, len(stresspoint_array)))
```

```
eshear_all = np.zeros(( len(g_o.Phases)-1, len(stresspoint_array)))
evol_all = np.zeros(( len(g_o.Phases)-1, len(stresspoint_array)))
edev_all = np.zeros(( len(g_o.Phases)-1, len(stresspoint_array)))

for i in range (len(g_o.Phases)-1):
    ehor_all[i] = g_o.getresults(g_o.Phases[i+1],
            g_o.ResultTypes.Soil.Epsxx, 'stresspoint')
    ever_all[i] = g_o.getresults(g_o.Phases[i+1],
            g_o.ResultTypes.Soil.Epsyy, 'stresspoint')
    eshear_all[i] = g_o.getresults(g_o.Phases[i+1],
            g_o.ResultTypes.Soil.Gamxy, 'stresspoint')
    evol_all[i] = g_o.getresults(g_o.Phases[i+1],
             g_o.ResultTypes.Soil.TotalVolumetricStrain, 'stresspoint')
    edev_all[i] = g_o.getresults(g_o.Phases[i+1],
             g_o.ResultTypes.Soil.TotalDeviatoricStrain, 'stresspoint')

e1_all =  np.zeros(( len(g_o.Phases)-1, len(stresspoint_array)))
e2_all =  np.zeros(( len(g_o.Phases)-1, len(stresspoint_array)))
e3_all =  np.zeros(( len(g_o.Phases)-1, len(stresspoint_array)))

for i in range (len(g_o.Phases)-1):
    e1_all[i] = g_o.getresults(g_o.Phases[i+1],
            g_o.ResultTypes.Soil.Eps1, 'stresspoint')
    e2_all[i] = g_o.getresults(g_o.Phases[i+1],
            g_o.ResultTypes.Soil.Eps2, 'stresspoint')
    e3_all[i] = g_o.getresults(g_o.Phases[i+1],
            g_o.ResultTypes.Soil.Eps3, 'stresspoint')
```

G.5. Postprocessing

Define functions which returns arrays per stress point

```
def result_sigmaeffective1(noStressPoint):
    sigmaeffective1 = np.zeros(len(g_o.Phases)-1)
    for i in range(len(g_o.Phases)-1):
        sigmaeffective1[i] =  sigmaeffective1_all[i, noStressPoint-1]
    return(sigmaeffective1)

def result_sigmaeffective2(noStressPoint):
    sigmaeffective2 = np.zeros(len(g_o.Phases)-1)
    for i in range(len(g_o.Phases)-1):
        sigmaeffective2[i] = sigmaeffective2_all[i, noStressPoint-1]
    return(sigmaeffective2)

def result_sigmaeffective3(noStressPoint):
    sigmaeffective3 = np.zeros(len(g_o.Phases)-1)
    for i in range(len(g_o.Phases)-1):
        sigmaeffective3[i] = sigmaeffective3_all[i, noStressPoint-1]
    return(sigmaeffective3)

def result_sigmaTangle(noStressPoint):
    variable = np.zeros(len(g_o.Phases)-1)
    for i in range(len(g_o.Phases)-1):
        variable[i] = sigmaangle_all[i, noStressPoint-1]
    return(variable)
```

Development of stresses/strains in a point

```
def plot_se_development(noStressPoint):
    #index = noStressPoint -1
    se1 = result_sigmaeffective1(noStressPoint)
    se2 = result_sigmaeffective2(noStressPoint)
    se3 = result_sigmaeffective3(noStressPoint)
    phase_range = np.arange(1, len(g_o.Phases), 1)
    plt.plot(phase_range, se1, '--bo', label ='$\sigma_{eff}1$')
    plt.plot(phase_range, se2, '--co', label ='$\sigma_{eff}2$')
    plt.plot(phase_range, se3, '--go', label ='$\sigma_{eff}3$')
    plt.xlabel('Phase␣step')
    plt.ylabel('$\sigma_{eff}$␣[kPa]')
    plt.grid()
    plt.legend()
    plt.title('Effective␣principal␣stress␣development␣for␣StressID:␣'+str(noStressPoint))
    return

def peffq(noStressPoint):
    stress1 = result_sigmaeffective1(noStressPoint)
    #se2 = result_sigmaeffective2(noStressPoint)
    stress3 = result_sigmaeffective3(noStressPoint)
    p = np.zeros(len(stress1))
    q = np.zeros(len(stress1))
    for i in range(len(p)):
        p[i] = (stress1[i]+stress3[i])/2
        q[i] = (stress1[i]-stress3[i])/2
    return (p, q)

def plot_pq_development(noStressPoint):
    p,q = peffq(noStressPoint)
    plt.plot(p,q, 'mo--')
    plt.xlabel('$␣q␣=␣(\sigma_{eff}1␣-␣\sigma_{eff}3)/2$␣')
    plt.ylabel('$␣p␣=␣(\sigma_{eff}1␣+␣\sigma_{eff}3)/2$␣')
    plt.grid()
    #plt.legend()
    plt.title('Stress␣path␣for␣StressID:␣'+str(noStressPoint))
    plt.gca().invert_xaxis()
    plt.gca().invert_yaxis()
    return

def plot_st_development(noStressPoint):
    st_xx = sigxxT_all[:, noStressPoint-1]
    st_yy = sigyyT_all[:, noStressPoint-1]
    st_zz = sigzzT_all[:, noStressPoint-1]
    s_xy = sigxy_all[:, noStressPoint-1]
    phase_range = np.arange(1, len(g_o.Phases), 1)
    plt.plot(phase_range, st_xx, '--o',color = 'slateblue',
            label ='$\sigma_{tot,␣xx}$')
    plt.plot(phase_range, st_yy, '--o', color='lime',
            label ='$\sigma_{tot,␣yy}$')
    plt.plot(phase_range, st_zz, '--o', color = 'darkkhaki',
            label ='$\sigma_{tot,␣zz}$')
    plt.plot(phase_range, s_xy, '--o', color='olive', label ='$\sigma_{xy}$')
    plt.xlabel('Phase␣step')
    plt.ylabel('$\sigma_{tot}$␣[kPa]')
    plt.grid()
```

```
    plt.legend()
    plt.title('Total␣cartesian␣stress␣development␣for␣StressID:␣'+str(noStressPoint))
    return

def plot_pwp_development(noStressPoint):
    #index = noStressPoint -1
    p_a = pactive_all[:, noStressPoint-1]
    p_e = pexcess_all[:, noStressPoint-1]
    phase_range = np.arange(1, len(g_o.Phases), 1)
    plt.plot(phase_range, p_a, '--o', color = 'indigo', label ='$p_{active}$')
    plt.plot(phase_range, p_e, '--o', color = 'mediumorchid', label ='$p_{excess}$')
    plt.xlabel('Phase␣step')
    plt.ylabel('pore␣water␣pressure␣[kPa]')
    plt.grid()
    plt.legend()
    plt.title('Pore␣water␣pressure␣development␣for␣StressID:␣'+str(noStressPoint))
    return


def plot_ehorvershear_development(noStressPoint):
    e_hor = ehor_all [:, noStressPoint-1]
    e_ver = ever_all[:, noStressPoint-1]
    e_shear = eshear_all[:, noStressPoint-1]
    phase_range = np.arange(1, len(g_o.Phases), 1)
    plt.plot(phase_range, e_hor, '--o', color = 'slateblue',
             label ='$\epsilon_{xx}$')
    plt.plot(phase_range, e_ver, '--o',color='lime',
            label ='$\epsilon_{yy}$')
    plt.plot(phase_range, e_shear, '--o',color='olive',
            label ='$\gamma_{xy}$')
    plt.ylabel('Strain')
    plt.xlabel('Phase␣step')
    plt.grid()
    plt.legend()
    plt.title('Cartesian␣strain␣development␣for␣StressID:␣'+str(noStressPoint))
    return

def plot_evoldef_development(noStressPoint):
    e_vol = evol_all[:, noStressPoint-1]
    e_dev = edev_all[:, noStressPoint-1]
    e_1 = e1_all[:, noStressPoint-1]
    e_2 = e2_all[:, noStressPoint-1]
    e_3 = e3_all[:, noStressPoint-1]
    phase_range = np.arange(1, len(g_o.Phases), 1)
    plt.plot(phase_range, e_1, '--bo', label ='$\epsilon1$')
    plt.plot(phase_range, e_2, '--co', label ='$\epsilon2$')
    plt.plot(phase_range, e_3, '--go', label ='$\epsilon3$')
    plt.plot(phase_range, e_vol, '--yo', label ='$\epsilon_{vol}$')
    plt.plot(phase_range, e_dev, '--o', color='chocolate', label ='$\gamma_{s}$')
    plt.ylabel('Strain')
    plt.xlabel('Phase␣step')
    plt.grid()
    plt.legend()
    plt.title('Strain␣development␣for␣StressID:␣'+str(noStressPoint))
    return
```

```python
def plot_stressstrain_development(noStressPoint):
    e_1 = e1_all[:, noStressPoint-1]
    e_2 = e2_all[:, noStressPoint-1]
    e_3 = e3_all[:, noStressPoint-1]
    stress1 = result_sigmaeffective1(noStressPoint)
    stress2 = result_sigmaeffective2(noStressPoint)
    stress3 = result_sigmaeffective3(noStressPoint)
    plt.plot(e_1,stress1, '--bo', label ='Pr.␣$\sigma1-\epsilon1$:␣major')
    plt.plot( e_2,stress2, '--co', label ='Pr.␣$\sigma2-\epsilon2$:␣in-plane')
    plt.plot(e_3,stress3, '--go', label ='Pr.␣$\sigma3-\epsilon3$:␣minor')
    plt.xlabel('Strain␣[-]')
    plt.ylabel('Effective␣stress␣[kPa]')
    #plt.xlim(-0.5, 0.5)
    plt.grid()
    plt.title('Stress-Strain␣graphs␣for␣StressID:␣'+str(noStressPoint))
    e_hor = ehor_all [:, noStressPoint-1]
    e_ver = ever_all[:, noStressPoint-1]
    e_shear = eshear_all[:, noStressPoint-1]
    st_xx = sigxxT_all[:, noStressPoint-1]
    st_yy = sigyyT_all[:, noStressPoint-1]
    #st_zz = sigzzT_all[:, noStressPoint-1]
    s_xy = sigxy_all[:, noStressPoint-1]
    p_a = pactive_all[:, noStressPoint-1]
    plt.plot(e_hor,st_xx-p_a,  '--o', color = 'slateblue',
            label ='Cart.␣$\sigma-\epsilon$:␣xx')
    plt.plot( e_ver, st_yy-p_a, '--o',color='lime',
            label ='Cart.␣$\sigma-\epsilon$,␣yy')
    plt.plot(e_shear,s_xy,  '--o',color='olive',
            label ='Cart.␣$\sigma-\epsilon$,␣xy')
    plt.legend()
    return

def plot_MC_2(noStressPoint, cc='g',  c=20, phi=5, st=10):
    #define variables
    x = np.linspace(st,-20,100)
    phase_range = np.arange(1, len(g_o.Phases), 1)
    #plot Mohr Coulomb envelope
    y = -c + np.tan(radians(phi))*x
    plt.plot(x,y, 'k-', label='Mohr␣Coulomb␣failure␣envelope')
    plt.plot((st,st), (0, -c - np.tan(radians(phi))*(-st)), 'k-')
    #plot pole
    for i in range(len(phase_range)):
        angledegreepoint = result_sigmaTangle(noStressPoint)[i]
        side1 = np.cos(radians(90-angledegreepoint))*
            (result_sigmaeffective1(noStressPoint)[i]
            - result_sigmaeffective3(noStressPoint)[i])
        side2 = np.cos(radians(90-angledegreepoint))*side1
        xpole = side2 + result_sigmaeffective3(noStressPoint)[i]
        ypole = np.tan(radians(90-angledegreepoint))*side2
        plt.plot(xpole, -ypole, 'kx')
    #plot pq
        plt.text(peffq(noStressPoint)[0][i], peffq(noStressPoint)[1][i], str(i+1))
    plt.plot(peffq(noStressPoint)[0], peffq(noStressPoint)[1], 'o', color = cc)
    #Layout plot
    plt.ylim(bottom = 0)
    plt.gca().invert_xaxis()
```

```
    plt.gca().invert_yaxis()
    plt.xlabel('Effective␣normal␣stress/isotopic␣stress␣[kPa]')
    plt.ylabel('Shear␣stress/deviatoric␣stress␣[kPa]')
    plt.title('Mohr␣Coulomb/␣$p_{eff}$-q␣plot␣for␣stressID␣'+str(noStressPoint))
    plt.grid()
    #plot circles
    for i in range(len(phase_range)):
        ax.add_patch(Circle((peffq(noStressPoint)[0][i], 0),
             peffq(noStressPoint)[1][i], facecolor='none', edgecolor = cc,
             linewidth=3, alpha=0.3))
    return

def plot_location(noStressPoint, cc ='g'):
    plt.title('Location␣of␣stress␣point␣'+str(noStressPoint)+'␣in␣soil␣beam')
    plt.plot(xcoor_array[noStressPoint-1], ycoor_array[noStressPoint-1], 'o',
            color = cc)
    rect = Rectangle((0,0), xmax, -ymax, fill = None, hatch = '//', color = 'silver')
    plt.text(xcoor_array[noStressPoint-1], ycoor_array[noStressPoint-1],
            'stressID:␣'+str(noStressPoint) +'\n
␣␣␣␣␣␣␣␣␣␣␣␣x␣=␣' +str(np.round(xcoor_array[noStressPoint-1],3))+'\n
␣␣␣␣␣␣␣␣␣␣␣␣y␣=␣'+str(np.round(ycoor_array[noStressPoint-1],3)), fontsize=12)
    plt.xlim(-1, xmax+1)
    plt.ylim(-ymax-1, 1)
    ax2.add_patch(rect)
    plt.xlabel('x-coordinate␣[m]')
    plt.ylabel('y-coordinate␣[m]')
    return
```

Plot figures using previous defined functions

```
no_stresspoint = 87
plt.figure(figsize=(12,18))
ax = plt.subplot(421)
plot_MC_2(no_stresspoint, cc='indigo', c=c_a, phi=phi_a, st=ts_a)
ax2 = plt.subplot(422)
plot_location(87, 'indigo')
ax3 = plt.subplot(423)
plot_se_development(no_stresspoint)
ax4 = plt.subplot(424)
plot_st_development(no_stresspoint)
plt.subplots_adjust(wspace=0.2, hspace=0.3)
ax5 = plt.subplot(425)
plot_evoldef_development(no_stresspoint)
plt.ylim(-0.5, 0.5)
ax6 = plt.subplot(426)
plot_ehorvershear_development(no_stresspoint)
plt.ylim(-0.5, 0.5)
ax7 = plt.subplot(427)
plot_stressstrain_development(no_stresspoint)
plt.xlim(-0.5, 0.5)
ax8 = plt.subplot(428)
plot_pwp_development(no_stresspoint)
```

Function to plot stress profile, calculate bending moment and shear force

```
def function(xboundmin, xboundmax, nophase = 2, xcoor_array = xcoor_array,
            stresspoint_array=stresspoint_array, sigxxT_all = sigxxT_all):
    #find right stressIDs in x_range
```

```
xcoor_array_part1 = xcoor_array[xcoor_array<xboundmax]
stresspoint_array_part1 = stresspoint_array[xcoor_array<xboundmax]
xcoor_array_part2 = xcoor_array_part1[xcoor_array_part1>xboundmin]
stresspoint_array_part2 = stresspoint_array_part1[xcoor_array_part1>xboundmin]

#define new variables
phaseindex = nophase - 1
deltasigmah =  np.zeros(len(stresspoint_array_part2))
yh =  np.zeros(len(stresspoint_array_part2))
sigmaxy =  np.zeros(len(stresspoint_array_part2))
epsilonhor = np.zeros(len(stresspoint_array_part2))
epsilonver = np.zeros(len(stresspoint_array_part2))
epsilonshear = np.zeros(len(stresspoint_array_part2))
yinternodes = np.linspace(0, -ymax, len(stresspoint_array_part2)+1)
Mtotal = 0
Vtotal = 0

#calculate variables, sorted
for i in range(len(stresspoint_array_part2)):
    index = int(stresspoint_array_part2[i] - 1)
    deltasigmah[i] = (sigxxT_all[phaseindex, index] - sigxxT_all[0, index])
    sigmaxy[i] = sigxy_all[phaseindex, index]
    epsilonhor[i] = ehor_all[phaseindex, index]
    epsilonver[i] = ever_all[phaseindex, index]
    epsilonshear[i] =  eshear_all[phaseindex, index]
    yh[i] = (ycoor_array[index])
sortindex = np.argsort(yh)
yh_sorted = yh[sortindex[::-1]]
deltasigmah_sorted = deltasigmah[sortindex[::-1]]
sigmaxy_sorted = sigmaxy[sortindex[::-1]]
epsilonhor_sorted = epsilonhor[sortindex[::-1]]
epsilonver_sorted = epsilonver[sortindex[::-1]]
epsilonshear_sorted = epsilonshear[sortindex[::-1]]
for i in range(len(yh_sorted)-1):
    yinternodes[i+1] = (yh_sorted[i] + yh_sorted[i+1])/2

#plot
fig = plt.figure(figsize=(12,12))
plt.subplot(321)
plt.xlabel('x-coordinate␣[m]')
plt.ylabel('y-coordinate␣[m]')
plt.plot(xcoor_array, ycoor_array, 'b.')
for i in range(len(stresspoint_array_part2)):
    index = int(stresspoint_array_part2[i] - 1)
    plt.plot(xcoor_array[index], ycoor_array[index], 'ro')
plt.subplot(322)
for i in range(len(stresspoint_array_part2)):
    index = int(stresspoint_array_part2[i] - 1)
    plt.plot( sigxxT_all[0, index], ycoor_array[index], 'ko')
    plt.plot( sigxxT_all[phaseindex, index], ycoor_array[index], 'mo')
plt.plot( sigxxT_all[0,int(stresspoint_array_part2[0])],
        ycoor_array[int(stresspoint_array_part2[0])], 'ko',
        label='initial␣stress␣distribution')
plt.plot(sigxxT_all[phaseindex,int(stresspoint_array_part2[0])],
        ycoor_array[int(stresspoint_array_part2[0])], 'mo',
        label='stress␣distribution␣after␣load')
```

```python
plt.legend()
plt.grid()
plt.xlabel('Total␣horizontal␣stresses␣[kPa]')
plt.ylabel('y-coordinate␣[m]')
ax = plt.subplot(324)
plt.plot(deltasigmah_sorted,  yh_sorted,  'ro', label='difference␣in␣stress')
plt.legend()
plt.grid()
plt.xlabel('Horizontal␣stresses␣contributing␣to␣moment␣[kPa]')
plt.ylabel('y-coordinate␣[m]')
for i in range(len(yh_sorted)):
    #calculate contributing moment
    sigma_M = deltasigmah_sorted[i]
    deltax_M = yinternodes[i+1]-yinternodes[i]
    Mtotal += sigma_M*(yinternodes[i]+0.5*deltax_M)*deltax_M
    #plot stress diagram
    rect = Rectangle((min(0,sigma_M),yinternodes[i]), np.abs(sigma_M),
            deltax_M, alpha =0.3)
    ax.add_patch(rect)
    plt.title('M␣=␣'+str(-np.round(Mtotal,3))+'␣kNm␣per␣m␣width')
ax = fig.add_subplot(323)
plt.plot(sigmaxy_sorted, yh_sorted, 'ro', label='shear␣stress')
plt.legend()
plt.grid()
plt.xlabel('Shear␣stresses␣contributing␣to␣shear␣force␣[kPa]')
plt.ylabel('y-coordinate␣[m]')
for i in range(len(yh_sorted)):
    #calculate net shear force
    tau_M = sigmaxy_sorted[i]
    #y_M = yh_sorted[i]
    deltax_M = yinternodes[i+1]-yinternodes[i]
    Vtotal += tau_M*deltax_M
    #plot stress diagram
    rect = Rectangle((min(0,tau_M),yinternodes[i]), np.abs(tau_M),
            deltax_M, alpha =0.3)
    ax.add_patch(rect)
    #plt.plot(tau_M, y_M, 'ro')
    plt.title('V␣=␣'+str(-np.round(Vtotal,3))+'␣kN␣per␣m␣width')
plt.subplot(325)
plt.plot(epsilonshear_sorted, yh_sorted, 'o',color='purple',
        label = '$\gamma_{xy}$')
plt.title('Total␣cartesian␣shear␣strain')
plt.legend()
plt.grid()
plt.xlabel('Cartesian␣shear␣strain␣[-]')
plt.ylabel('y-coordinate␣[m]')
plt.subplot(326)
plt.plot(epsilonhor_sorted, yh_sorted, 'o',color='indigo',
        label = '$\epsilon_{xx}$')
plt.plot(epsilonver_sorted, yh_sorted, 'o',color='mediumorchid',
        label = '$\epsilon_{yy}$')
plt.title('Total␣cartesian␣normal␣strains')
plt.legend()
plt.grid()
plt.xlabel('Cartesian␣normal␣strains␣[-]')
plt.ylabel('y-coordinate␣[m]')
```

```
    plt.subplots_adjust(wspace=0.2, hspace=0.3)
    return (-Mtotal)
```

Find interesting stress point and plot figures of stress development of that point

```
findstresspoints(xboundmin=19, xboundmax=20, xcoor_array = xcoor_array,
        stresspoint_array=stresspoint_array)
```

```
function(xboundmin=1, xboundmax=1.5, nophase=7, xcoor_array=xcoor_array,
        stresspoint_array=stresspoint_array)
```

Calculate moment and shear only from stress profiles (no plots)

```
def calculatemoment(xboundmin, xboundmax, nophase = 2, xcoor_array = xcoor_array,
            stresspoint_array=stresspoint_array, sigxxT_all = sigxxT_all):
    #find right stressIDs in x_range
    xcoor_array_part1 = xcoor_array[xcoor_array<xboundmax]
    stresspoint_array_part1 = stresspoint_array[xcoor_array<xboundmax]
    xcoor_array_part2 = xcoor_array_part1[xcoor_array_part1>xboundmin]
    stresspoint_array_part2 = stresspoint_array_part1[xcoor_array_part1>xboundmin]
    #define new variables
    phaseindex = nophase - 1
    deltasigmah =  np.zeros(len(stresspoint_array_part2))
    yh =  np.zeros(len(stresspoint_array_part2))
    sigmaxy =  np.zeros(len(stresspoint_array_part2))
    yinternodes = np.linspace(0, -ymax, len(stresspoint_array_part2)+1)
    Mtotal = 0
    Vtotal = 0
    #calculate variables, sorted
    for i in range(len(stresspoint_array_part2)):
        index = int(stresspoint_array_part2[i] - 1)
        deltasigmah[i] = (sigxxT_all[phaseindex, index] - sigxxT_all[0, index])
        sigmaxy[i] = sigxy_all[phaseindex, index]
        yh[i] = (ycoor_array[index])
    sortindex = np.argsort(yh)
    yh_sorted = yh[sortindex[::-1]]
    deltasigmah_sorted = deltasigmah[sortindex[::-1]]
    sigmaxy_sorted = sigmaxy[sortindex[::-1]]
    for i in range(len(yh_sorted)-1):
        yinternodes[i+1] = (yh_sorted[i] + yh_sorted[i+1])/2
    for i in range(len(yh_sorted)):
        #calculate contributing moment
        sigma_M = deltasigmah_sorted[i]
        deltax_M = yinternodes[i+1]-yinternodes[i]
        Mtotal += sigma_M*(yinternodes[i]+0.5*deltax_M)*deltax_M
        tau_M = sigmaxy_sorted[i]
        Vtotal += tau_M*deltax_M
    return (-Mtotal, Vtotal)

xstep = np.arange(0,40.1,0.5)
phase_string = np.arange(1, len(g_o.Phases), 1)

def calculate_MVline(nophase=2, xstep=xstep):
    M_range = np.zeros(len(xstep)-1)
    V_range = np.zeros(len(xstep)-1)
    for i in range(len(xstep)-1):
        M_range[i], V_range[i] = calculatemoment(xboundmin=xstep[i],
```

```
                xboundmax=xstep[i+1], nophase=nophase, xcoor_array = xcoor_array,
                stresspoint_array=stresspoint_array)
    return M_range, V_range
```

Plot bending moment and shear force diagram

```
plt.figure(figsize=(12,6))
for i in range(len(phase_string)):
    M_range, V_range = calculate_MVline(nophase=phase_string[i], xstep=xstep)
    plt.subplot(121)
    plt.plot(xstep[:-1], M_range, '.',
            label='q='+str(np.round(load_string[phase_string[i]-1], 2)))
    plt.legend()
    plt.xlabel('x-coordinate␣[m]')
    plt.ylabel('bending␣moment␣[kNm␣per␣m␣width]')
    plt.title('Bending␣moment␣in␣the␣beam␣under␣different␣loads')
    plt.grid()
    plt.subplot(122)
    plt.plot(xstep[:-1], V_range, '.',
            label='q='+str(np.round(load_string[phase_string[i]-1], 2)))
    plt.legend()
    plt.xlabel('x-coordinate␣[m]')
    plt.ylabel('shear␣force␣[kN␣per␣m␣width]')
    plt.title('Shear␣force␣in␣the␣beam␣under␣different␣loads')
    plt.grid()
```

H

ANALYTICAL DERIVATION OF CRITICAL THICKNESSES FOR TENSILE CRACKS

H.1. INTRODUCTION

In this Appendix, a detailed description is given on how the proposed analytical equations are obtained including step wise equations. The analytical equation for tensile cracks is discussed here. The uplifted cover layer is schematized as a beam, with a constant upward pressure q, see Figure H.1.

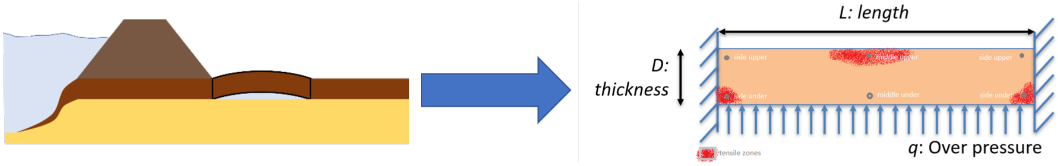

Figure H.1: Beam schematization of the uplift zone in the hinterland

H.2. CRITICAL THICKNESS FOR TENSILE CRACKS

Using the same approach as deriving the Rankine states and the free-standing height (Verruijt and Van Baars, 2007), a formulation for the critical thickness against tensile cracks can be found. This approach is based on the Mohr-Coulomb criterion. First, the point of interest is explained before explaining the key features of the critical Mohr's circle in Figure H.3. Subsequently, the derivation of the critical thickness against tensile cracks is explained, and the influence of the type of soil on the stress path is discussed.

POINT OF INTEREST

The location of the point of interest to evaluate the Mohr's circle is at the edge of the beam, at the bottom of the cover layer. Here, the bending moment is nonzero, as is proven by results from Plaxis, see Figure H.2. For small loads, the beam's ends act as fixities, and the beam responds elastically. The moment- and shear diagrams then correspond to the outcomes from the linear elastic beam theory. For larger loads, the soil starts to behave plastically and the beam's ends can be schematized as pinned supports with a torsional spring. Either way, a tensile zone is expected at the bottom of the cover layer, which is also observed in results by Hoffman (2019). If a tensile crack opens up at this location, it will propagate to the top and form an exit point in the cover layer. Also, the shear force is largest at the end of the beam and could lead to a shear fracture.

KEY FEATURES OF MOHR'S CIRCLES AND THE COULOMB ENVELOPE

To evaluate the stress-state, Mohr's circles can be used. The Mohr-Coulomb theory is explained first: A point on the Mohr's circle defines the normal stress and the shear stress in a certain plane. The Coulomb envelope defines the failure criterion for shear and contains the strength parameters cohesion and friction. When the Mohr's circle touches the Coulomb envelope, the maximum shear stress has reached (Verruijt and Van Baars, 2007). Furthermore, a vertical line is added to represent the tensile strength to account for the tensile failure

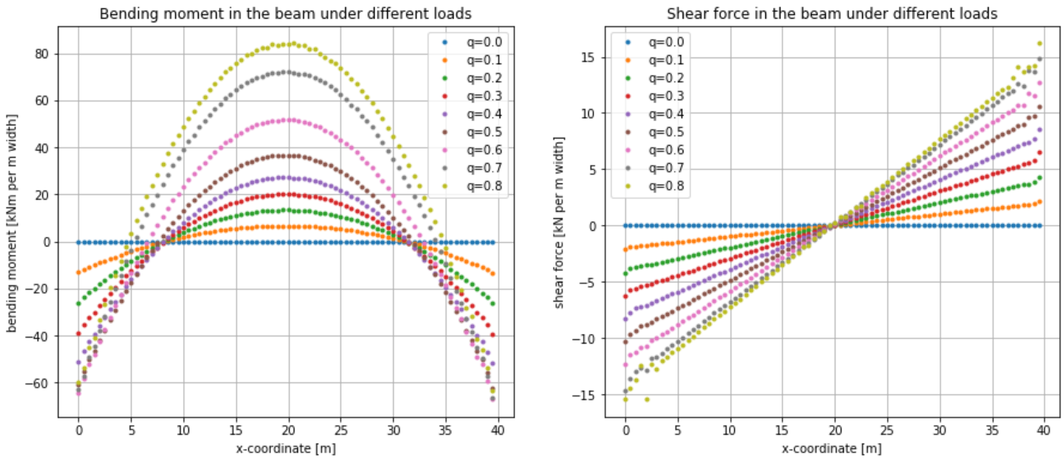

Figure H.2: Plaxis results of bending moment and shear force in the beam under different loads (Mohr-Coulomb soil model, L=40m, D=4 m, c'=5 kPa, '=25°, '=0.35, E' = 1 MPa, tension cut-off = 2.5 kPa, no tensile softening)

criterion.

One specific Mohr's circle (Figure H.3) is defined for finding the critical thickness for tensile failure. This circle is positioned such that it represents the transition circle between tensile and shear failure. When the soil hits the tensile capacity, it fails in a brittle way (see Appendix E). With this Mohr's circle defined, the critical effective isotropic stress is found at failure. This critical value has the following meaning: if p' at failure is higher, the soil at the bottom-end location reaches the maximum shear stress. If p' at failure is lower, a tensile failure is expected. The critical value p' depends on the strength parameters cohesion (c'), friction (ϕ'), and tensile strength (σ'_t).

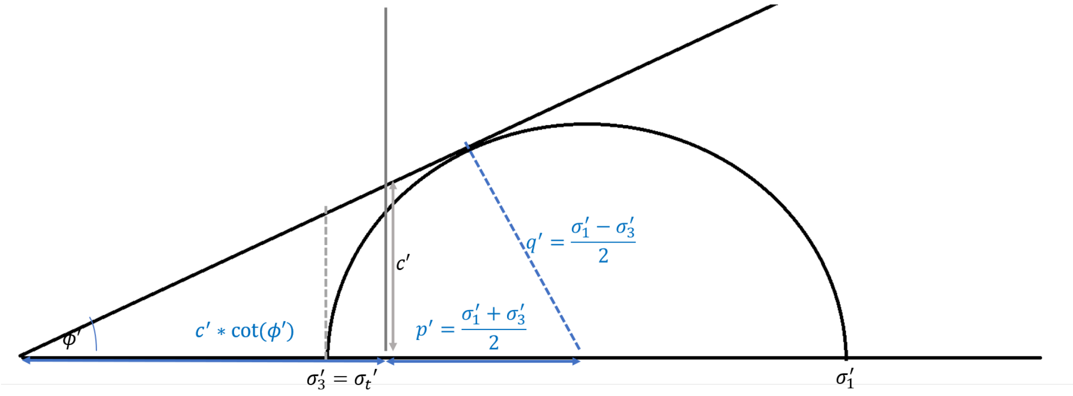

Figure H.3: Mohr-Coulomb circle for critical thickness

For the Mohr's cirlce in Figure H.3, one can come to an expression for the effective isotropic stress in the following way:

$$\sin(\phi') = \frac{q'}{p' + c' * cot(\phi)} = \frac{\frac{\sigma'_1 - \sigma'_3}{2}}{\frac{\sigma'_1 + \sigma'_3}{2} + c' * cot(\phi')}$$

$$\frac{\sigma'_1 - \sigma'_3}{2} = \sin(\phi')\left(\frac{\sigma'_1 + \sigma'_3}{2} + c' * \cot(\phi\prime)\right)$$

$$\sigma'_1 - \sigma'_3 = \sigma'_1 * \sin(\phi') + \sigma'_3 * \sin(\phi') + 2c' * \cot(\phi\prime) * \sin(\phi')$$

$$\sigma_1' - \sigma_1' * \sin(\phi') = \sigma_3' + \sigma_3' * \sin(\phi') + 2c' * \frac{\cos(\phi')}{\sin(\phi')} * \sin(\phi')$$

$$\sigma_1' * (1 - \sin(\phi')) = \sigma_3' * (1 + \sin(\phi')) + 2c' * \cos(\phi')$$

$$\sigma_1' = \frac{1 + \sin(\phi')}{1 - \sin(\phi')} * \sigma_3' + 2c' * \frac{\cos(\phi')}{1 - \sin(\phi')}$$

In which, from Verruijt and Van Baars (2007):

$$\frac{\cos(\phi')}{1 - \sin(\phi')} = \frac{\sqrt{1 - \sin^2(\phi')}}{1 - \sin(\phi')} = \frac{\sqrt{(1 - sin(\phi'))(1 + sin(\phi'))}}{1 - \sin(\phi')} = \sqrt{\frac{1 + \sin(\phi')}{1 - \sin(\phi')}}$$

So, substituting this, finding a relation between the principal stresses when touching the MC-envelope:

$$\sigma'_1 = \frac{1 + \sin(\phi')}{1 - \sin(\phi')}\sigma'_3 + 2c'\sqrt{\frac{1 + \sin(\phi')}{1 - \sin(\phi')}}$$

When substituting σ'_3 for σ'_t, then isotropic stress can be computed:

$$p' = \frac{\sigma_1' + \sigma_3'}{2} = \frac{\frac{1+\sin(\phi')}{1-\sin(\phi')}\sigma'_3 + 2c'\sqrt{\frac{1+\sin(\phi')}{1-\sin(\phi')}} + \sigma'_3}{2}$$

H.2.1. VERTICAL EFFECTIVE STRESS PATH

The first assumption is based on a vertical effective stress path. Then, using the following assumptions:

- $K_o = 1 - \sin(\phi')$
- $\sigma'_{1,\,init} = \gamma_{eff} * D$, in which D is the maximum thickness a crack can occur

$$p' = \frac{\sigma'_{1,\,init} + \sigma'_{3,\,init}}{2} = \frac{\sigma'_{1,\,init} + \sigma'_{1,\,init}(1 - \sin(\phi'))}{2}$$

$$\frac{\frac{1+\sin(\phi')}{1-\sin(\phi')}\sigma'_3 + 2c'\sqrt{\frac{1+\sin(\phi')}{1-\sin(\phi')}} + \sigma'_3}{2} = \frac{\sigma'_{1,\,init} + \sigma'_{1,\,init}(1 - \sin(\phi'))}{2}$$

$$\frac{1 + \sin(\phi')}{1 - \sin(\phi')}\sigma'_3 + 2c'\sqrt{\frac{1 + \sin(\phi')}{1 - \sin(\phi')}} + \sigma'_3 = \sigma'_{1,\,init} + \sigma'_{1,\,init}(1 - \sin(\phi))$$

$$\gamma_{Eff} * D * (2 - \sin(\phi)) = \frac{1 + \sin(\phi')}{1 - \sin(\phi')}\sigma'_3 + 2c'\sqrt{\frac{1 + \sin(\phi')}{1 - \sin(\phi')}} + \sigma'_3$$

$$D = \frac{\frac{1+\sin(\phi')}{1-\sin(\phi')}\sigma'_3 + 2c'\sqrt{\frac{1+\sin(\phi')}{1-\sin(\phi')}} + \sigma'_3}{\gamma_{Eff}(2 - \sin(\phi'))}$$

H.2.2. Stress paths and Skempton's A parameter

Skempton's experimental formula is the change in pore water pressure as an expression by the change in total stress. Skempton's B stands for the change in pore pressure as a result of a change in confining stress. If B=0, the case is fully drained, and B=1, the case is idealized undrained (poisons ratio = 0.5). The value of B depends on the degree of saturation and the soil type. Skempton's A stands for the change in pore pressure by changing deviatoric stress. This is the so-called shear-induced pore pressure. For an idealized undrained test with a linear elastic, A=1/3 and the p-q-diagram shows a vertical line. The value of A depends on the soil type too (Brinkgreve, 2019).

For normally consolidated soil, the material tends to shrink during shear. This leads to a relatively large increase in the pore pressures, thus a decrease in the isotropic effective stress. The stress path will have a curve to the left. An indication is that A is between 1/3 and 5/6 for normally consolidated clay. For very soft clay and peat, A lies between 5/6 and 4/3.

For heavily overconsolidated soils, the change in pore pressure is relatively small or absent. Any increase in deviatoric load leads to an increase in mean effective stress. As a result, the stress path goes to the right. For heavily overconsolidated clay, A is about -1/6.

Taking the conservative value for soft soils, A=4/3, this leads to another assumption. The stress path then develops under an angle of 45 degrees. The starting point for the initial istropic stress differs, and it leads to twice the value for critical thickness.

$$p'_{init} = p'_{failure} + q_{failure} = \frac{\sigma'_1 + \sigma'_3}{2} + \frac{\sigma'_1 - \sigma'_3}{2} = \sigma'_{1,failure} = \frac{1+\sin(\phi')}{1-\sin(\phi')} * \sigma'_t + 2c'\sqrt{\frac{1+\sin(\phi')}{1-\sin(\phi')}}$$

For very soft and normally consolidated soils, the critical thickness is better to use double the value than the value found before based on the Mohr-Coulomb model. However, this conservative assumption can be avoided by obtaining the overconsolidation ratio in the field. Also, when the pore water pressures intrude, the effective stress decreases thus the overconsolidation ratio increases. It can be argued that the cover layer in uplift conditions behaves overconsolidated.

I

CASE WAM DP47

This Appendix contains the results of determining the safety against uplift using different methods. The location of interest is within the project Wijk bij Duurstede - Amerongen (WAM), the Netherlands. It is the north dike stretch of river 'Lek' and part of dike ring 44, under the water board 'Hoogheemraadschap De Stichtse Rijnlanden' (HDSR).

The cross-section selected here is at DP47, just south of the Willemshoeve, which is part of trajectory 44-04. This location is selected because of various reasons. Firstly, it has a thick cover layer of about 5 meters thick, and it is considered not safe enough based on a current assessment. Secondly, abundant geotechnical information is available, including results of CPTs, borings, and lab experiments.

This case has the following structure: First, the relevant data of the cover layer at this location is collected. Second, the safety assessment for this stretch is gone through in different steps:

- a. The current (semi-probabilistic) approach is reproduced and discussed.
- b. An updated semi-probabilistic approach
- c. A fully probabilistic approach
- d. A new model for uplift

Lastly, the outcomes of the different models are compared and discussed. The data is provided generously by Leo Kwakman of Arcadis.

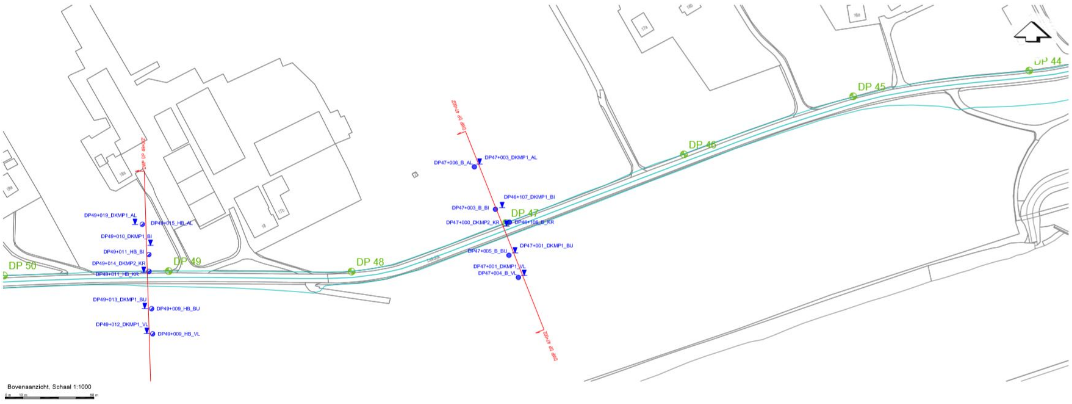

Figure I.1: Location of DP 47 (note: the Willemshoeve is located at the upper left)

I.1. DATA COLLECTION FOR DIKERING 44 DP47

I.1.1. LOCATION

The location of the area of interest is shown in Figures I.1 and I.2. Figure I.3 shows the cross section as indicated in Figure I.1, including the CPTs and the borings. For uplift, the interest goes to the subsoil composition at the hinterland (’*Achterland*’ = AL). The subsoil is discussed further in section I.1.3.

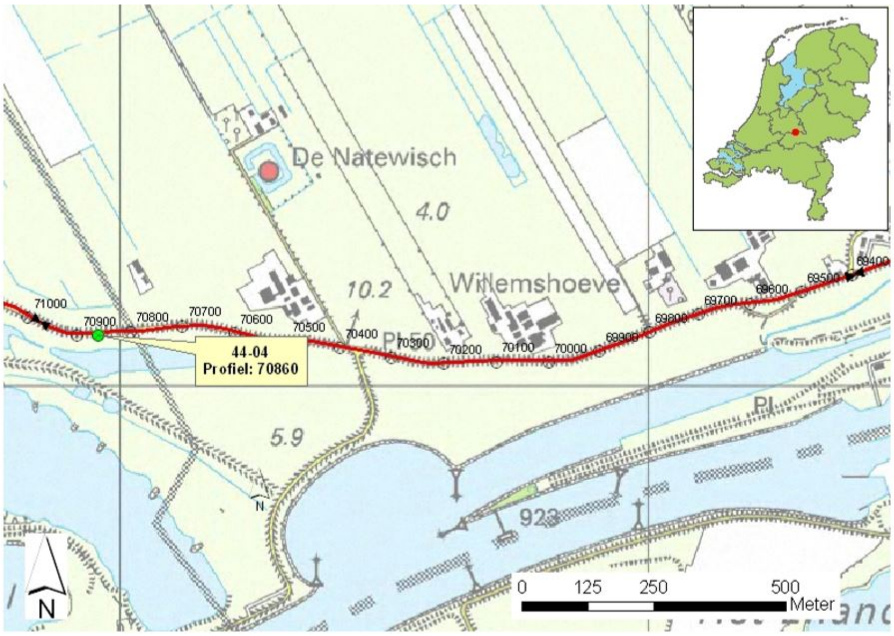

Figure I.2: Dike stretch 44-04 (Bisschop et al., 2011)

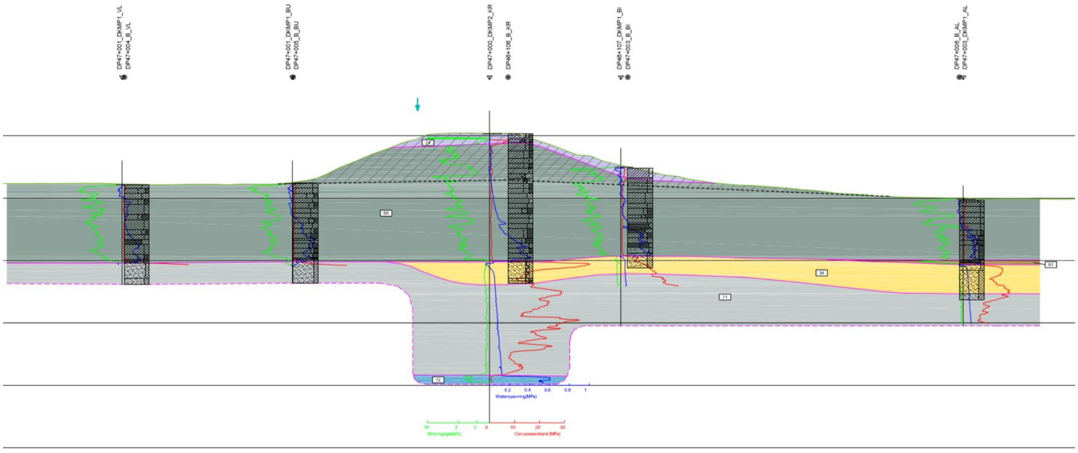

Figure I.3: Cross-section of DP 47

I.1.2. HYDRAULIC CONDITIONS

The design water level (’maatgevend waterhoogte’ = MHW) equals 9.21 m, which includes 0.1 m of subsoil subsidence, corresponding to a return period of 10000 years. This value holds for DP40 to DP48, within dike stretches 44-03 and 44-04. At dike stretch 44-06, there are water levels known per return period:

- T = 300 years: h = 8.363 m + NAP
- T = 1000 years: h = 8.678
- T = 3000 years: h = 9.005

- T = 10 000 years: h = 9.377
- T = 30 000 years: h = 9.714
- T = 100 000 years: h = 10.083

Approximating the decimate height $h_{dec} \sim 0.7m$, the local Gumbel parameters are obtained:

$$\alpha = \frac{ln(-ln(1-F_{exc})) - ln(-ln(1-F_{exc}/10))}{h_{dec}} = \frac{ln(-ln(1-1/10000)) - ln(-ln(1-1/100000))}{0.7} = 3.29 \quad (I.1)$$

$$u = MHW + \frac{1}{\alpha} * ln(-ln(1-F_{exc})) = 9.21 + \frac{1}{3.29} * ln(-ln(1-1/10000)) = 6.41 \quad (I.2)$$

I.1.3. SUBSOIL (CPTS AND BORINGS)

The boring of the hinterland at DP47 is shown in Figure I.5. The CPT at the same location is shown in Figure I.6. In the interpretation of the CPT, one makes a distinction between light and heavy clay. This distinction is used later for determining an average volumetric weight.

I.1.4. VOLUMETRIC WEIGHT

The volumetric weight was measured at the laboratory. Table I.1 gives an overview of the obtained volumetric weights for different soil types. From Figure I.4, the average volumetric weights are retrieved, which are 16.5, 19, and 12 kN/m3 for light clay, heavy clay, and peat, respectively. The coefficient of variation is assumed to be 5%.

Table I.1: Volumetric weight of DP46-47

soil type	γ [kN/m3]	location	soil type	γ [kN/m3]	location	soil type	γ [kN/m3]	location
light clay	14,3	DP47AL	heavy clay (unsat)	15,5	DP47VL	peat	11,6	DP47BI
light clay	15,2	DP46KR	heavy clay (unsat)	17,2	DP47VL	peat	12	DP47BI
light clay	15,2	DP46KR	heavy clay (sat)	18,4	DP46KR	peat	12	DP47BI
light clay	15,3	DP47BU	heavy clay (sat)	18,6	DP46KR	peat	12,1	DP47AL
light clay	15,9	DP47AL	heavy clay (sat)	18,9	DP46KR	peat	12,5	DP47VL
light clay	16	DP47VL	heavy clay (sat)	18,9	DP46KR			
light clay	16	DP47BU	heavy clay (top)	19,2	DP47BU			
light clay	16	DP47AL	heavy clay (unsat)	19,3	DP47BU			
light clay	16,3	DP47AL	heavy clay (unsat)	19,3	DP47BU			
light clay	16,4	DP47BU	heavy clay (sat)	19,4	DP46KR			
light clay	17	DP46KR	heavy clay (sat)	19,5	DP46KR			
light clay	17	DP47VL	heavy clay (top)	19,7	DP47VL			
light clay	17,2	DP46KR	heavy clay (sat)	19,9	DP46KR			
light clay	17,5	DP47BU						
light clay	17,8	DP47BU						
light clay	18,4	DP46KR						

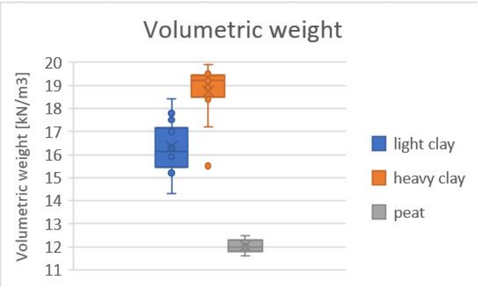

Figure I.4: Box and whisker plot of volumetric weight

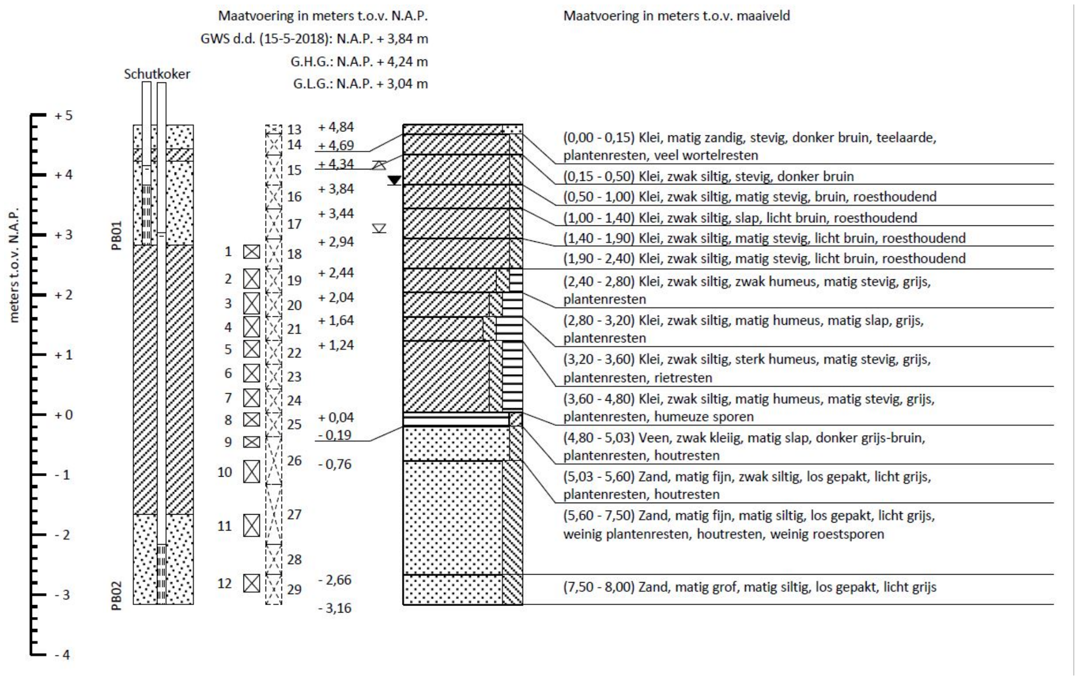

Figure I.5: Boring of hinterland at DP 47

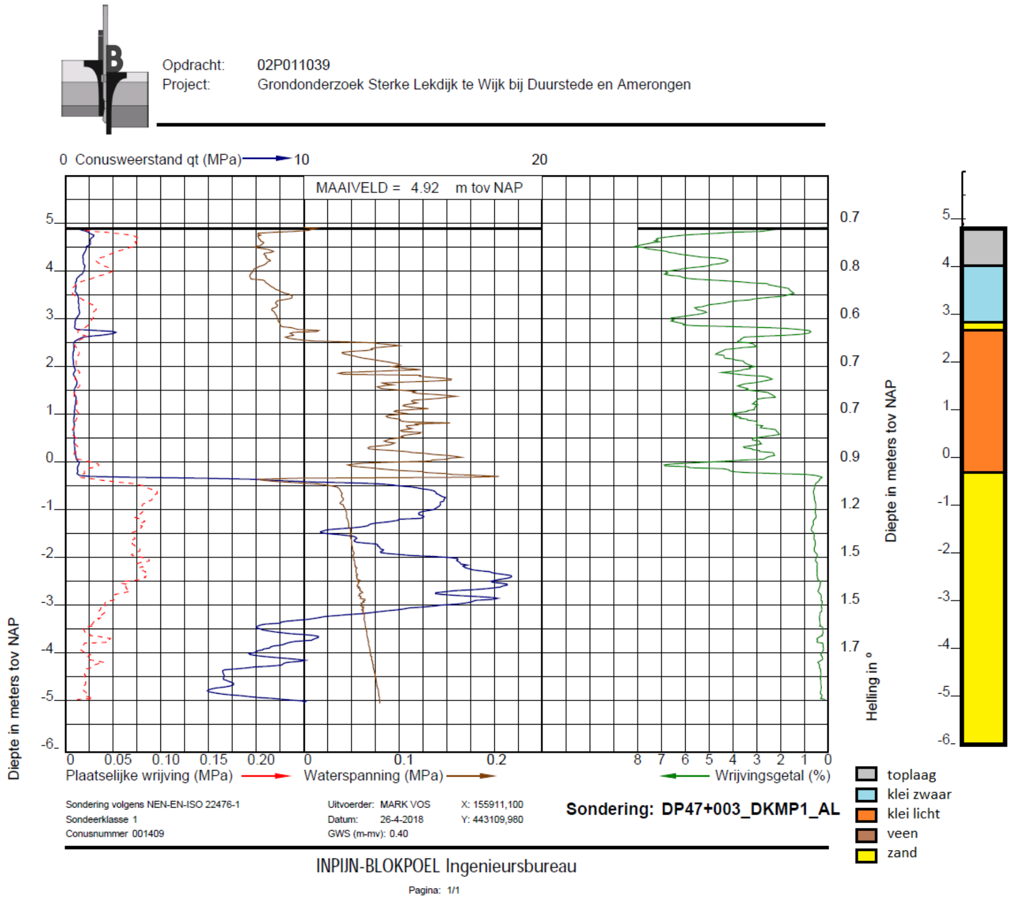

Sondering volgens NEN-EN-ISO 22476-1
Sondeerklasse 1
Conusnummer 001409

Uitvoerder: MARK VOS
Datum: 26-4-2018
GWS (m-mv): 0.40

X: 155911,100
Y: 443109,980

Sondering: DP47+003_DKMP1_AL

INPIJN-BLOKPOEL Ingenieursbureau

Pagina: 1/1

Figure I.6: CPT of hinterland at DP 47, including interpretation

I.1.5. OTHER PARAMETERS

There are also other parameters. These are given in Table I.2 and based on extensive geotechnical studies (Kwakman, 2019).

Table I.2: Overview of other parameters

Parameter	Value	Comment
Permeability cover layer	$k_{cover} = 0.2\ m/d$	Default value
Permeability aquifer	$k_{aq} = 70\ m/d$	Obtained using tests
Permeability foreland	$k_f = 1\ m/d$	Default value
Thickness aquifer	$D_{aq} = 11.75\ m$	from CPT DP47KR
Thickness foreland	$D_f = 1.5\ m$	measured in field
Length foreland	$L_f = 15\ m$	Real value = 5 m, characteristic value = 15 m
Length hinterland	$L_h = 5000\ m$	distance to Amerongse Wetering = 1.35 km, default value = 5000 m
Toe-to-toe distance dike	$B = 51\ m$	measured in field
Hinterland waterlevel (PolderPeil)	$PP = 5.27m$ +NAP	PP = 2.6 m +NAP, Lowest point = 4.37 m+NAP, characteristic value = Lowest point in hinterland + 0.3 m safe value = ground surface = 5.27 m +NAP

I.2. SAFETY ASSESSMENT

I.2.1. REPRODUCTION OF CURRENT APPROACH

The current approach, as presented in the Excel sheets, makes use of the parameter as presented in Section I.1. The calculated safety factor is 1.256, whereas the prescribed safety factor is 1.78 for piping which a return period of 10000 years and $\omega = 0.24$.

$$\gamma_{up} = \frac{(\gamma_{sat} - *\gamma_{water}) * D_{cover}}{((MHW - PP) * r_{exit} + PP - h_{exit}) * \gamma_{water}} = \frac{(18.35 - 9.81) * 5}{((9.21 - 5.27) * 0.874 + 5.27 - 5.27) * 9.81} = 1.26 \tag{I.3}$$

Some values are explained in detail hereafter.

VOLUMETRIC WEIGHT

It assumes that the volumetric weights for light clay and heavy clay are 16.6 and 19.5 kN/m^3, respectively. Also, for every location, it is assumed that the first 3 meters consist of heavy clay, and the remaining thickness consists of light clay. The average volumetric weight taken is 18.35 kN/m^3.

$$\gamma_{sat} = (3 * 19.5 + (D_{cover} - 3) * 16.6)/D_{cover} = (3 * 19.5 + (2) * 16.6)/5 = 18.35\ kN/m^3 \tag{I.4}$$

However, looking at the CPT and boring, this assumption can be improved. Neglecting the thin peat layer, a better subsoil characterization would be 2 meters of heavy clay and 3 meters of light clay. Using the volumetric weights from Figure I.4, the average volumetric weight is:

$$\gamma_{sat} = (2 * 19 + 3 * 16.5)/d_{cover} = (2 * 19 + 3 * 16.5)/5 = 17.5\ kN/m^3 \tag{I.5}$$

DAMPING FACTOR

The damping factor is computed as follows:

$$r_{exit} = \frac{\lambda_h * tanh(L_h/\lambda_h)}{B + \lambda_f * tanh(L_f/\lambda_f) + \lambda_h * tanh(L_h/\lambda_h)} = \frac{453.5 * tanh(\frac{5000}{453.5})}{51 + 35.12 * tanh(\frac{15}{35.12}) + 453.5 * tanh(\frac{5000}{453.5})} = 0.874 \tag{I.6}$$

In which:

$$\lambda_h = \sqrt{k_{aq} * D_{aq} * D_{cover} / k_{cover}} = \sqrt{70 * 11.75 * 5/0.02} = 453.5$$

$$\lambda_f = \sqrt{k_{aq} * D_{aq} * D_f / k_f} = \sqrt{70 * 11.75 * 1.5/1} = 35.12$$

HINTERLAND POLDER WATER LEVEL

In many calculations, the far-field polder head is assumed to equal to the head in the cover layer at the exit point ($h_{exit} \approx \phi_{polder}$). Figure I.7 shows the location and the definition of these heads.

$$\phi_{exit} = \phi_{polder} + r_{exit}(h - \phi_{polder}) \qquad (1)$$

Waarin:

h	Niveau van de buitenwaterstand ten opzichte van NAP (verondersteld als stijghoogte bij intredepunt) [m].
ϕ_{exit}	Stijghoogte in de watervoerende laag bij het uittredepunt ten opzichte van NAP [m].
ϕ_{polder}	Stijghoogte in polder (stationaire toestand, randvoorwaarde aan rechterkant) [m].
r_{exit}	Dempingsfactor (over de afstand intredepunt – uittredepunt) [-].

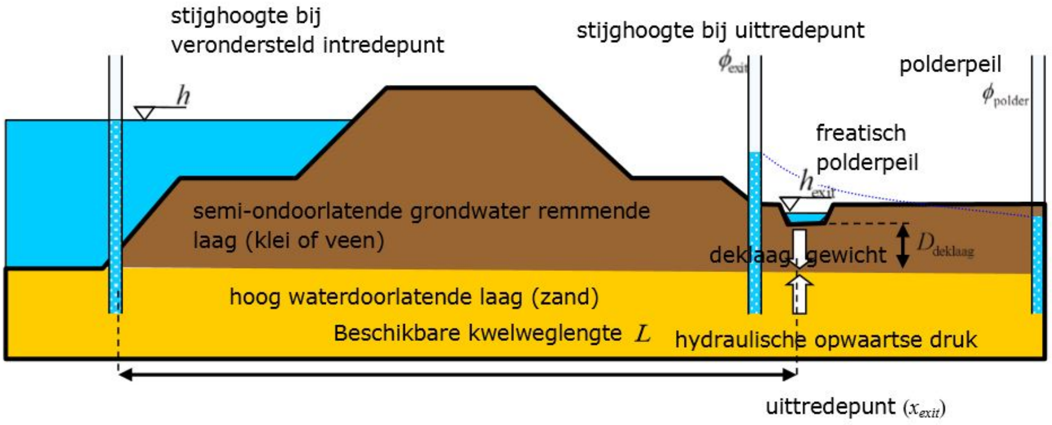

Figuur C.1 Schematische dwarsdoorsnede dijk met de voor piping relevante parameters

Figure I.7: Graphic visualization of heads (Ministerie van Infrastructuur en Milieu, 2017)

In the current calculations, both h_{exit} and ϕ_{polder} are taken as 5.27 m+NAP, which equals to the ground surface at the exit point. However, the characteristic value for ϕ_{polder} is 4.67 m. This value is taken as the lowest location in the hinterland + 0.3 m.

I.2.2. UPDATED SEMI-PROBABILISTIC APPROACH

The current approach in Excel makes use of conservative assumptions, but it is unclear which values are deterministic and which are characteristic design values. Table I.3 shows clearly which standard deviations are used for the characteristic values. The safety factor should be computed with characteristic values. Compared to the current approach, as is done in the WAM report, this value is lower.

$$\gamma_{up} = \frac{\gamma_{eff,sat,cover} * d_{cover}}{((MHW - PP) * r_{exit} + PP - h_{exit}) * \gamma_{water}} = \frac{6.25 * 4.19}{((9.21 - 4.67) * 0.954 + 4.67 - 5.16) * 9.81} = 0.69 \qquad (I.7)$$

I.2.3. FULLY PROBABILISTIC APPROACH

The probabilistic equation of the current safety assessment is:

$$Z = m_u * D_{cover} * \gamma_{eff}/\gamma_w - \left(h_{polder} + (h_{river} - h_{polder}) * r_{exit} - h_{exit}\right) \tag{I.8}$$

The reliability index for DP47 is $\beta = 3.74$, corresponding to a return period of 5988 years. The probabilistic calculation is based on a Monte Carlo analysis with $n = 10^7$. The input parameters are given in Table I.3. When looking critically at the uplift assessment, a sensibility analysis is done for several propositions. Firstly, the model factor is a matter of discussion. When this factor is ignored, the β increases to 3.91. Secondly, it is argued that sometimes the Monte Carlo simulation might give unrealistic values due to high deviations. In this case, if the values of the volumetric weight and damping factor are clipped, i.e., specifying a minimum and maximum value, it does not change the reliability index. Thirdly, the standard deviations for the effective volumetric weight and effective thickness might be too large as a result of an over-conservative assumption. It leads to a safety factor of 3.89 and 3.77, respectively. The conclusion from this sensitivity analysis is that an improvement in the model factor and the deviation of the volumetric weight would lead to the largest increase in the reliability index.

Table I.3: Input parameters for uplift calculation

Symbol [unit]	Description	Distribution type	Mean	Variation	$char$ value
m_u [-]	Model factor for uplift	log-normal	$\mu = 1.0$	$cov = 10\%$	1.0
γ_{water} [kN/m^3]	Volumetric weight of water	-	9.81	-	9.81
$\gamma_{eff,sat,cover}$ [kN/m^3]	Effective saturated volumetric weight of the cover layer	log-normal	$\mu = 17.5\text{-}9.81$	$cov = 5\%$	6.25
r_{exit} [-]	Damping factor at exit	log-normal	0.874	$cov = 5\%$	0.954
D_{cover} [m]	Effective thickness of the cover layer	log-normal	$\mu = 5$	$\sigma = 0.25$	4.17
h_{exit} [m + NAP]	Phreatic level at the exit point	normal	$\mu = 5.27$	$\sigma = 0.05\%$	5.17
ϕ_{polder} [m + NAP]	Hinterland water level	normal	$\mu = 4.37$	$\sigma = 0.15$	4.67
h [m + NAP]	Outside water level	Gumbel	u = 6.41	$\alpha = 3.29$	MHW = 9.21

RESULTS FOR DP42-47

Table I.4: Result with average values, except MHW and hp

DP	**safety factor**
42	1.078139
43	1.128359
44	1.398158
45	1.572036
46	1.523414
47	1.162842

Table I.5: Result with characteristic values and $(\gamma_{eff,sat}) = 5\%$, $\sigma(d) = 0.25\ m$

DP	**beta**	**safety factor**
42	3.459	0.768952
43	3.631	0.806337
44	4.293	0.999638
45	4.645	1.129619
46	4.519	1.099906
47	3.744	0.821492

Table I.6: Result with ignoring model factor and $(\gamma_{eff,sat}) = 5\%$, $\sigma(d) = 0.25$ *m*

DP	beta	safety factor
42	3.668	0.768952
43	3.826	0.806337
44	4.506	0.999638
45	4.825	1.129619
46	4.825	1.099906
47	3.910	0.821492

Table I.7: Result with clipped values for rexit, $(\gamma_{eff,sat}$ *and cov* $(\gamma_{eff,sat}) = 5\%$, $\sigma(d) = 0.25$ *m*

DP	beta	safety factor
42	3.455	0.768952
43	3.630	0.806337
44	4.260	0.999638
45	4.700	1.129619
46	4.482	1.099906
47	3.739	0.821492

Table I.8: Result with cov$(\gamma_{eff,sat}) = 2.5\%$, $\sigma(d) = 0.25$ *m*

DP	beta	safety factor
42	3.635	0.851929
43	3.793	0.891667
44	4.494	1.105715
45	4.803	1.249350
46	4.753	1.217023
47	3.888	0.912603

Table I.9: Result with cov $(\gamma_{eff,sat}) = 5\%$, $\sigma(d) = 0.125$ *m*

DP	beta	safety factor
42	3.502	0.804999
43	3.661	0.844540
44	4.301	1.042602
45	4.601	1.173964
46	4.592	1.142115
47	3.770	0.859680

I.2.4. UPLIFT SOIL BEAM MODEL

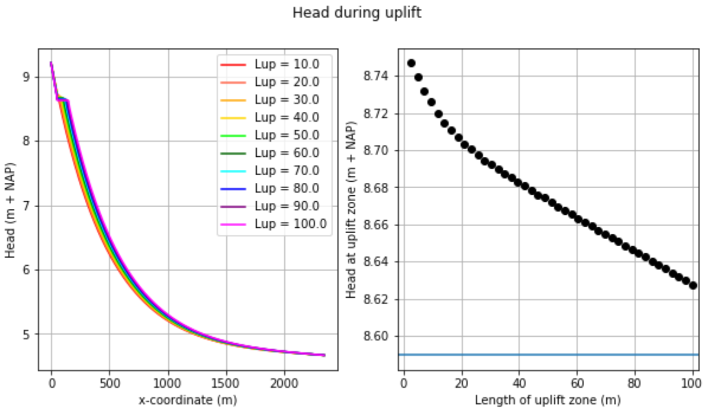

Figure I.8: Head profile and head in uplift zone for DP47, MHW=9.21 m +NAP

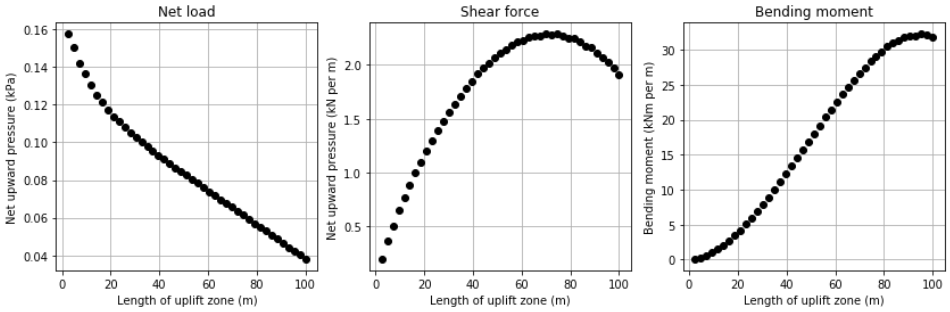

Figure I.9: Expected shear en bending loads DP47, MHW=9.21 m +NAP

WATER/LOAD

The evaluation of the new model is done for location DP47. The leakage factor of the hinterland equals 458 m. The model domain is taken as five times the leakage length, which is here 2342 m. Using the geometry and hydraulic conductivity values from Table I.2, the FD geohydrological model is set up. Figure I.8 shows the result of the model outcome, in terms of the range of heads and corresponding uplift lengths for a mean high water river level of 9.21 m.

SOIL/RESISTANCE

Based on Figure I.9, failure is expected either for L=70 m, q=0.07 kPa (normative for shear) or for L=90 m, q=0.05 kPa (normative for bending). Both lengths were evaluated in Plaxis. For L=90 m, the failure of the beam occurred at 0.3 kPa. For L=70 m, this was at 0.5 kPa.

Extra input parameters are needed to evaluate the soil beam behavior. For clay at DP47, the E_{oed} is found at 1.8 MPa from an oedometer test. From a CD triaxial test, E_{50} is found at 2.8 MPa. E_{ur} is assumed eight times larger than E_{50} (CUR2003-7) , thus equals 22.4 MPa. For the remaining soil parameters, a distinction is made between light clay and heavy clay. For light clay, $\gamma = 16.5 kN/m^3$, $\phi' = 30.8°$, and $c' = 3.28 kPa$. For heavy clay, $\gamma = 19 kN/m^3$, $\phi' = 30.4°$, and $c' = 4.93 kPa$ (Kwakman, 2019). For both clay types, the tensile capacity is assumed to be half the value of the effective cohesion (Bagge, 1985).

Using both 2D models for the geohydrology and the soil beam, it is found that for cross-section DP47 the forming of a full crack during uplift will not occur. However, using this approach, it is difficult to define a degree of safety by means of a safety factor or reliability index.

I.2.5. SHEAR AND TENSILE CRACKS

Here, the safety against shear and tensile cracks is evaluated, based on the equations below. A probabilistic calculation is performed for shear cracks only because these are normative over tensile cracks. The probabilistic approach is based on a Monte Carlo analysis with $n = 10^8$ draws and the input parameters from Table I.10. For DP47, the reliability index against cracking is found to be 4.56, which is below the requirement of 5.03. However, for some other cross-sections between DP42 and DP47, the calculated reliability index exceeded the requirement, see Table I.11.

$$Z_{tensilecrack} = m_u * D_{cover} * \gamma_{eff} * (2 - \sin(\phi')) - \left(\frac{1+\sin(\phi')}{1-\sin(\phi')} \sigma'_t + 2c' * \sqrt{\frac{1+\sin(\phi')}{1-\sin(\phi')}} + \sigma'_t \right) \tag{I.9}$$

$$Z_{shearcrack} = m_u * D_{cover} * D_{aq} * K_{aq} * \gamma_{eff}^2 + f(s_u) - D_{aq} * K_{aq} * \gamma_{eff} * \gamma_w * \Delta h_{up} \tag{I.10}$$

In which:

$$\Delta h_{up} = h_{polder} + 0.71 * (h_{river} - h_{polder}) - h_{exit} \tag{I.11}$$

$$f(s_u) = 8 * \sqrt{D_{aq} * K_{aq} * k_{cover} * \gamma_{eff} * \gamma_w * \Delta h_{up} * s_u^2 + 16 * k_{cover}^2 * s_u^4} - 32 * k_{cover} * s_u^2 \tag{I.12}$$

$$s_u = \alpha * \gamma_{eff} * 0.5 * D_{cover} * OCR^m \tag{I.13}$$

Table I.10: Input parameters for uplift calculation, for shear and tensile cracks

Symbol [unit]	Description	Distribution type	Mean	Variation	*char* value
m_u [-]	Model factor for uplift	log-normal	$\mu = 1.0$	$cov = 10\%$	1.0
γ_{water} $[kN/m^3]$	Volumetric weight of water	-	9.81	-	9.81
$\gamma_{eff,sat,cover}$ $[kN/m^3]$	Effective saturated volumetric weight of the cover layer	log-normal	$\mu = 17.5$-9.81	$cov = 5\%$	
r_{exit} [-]	Damping factor at exit	log-normal	$\mu = 0.874$	$cov = 1\%$	
D_{cover} $[m]$	Effective thickness of the cover layer	log-normal	$\mu = 5$	$\sigma = 0.25$ m	
D_{aq} $[m]$	Thickness of the aquifer	log-normal	$\mu = 10$	$\sigma = 0.5$ m	
k_{cover} $[m/d]$	Vertical permeability of the cover layer	log-normal	$\mu = 0.02$	$cov = 10$ %	
k_{aq} $[m/d]$	Horizontal permeability of the aquifer	log-normal	$\mu = 70$	$cov = 10$ %	
h_{exit} $[m +$ NAP]	Phreatic level at the exit point	normal	$\mu = 5.27$	$\sigma = 0.05$ m	
ϕ_{polder} $[m +$ NAP]	Hinterland water level	normal	$\mu = 4.37$	$\sigma = 0.15$ m	
h $[m +$ NAP]	Outside water level	Gumbel	u = 6.41	$\alpha = 3.29$	MHW = 9.21
α [-]	SHANSEP α parameter (sometimes S)		0.3		0.3
m [-]	SHANSEP m parameter		0.8		0.8
OCR [-]	Overconsolidation ratio	normal	$\mu = 2$	cov = 10%	
ϕ' [°]	Internal friction angle	normal	$\mu = 30$	$\sigma = 5$ m	
c' [kPa]	Cohesion	normal	$\mu = 4$	cov = 25%	
σ'_t [kPa]	Tensile strength	normal	$\mu = 2$	$cov = 25\%$	

Table I.11: Results for cracking phase in uplift

DP	γ tensile cracks	γ shear cracks	β shear cracks
42	6.498023	1.366719	4.179
43	6.647593	1.473633	4.411
44	7.266164	1.935916	5.452
45	7.944678	2.330721	6.468
46	8.058175	2.184293	6.038
47	6.259920	1.588278	4.559

BIBLIOGRAPHY

Ajaz, A. and Parry, R. H. G. (1975). Stress–strain behaviour of two compacted clays in tension and compression. *Geotechnique*, 25(3):495–512.

Ammeri, A., Jamei, M., Guiras, H., Bouassida, M., Villard, P., Plé, O., Camp, S., and Gourc, J.-P. (2006). A numerical study of compacted clay tensile strength by discrete element modelling: A bending test application. In *First Euro Mediterranean In Advance on Geomaterials and Structures*.

Bagge, G. (1985). Tension cracks in saturated clay cuttings. In *International conference on soil mechanics and foundation engineering. 11*, pages 393–395.

Bakker, M. (2019). Course material of course CIE5440 Groundwater Modelling (2018-2019). TU Delft Brightspace.

Barends, F. B. J. (1999). Opdrijven van het achterland bij hoogwater. *Grondmechanica Delft voor Provincie Zuid-Holland*.

Bisschop, C., Huisman, C. E., Jansen, P., Westhof, W., and Zantige, A. M. (2011). Veiligheid Nederland in Kaart 2. Dijkring 44: Achtergrondrapport.

Brinkgreve, R. B. J. (2019). Lecture slides of course CIE4361 Behaviour of Soils and Rocks (2019-2020). TU Delft Brightspace.

Calle, E. O. F. (2002). Dijkdoorbraakprocessen: Beschrijving, doorbraakprocessen en reststerkte.

CUR2003-7 (2003). Bepaling geotechnische parameters. Technical report.

Diana FEA (2017). *Theory Manual Chapter 38 Cracking*. DIANA FEA bv, Delft. Retrieved from: `https://dianafea.com/manuals/d102/Theory/Theorych38.html#mat:conc:multfix`.

Förster, U., Van den Ham, G., Calle, E. O. F., and Kruse, G. (2012). Zandmeevoerende wellen. *Deltares rapport 1202123-003-GEO-0002 voor Rijkswaterstaat*.

Helenelund, K. V. (1967). *Tension Tests on Fibrous Peat*. Internal Report; no. DBR-IR-346. National Research Council of Canada, Division of Building Research, Ottawa, Canada. doi: `https://doi.org/10.4224/20338044`.

Hoffman, C. (2019). POVM Rekentechieken - FEM Analysis of Uplift. Technical report, POV-Macrostabiliteit. Projectnummer 11201267.

Hong, Y. and Wang, L. (2016). *Deformation and failure mechanism of excavation in clay subjected to hydraulic uplift*. Springer.

Ismail, F., Mohamed, Z., and Mukri, M. (2008). A study on the mechanism of internal erosion resistance to soil slope instability. *Electronic Journal of Geotechnical Engineering*, 13.

Jongejan, R. B. (2017). WBI2017 Code Calibration: Reliability-based code calibration and semi-probabilistic assessment rules for the WBI2017. Technical report, Rijkswaterstaat Ministerie van Infrastructuur en Milieu.

Jongejan, R. B. and Calle, E. O. F. (2013). Calibrating semi-probabilistic safety assessments rules for flood defences. *Georisk: Assessment and Management of Risk for Engineered Systems and Geohazards*, 7(2):88–98.

Jonkman, S. N., Jorissen, R. E., Schweckendiek, T., and van den Bos, J. P. (2018). *Flood Defences: Lecture Notes CIE5314*. Delft University of Technology, 3 edition.

Kanning, W., Teixeira, A., van der Krogt, M., and Rippi, K. (2017). Derivation of the semi-probabilistic safety assessment rule for inner slope stability. Technical report, Deltares. Project 1230086-009-GEO-0030 voor Rijkswaterstaat.

Konrad, J. M. and Ayad, R. (1997). A idealized framework for the analysis of cohesive soils undergoing desiccation. *Canadian Geotechnical Journal*, 34(4):477–488.

Kwakman, L. (2019). Beoordeling binnen- en buitenwaartse macrostabiliteit, Dijkversterking Wijk bij Duurstede - Amerongen. *Sweco en Arcadis rapport C03011.000750 voor Hoogheemraadschap "De Stichtse Rijnlanden"*.

Lanzafame, R. (2019). Lecture slides of course CIE5314 Flood defences (2018-2019). TU Delft Brightspace.

Li, H.-D., Tang, C.-S., Cheng, Q., Li, S.-J., Gong, X.-P., and Shi, B. (2019). Tensile strength of clayey soil and the strain analysis based on image processing techniques. *Engineering Geology*, 253:137–148.

Marchi, M., Gottardi, G., and Soga, K. (2013). Fracturing pressure in clay. *Journal of Geotechnical and Geoenvironmental Engineering*, 140(2):04013008.

Ministerie van Infrastructuur en Milieu (2017). Schematiseringshandleiding piping WBI 2017. Technical report, Den Haag.

Mitchell, J. K. and Soga, K. (2005). *Fundamentals of soil behavior*, volume 3. New York, John Wiley & Sons.

Moallemi, S. and Pietruszczak, S. (2017). Analysis of localized fracture in 3d reinforced concrete structures using volume averaging technique. *Finite Elements in Analysis and Design*, 125:41–52.

Mohammed, A. S. and Vipulanandan, C. (2014). Compressive and tensile behavior of polymer treated sulfate contaminated cl soil. *Geotechnical and Geological Engineering*, 32(1):71–83.

Ponsteen, W., Willemsen, G., Hogervorst, F., and Halter, W. (2019). Droogtescheuren in dijken afdichten met zwelklei - nut and noodzaak. *Geotechniek*, 23 - 4.

Robinson, S., Arbez, G., Birta, L. G., Tolk, A., and Wagner, G. (2015). Conceptual modeling: Definition, purpose and benefits. *2015 Winter Simulation Conference (WSC)*, pages 2812–2826.

Schick, P. (2003). *Ein quantitatives Zwei-Komponenten-Modell der Porenwasser-Bindekräfte in teilgesättigten Böden*. PhD thesis, Inst. für Bodenmechanik und Grundbau.

Schweckendiek, T., Vrouwenvelder, A. C. W. M. (promotor)., and Vrijling, J. K. (promotor). (2014). *On reducing piping uncertainties: A Bayesian decision approach*. PhD thesis, Delft Univeristy of Technology. ISBN: 9789053358801 `https://doi.org/10.4233/uuid:f9be2f7e-7009-4c73-afe5-8b4bb16e956f`.

Šuklje, L. (1969). *Rheological aspects of soil mechanics*. Wiley-Interscience London.

Šuklje, L., Vercon, M., Oliver-Martin, D., and Trollope, D. H. (1961). Barrages en terre, talus et tranchees ouvertes - Earth dams, slopes and open excavations. Technical report. Retrieved from `https://www.issmge.org/uploads/publications/1/40/1961_03_0008.pdf`.

’t Hart, R. (2018). Fenomenologische beschrijving - Faalmechanismen WBI. *Deltares rapport 11200574-007-GEO-0005 voor Rijkswaterstaat*.

Tang, C.-S., Pei, X.-J., Wang, D.-Y., Shi, B., and Li, J. (2014). Tensile strength of compacted clayey soil. *Journal of Geotechnical and Geoenvironmental Engineering*, 141(4):04014122.

TAW (2004). Technisch rapport waterspanningen bij dijken. Technical report. TR26-DWW-2004-057, ISBN 90.269. 5565.3.

Teixeira, A., Wojciechowska, K., and ter Horst, W. (2016). Derivation of the semi-probabilistic safety assessment for piping. wti 2017: Cluster c, piping failure mechanism. *Deltares rapport 120080-002-ZWS-0006 voor Rijkswaterstaat*.

Thusyanthan, N. I., Take, W. A., Madabhushi, S. P. G., and Bolton, M. D. (2007). Crack initiation in clay observed in beam bending. *Geotechnique*, 57(7):581–594.

Tollenaar, R. N. (2017). *Experimental Investigation on the Desiccation and Fracturing of Clay*. PhD thesis, Delft University of Technology.

van Balen, W. (2016). Hydra-Ring 2.0 Software for the assessment of primary flood defences. Technical report, Deltares. Project 1230088-021-DSC-0070 voor Rijkswaterstaat.

Van Esch, J., Verkaik, J., and Nuttall, J. (2016). Numerical modelling of water pressures in dikes. In *RD Highlights 2016*. Deltares.

Vaníček, I. (2013). The importance of tensile strength in geotechnical engineering. *Acta Geotechnica Slovenica*, 10(1):5–17.

Verruijt, A. and Van Baars, S. (2007). *Soil mechanics*. VSSD Delft, the Netherlands.

Wang, J.-J., Zhu, J.-G., Chiu, C., and Zhang, H. (2007). Experimental study on fracture toughness and tensile strength of a clay. *Engineering Geology*, 94(1-2):65–75.